Processes of magmatic and tectonic accretion of oceanic lithosphere at mid-ocean ridges

Constraints from a seismic refraction study at the Mid-Atlantic Ridge near 21.5° N

Dissertation
zur Erlangung des Doktorgrades
der Mathematisch-Naturwissenschaftlichen Fakultät
der Christian-Albrechts-Universität zu Kiel

vorgelegt von
Anke Dannowski

Kiel, 2009

Referent: PD Dr. Ingo Grevemeyer
Korreferent: Prof. Dr. Wolfgang Rabbel

Tag der mündlichen Prüfung: 30. Juni 2009
Zum Druck genehmigt: 15. Juli 2009

gez. Prof. Dr. Lutz Kipp, Dekan

Abstract

Mid-oceanic ridges are plate boundaries where new oceanic crust is created. Especially slow-spreading ridges, like the Mid-Atlantic Ridge (MAR), reveal a complex structure denoted by magmatic and tectonic processes. In the working area of this seismic refractions study both types of crustal accretion are present. The northern segment (22.2° N) compensates tectonically the tensional stresses caused by the plate tectonic movements of the African and the Northern American plates. So called detachment faults or oceanic core complexes (OCCs) develop during that tectonic phase. In the meantime the southern segment (21.5° N) is a magmatically robust segment. The peculiarity of this segment is that it growths south- and northwards along the ridge axis, starting at about 5 m.y. ago. Ridge propagation was strong enough to break through a stable small offset transform fault. During propagation the transform migrated southwards, leaving behind a V-shaped structure the so called inner and outer pseudofaults.

From five seismic refraction and wide-angle profiles, ridge-parallel and ridge-crossing, the seismic velocity structure was observed. The results show a strong crustal variation. The ridge-crossing profiles illustrate the temporal evolution of the crustal accretion within the magmatic robust segment. Past magmatic activities can be reconstructed.

The different morphological and geological features of the area required different inversion and modelling procedures. A broad variety of methods for interpretation of the collected geophysical data were applied to gain a subsurface image and to allow a geological reconstruction. First arrival seismic tomography, joint refraction and reflection tomography, and joint seismic and gravimetric tomography were used. Along the northern profile tomography for the near offset travel time arrivals was used, yielding the shallow part of the subsurface. Joint forward modelling of seismic travel times and gravimetric data made it possible to resolve the structure at greater depth.

The southern and hence magmatically dominated ridge segment shows crustal thickening along the ridge axis from 4 km at the segment ends to about 8 km in the segment centre whereas the crust in the northern basin thins more than beneath the southern ridge tip. Layer 2 is rather constant and the main thickening is taken by layer 3. The seismic velocities in the ridge tip tend to be lower, which could be caused by strong fracturing and partial alteration. In the seismic velocity models crustal thinning has been observed also with increasing distance to the spreading axis. The latter suggests intensified magmatic activity with focussed melt supply in the segment centre leading to an upwelling of the seafloor and an hourglass shaped bathymetry with a small axial valley at the segment centre that widens towards its ends. Melts are transported laterally at crustal levels towards the segment ends, preferable towards the southern ridge tip, while the larger part remains at the segment centre.

The northern segment has a much larger variation of the crustal thickness across the ridge axis. Tectonically dominated crust thins extremely to approximately 40% of average oceanic crust at the western ridge flank near 22°19’. Partly the upper crust is completely missing and high seismic velocities of 7 km/s are reached already a few hundred metres below the seafloor. The asymmetric crustal accretion is also reflected in the seismic velocities that reach a level of normal oceanic young crust on the eastern ridge crest.

This long lived detachment fault shifted the plate boundary towards the west. However, it does not expose mantle material in its central surface. This can be caused at least by two factors: 1) during the tectonic phase the area is magmatically starved but still magmatic accretion occurs. 2) The detachment fault is a steep normal fault, marked by higher seismicity, near the ridge axis and is rotated based on the “rolling-hinge” model to a shallow low-angle fault caused by the slip and the tensional stresses. If the fault is rotated from an optimum angle a new fault will be generated and this fault block (rider or rafted block) stays on the surface of the detachment fault. A petrologic survey detected serpentinised mantle at the steep southern wall of the core complex facing towards the southern segment end. This suggests a three-dimensional structure of the core complex with a detachment fault rooted in an intrusive zone in the mid-segment setting, exposing gabbroic rocks, and a detachment fault rooted near crust-mantle boundary zone towards the segment end unroofing mantle rocks. The uplift of the massif can not be only explained by flexural rotation caused by the tension of the plate tectonic processes. There has to be an additional force. This could be a result of lower dense serpentinised mantle. The density difference will be compensated by an uplift to reach the isostatic equilibrium.

Zusammenfassung

Mittelozeanische Rücken sind Plattengrenzen an denen neue Kruste gebildet wird. Insbesondere langsam spreizende Rücken, wie der Mittelatlantische Rücken, zeigen eine komplexe Struktur und sind durch magmatische und tektonische Prozesse gekennzeichnet. Im Arbeitsgebiet dieser refraktionsseismischen Studie sind beide Formen der Krustenneubildung präsent. Während das nördliche Segment (22.2° N) die durch die Plattentektonik entstehende Dehnungsbeanspruchung hauptsächlich tektonisch kompensiert, in der englischsprachigen Fachliteratur als detachment fault (Trennungsbruch) oder core complex bezeichnet, ist das südlichere Segment bei 21.5° N ein magmatisch sehr aktives Segment. Die Besonderheit dieses Segmentes liegt auch darin, dass es mit seiner Entstehung, vor etwa 5 Mio. Jahren, nach Süden und Norden wächst. Es hatte die Kraft, ein bis dahin scheinbar stabiles System einer Transformstörung zu durchbrechen. Im Verlauf der Fortpflanzung des Segmentes hat sich eine charakteristische V-förmige Struktur des Ozeanbodens herausgebildet.
Aus fünf refraktionsseismischen Profilen, entlang und quer zur Rückenachse, konnten seismische Geschwindigkeitsmodelle bestimmt werden, die eine starke Variation der Krustenmächtigkeit zeigen. Quer zum Spreizungszentrum verlaufende Profile stellen dabei vor allem den zeitlichen Verlauf der Krustenneubildung dar. Veränderungen der Krustenmächtigkeit im südlichen Segment geben so Aufschluss über dessen magmatische Aktivität in der Vergangenheit.
Um die gesammelten geophysikalischen Daten auszuwerten und zu einer Abbildung des Untergrundes zu führen, die eine geologische Interpretation zulässt, wurden in dieser Arbeit verschiedene Methoden angewandt. Tomographie der Ersteinsätze, eine gemeinsame Tomographie aus Ersteinsätzen und Reflektionen, sowie eine gemeinsame Tomographie aus seismischen Einsätzen und gravimetrischen Messungen wurden angewendet. Die unterschiedlichen morphologischen und geologischen Begebenheiten erforderten diese große Bandbreite der Auswertung. Entlang des nördlichen Profils konnte ein strukturgeologisches Modell unter Verwendung einer Ersteinsatztomographie der Nahbereichseinsätze, geringe Eindringtiefe der Wellen in den Untergrund, und einer parallelen Vorwärtsmodellierung aus seismischen und gravimetrischen Daten des größeren Tiefenbereichs entwickelt werden.
Im südlichen Rückensegment ist eine Verdickung der Kruste entlang der Rückenachse von etwa 4 km an den Segmentenden auf ca. 8 km im zentralen Bereich zu beobachten, wobei die Kruste im nördlichen Becken stärker ausdünnt als im Süden und ausschließlich die untere Kruste davon betroffen ist. Das südliche Segmentende, die Spitze des propagierenden Rückensegmentes, zeigt eine deutliche Verringerung der seismischen Geschwindigkeiten, was auf eine Schwächezone mit starker Zerklüftung und teilweiser methamorpher Veränderung der Kruste hinweist, Alteration. Hier ist die Ursache für den südlichen Versatz der Transformstörung zu suchen. Eine Verringerung der Krustenmächtigkeit, nicht nur zu den Segmentenden, ist aus den tomographischen Geschwindigkeitsmodellen

ersichtlich, sondern auch mit zunehmendem Abstand zur Spreizungsachse. Das lässt auf eine Zunahme der magmatischen Aktivität mit fokussiertem Mantelaufstieg im Segmentzentrum schließen, die zu einer Aufwölbung des Meeresbodens führte und auch in der eieruhrförmigen Struktur des Achsentales ausgeprägt ist. Magma wird im Segmentzentrum in die Kruste injiziert und in Richtung der Segmentenden transportiert, vorwiegend in Richtung des südlichen Endes. Der Hauptanteil verbleibt jedoch im Segmentzentrum und führt zur beobachteten Krustenverdickung.
Das nördliche Segment zeigt eine noch stärkere Variation der Krustenmächtigkeit quer zur Rückenachse. Vor allem im Bereich der westlichen Rückenflanke dünnt die Kruste um 40%, im Vergleich zu durchschnittlicher Krustenmächtigkeit entlang des Atlantischen Rückens, aus. Hierbei ist die Oberkruste teilweise komplett verloren gegangen und hohe seismische Geschwindigkeiten von 7 km/s werden bereits wenige hundert Meter unter dem Meeresboden erreicht. Eine asymmetrische Krustenbildung spiegelt sich darin wieder dass auf der östlichen Seite der Plattengrenze seismische Geschwindigkeiten „normaler“ junger ozeanischer Kruste erreicht werden. Der Trennungsbruch (detachment fault), die Plattengrenze, ist sehr langlebig, dennoch wurde bisher kein anstehendes Mantelgestein direkt auf solchen Brüchen gefunden. Das hat zwei Gründe: 1) Der tektonische Prozess ist von zwar verringerter aber steter magmatischer Krustenbildung begleitet. 2) Die Bildung dieses an der Oberfläche flach erscheinenden Bruchs basiert auf einem „rolling-hinge“ (Scharniergelenk) Model. Hierbei kommt es durch die Dehnungskräfte zu normalem Bruchverhalten der das Achsental begrenzenden Brüche, die sich auch in der seismologischen Registrierung bemerkbar machen. Durch die Spreizungskräfte kommt es zu Gleitvorgängen im Übergangsbereich von sprödem und dehnbaren Krustenmaterial und einer Rotation der Bruchblöcke. Durch Überschreiten eines optimalen Bruchwinkels wird eine neue Bruchfläche generiert. Die so entstandenen rotierten Bruchblöcke werden auf dem langlebigen großen Trennungsbruch mitgezogen aber auch erodiert. Die Hebung des ganzen Gebietes kann jedoch nicht allein durch die entstehenden Biegungskräfte erklärt werden. Hier ist ein zusätzlicher Prozess notwendig. Aus dem seismischen Geschwindigkeitsmodell wird erkennbar, dass der Mantel unter der Rückenachse und dem Berg langsamere Bereiche aufweist. Dies könnte auf eine teilweise Serpentinisierung hindeuten die eine Verringerung der Dichte mit sich führt. Der Dichteunterschied wird durch die Hebung kompensiert um das isostatische Gleichgewicht wieder herzustellen. Ein Tauchgang entlang der sehr steilen Südflanke des Massivs brachte serpentinisierten Mantel hervor. Dies lässt auf eine drei-dimensionale Struktur des gesamten Berges schließen. Es wird angenommen, dass der Bruch im Segmentzentrum in einem intrusiven magmenreichen Gebiet endet, und damit vorwiegend Gabbro an die Oberfläche zieht, währen zum Segmentende hin die Kruste ausdünnt, da nicht genug Magma generiert werden kann. Damit liegt das untere Ende des Bruches nahe der Krusten-Mantel Grenze und der Transport von Mantelgestein bis an die Oberfläche wird ermöglicht.

Contents

1 Introduction and Background 9
1.1 Structure of this work 10
1.2 Mid-Ocean Ridges 10
1.2.1 Ridge Types 10
1.2.2 Large-scale variations in axial morphology 12
1.2.3 Segmentation and discontinuities at the MAR 13
1.2.4 Structure of Mid-Oceanic crust 13
1.2.5 Types of Mid-Ocean ridge spreading 15
1.2.6 Serpentinisation at MOR's 17
1.2.7 Segment propagation 18
1.2.8 Proposed models for oceanic core complexes 21
1.2.9 Conceptual physical model on flexural rotation of normal faults 21
1.3 Study area and motivation 23
1.3.1 Why do we want to study ridge propagation? 26
1.3.2 Question about the northern part of the study area 26
1.4 Tectonic settings 27
1.4.1 Propagating ridge segment 27
1.4.2 Active core complex 28
1.5 Related Work 30
1.5.1 Evolution of the segmentation during last 10 million years 30
1.5.2 Dredges and TAMMAR Dive-21 31
1.5.3 Petrology of the TAMMAR Dive-21 32
2 Data and methodology 35
2.1 Data acquisition 35
2.2 OBH data and processing 35
2.2.1 OBH data 36
2.2.2 Data processing 36
2.2.3 Data examples in seismic sections of the profiles 44
2.2.4 Contemplation to the observed shear waves 48
2.2.5 Appearance of crustal magma chambers in seismic data 50
2.3 Gravity data from the study area 53
2.3.1 Instrumentation 53
3 Seismic traveltime forward and tomographic modelling 55
3.1 Forward method 55
3.1.1 Velocity model parameterisation 56
3.1.2 Ray tracing 56
3.2 Inverse method 57
3.2.1 Model parameterisation 57
3.2.2 Forward problem 57
3.2.3 Inverse problem 58
3.3 Gravity modelling 60
3.3.1 Joint seismic and gravity inversion in general 60
3.3.2 The method of joint seismic and gravity inversion 60
3.3.3 Off-axis gravity modelling as a combined forward modelling 62
3.4 Modelling strategy 62
3.4.1 Picking 62
3.4.2 Data uncertainties and traveltime reciprocity 63

3.4.3 Forward versus inverse modelling *63*
3.4.4 Initial model and choice of inversion parameters *64*
3.5 Data misfit and resolution 65
4 Results 67
4.1 Results for profile 2 67
4.1.1 Forward ray tracing *68*
4.1.2 Joint refraction and reflection tomography *68*
4.1.3 Converted shear waves *72*
4.1.4 Joint seismic and gravity inversion *73*
4.2 Profiles 4 and 5 76
4.2.1 Results of profile 4 *76*
4.2.2 Results of profile 5 *77*
4.2.3 Resolution tests for P04 and P05 *80*
4.2.4 Gravity modelling *82*
4.3 Profile 8 85
4.3.1 Tomographic model *85*
4.3.2 Forward Model including Pn-phase and gravity data *87*
4.3.3 Observed PmP reflections *89*
4.3.4 Intracrustal reflections *90*
5 Interpretation and discussion 93
5.1 Along-axis variation 93
5.1.1 Shallow crust *94*
5.1.2 Lower crust and mantle *98*
5.2 Off-axis structures – a temporal evolution 101
5.2.1 Seismic interpretation *101*
5.2.2 Gravity modelling *103*
5.3 Origin of oceanic detachments 103
5.3.1 Models of core complex formation *104*
5.3.2 Data from drilling and dredging *105*
5.3.3 Interpretation for the OCC-study *108*
5.3.4 Constraints on the PmP-phase *109*
5.3.5 Evolution of the core complex *110*
6 Conclusions 115
6.1 Conclusions for the propagating ridge segment 115
6.2 Conclusions for the oceanic core complex 116

Acknowledgement 119
References 120

Appendix A-D 131

1 Introduction and Background

The concept of the mobility of the Earth was proposed more than half a century before the theories of plate tectonics were established. Plate tectonic theory had its beginnings as early as 1596 when the Dutch map maker Abraham Ortelius suggested that America has been “torn away from Europe and Africa … by earthquakes and floods” in his work *Thesaurus Geographicus* [*Kious and Tilling*, 1996]. He already considered the coasts of the three continents. His idea surfaced again in the 19th century. However, it was not until 1912 that the idea of moving continents was seriously considered as a scientific theory. The meteorologist Alfred Wegener proposed the theory of “continental drift” in 1915. He observed that many coastlines (South America – Africa) look as though they fit together like a puzzle. Magellan and other explorers noticed this before him but he was one of first who realised that the Earth’s surface had changed through time. Palaeontologists presented fossils of similar species found on continents that are now separated. Wegener’s ideas were very controversial because he could not explain why the continents moved. At that time, many geologists believed that the separation and collision of continents was caused by cycles of heating and cooling, which resulted in expansion and contraction of the land masses. Although Wegener’s “continental drift” theory was later disproved, it was an important milestone for the development of modern plate tectonics.

A fundamental component of modern plate tectonics is the existence of constructive and destructive plate boundaries in the form of mid-ocean ridges and subduction zones, respectively. Both sites have been studied in ever-increasing detail confirming the initial hypothesis that they are areas of lithospheric generation and recycling, leading to new insights into how the processes operate that affect the face of the solid earth.

The existence of mid-ocean ridges was not known until the 1950s, when they were first discovered by Tharp and Heezen in 1952 with the RV Vema that traversed the Atlantic Ocean and recorded data of the ocean floor. From that time on geoscientists discovered and proposed mechanisms for seafloor spreading [*Hess*, 1962; *Dietz*, 1961].

The mid-ocean ridge system stretches about 80000 km around the globe and accounts for approx. 80% of the Earth’s volcanism. At mid-ocean ridges the stratification used to describe the outer parts of the Earth’s structure diminishes and an interaction between the components occurs. The magmatic and tectonic processes

associated with the construction of new oceanic crust at mid-ocean ridges have a large impact on the crustal structure and the evolution of the oceanic lithosphere.

1.1 Structure of this work

Subject of this thesis are two segments of the slow-spreading Mid-Atlantic ridge that expose an excellent example of a propagating ridge segment and an active detachment fault. Both features are expressions of the large variability of crustal formation at mid-ocean ridges. Ridge propagation might be governed by enhanced magmatic activity whereas detachment faulting is related to starved magma supply. The work focuses on the seismic velocity structure of the oceanic crust, in particular the structures along and across the ridge in the area studied. Gravimetric data and information on rock samples have been integrated into the work.
The three southern profiles (P03, P04, P05) and the along axis profile (P02) investigate the features of the propagating ridge segment. The northern most profile (P08) handles a different segment; the second object of interest, the oceanic core complex with a different style of crustal accretion compared to the southern propagating ridge segment. Thus, from the geological point of view the work is divided into two parts. Since the processing of the data is very similar for all profiles, each chapter covers both main targets of this work with general descriptions in the beginning.
The southern line P03 and the seismologic network have been interpreted by a project partner at the University of Cambridge (Kahle, 2007).

The thesis gives an overview on the basic knowledge of mid-ocean ridges and describes the study area from the geological point of view. Chapter 2 summarizes the data set that has been used. The description of the methodology applied to interpret the data is followed by the presentation of the results for each seismic line in Chapter 4. The interpretation and discussion of the results is performed in Chapter 5. The two main study objects are treated separately starting with the southern segment lines p02, p04, and p05. While p02 displays the along axis variation at zero-age crust, p04/05 give information about the recent past 5 m.y. of magmatic crustal accretion. Line p08 and the data from former studies are discussed in the second part of section 5. The conclusion in Chapter 6 is also divided into two parts.

1.2 Mid-Ocean Ridges

1.2.1 Ridge Types

Ridge-push and slab-pull are forces thought to be responsible for the spreading at mid-ocean ridges. The strength of these forces is different, thus, the rate at which mid-ocean ridges create new material differs between different plates. Spreading ridges are generally classified as fast, medium, and slow with values of >100 mm/yr, 100 – 55 mm/yr and <55 mm/yr, respectively, for full spreading rate. Two more classes can

be found: ultra-slow with <20 mm/yr and ultra-fast spreading with up to 210 mm/yr. While ultra-slow ridges are mostly found in polar or near-polar regions (Gakkel Ridge and South West Indian Ridge in the northern and southern hemisphere, respectively), ultra-fast spreading occurred in the South central Pacific Ocean. Tab. 1.1 gives a short overview of the main characteristics of spreading centers as a function of spreading rate. The ridge types differ not only in the spreading rate but also in morphology, magmatic activity, and crustal thickness.

Tab. 1.1 Morphology and characteristics of ridges by spreading rate [*Macdonald*, 1982]. The morphology along the ridge is strongly dependent on the magma supply.

	spreading rate	morphology	magmatic activity	crustal thickness
slow-spreading 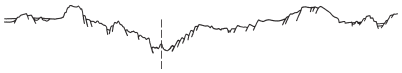 Mid-Atlantic Ridge	20 – 55 mm/yr	10 – 20 km wide and 1-3 km deep axial valley;	Very low, sporadic magma supply Rarely hydrothermal events (fault related); Extensive fissuring	Highly variable; Narrow low velocity zone Thick layer 2A beneath axial volcanic ridges.
medium-spreading 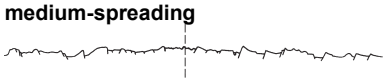 Juan de Fuca Ridge	55 – 100 mm/yr	Axial high or rift valley depending on the magma supply.	In-between and strongly dependent on the magma supply	
fast-spreading 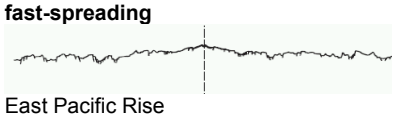 East Pacific Rise	> 100 mm/yr	A few hundred metres elevated axial high; Almost no normal faulting within 2 km of the ridge axis	highly magmatic, less crustal fissuring; hydrothermal venting abundant	Thin crust with melt that flows away from the upwelling zone. Layer 2A thinnest along axis.

Models correlate the crustal thickness with magmatic activity and the resulting magma supply [*Macdonald*, 1991]. The axial depth of mid-ocean ridges undulates. In contrast to fast and intermediate spreading rates, the wavelength of the undulation at slow-spreading ridges is shorter and the amplitude is higher [*Macdonald*, 1998]. Discontinuities occur along the ridge axis, including transform faults, overlapping spreading centres and higher order discontinuities. However, even at the segment scale the seafloor shows a number of regularities [*Chen and Lin*, 1999]: the seafloor is often most elevated at the midpoint of a segment but deepens systematically towards segment offsets; the rift flank topography is most symmetric at segment centres but becomes highly asymmetric near ridge offsets; spacing and throw of rift-bounding normal faults appear to be smallest at segment midpoints; large-amplitude normal faults tend to be located at inside corners. The seafloor deepens from a global average of ~2600 m at the spreading centre to > 5000 m beyond the ridge flanks [*Macdonald*, 1998].

1.2.2 Large-scale variations in axial morphology

The axial depth profile of the Mid-Atlantic ridge (MAR) undulates with a much shorter wavelength compared to intermediate and fast spreading centres [*Macdonald*, 1998]. However, it also shows a large variation of the across-axis morphology.

Gravity studies [*Lin and Phipps Morgan*, 1992] indicate that the amplitude of along-axis crustal thickness variation decreases with increasing spreading rate, suggesting that the crustal accretion style depends on mantle temperature variation and plate spreading rate: mantle upwelling is intrinsically plume-like (three-dimensional) beneath a slow-spreading ridge but more sheet-like beneath a fast-spreading ridge. The crustal thickness variation is significantly reduced at fast-spreading ridges. Along the fast-spreading East Pacific Rise (EPR) the crustal accretion is relatively uniform compared to the complex and variable structure of slow-spreading ridges, such as the MAR [*Niu et al.*, 2001].

Studies of many MAR segments show a correlation of the bathymetric structures with circular gravity lows - the so called ‘bull’s eyes’ [*Tolstoy et al.*, 1993; *Detrick et al.*, 1995]. The segment centres are characterized by negative Bouger gravity anomalies. Explanations for the gravity observation have been given by *Magde et al.* [1995; 1997] in studies of the OH-1 segment (between Oceanographer, 35° N, and Hayes, 33° N, transform), where they suggest that the along-axis crustal thickness variation is a result of three-dimensional mantle flow patterns and melt migration. The thinnest crust can be found at segment ends, whereas the crust is thickest at the segment centre [*Detrick et al.*, 1995]. *Canales et al.* [2000] proposed that the Moho does not correlate with a unique geological structure. At the segment centre the Moho is likely to be related to the gabbro-dunite transition zone, whereas at the segment ends it could correspond to an alteration front (Figure 1.1).

Fig. 1. [*Cannat et al.*, 1995] shows that most crustal thinning occurs in layer 3. A low velocity zone in the lower crust and upper mantle may promote focused melt supply at the segment centre [*Dunn et al.*, 1997].

Nevertheless, the extent of mantle melting and crustal production vary between segments of different length though they have similar spreading rate. *Niu et al.* [2001] demonstrate that the observed differences reflect the extent of mantle melting, melt production, and crustal mass between segments. They are controlled by their fertile mantle source composition. Deeper melt areas lead to a taller melting column, higher degrees of decompression melting, greater melt production, thus thicker crust and a more negative Bouger gravity anomaly.

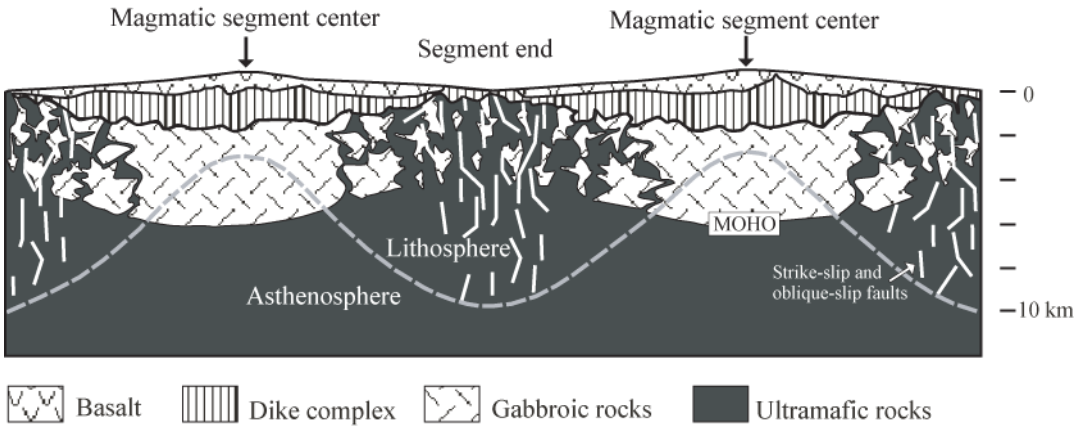

Fig. 1.1 Crustal and upper mantle structure along the ridge axis of a slow-spreading oceanic ridge [*Cannat et al.*, 1995]. Thick crust but thin lithosphere is depicted in the segment centre whereas the segment ends show crustal thinning by a thickening of the lithosphere.

1.2.3 Segmentation and discontinuities at the MAR

The continuity of the ridge system is disrupted by offsets of various magnitudes every 50 - 100 km [*Macdonald et al.*, 1988]. Thus, the ridge crest is strongly segmented. Distinct discontinuities define the segment boundaries. A hierarchy for the ridge-axis segmentation has been established based on the continuity of the ridge axis, the offset distance, and the presence of topographic or structural traces [*Schouten et al.*, 1985; *Macdonald et al.*, 1991; *Sempere et al.*, 1990]. First order discontinuities in both slow and fast spreading crust are transform faults like the Kane transform fault boundary to the north and the Fifteen-Twenty transform fault south of the study area (Fig. 1.7). They normally offset the ridge by up to 30 km or even more (0.5-2 ma). Overlapping spreading centres are examples for fast spreading second-order discontinuities (EPR at 9° N). They have smaller offsets ranging down to <10 km. In slow spreading crust like the MAR they appear as deep bathymetric depressions [*Tucholke and Lin*, 1994]. Second and third order segments are non-offset discontinuities.

Fossil transform zones, i.e., fracture zones, trace the history of relative plate motion for tens of millions of years [*Tucholke and Schouten*, 1988] while the traces of second order discontinuities are moderately developed as a series of crustal depressions that have a variety of orientations and do not follow the directions of relative plate motion. In slow spreading crust they persist for 10 ma or more [*Tucholke and Schouten*, 1988]. Higher-order segments that cause only small offsets (<2 km) of the volcanic ridges or are only an interruption of the neogonic magmatic zone are not known to create coherent morphologic patterns [*Tucholke and Lin*, 1994].

1.2.4 Structure of Mid-Oceanic crust

Crustal rocks are divided into granitic type continental crust (average density 2.8 g/cm³) and basaltic type oceanic crust (average 3.0 g/cm³). The oceanic crust is about 6 km thick compared to the continental granitic crust of 30-60 km. The oceanic crust is remarkably similar in composition and thickness in all oceans. A complete section of oceanic crust has not been drilled so far. However there exist good estimations of their composition by indirect observations (boreholes, submersible dives, gravimetric,

seismic, and magnetic data, ophiolites among others). The oceanic crust accreted at Mid-Ocean Ridges (MOR) can be described by a three layer model presented in Figure 1.2. The layers have been derived based on the analyses of seismic structures of the oceanic crust compared with laboratory determinations of seismic velocities in known rock types and ophiolites. Rock samples have been recovered from the ocean floor by dredging, drilling, and by submersibles. Ophiolites are uplifted or emplaced sections of oceanic crust, and possibly underlying upper mantle, exposed within continental crust. Well known ophiolites can be found, for example, in Oman and United Arab Emirates, Troodos (Cyprus), Jormua (Finland), and Bay of Island (Newfoundland).

Generally the oceanic crust is divided into three main seismic layers:
Layer 1 consists of unconsolidated or semi-consolidated sediments. This layer is usually thin or may even be absent at the spreading centre and thickens further away from the ridge axis. Near continental margins the sediment enters from land. Deep sea sediments originate from volcanic ash and sediments transported by turbidity currents or are made of tiny shells of marine organisms.
Layer 2 is typically subdivided into two separate layers. Seismic Layer 2A, the uppermost volcanic layer, has a thickness of roughly 500 m. This layer consists of glassy crystalline basalt - usually pillow basalt. This low-seismic-velocity layer (< 3.0 km/s) is underlain by a high-velocity-gradient region (> 5.0 km/s reached in a few hundred metres). Layer 2B is up to 1.5 km thick, has a velocity gradient as high as 2 s^{-1}, and is primarily composed of diabase dikes.
Layer 3 is a layer of coarse grained gabbros and cumulated with ultramafic rocks. The gabbros are chemically equivalent to the basalts but formed by slow cooling of magma that was trapped beneath the surface. The layer thickness is typically about 4 km, has velocities of about 6.7 to 7.2 km/s, and is characterised by low velocity gradients of 0.1 s^{-1}.
Layer 3 is separated from the upper mantle by the Mohorovičić discontinuity (Moho), a transition zone varying in thickness from a few hundred metres to 1-2 km, with a more or less abrupt change in seismic velocities (from about 7.2 km/s to mantle velocities). The boundary between layer 1 and layer 2 is connected to a sudden change in velocities leading to a prominent reflection in the seismic data, whereas the transition from layer 2 to layer 3 is more gradual in terms of seismic velocities.
The seismic layer 2A is often interpreted as the geologic boundary between lavas and dykes [*Christeson et al.*, 1992]. Alternatively the layer 2A/B boundary is assumed to be an alteration front within the lava unit [*Rohr et al.*, 1988; *Christeson et al.*, 2006]. *Purdy* [1987] confirmed the existence of this layer at the MAR at 23° N using on-bottom sources and receivers. A seismic velocity of 2.1 km/s in the median valley was documented. The layer is highly variable at the MAR compared to the fast-spreading EPR. *Grevemeyer and Weigel* [1996] concluded that crustal velocity doubles within 5 million years and remains constant thereafter. Hydrothermal alteration has been recognized as cracks being filled with alteration products. Most alteration occurs within the first 3 million years and continues to 15 million years [*Carlson*, 1998].

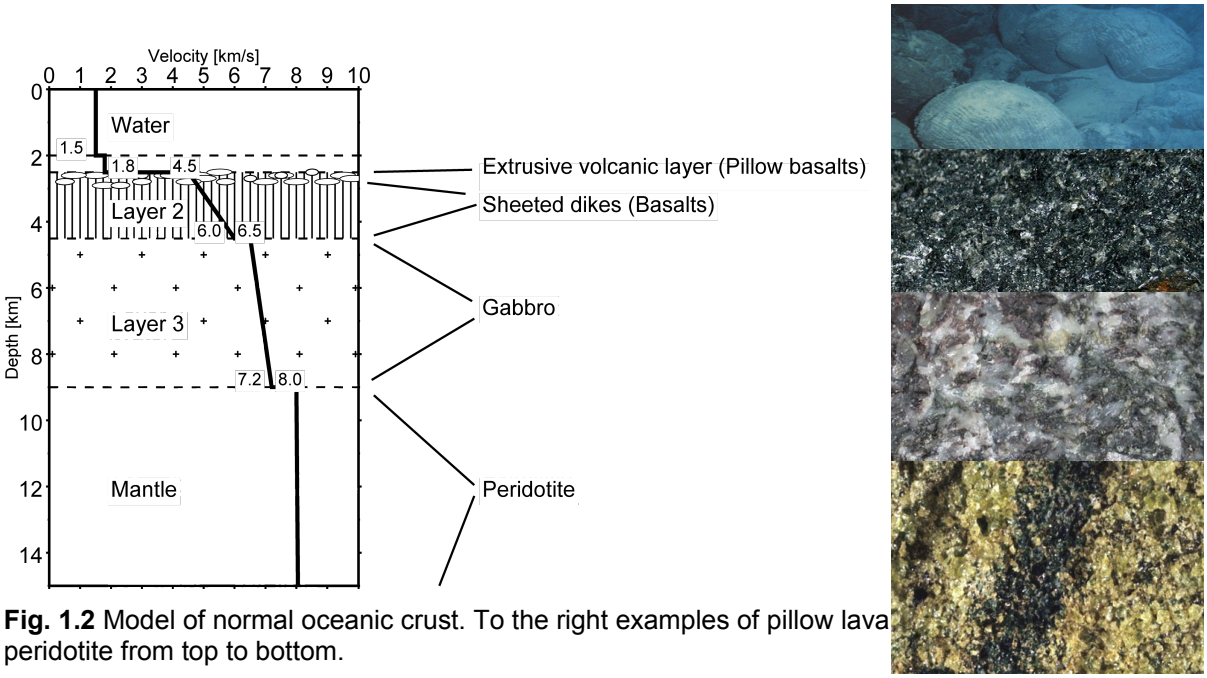

Fig. 1.2 Model of normal oceanic crust. To the right examples of pillow lava peridotite from top to bottom.

The youngest oceanic lithosphere can be found at oceanic ridges. It progressively gets older with distance to the ridges. Generally, it reaches an age of not more than 150 million years before subduction. The oldest oceanic lithosphere discovered is a 3.8 billion year old rock formation in Greenland [*Mehta*, 2007] in form of an ophiolit. However, ophiolites are no longer 'normal' oceanic crust, as they have been exposed. Thus, the oldest oceanic crust in the cycle of generation and recycling is up to 180 million years at the passive margins of the North Atlantic, east of Africa, and near Japan. Still in discussion are parts of the Mediterranean Sea. If this is in fact oceanic crust, then the oldest oceanic crust by far can be found in the ancient Thetys, with an age of up to 280 m.y. [*Muller et al.*, 2007].

1.2.5 Types of Mid-Ocean ridge spreading

The segmentation of the slow-spreading ridge centres is complex (section 1.1.1). This is also reflected in axial outcrops of deep crustal and mantle derived rocks. Nearly all known oceanic exposures of serpentinised mantle are located along slow-spreading ridges [*Cannat*, 1993]. Recent studies distinguish two types of oceanic lithosphere accretion at slow-spreading ridges: i) magmatic accretion where space generated by the plate tectonic processes is filled by magmatic dike intrusion at lower stress than for the second type, and ii) tectonic accretion with faults that slip and accommodate tension [*Price and Cosgrove*, 1990]. For this reason many authors assume that large slip faults form only during periods when no magma is available for dike intrusion and that the total slip on faults depends on the total time interval between magmatic events [*Thatcher and Hill*, 1995].

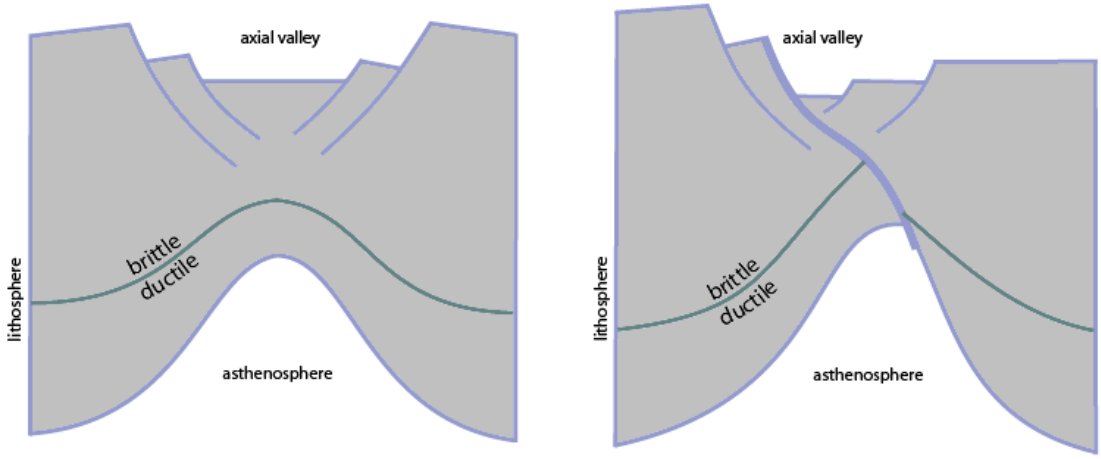

Fig. 1.3 Sketch after *Cannat* [1993] of two possible configurations of the axial deformation zone. To the left: symmetrical stretching while the overall pattern of the brittle-ductile shear zone is symmetrical, a magmatic active segment. To the right: asymmetrical detachment faulting. The extensional strain is concentrated along a single shear zone.

These long-lived slip faults, detachment faults, are the surface of so called 'oceanic core complex' (OCC) or 'megamullion' structures [*Karson et al.*, 1987a; *Cann et al.*, 1997; *Tucholke et al.*, 1998]. Detachment faulting dominates the MAR spreading compared to the aseismic magmatic accretion [*Escartin et al.*, 2008]. Characteristics of fault-dominated segments are blocky topography with domal core complexes that are often corrugated [*Cann et al.*, 1997; *Blackman et al.*, 1998; *Tucholke et al.*, 1998]. Active detachment faulting is associated with high seismic activity in the colder thermal regime compared to magmatic segments [*Smith et al.*, 2006]. They can develop at slow- and intermediate spreading mid-ocean ridges anywhere along the segment [*Cannat et al.*, 2006]. The area of interest in this thesis (Fig. 1.7) shows both types of crustal accretion (Fig. 1.3) that will be discussed and studied in the following chapters.
The asymmetrical tectonic process exposes gabbroic plutons and partially serpentinised peridotite [*Cannat*, 1993]. In some cases, lava flows lie directly over mantle peridotite without intervening gabbroic lower crust; thus, this region is "magma-starved".
Magmatically active segments display an important variability in axial valley morphology, faulting pattern, and volcanic activity between segment centre and discontinuities [*Karson et al.*, 1987a; *Purdy et al.*, 1990; *Sempéré et al.*, 1993, *Durand et al.*, 1995]. A narrow inner valley with intense volcanism bordered by few large faults reaching a vertical throw of 800 m marks the segment centre. The deep and wide axial valley at the segment ends exhibits low volcanic activity (Fig. 1.4). The crust produced by melting of upper mantle material, thins towards segment ends and frequently mantle rocks outcrop near the segment ends [*Cannat et al.*, 1995]. This result is consistent with the presence of microseismicity studies that show an increase in the maximum depth of earthquakes from segment centres to segment ends [*Kong et al.*, 1992; *Toomey et al.*, 1990]; thus, reflecting a deepening of the brittle-ductile transition (Figure 1.4).

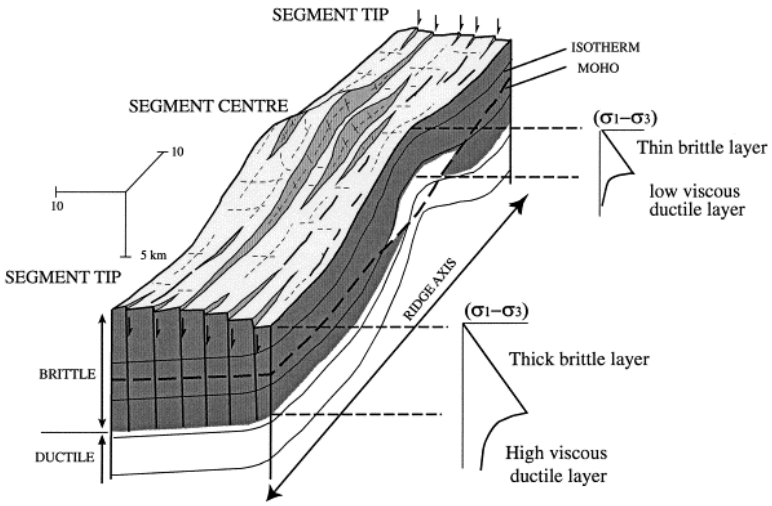

Fig. 1.4 Schematic view of the along axis variation in rheologic profile and observed morphology along a slow-spreading segment with strong variation in along-axis thermal structure [*Thibaud et al.*, 1999].

1.2.6 Serpentinisation at MOR's

Serpentinite is a more or less green metamorphic rock consisting predominantly of serpentine minerals. The name (Latin: serpentis = snake) may refer to the flecked appearance or possibly has been derived from its alleged antidotal effect against snake poison [*Schuhmann*, 1985]. It originates during regional metamorphism from ultra-basic igneous rocks (peridotite, pyroxenite) through the alteration (serpentinisation) of olivine or more rarely pyroxenes.

Serpentinisation of mantle peridotite is believed to play a key role in the tectonic evolution of the slow-spreading ridges [*Francis*, 1981]. Exhumed peridotite is 95-100% serpentinised. Generally spoken, the process of serpentinisation represents the formation of serpentine minerals from pre-existing minerals like olivine and pyroxene. For example [*Alt and Shanks*, 1998]:

Olivine + Water → Serpentine + Brucite + Magnetite

These mineral alteration reactions can proceed in two different temperature regimes. High-temperature serpentinisation (200°-400° C) occurs in transform faults where water can penetrate to great depths. Low-temperature serpentinisation of mantle peridotites is characterized by temperatures of 20°-200° C and high water/rock ratios [*Alt and Shanks*, 1998]. The reaction occurs at shallower depths.

Skelton and Valley [2000] have emphasized a low frictional strength of serpentinite. Thus, the uppermost portion of the serpentinised mantle represents a low shear strength zone that is favourable for the development of a detachment fault. The ability of serpentinite to flow plastically at low stresses means that it can act as a lubricant during fault block rotation.

From the geophysical point of view, the effects of serpentinisation concern the change in physical properties. According to *Francis* [1981], a completely serpentinised mantle rock has a density of 2.55 g/cm³ and a P-wave velocity of 4.5 km/s [*Carlson and Miller*, 2003], whereas a 50% serpentinisation results in a density of 2.90 g/cm³ and a P-wave

velocity of 6.7 km/s. For comparison, an unaltered peridotite is characterised by a density of 3.3 g/cm³ and velocities of > 8 km/s. Fracturing, however, may also decrease values significantly. Thus, no reliable discrimination between different rock types can be made based on seismic velocity data alone.
Canales et al. [2008] found that areas where serpentinites have been dredged were characterised by P-wave velocities of < 3.5 km/s, whereas velocities of > 4 km/s generally occur where gabbros have been found. This might be because of strong fracturing in the upper metres of the subsurface.

1.2.7 Segment propagation

Rift propagation along mid-ocean ridges was first recognised by *Hey* [1977]. It has been observed along mid-ocean ridges independent of their spreading rate. Fig. 1.5 shows several areas were segments do propagate at different scales.
While propagating ridge wakes from offsets greater than ~ 10 km occur at slow- and intermediate-spreading ridges, at ridges spreading faster than ~ 75 mm/yr the amplitude of the wake topography decreases strongly [*Phipps Morgan and Sandwell*, 1994].
In general, the term propagating ridge represents the lengthening of one spreading segment at the expense of its neighbouring segment. The offset between them migrates into the old lithosphere created by the shortening segment.
Geometrically, a model of a propagating ridge system can be described as in figure 1.6. A constant propagation rate is assumed for the lengthening ridge. The shortening segment is known as the doomed ridge (DR). Two pseudofaults (PF) in a V-shape is a characteristic signature [*Schouten et al.*, 1987; *Gente et al.*, 1995; *Thibaud et al.*, 1998] of the propagation, demarking the boundary between the two segments. A transform zone between the propagating and the doomed ridge is created. Within the transform zone, active deformation takes place as material is transferred from one plate to the other. This area is marked as transferred lithosphere (TL) compare to Figures 1.6 and 1.7 between the failed ridge (FR) and the inner pseudofault (PFi). The tectonic elements are marked in the bathymetric map (Figure 1.7) of the study area.

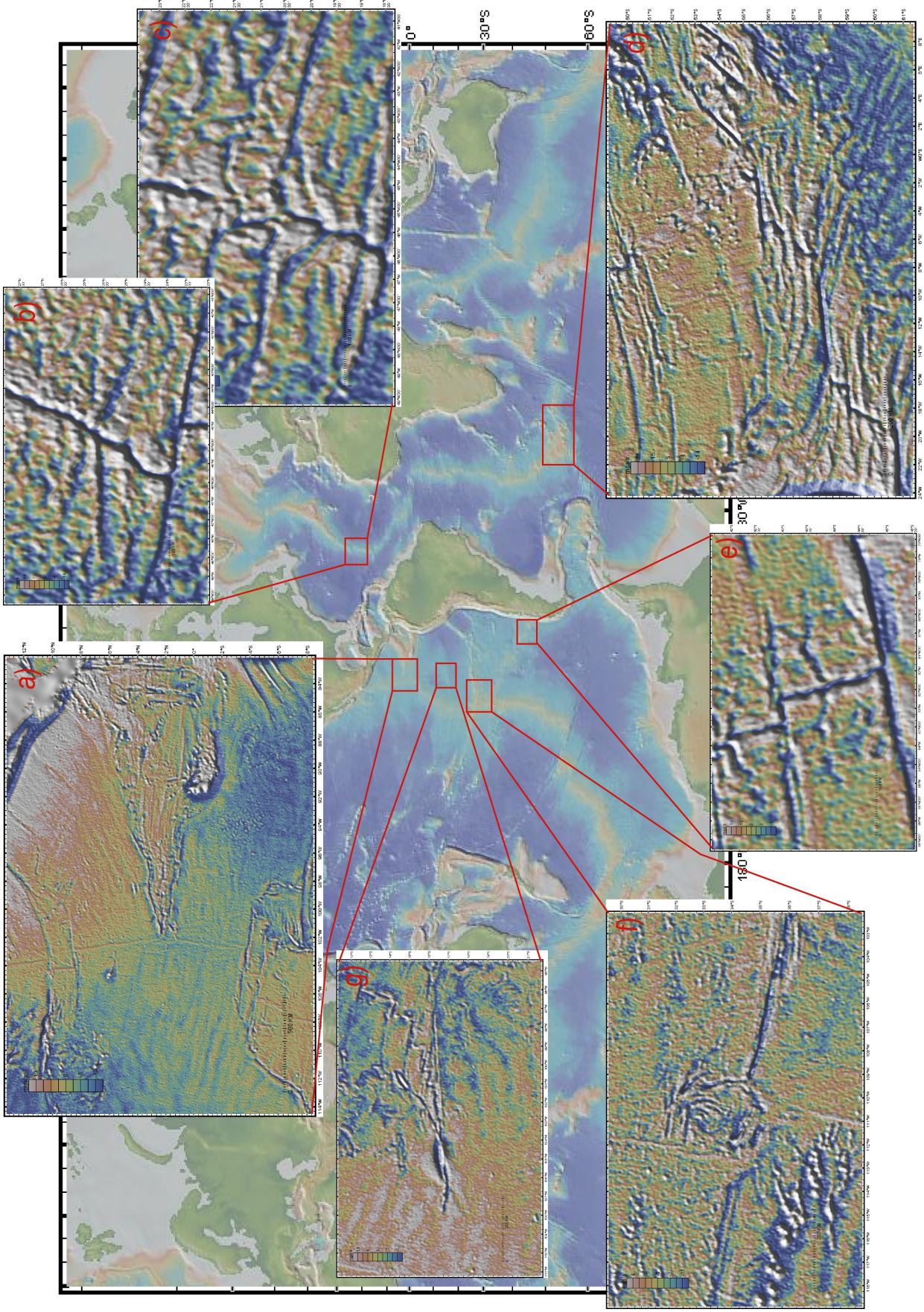

Fig. 1.5 World map indicating propagating Mid-ocean ridge segments. The world map is a topographic map (Smith and Sandwell, 1997). The figures a – g are a zoom into the marked areas and presenting the gravimetric response (Smith and Sandwell, 1997).

Attempts to describe the nature of propagating ridges have been made:

- *Phipps Morgan and Parmentier* [1985] and *Phipps Morgan and Sandwell* [1994] showed that rifts at medium and fast spreading ridges tend to propagate down the along-axis topographic gradient. Stresses at the crack tip are concentrated, caused by differential gravitational sliding stresses.
- *Phipps Morgan and Sandwell* [1994] figured out that all off-axis V-shaped traces between the Azores platform (39° N) and 27° N point southward, in crust less than 10 million years.
- South of this they point randomly to the north or to the south, splitting the ridge flanks into rhomb-shaped areas [*Gente et al.*, 1995].
- *Macdonald et al.* [1991] related crack length with the crack propagation driving force: a longer ridge section should lengthen at the expense of adjacent shorter sections.
- For segments located south of 27° N *Thibaud et al.* [1998] observed that segments presenting a stronger ΔMBA systematically propagate into those with a lower ΔMBA.
- Changes in the direction of seafloor spreading have coincided with rift propagation [*Wilson et al.*, 1984; *Hey et al.*, 1989].
- Correlations with residual gravity data imply that crustal thinning and/or mantle cooling occurred coevally with the initiation and migration of the propagators [*Lin et al.*, 1993; *Tucholke et al.*, 1997; *Kleinrock et al.*, 1997]. Thus the propagators seem to have developed during transition from more magmatic to less magmatic periods of spreading.

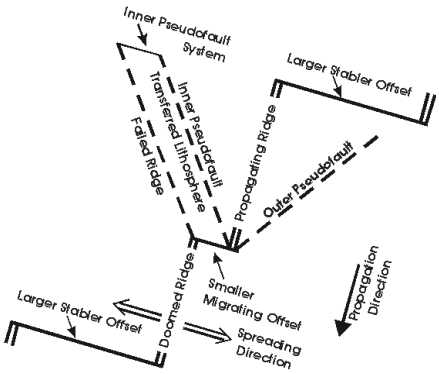

Fig. 1.6 Schematic diagram of the tectonic elements of a propagating rift after *Hey et al.* [1986].

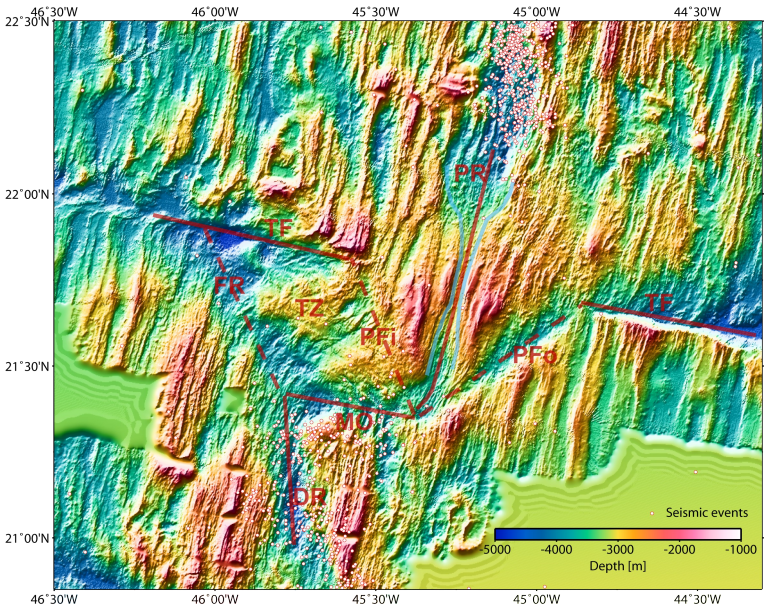

Fig. 1.7 Tectonic elements in the bathymetric map of the propagating ridge system. Shown are propagating ridge (PR), doomed ridge (DR), failed ridge (FR), ancient transform (TF), migrating offset (MO), sheared zone of transferred lithosphere (TL), inner pseudofault (PFi) and outer pseudofault (PFo). In light blue the axial valley is marked.

1.2.8 Proposed models for oceanic core complexes

The extension of the oceanic lithosphere during seafloor spreading creates oceanic core complexes defined by broad, elevated massifs [*Karson et al.*, 2006]. These low-angle detachments may accommodate tens of kilometres of extension, leading to exhumation and uplift of lower crust and mantle rock sections [*Mutter and Karson*, 1992; *Cannat et al.*, 1995; *Tucholke et al.*, 1998]. The ridgeward-dipping of detachments with a convex-upward geometry flattening updip from 30° to less than 15° has been shown in seismic reflections studies [*Ranero and Reston*, 1999]. However, little is known about the subsurface dip of active detachment faults.

Two competing models exist that describe the subsurface geometry: The first envisages a constant dip low-angle detachment cutting through the magmatic zone under the ridge axis [*Karson and Winters*, 1992]. The second suggests a steepening detachment and offers three end-member models, as can be seen in Figure 1.8: i) the detachment is rooted at the shallow cold lithosphere, possibly related to serpentinisation fronts as shown in Figure 1.8a [*Escartin et al.*, 2003], ii) *Tucholke et al.* [1998, 2001] proposed a detachment fault rooting at the brittle ductile transition under the ridge axis, at the base of the lithosphere (Figure 1.8b). The amagmatic extension results in the formation of a detachment fault that accretes lithospheric mantle and exposes the deep lithosphere. iii) And a third type of model roots the detachment fault near a melt-rich zone near the ridge-axis [*Dick et al.*, 2000]. A continuous magmatic crust is formed during detachment faulting that result mainly in exposed gabbros (Figure 1.8c).

1.2.9 Conceptual physical model on flexural rotation of normal faults

When strain is built up in a rock and reaches a certain level that exceeds the strain threshold, the accumulated potential energy is released as strain, which is focused onto a plane along which relative motion is accommodated. Three major types of faults exist: strike-slip, normal, and reverse. Each different type of plate boundary is characterized by one of the three main types. Reverse faulting can be found at convergent boundaries. Strike-slip faulting occurs in areas with lateral motion of the crust like at transform boundaries. Normal faulting is associated with crustal extension, as occurs at divergent plate boundaries.

The fault mechanics theory predicts that faults have a range of optimal orientations to the principal stresses. If a fault segment is significantly rotated from an optimum angle of slip relative to the crustal stress field, then a new planar fault oriented in the optimum direction will replace it [*Buck*, 1988]. According to the Mohr-Coulomb criterion [*Coulomb*, 1773], shear failure will occur once the shear strength and internal friction of a material are overcome.

Based on the assumption that the maximum compressive stress σ_1 is vertical and the minimum compressive stress σ_3 is horizontal the simple fault mechanics theory [*Anderson*, 1951] predicts preferred fault dips of 45° to 70° from the horizontal.

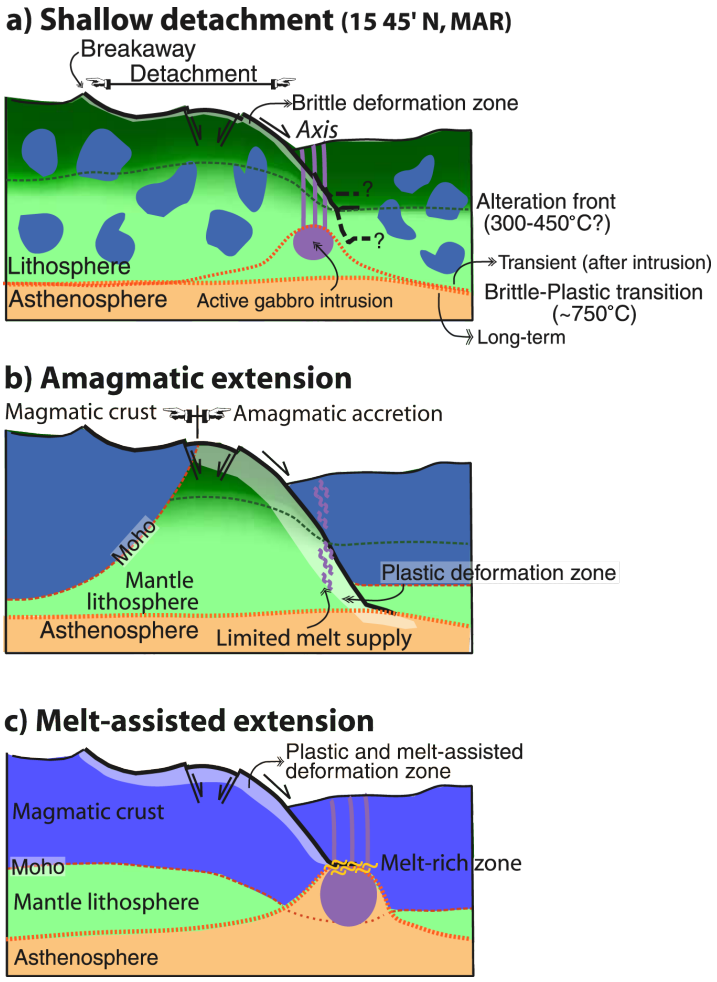

Fig. 1.8 Proposed models for oceanic core complexes from *Escartin et al.* [2003]. (a) *Escartin* presents a model of a detachment fault rooting in the shallow lithosphere possibly related to an alteration front. (b) *Tucholke et al.* [1998] proposed a detachment rooting at the base of the lithosphere leading to exposure of deep lithosphere. (c) Mainly gabbroic rocks deformed at high temperatures are exposed by *Dick's et al.* [2000] model where the detachment fault roots at a melt-rich zone.

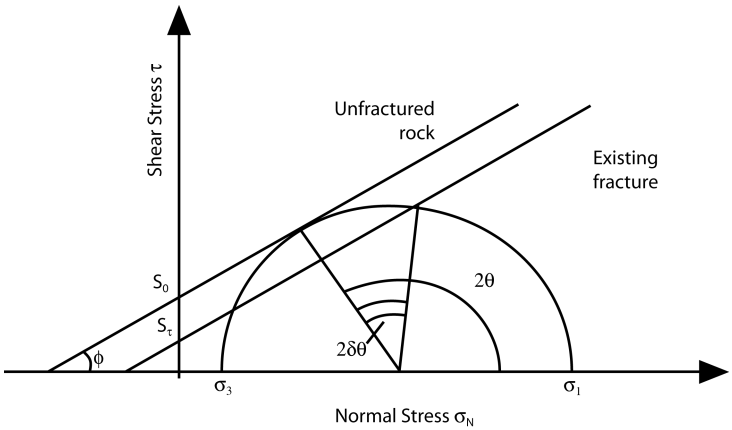

Fig. 1.9 Shear failure; *Buck* [1988].

1.3 Study area and motivation

The area was first explored by cruise 44 of R/V Chain [*van Andel et al.*, 1965; *Melson and van Andel*, 1966] and in a second cruise on R/V Thomas Washington in 1965 [*Melson et al.*, 1968]. Rock samples were collected during this second expedition. RC2511 [*Detrick et al.*, 1984] was followed by a cruise in 1991 (SEADMA1) aboard R/V L'Atalante [*Gente et al.*, 1991, 1995], during which multibeam bathymetry, gravity and magnetic data were obtained [*Maia and Gente*, 1998]. From these observations the previous collected bathymetry data had been extended. In May 1996, the TAMMAR cruise of R/V Nadir and submersible Nautile continued the multidisciplinary studies of this area by conducting 21 dives. Rock samples were collected and magnetic measurements were performed.

The increasing knowledge of this part of the Mid-Atlantic ridge gave space to more questions and for that reason the R/V Meteor went to the location and shot several seismic lines and deployed a long term seismologic network. The seismic refraction and wide-angle reflection data collected during the cruise are the basis of this thesis.

The study area in the frame of this work reaches from 20.8° N to 22.2° N and 44° W to 46°W (Fig. 1.10). It has a complex tectonic history associated with the movement of the North-American and the African plates. The complexity of this area is represented by the prominent V-shaped and domed features visible in the bathymetric and gravity data (Figures 1.11 and 1.12) and the exposure of lower crustal and upper mantle rocks.

Both types of crustal accretion (described in section 1.2.5) occur in the area and they are marked not only by the bathymetric and gravity data but also in the micro earthquake distribution (Figure 1.12). In the central part, around 21.5° N of the ridge axis, magmatic crustal generation is observed and this is highlighted by a seismic gap along the MAR. Meanwhile, the discontinuity in the north at 22.2° N shows seismicity mainly beneath the ridge axis and creates new crust by tectonic processes. While the southern segment (TAMMAR segment) is stable at the northern end, the southern end migrates towards the south and replaces the next southern segment. The segment is growing along axis; thus it propagates southwards. Both features will be examined carefully in this work.

The field program of this study took place between 8th December 2003 and 12th January 2004 during the Meteor cruise M60/2. Four seismic refraction profiles were situated along and across the ridge axis of the propagating ridge segment (profiles illustrated and named in Figure 1.11). An additional refraction line across the ridge axis north of the propagating ridge segment could be acquired to study the behaviour of non-magmatic spreading. Wherever possible, the exact location of the ocean bottom hydrophones was chosen by the seafloor information gathered by French dives and high-resolution bathymetric data.

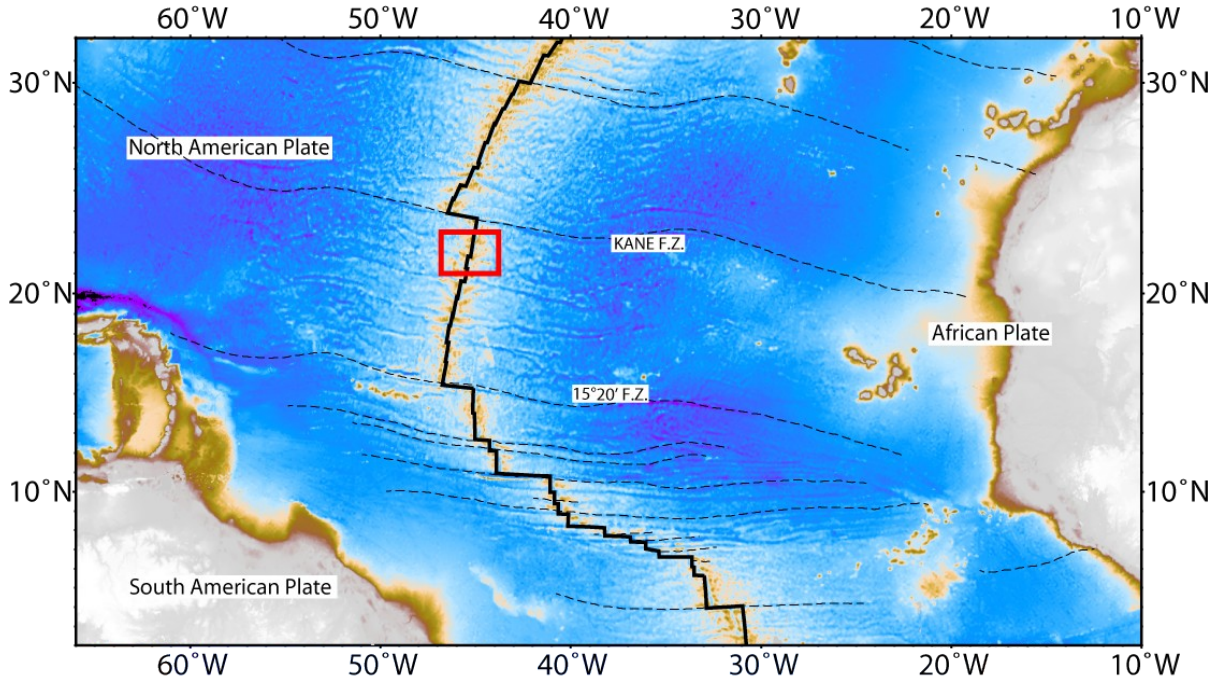

Fig. 1.10 Bathymetric map (satellite derived data [*Sandwell and Smith*, 1997]) of the Mid-Atlantic Ridge. The red rectangle marks the study area of this thesis that is situated at the divergent plate boundary of North American Plate and the African Plate. North of this area towards the Kane fracture zone follows the well studied MARK area (Mid-Atlantic Ridge south of Kane fracture zone).

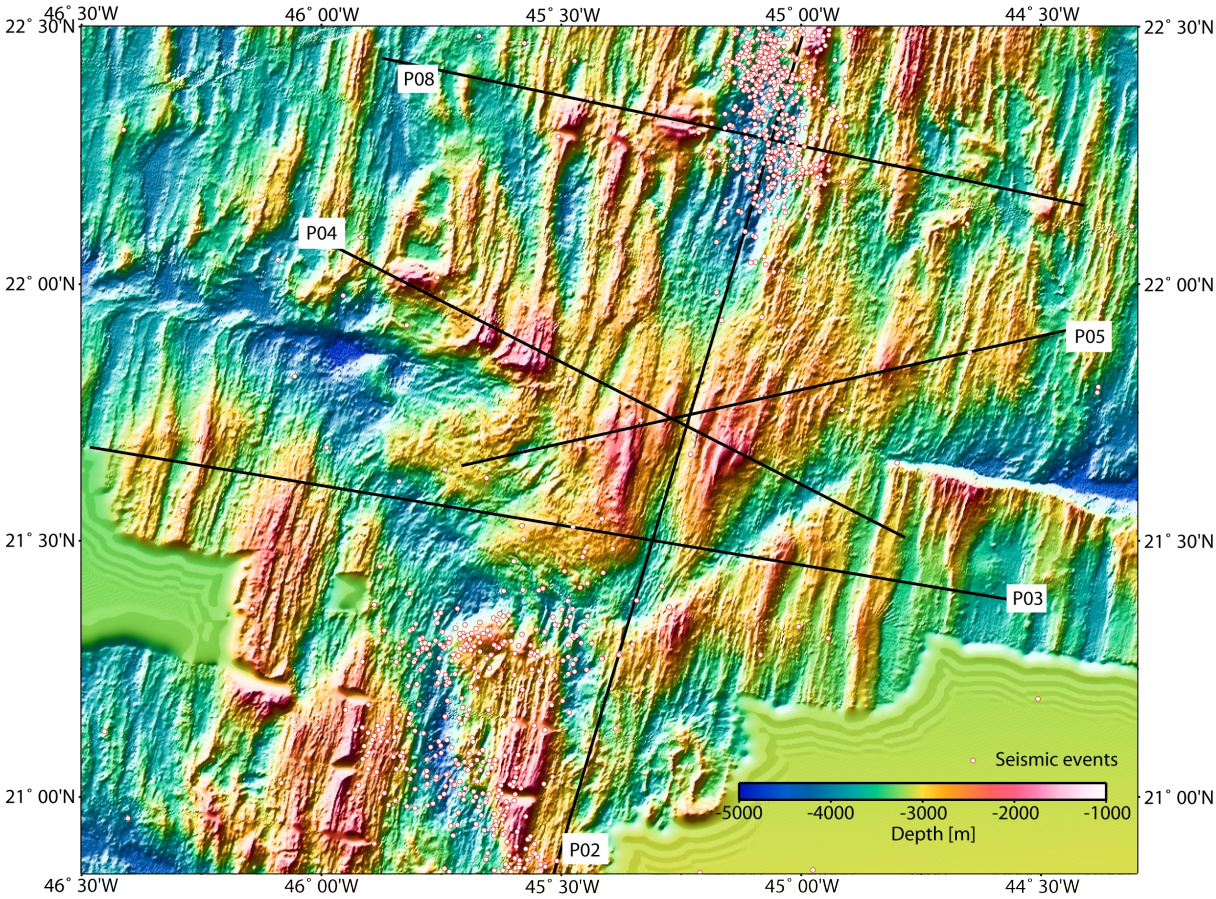

Fig. 1.11 Higher resolved bathymetric map of the study area. Clearly visible the V-shaped trace caused by the propagation of the ridge segment. In the northern part an active detachment fault generated a core complex structure (along profile 8). This northern non-offset discontinuity is a seismically active area while the propagating segment is aseismic.

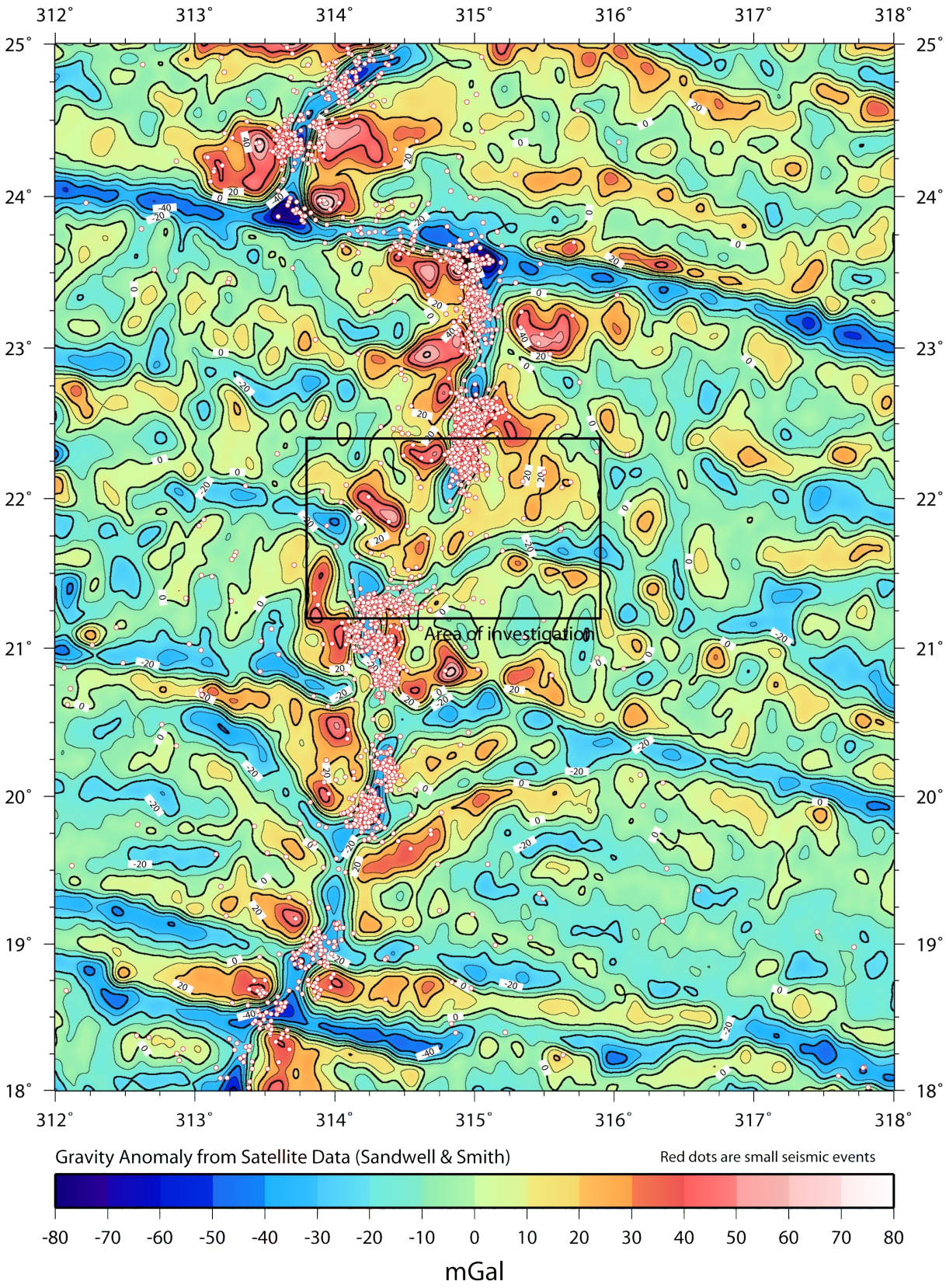

Fig. 1.12 Satellite derived gravity anomaly map based on data of *Sandwell and Smith* [1997]. The investigated area is marked by the black rectangle. Micro earthquakes [*Smith et al.*, 2003] are plotted. A gap in seismicity is visible within the study area.

1.3.1 Why do we want to study ridge propagation?

Ridge propagation occurs at different scales at all mid-ocean ridges from fast to slow spreading rates. Examples of ridge propagation can be found at 95.5° W at the Cocos-Nazca spreading centre [*Hey et al.*, 1989; *Sinton et al.*, 1983], East Pacific Rise [*Naar and Hey*, 1986], Southern Mid-Atlantic Ridge [*Carbotte et al.*, 1991] and some more areas are pointed out in Figure 1.5.

Why does it propagate southwards? In the early nineties the main concept exists that explains ridge propagation caused by asthenospheric flow away from hotspots. This means that either magma sources or the magmas themselves migrate away from their respective hotspots [*Sinton et al.*, 1983]. However, a view to the north and south of this study area shows that there is no general trend of the propagation direction; thus, ridge propagation is connected to different dynamic processes.

What was triggering the propagation of the southern segment? Nowadays, several theories try to explain the mechanism of active ridge propagation. This will be discussed in detail during this work.

From the diversity of examples it becomes evident that ridge propagation is a result of important thermal, mechanical, and melting processes shaping ridge segmentation. The primary reason to study ridge propagation as part of ridge segmentation is that this is the place where the fundamental structure of the oceanic crust is shaped.

Until now, only non-propagating median valley ridge segments have been explored by seismic methods. Another reason to study ridge propagation in a median valley environment is that this is a natural place to study the mechanics of ridge propagation itself.

1.3.2 Questions about the northern part of the study area

In the northern area a large massif has been observed in the bathymetry, just west of the spreading centre. The peak of the mountain is about 1300 m higher than the surrounding bathymetry. This feature is up to 4 times wider than most abyssal hills. Dredges taken in that area yielded rocks that are expected to be found in deeper parts of normal oceanic crust. This is a so called oceanic core complex (OCC). However, it is not the only OCC on Earth. Recent studies [*Escartin et al.*, 2008] show that 50 percent of the oceanic crust along slow-spreading ridges occur in a non-symmetrical tectonically dominated environment. But since this is a well known place from dredges, gravity and magnetic studies, it is an interesting place to extend the pre-existing data set.

What is the nature of this massif? How has it formed and which forces are responsible for its uplift? What causes the change of style of oceanic crustal formation? Which material is uplifted? And when might this area return to its ‘normal’ state as before 4.5 ma?

Other key questions are:

Where do oceanic core complexes occur?

- Large offset transforms
- Non-offset segments
- End of segments

What was triggering detachment faulting?
- Increase in spreading rate
- Does detachment faulting induce a higher spreading rate, or vice versa?
- Does this lead to ridge migration?

It is important to understand ridge fault systems because they also affect major hydrothermal mineral deposits.
The understanding of why the magmatic accommodation of plate separation varies so much along the ridge, and why it seems to occur in various modes rather than vary smoothly, is a clear challenge to understanding how spreading centres work.

1.4 Tectonic settings

The study area can be divided into two main tectonic settings. Section 1.4.1 describes the slightly asymmetric spreading but magmatically robust and symmetrical crustal accretion regardless of the lengthening of this ridge segment towards the south giving this marked V-shaped structure. This segment has been named TAMMAR [*Gente et al.*, 1996]. The northern part of the area shows asymmetric accretion with a domed feature. A view into morphological details is given in section 1.4.2.

1.4.1 Propagating ridge segment

The TAMMAR segment at 21.5° N on the MAR is characterised by a large bulge, 50 km in diameter. This corresponds to a large mantle Bouger anomaly of -40 mgals. It is one of the largest anomalies along the MAR [*Maia and Gente*, 1998].
The segment is highly magmatic [*Gente et al.*, 1996] and has been continuously opening over millions of years. The southern segment boundary corresponds to a 40 km long offset at 21°20’ N. A second ridge-normal feature at 21°40’ N is an old transform fault. However, this is no stable setting of a transform fault since the structures disappear near the ridge axis. The continuous structures of the ancient fault zone (Figure 1.11) illustrate the stability of this spreading segment over time [*Gente et al.*, 1995]. The V-shaped traces connect the ancient now inactive transform with the present offset feature. While the eastern trace is an elongate, narrow depression, the western trace is a tectonically wide, disturbed area.
Those traces correspond to a southward shift of the transform fault, associated with propagation of the ridge axis. Southward propagation started 4.5 m.y. ago, producing the V-shaped wake in the lithosphere (Fig. 1.11). The process of rift propagation generally involves the lengthening of the spreading segment at the expense of the neighbouring segment [*Hey*, 1980].
The linear wake is caused by a constant propagation rate of approx. 16 mm/y after a rapid initiation of propagation [*Phipps Morgan and Sandwell*, 1994] while the spreading rate is constant [*DeMets et al.*, 1990]. Knowing the half-spreading rate v from magnetic anomalies, the propagation rate p can be estimated by measuring the acute angle θ between the propagating ridge and a pseudofault [*Kleinrock et al.*, 1997]:

$$p = v \tan\theta \quad (1.1)$$

The PR is slightly asymmetric with an average half spreading rate of 14 mm/yr on the western flank compared to 12 mm/yr on the eastern flank [*Maia and Gente*, 1998]. The eastern flank shows a clear wake, while the western side leaves a less significant topography with "bookshelf" faulting [Kahle, 2007]. The PR was strong enough to cut the above-named transform at 21.4° N and migrate it to the south.

A comparison of the along-axis satellite-derived mantle Bouger anomaly (MBA) with marine-derived MBA profiles computed for the study area shows a good agreement of the MBA between both types of data [*Ravilly et al.*, 1998]. In Figure 1.12, the main gravimetric features are shown together with the seismic events for that region.

In the northern basin, mantle rocks have been found. This could be associated with reduced crustal thickness [*Tucholke and Lin*, 1994]. Oceanic crust at slow spreading ridges has a large variability in thickness and seismic velocity due to variations in magmatic and tectonic processes [*Tucholke and Lin*, 1994].

The TAMMAR segment shows smooth axial valley morphology changing from the segment centre towards the segment ends. At 21°47 N the shallowest on-axis area of the segment has a width of 2 km and is ~3000 m deep [*Gente et al.*, 1996]. The walls of the rift valley are 600 m high. Volcanism and tectonism are focused at the centre and sparse at the tip of the segment [*Durand et al.*, 1995]. Two types of volcanism have been identified in the inner floor by *Gente et al.* [1996]. Isolated volcanoes 500 m to 1000 m in diameter consist mainly of pillow lava and lava tubes. Flat areas of the inner floor are covered by very shallow (6-7 m) lava lakes. Those lava lakes represent the larger area of the inner floor compared to the isolated volcanoes.

These flat areas can also be found in the northern part of the segment in contrast to the southern end. Mainly pillow lava has been observed at the inner floor of the southern median valley, whereas in the northern wide median valley fresh lava lakes have been observed [*Gente et al.*, 1996].

In the southern part of the segment, the inner floor of the axial valley is 4 to 5 km wide and reaches a depth of 3500 m on average. The slopes are made of steps of 150 m to 250 m.

1.4.2 Active core complex

A possibly active core complex can be seen in the bathymetric data (Figure 1.11) in the northern part of the study area. The massif rises at 22°18' N west of the ridge axis and is interpreted as a detachment fault system without connection to an offset-discontinuity.

The segment is situated north of the propagating ridge segment and alongside typical long abyssal hill topography with axis parallel faults bounded to the north. The domal structure within the investigated area is interpreted as a detachment fault with a developed core complex and the break away to the west (Figure 1.13). However, almost no spreading-parallel corrugations occur, as seen at Atlantis Massif near 30° N [*Cann et al.*, 1997; *Blackman et al.*, 1998]. Nevertheless, the structure is not directly associated with any clear transform discontinuity. It is part of a short ridge segment of approx. 20 km length [*Gente et al.*, 1995]. The ridge axis is shifted by less than 2 km

to the west. The core complex is located at 22°18' N, approximately 10 km off-axis to the west. The summit of the domal structure is at the magnetic anomaly 2 that indicates an age of about 1.8 Ma [*Gente et al.*, 1995]. The fault may still be active.

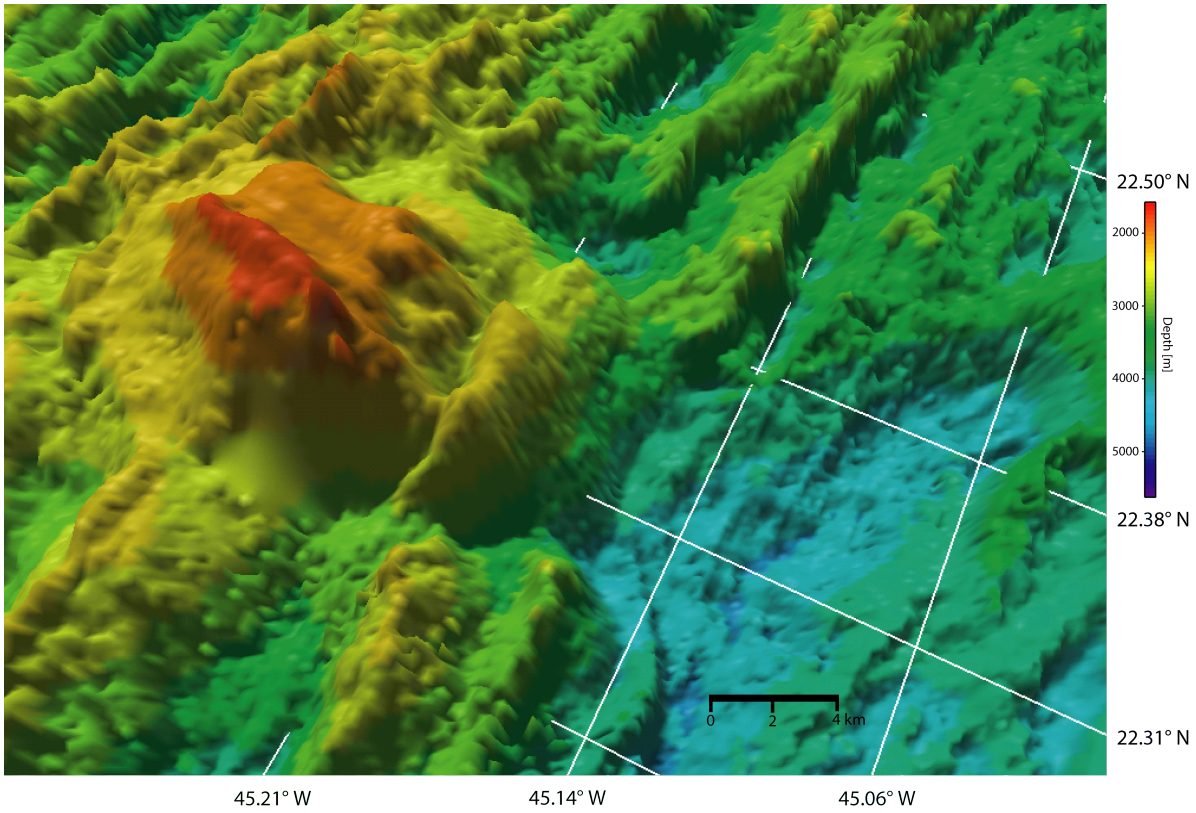

Fig. 1.13 A three-dimensional view of the bathymetric data of the core complex that shows the corrugated surface at the domed structure but also the young fault block to the east and the following faults towards the ridge axis.

Figure 1.13 shows the northern end of the 35 km long basin that reaches a depth of about 3800 m at the ridge axis. The eastern flank of the hill dips at an angle of 42°, which is suggested to be the active fault. The fault hits the valley surface approx. 6-7 km away from the ridge axis. The break-away is difficult to define using the existing bathymetric data. However, the western end of the dome occurs 20-25 km off the ridge axis and may suggest that the fault system has been active for about 2 million years. Several ridge-parallel features cross-cut the core complex and may represent rotated fault (rafted) blocks covering the surface of the detachment fault or secondary ridge parallel fault zones. Further west, abyssal hills are aligned with the core complex, though westward, a domal structure occurs which is possibly a fossil core complex.

To the eastern side of the ridge axis a row of spreading axis parallel ridges separated by basins have been identified. According to studies of the Mid-Atlantic ridge between 13°-15° N by *Smith et al.* [2008] these could be outward rotated sections of flat-lying volcanic seafloor.

Ultramafic and gabbroic rocks have been dredged in that area of the western high by *Cannat et al.* [1995], while in the basin and on the eastern side of the ridge axis only basalts and diabase have been found [*Karson et al.*, 1987b; *Gente et al.*,1995].

1.5 Related Work

1.5.1 Evolution of the segmentation during last 10 million years

The topography is dominated by ridge-normal and oblique lows that represent the off-axis traces of axial discontinuities and split the ridge flank into rhomb-shaped areas of relatively high elevation [*Gente et al.*, 1995]. The area has been studied by *Gente et al.* [1995] and *Maia and Gente* [1998] taking the bathymetric, gravity, and magnetic data of the two preceding cruises (CR1125 and the SEADMA I).

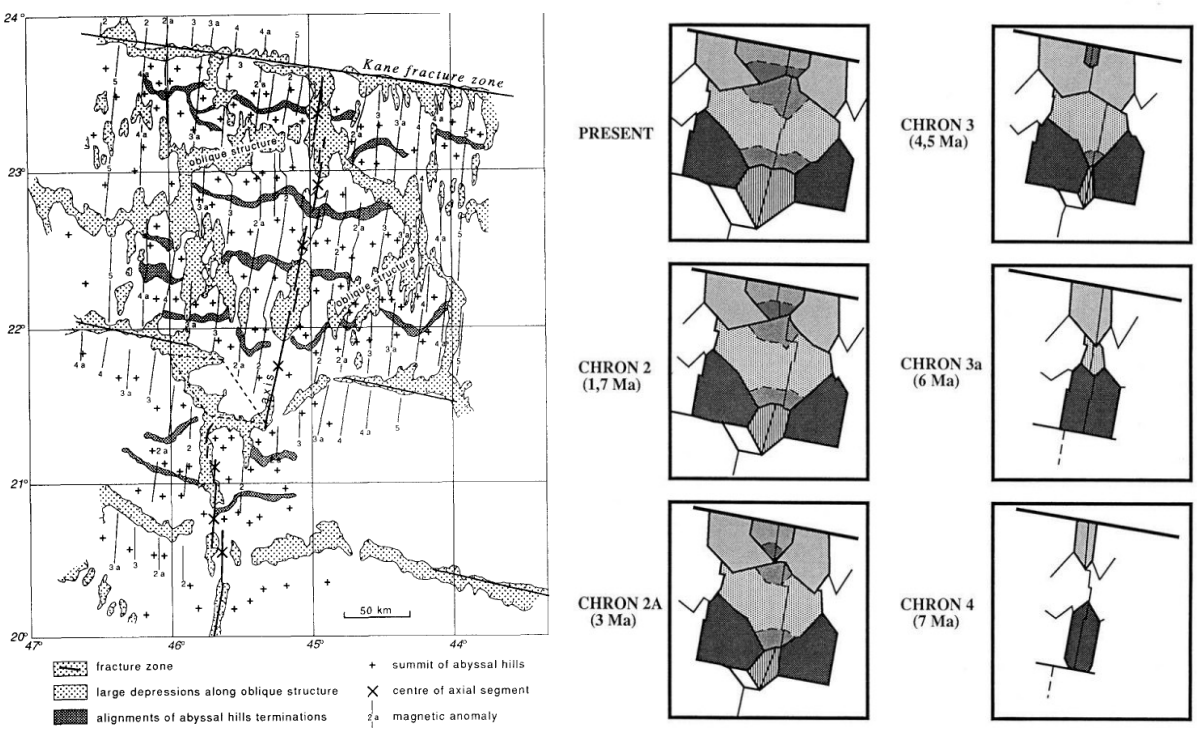

Fig. 1.14 Taken from *Gente et al.* [1995]. To the left: interpretation of the bathymetric map indicating the location of the various discontinuities. Within the magnetic anomalies are shown. To the right a time sequence of the reconstructed tectonic evolution 20° N to 24° N south of the KANE fracture zone.

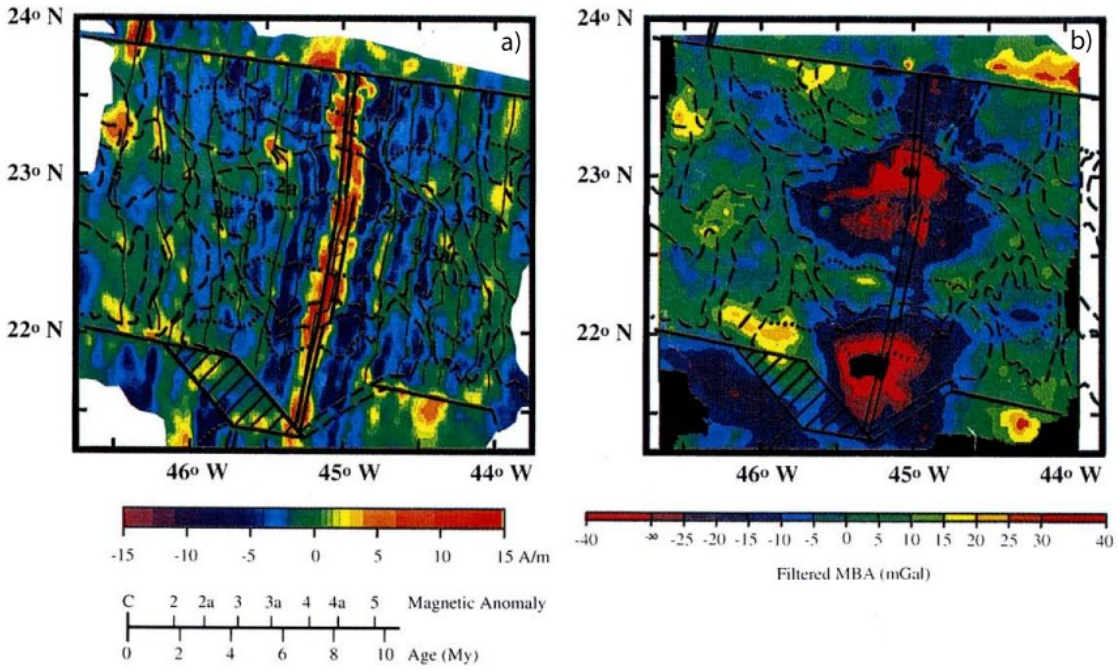

Fig. 1.15 Maps from *Gente et al.* [1995]. a) Crustal magnetisation of the survea area with identified magnetic anomalies and superimposed segmentation scheme. b) Residual mantle Bouguer anomaly map of the survey area with superimposed segmentation scheme.

The complex migration history is depicted in Figure 1.14b taken from *Gente et al.* [1995]. The bathymetric footprint generated by different discontinuities during the last 7 ma shows that the segment length has grown from 20 km to 120 km. The maximum rate is comparable to the spreading rate and is of about 25 mm/a. In both previous cruises, the CR1125 and the SEADMA, the magnetic data were collected with a surface-towed precession magnetometer. The anomalies in the map in Figure 1.14a [*Gente et al.*, 1995] were computed by removing the geomagnetic reference field and by assuming a 1 km thick source layer.
A map of crustal thickness was derived from the gravimetric data by *Maia et al.* [1998]. For the centre of the segment, they calculated a deviation of up to 3 km more than observed for normal thick oceanic crust. The calculated mantle Bouger anomaly (MBA) shows a clear minimum, suggesting a thin lithosphere that can be associated with mantle upwelling in the centre of the segment (Fig. 1.15).

1.5.2 Dredges and TAMMAR Dive-21

A better understanding of the generation of oceanic crust depends upon reasonable estimates of oceanic crustal composition. For this purpose, rocks directly from the seafloor have been collected and studied. A cruise on RV Thomas Washington in 1965 was performed in the area between 22° and 23° N at the MAR. *Melson et al.* [1968] studied in detail the petrology and chemistry of the rocks obtained on that cruise. Cruise 44 of R.V. Chain [*van Andel et al.*, 1965; *Melson and van Andel*, 1966] explored this area for the first time.
Line B from *Melson et al.* [1968] is almost aligned to the seismic line P08 of this study. It covers the slope of the core complex. In Table 2 the dredged and dived rock

samples are listed and they are plotted in Figure 1.16. *Melson et al.* [1968] interpreted the greenstone to have originated by hydrothermal activity rather than regional metamorphism.

Tab. 2 Dredges, submersible dives of the MARK area. Presented are selected samples from the repository of the USGS1995.

Cruise		Lat (N)	Lon (W)	depth	Lithology
SDM Dr4	dredge	22°16'	45°13'	3050-2250	serpentinized harzburgit, dunite, gabbroic rock
SDM Dr33	dredge	22°13'	45°39'	3000-2710	serpentinized harzburgit
SDM Dr1	dredge	22°18'	45°00'	3930-2970	Basalt
SDM Dr2	dredge	22°06'	45°05'	4500-3090	Basalt
SDM Dr1	dredge	22°16'	45°07'	4200-3800	Basalt
SDM Dr2	dredge	22°18'	45°09'	4060-3680	Basalt
SDM Dr3	dredge	22°17'	45°11'	3350-2800	Basalt
SDM Dr5	dredge	22°18'	45°22'	3000-2700	Basalt
SDM Dr7	dredge	22°10'	45°30'	4140-3630	Metabasalt
SDM Dr8	dredge	22°16'	45°29'	3050-2250	metabasalt, basalt
CH44 Dr2	dredge	22°38'	44°58'	2400-2200	Greenstone
TW65 Dr4	dredge	22°31'	45°00'	2200-1600	Greenstone
TW65 Dr10	dredge	22°22'	45°12'	3400-3000	Basalt
TW65 Dr11	dredge	22°21'	45°15'	2600-2200	Greenstone
TAM21-Dive21	22°16' / 45°13' – 22°17' / 45°14'			3200 - 1960	Details see figure 1.16.

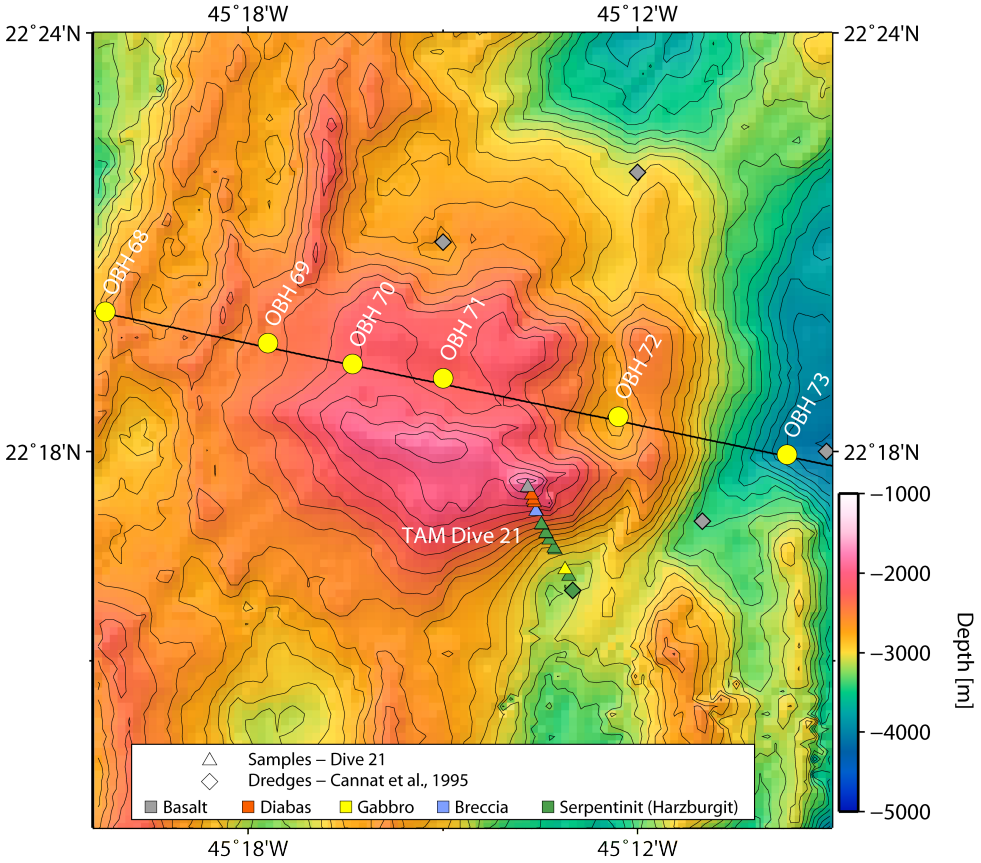

Fig. 1.16 Bathymetric map of the massif showing the location of the TAMMAR Dive-21, dredges as listed in the data repository from Cannat et al., 1995, and our active seismic line P08.

1.5.3 Petrology of the TAMMAR Dive-21

This section presents the unpublished results from the submersible *Nautile* along a SE-NW transect at the south eastern slope of the 22°19' N core complex.

G. Ceuleneer made the dive and analysed the rock samples and wrote the following section about these data as part of a joint paper in preparation.

By means of the submersible *Nautile* the southeastern slope of the 22°19' N core complex has been explored along a SE-NW transect ~4 km in length and ~1.250 m in height (Fig. 1.16). The dive started in a heavily sedimented abyssal plain at a depth of about 3.250 m. Rare isolated angular blocks of serpentinite fallen down the nearby cliffs can be observed there. Close to the foothill, a narrow ~E-W trending ridge made of hard rocks emerges from the sediments. Sample examination revealed mylonitic, amphibolitized gabbros. Although a thick crust of Mn hydroxides prevented any *in situ* measurement of the orientation of the mylonitic foliation, a reasonable guess is that it strikes parallel to the E-W elongation of the outcrop. The first outcrop of serpentinized peridotites was encountered at a depth of 2960 m. Its contact with the mylonitic gabbro was not observed due to the thick cover of sediments. Serpentinites are intensely fractured, the main orientation of the diaclases being N-S with a westward dip of ~70°. They crop out up to a depth of 2230 m where a brecciated zone is encountered. This breccia is made of fragments of serpentinized peridotites and of metadolerites embedded in a fine matrix made of serpentine, chlorite and likely clay minerals. The thickness of the brecciated zone reaches several hundred metres and its general orientation is N-S with a sub-vertical dip. This "cold" contact separates the serpentinites from the overlying outcrops of diabase dykes and basalts. The orientation of the dykes is N-S with a high westward dip, i.e. parallel to the one of the diaclases cutting the serpentinites. At a depth of 2050 m a sub-horizontal E-W trending shear zone cross cuts the diabase dykes that are pervasively transformed into an assemblage of chlorite and other green schist facies minerals.

Amphibolitized gabbro.

The mylonitic gabbro sampled at the base of the section contains small porphyroclasts of clinopyroxene (cpx) and of plagioclase (plg) up to 0.5 mm in size; they are embedded in a fine-grained matrix made of a mosaic of plg and green hornblende a few tens of microns in size with sutured grain boundaries. Plg porphyroclasts present well developed mechanical twins. Cpx porphyroclasts have rounded shapes, are generally not kinked, and are heavily re-crystallized and transformed into hornblende on their borders. The matrix of the mylonite is made of a fine grained mosaic of plg and common green hornblende (average formula is $Na_{0.5}Ca_{1.8}(Mg,Fe)_{4.7}(OH,CL,F)_{2.0}Si_{7.0}Al_{I.0}$) indicating that deformation occurred in amphibolite facies conditions. No evidence for overprint by a lower T° deformation episode is found in this sample (no retromorphic assemblages, nor catactlastic deformation).

The protolith of this mylonite was a gabbro devoid of olivine and of oxides. The porphyroclasts allow us to infer the primary igneous phase composition. Plg porphyroclasts have an average An content of 0.55, which is identical to the one of plg from the mylonitic matrix. Some porphyroclasts present a slight inverse zoning with An

ranging from 0.48 to 0.57 but most of them are quite homogeneous in composition. Cpx porphyroclasts are augites with a Mg# of 0.78, a low Cr_2O_3 content (0,1 wt%), a moderate Al_2O_3 content (2,5 wt%) and a high TiO_2 content (0.7 wt%). These values are typical of evolved cumulates from N-MORB [e.g. *Elthon*, 1987; *Natland and Dick*, 1996]. In an Mg# (cpx) – An (plg) diagram, this sample plots perfectly in the differentiation trend defined by the gabbros drilled in the nearby ODP Site 923 (Fig. 1.17), indicating that they derive from similar parent melts. The composition of these gabbros is the one expected for cumulates from MORB of the MARK area [*Ross and Elthon*, 1997].

According to these data, this amphibolitized gabbro can be interpreted as a witness of a ductile, possibly detachment fault, rooted in a former magma body that accommodated shearing at high temperature (typically around 500°C-600°C).

Serpentinized peridotites.

Although 100% serpentinized (which prevented any geochemical analysis of the primary minerals), the serpentinized peridotites have preserved a coarse (up to 1 cm) grained mosaic texture diagnostic of hot working in low stress and high temperature (~1200°C) conditions. Such textures are classically attributed to deformation related to “asthenospheric” mantle flow [*Ceuleneer et al.*, 1988]. The orientation of the deformation plane, measured on one sample reoriented on board is sub-horizontal a situation similar to the one observed in the nearby peridotite massif drilled at DSDP Site 920 [*Ceuleneer and Cannat*, 1997]. No overprint of lower temperature deformation, equivalent to the one recorded by the foothill amphbolitized gabbro, was observed at this outcrop. The rock is harzburgitic in composition (i.e. a pre-alteration assemblage of olivine and orthopyroxene). Interstitial grains (likely former clinopyroxene) diagnostic of precipitation from a melt are observed in a few samples.

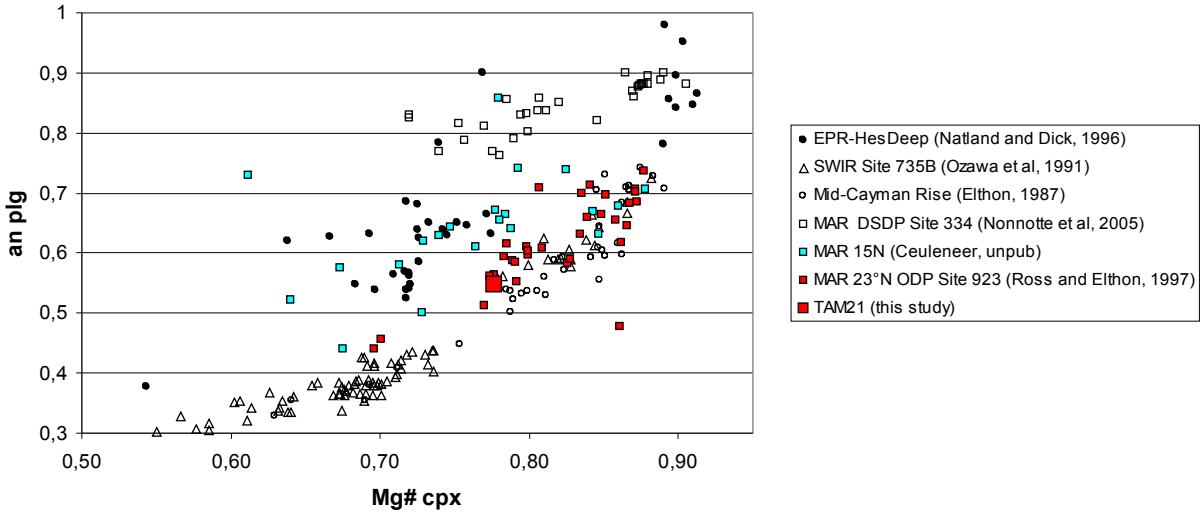

Fig. 1.17 Diagram of the Anorthit (An) content of plagioclase (plg) and (Mg#) of clinopyroxene (cpx) of the collected gabbros is similar to the gabbros drilled in the nearby ODP Site indicating that they derive from similar parent melts.

2 Data and methodology

2.1 Data acquisition

The area was mainly mapped on a cruise in 1991 (SEADMA1) with R/V L'Atalante [*Gente et al.*, 1991, 1995] with multibeam bathymetry, gravity and magnetic data [*Maia and Gente*, 1998] extending data coverage of the first cruise in that area by RC2511 [*Detrick et al.*, 1984]. The multibeam echo sounder EM-12 dual with 168 beams was used to collect the bathymetric data in 1991 and the gravity data were gained with a KSS30 Bodenseewerk gravimeter [*Maia and Gente*, 1998].
Thus, the bathymetric and the free-air gravity data shown in this work are provided by *Gente and Maia* [1995].
During the RV Meteor cruise M60-2, active seismic data had been collected from 80 OBH deployments along 5 profiles in the area of interest (Figure 2.8).

2.2 OBH data and processing

The marine seismic survey used an array of two airguns that released compressed air upon a trigger signal. The sudden release of the compressed air generates pressure waves that propagate through the water column and penetrate into the ground. On the seafloor, several ocean bottom hydrophones (pressure sensors) had been placed that received and recorded the waves that traveled through the water and the sub-seafloor. They measure the energy of the direct, reflected, and refracted waves and the arrival time corresponds to the travel time of a specific wave. The propagation depends on the physical properties of the subsurface and is sensitive to the elastic properties and the density of the rock. The signal is deformed and attenuated while travelling through the subsurface. It changes in frequency, phase and amplitude. The dominant frequencies of refraction data range from 5 to 20 Hz. Taking the general subsurface velocities between 1.6 km/s and 8 km/s, the wave length is about 80 to 1600 m. The vertical resolution is about a quarter of the wave length. It is also dependent on the signal-to-noise ratio.
A rapid change in velocity and density causes reflections, while critical refractions (head waves) require only a velocity change. Refractions (turning rays) can be observed by a continuous rising of velocity with depth. Diffractions, the scattering of

waves at discontinuities, can disturb the seismic phase identification significantly, especially for later arrivals.

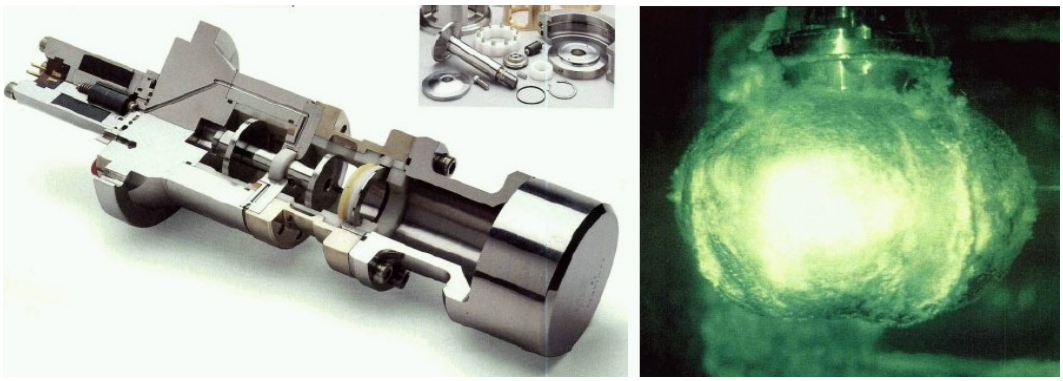

Fig. 2.1 - Example of an airgun (GI-Gun) and the bubble generated in the water [*Benz*, 2003].

2.2.1 OBH data

Shots of two 32 litre airguns, bolt guns (operating at a pressure of 130 bar) towed at 10 m depth, firing at every 60 s resulted in wide-angle data of high quality at most of the stations (Figure 2.1). With a ship velocity of approx. 4 knots over ground this gives an average shot spacing of 120 m along the profiles. The sampling interval is 100 Hz or 125 Hz (a few instruments with 200 Hz or 250 Hz), depending on the recorder specifications used at each station. This long shooting interval of 60 s was chosen to avoid the high “previous shot noise” in the water column that is caused by reverberation of seismic energy [*Nakamura et al.*, 1987].

Two types of recorders were deployed in a pressure tube mounted below a buoyant body, Marine Broadband Seismocorder (MBS) and Marine Longterm Seismocorder (MLS) of *SEND GmbH*. The MBS works at sampling rates between 50 Hz and 10 000 Hz while the MLS ranges from 1 Hz to 200 Hz and was mainly developed for seismology. The internal time base drift is less than 0.05 ppm. Storage media are PCMCIA flash disks. For more details see *Flueh and Bialas* [1996].

2.2.2 Data processing

To gain seismic sections of a good quality and without errors in time is important for the further use in travel time tomography or any other time and signal dependent modelling. This requires the accurate positioning of each shot and receiver as well as registering the exact times of shots and the recordings on the hardware in the accuracy of milliseconds.

Since 2000, the GPS signals are available without any signal degradation, reaching an accuracy of 10 to 15 m. Using the standard GPS on RV Meteor, the registrations during M60-2 were made without any notable interruptions. The shot positions were obtained from the onboard GPS-system and corrected for the distance between airgun array and GPS antenna. The depth of the airguns was controlled by the length of the chains connected to the floats.

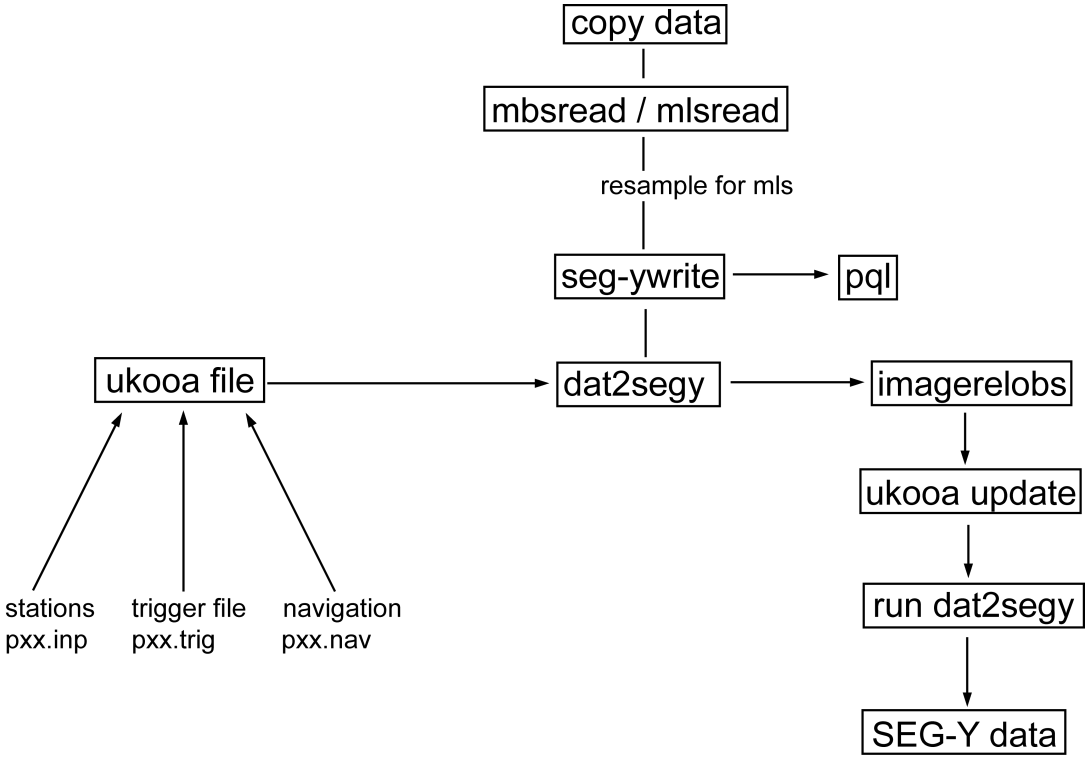

Fig. 2.2 Onboard seismic processing flow. Data are first stored on flash cards while the instrument is recording on the seafloor. After instrument recovery the data pre-processing will be done.

Due to problems with the onboard multibeam bathymetric system, Simrad EM-120, the accurate depth of each receiver was extracted from the previously collected high quality bathymetric data. The depth along the profiles beneath each shot was also tracked from this bathymetric grid (Figure 2.8). The OBH instruments drift during the deployment; thus the OBH position could be dislocated up to several 100 m. This would also lead to incorrect traveltime information in the seismic record sections. To correct for this, the receiver positions were relocated along the profile using the direct wave travel times. The picked traveltimes near the apex are needed and a least square minimisation problem has to be solved.
The data loggers, recording continuously, had been synchronized with a GPS-time signal to register an assumed linear clock drift and correct the data for these milliseconds. The recorded data with sampling rates of 100 to 250 Hz was reduced to standard SEG-Y format and corrected for the internal clock time drift. This continuous time series has been cut into segments of equal length (traces) starting at the trigger time for the airguns. Plotting all traces beside each other result in a seismic section (Figure 2.7). The data have been analysed following IFM-GEOMAR standard procedures [see *Flueh and Grevemeyer*, 2005]. An onboard working flow to process the data from their first storage medium (flash card in the recorder) to standard SEG-Y data is shown in Figure 2.2.

The SEG-Y raw data have to be processed to improve the signal-to-noise ratio. To compress the seismic signal to a minimum with information about the passed Earth,

only a deconvolution was required. Before the deconvolution step, a filter was applied to remove the low frequencies. As a result of deconvolution, the length of the signal is shortened and the resolution in the time domain is increased [*Wiener*, 1949]. The deconvolution is performed using the Wiener-Levinson least squares approximation. Finally, a Butterworth frequency filter is applied with the passband near the lower frequencies.

Raw data:
As an example, a record section of the OBH13 (profile 2) is shown in unprocessed form (Fig. 2.6). Only a Seismic-Unix (SU) band pass filter (1/4/30/40) has been applied. The seismic phases in this seismic section of raw data are strongly disturbed by noise of several sources. Especially at low frequencies of less than 2 Hz, constant and ambient signal noise are visible and show high amplitudes.

Frequencies filter analysis:
To determine the frequencies of the seismic energy, filter panels with narrow frequency band passes for the near offset range (Figure 2.3) and the far offset range (Figure 2.4) are shown. The lower section of the two figures presents the amplitude spectra of the corresponding filter panels. The main energy for the refracted phases is between 5 - 10 Hz. This means a resolution of 400 m to 1500 m, depending on the penetration depth and therewith the seismic velocities of the sub-surface. For the near offset traces, up to 20 Hz can be observed. The direct wave has even higher frequencies at up to 50 Hz. Time and offset dependent filtering was applied and is described below. The used Butterworth bandpass filter is described by four corner frequencies, i.e. a lower stop/pass band boundary and an upper pass/stop boundary. The operators are characterised by linear slopes.

Deconvolution analysis:
In these wide-angle data, the amplitude spectra of the seismic traces vary with time and offset (e.g. reflected and refracted phases). The spatial and temporal resolution of the seismic data can be improved by the application of a deconvolution. As a result, the seismic wavelet will be compressed. Disposing of the source signature, recording filter, and hydrophone response, deconvolution will leave the earth's reflectivity only. A Wiener deconvolution was applied.
The deconvolution must follow the time and offset variations in the amplitudes of data. For this reason, a multi-trace deconvolution was performed. This so called roll-along deconvolution uses autocorrelograms averaged over a number of traces. Here, deconvolution operators for every trace are calculated from the average over 11 traces and in data gates of 3-s with 1-s overlaps of each trace. The deconvolved trace results from a weighted merging of the independently deconvolved gates.
The best compromise between temporal resolution and signal-to-noise ratio is obtained from the deconvolution test panels for near offset ranges (Figure 2.5). Constant operator lengths of 1 sec with a variation of the prediction lag from 40 ms to

400 ms are displayed. A fixed operator length of 1 sec and the predictive length of 220 ms were applied to all data sets.

Final processing sequence:

- Input of SEGY-data with complete geometry information
- Tapering the first 0.5 s to zero to reduce the response of the de-bias filter operator
- Butterworth high-pass to centre the amplitudes around zero. Raw data recordings are influenced by a DC shift. Thus, a 1-3-Hz high-pass minimum delay Butterworth frequencies filter with 60 dB attenuation between the pass and reject zone was applied.
- Gated Wiener deconvolution: gate length 3 s, overlap 1 s, length of merge region 1 s, operator length 1 s (prediction interval included), prediction interval 220 ms
- Static correction to a fixed seafloor travel time of 11 s. The seafloor depth changes along the seismic lines. Each trace was statically corrected to the same date.
- Time and offset-dependent Butterworth frequencies filter
- Backshift of the traces to their original traveltimes

Processed data:

A comparison of the pre-processed data in Figure 2.7 to the unprocessed data in Figure 2.6 shows a clear reduction of the low and mono-frequent noise in the near and far offset traces. A moderate compression of the wavelet signal could be achieved.

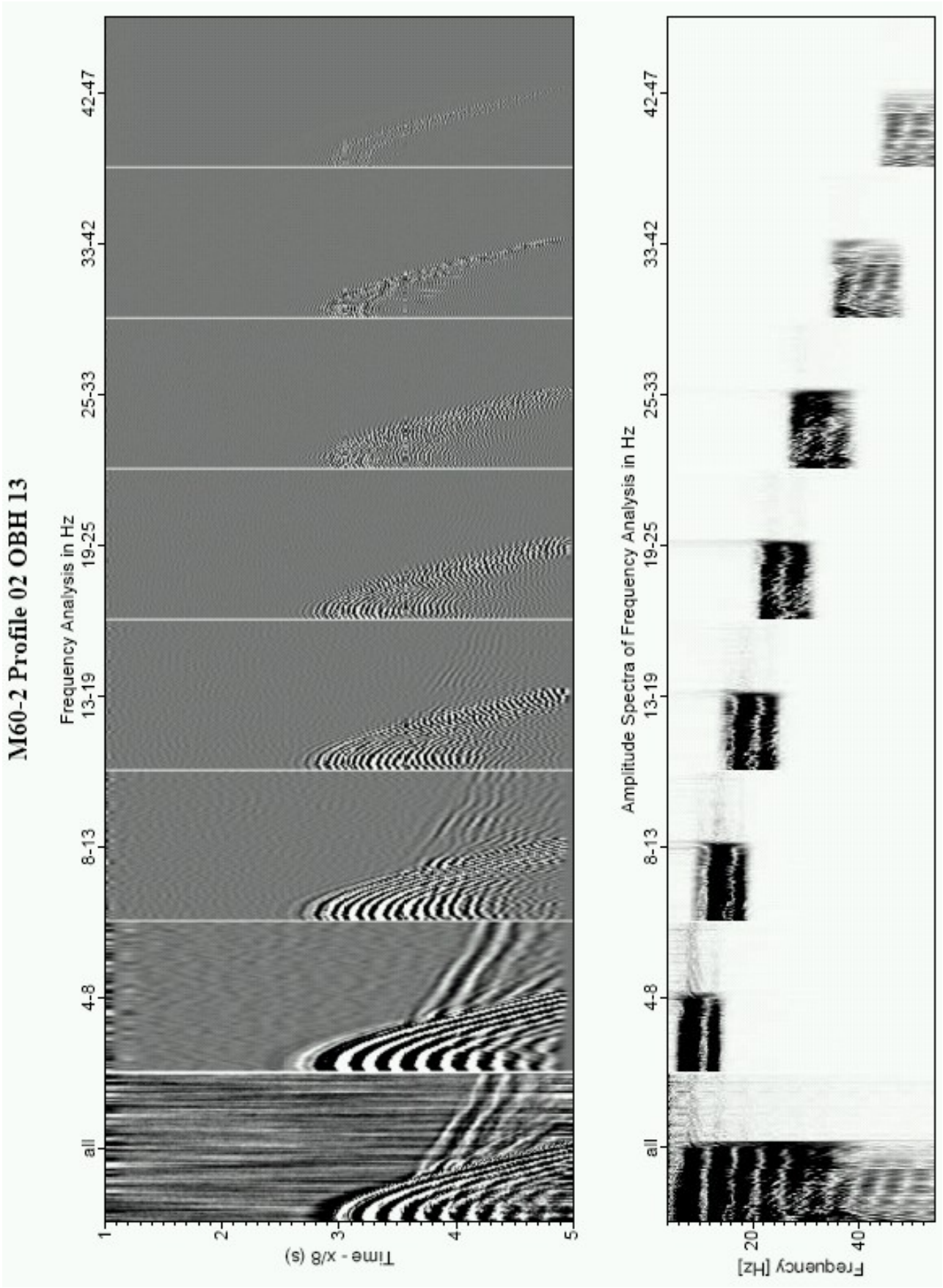

Fig. 2.3 Frequency analysis of the near offset for OBH13 of profile 2.

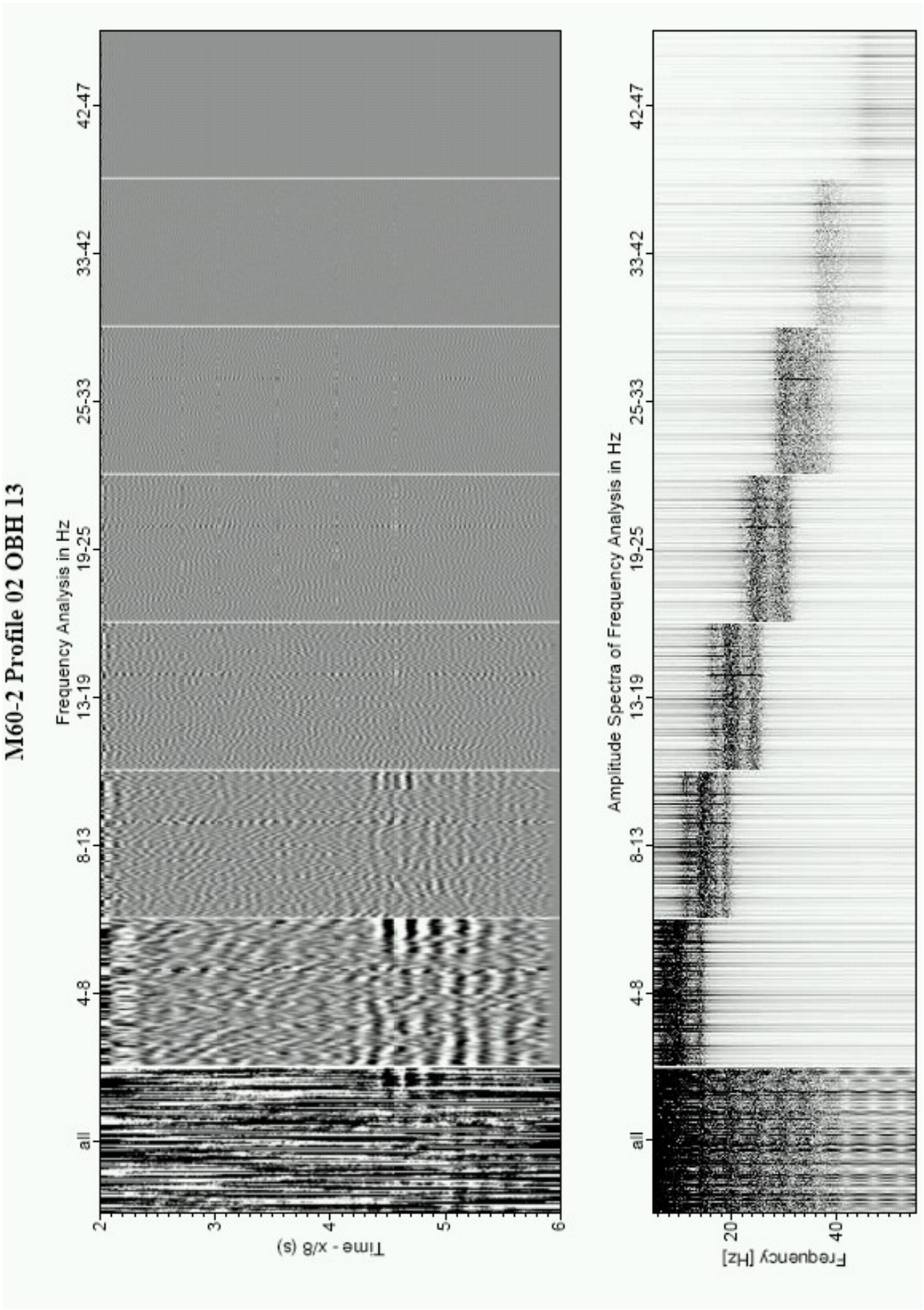

Fig. 2.4 Frequency analysis of the far offset for OBH13 of profile 2.

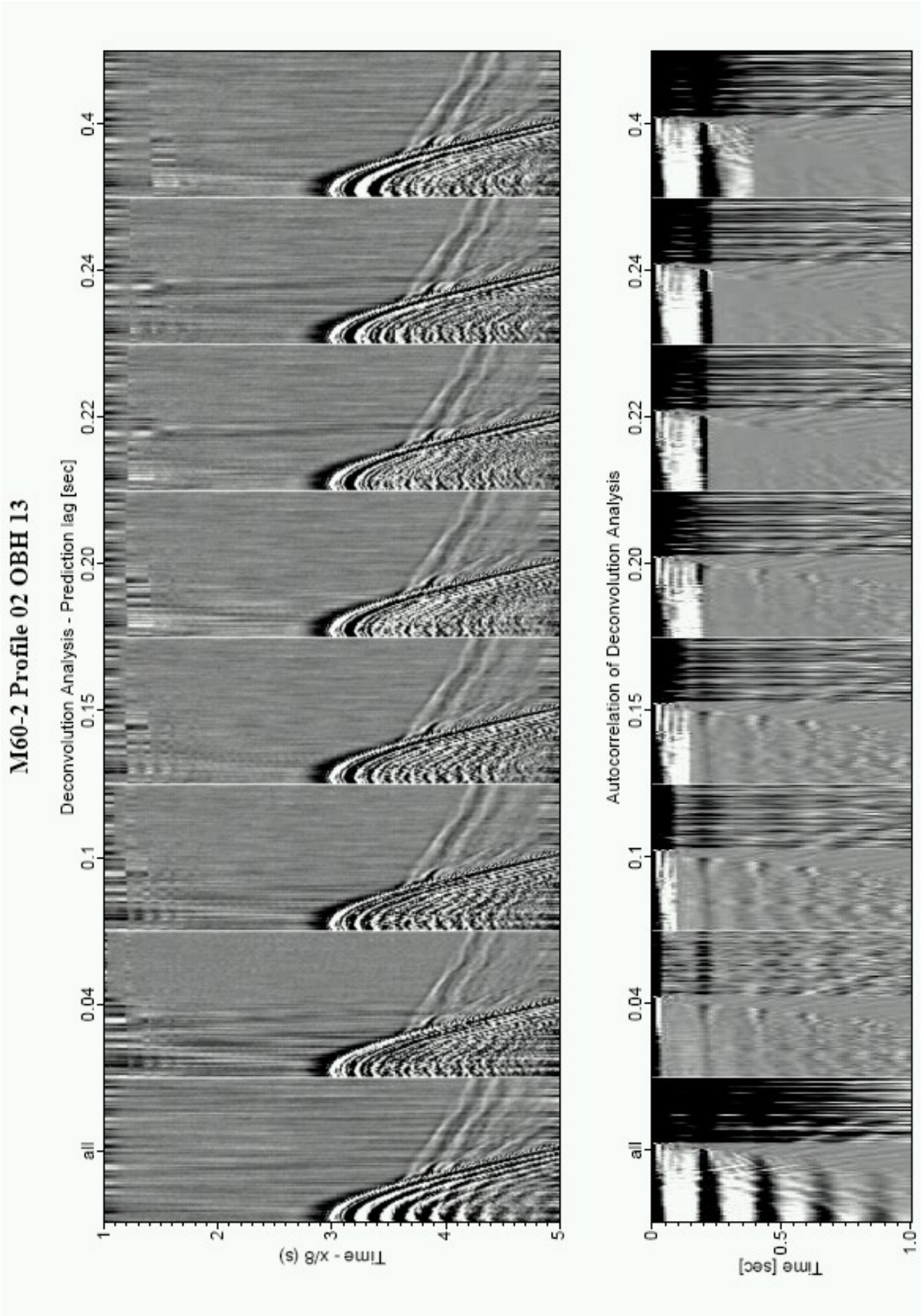

Fig. 2.5 Deconvolution analysis of the near offset for OBH13 of profile 2.

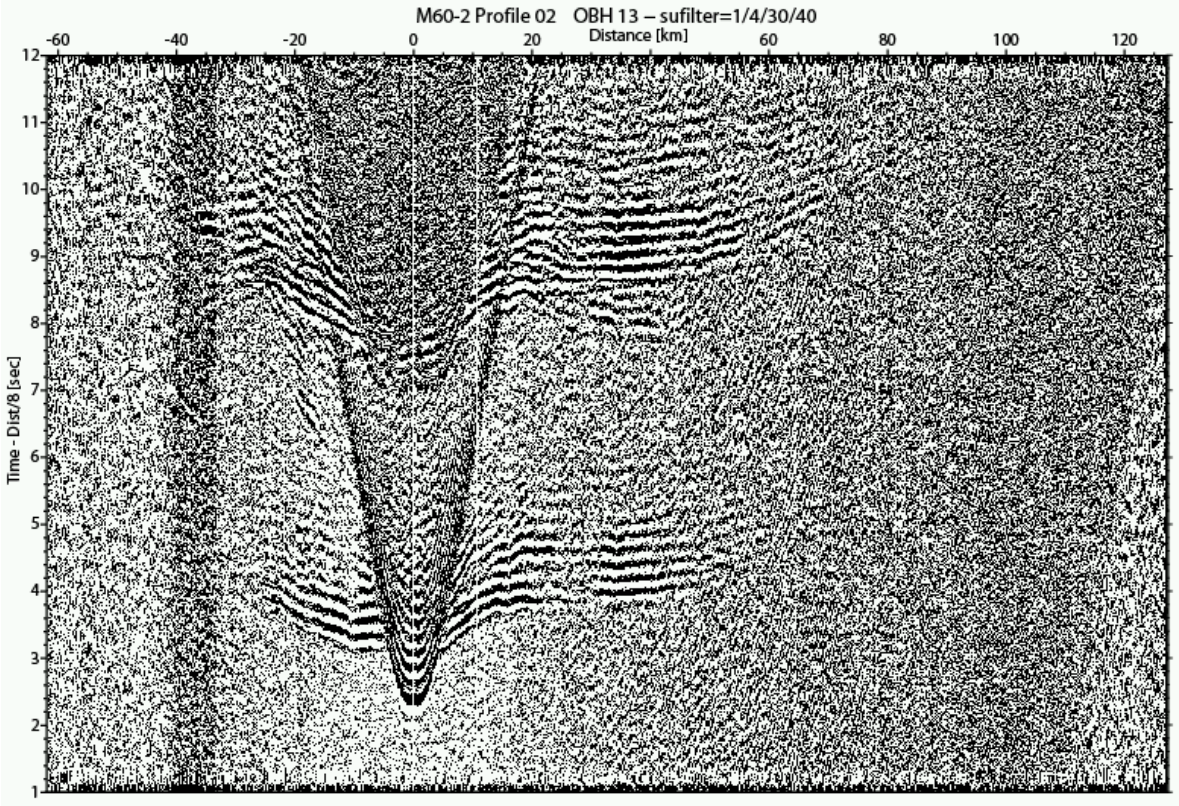

Fig. 2.6 Seismic section of the raw data of OBH13 from profile 2. Unprocessed data displayed with a SU bandpass filter of 1/4/30/40 Hz as the boundary frequencies.

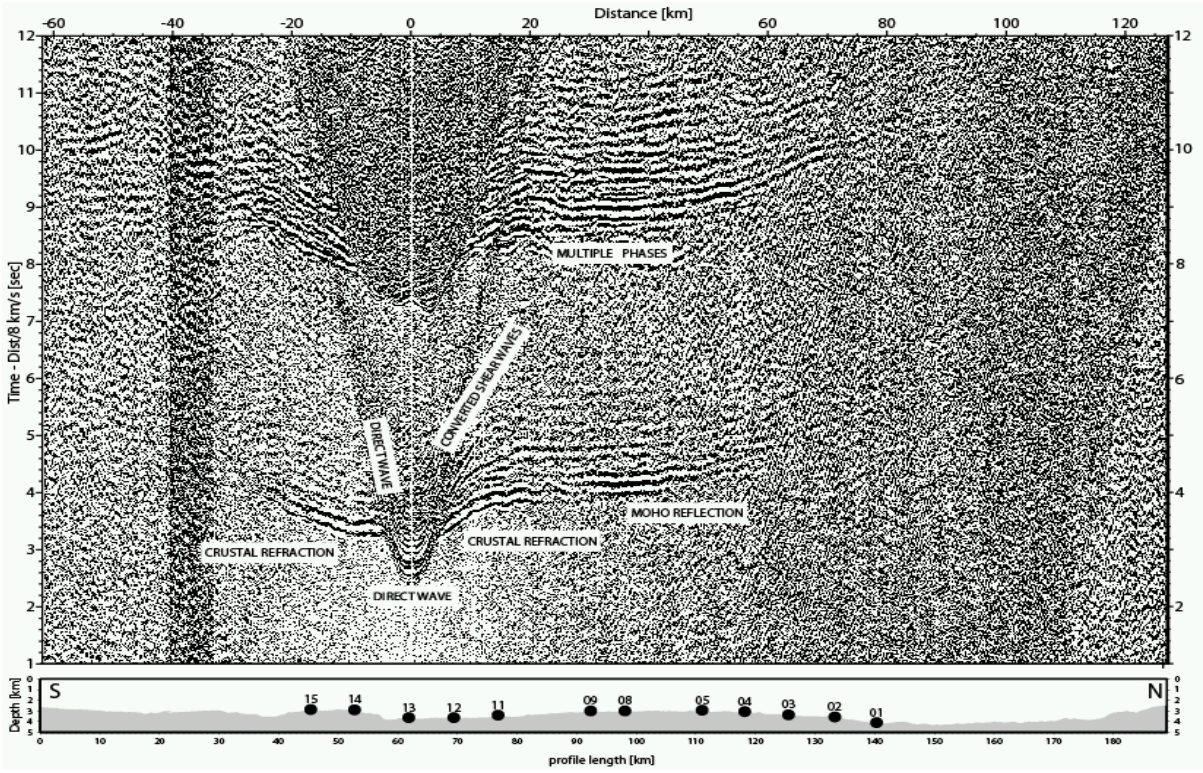

Fig. 2.7 Seismic section of station 13 at profile 2 after deconvolution and filtering. Significant arrivals are marked and named. Below the seismic section the entire profile is plotted containing all station that gave reasonably good quality data.

2.2.3 Data examples in seismic sections of the profiles

Fifteen ocean bottom hydrophones (OBH) were deployed along the 190 km long ridge-axis-parallel profile 2. The recovery of the instruments brought eleven stations with good data, three stations without any data and one station with a few data from the beginning of the shooting. Due to that, a second ridge-parallel profile 6 was shot afterwards to fill the gaps in the central part of the segment.

The seismic sections of this line (Figure 2.9) show different characteristics along the profile that can be divided into three parts, coincident with the bathymetric data: The northern most part (southern area of the wide median valley) including OBH 01 to 03, the middle section with the axial high from station 05 to 12 (including stations 42, 44, 57, and 60, redeployed at the line 6), and the southern part with the stations 13, 14, and 15 at the dying segment south of TAMMAR. The PmP arrivals could be consistently identified using reversed shots and the multiples among different stations. The Pn phase shows very weak amplitudes at larger offsets or is not visible. Low mantle velocities of less than 7.5 km/s may result in apparent velocities similar to the PmP phase and large offset Pg arrivals. Similar features have been observed elsewhere at MORs. Since they were not clearly differentiated from other phases or the background noise for P02, no mantle refractions have been used for further steps of modelling and interpretation.

As a result of the along axis smooth topography, the signal-to-noise ratio is high and even converted shear waves have been observed; a feature not so often seen at mid-ocean ridge centres.

The seismic section of profile 2 (Figure 2.7) shows an 8 km wide dark stripe vertical over the entire western side of the section. This is caused by a re-shooting of a part of the line due to a defect on the compressors for the airguns. For this part, more traces exist and this is visible in all seismic sections of this profile.

Profiles 4, 140 km long, and 5, with a length of 150 km, display a rougher nature of topography. The first thirteen OBH were deployed along profile 4 (OBH 31 to 43) and two additional (OBH 44 and 45) at line 5 (OBH 41, 43 to 55). The last five instruments (OBH41-45) recorded shots from both profiles.

The undulating seafloor makes it harder to identify the different phases of refracted and reflected waves travelling through the crust and mantle. Figure 2.10 shows the seismic sections of three selected stations from profile 5. The different phases Pg, Pn (crustal and mantle refraction, respectively), and PmP (mantle reflection) are marked.

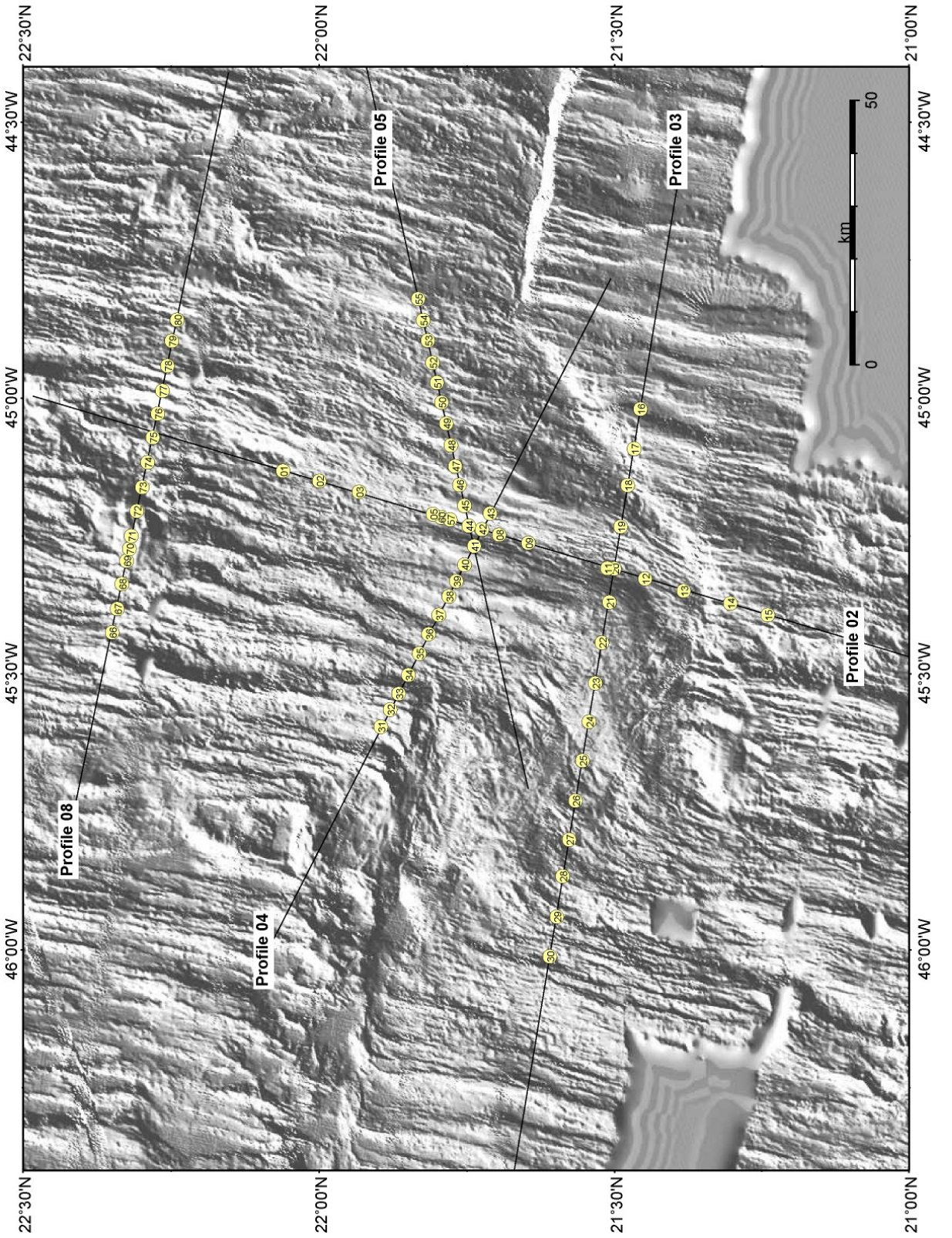

Fig. 2.8 Bathymetric map with instrument locations and their numbers. Black lines are the shot profiles.

Nevertheless, most of the seismic sections allow a clear identification of the phases corresponding to crustal refractions and mantle reflections. Compared to profile 2, the signal-to-noise ratio at larger offsets is higher. Thus, mantle refractions could be identified up to the profile limitations. The seismic discontinuity of the mantle (Moho)

still does not appear very strong or sharp, resulting in interference of the seismic phases. The critical distance seems to be rather constant along both lines.
With the deployments 66 to 80, another 15 ocean bottom instruments where deployed with full data recovered along the 150 km-long profile 8. In contrast to profiles 4 and 5, the identification of the mantle reflections in the seismic sections of the stations along profile 8 is difficult. The seafloor topography is even more undulating and the crust-mantle boundary is expected to vary in depth or is blurred. Diffractions may interfere with the seismic phases of interest. However, like at most of the deployed stations the multiple often gives a better image and it is easier to follow the phases.

Profile 3 with fifteen instruments crossing the propagator ridge tip contains the stations OBH 16 to 30. This line was processed and modelled by *Kahle* [2007].

For picking of the events and the model building by raytracing, both pre-processed and unprocessed seismic sections were used to keep all available seismic information.

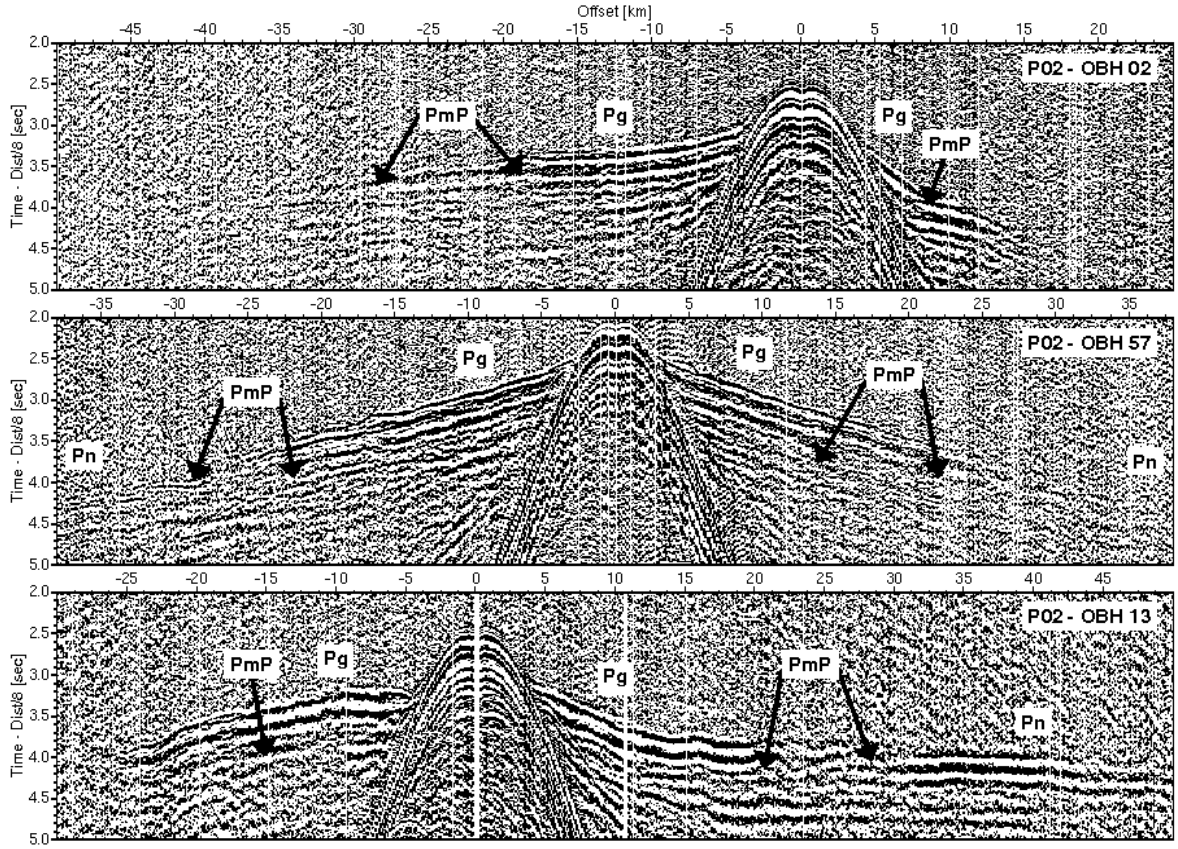

Fig. 2.9 Three seismic data examples of the along-axis profile 2. The different phases are marked with Pg (crustal refraction arrivals), PmP (mantle reflection phase), and Pn (refractions through the mantle).

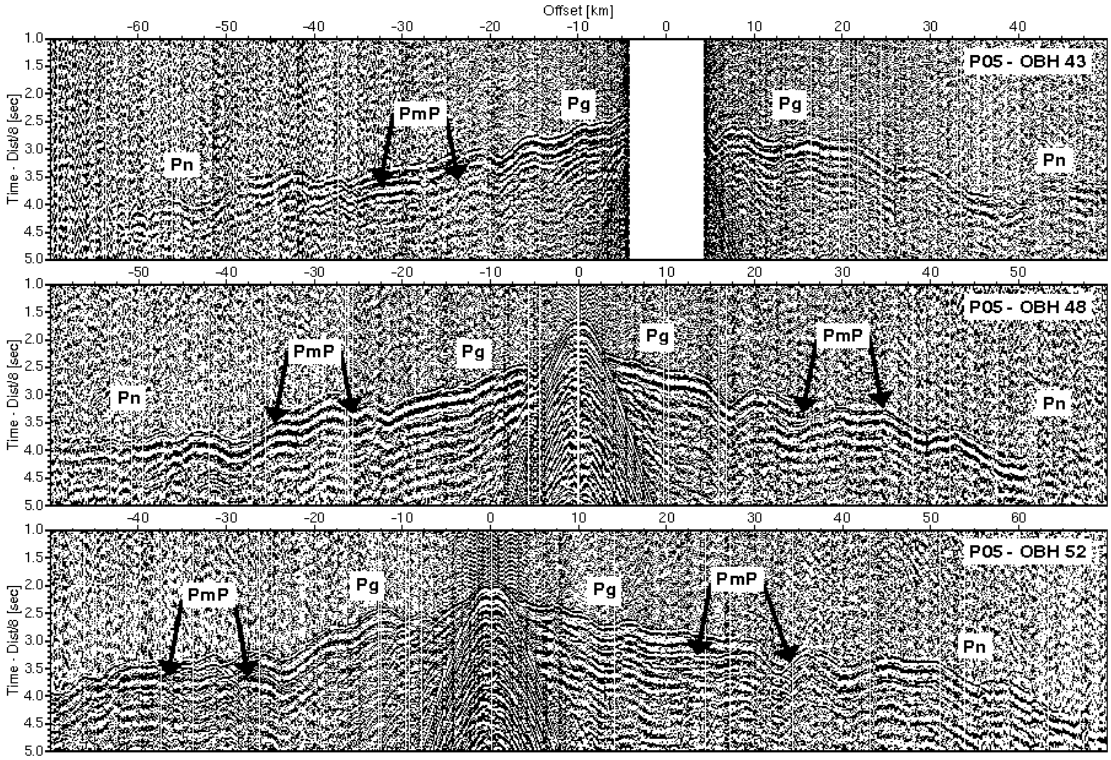

Fig. 2.10 Three seismic data examples of the TAMMAR-segment crossing profile 5. The different phases are marked with Pg (crustal refraction arrivals), PmP (mantle reflection phase), and Pn (refractions through the mantle). Seismic records of all recovered stations can be found in Appendix C.

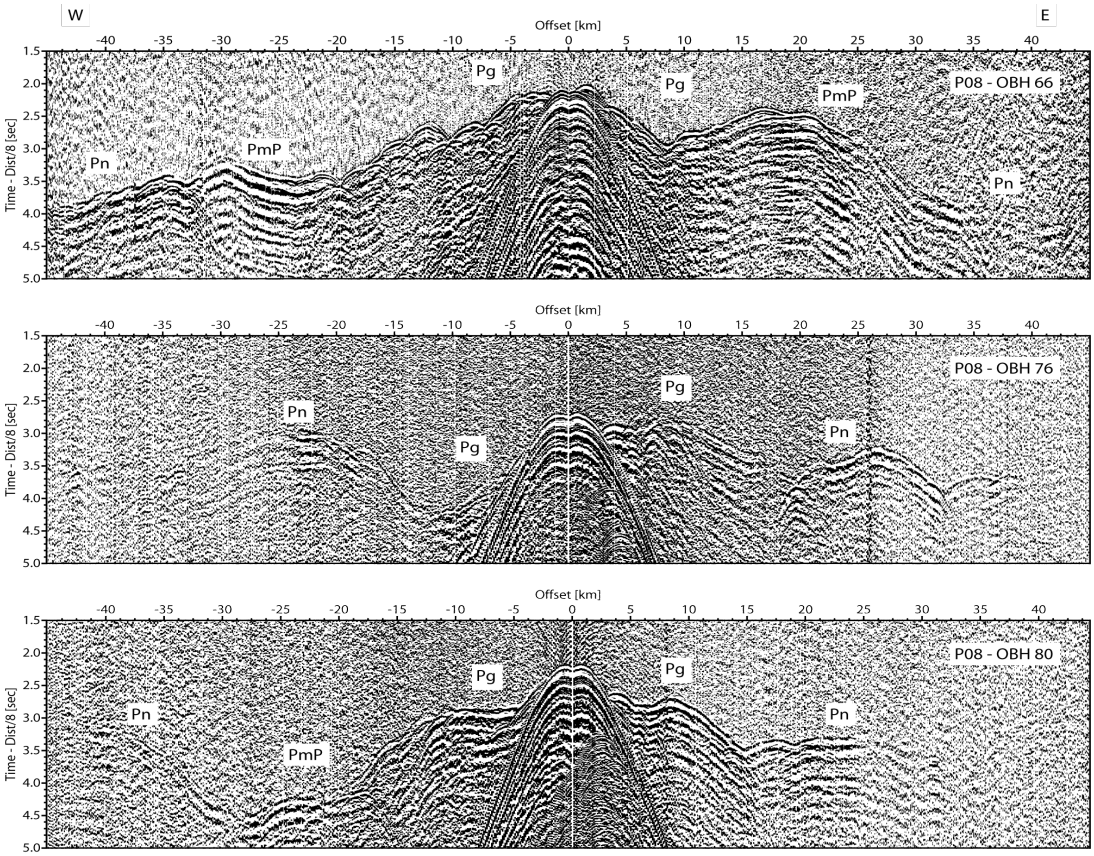

Fig. 2.11 Three seismic data examples of profile 8. The different phases are marked with Pg (crustal refraction arrivals), PmP (mantle reflection phase), and Pn (refractions through the mantle). Seismic records of all recovered stations can be found in Appendix D.

2.2.4 Contemplation to the observed shear waves

Converted shear waves could be observed on profile 2 along the ridge axis. Since the source is operated in the water layer, a compressional wavefield is radiated and observed shear waves have to be generated through mode conversion. Special conditions are required to effectively produce wave conversion. A non-normal incident P wave generates a S_v-wave at any interface. However, the amplitudes for these waves depend on the velocity and density contrast across the interface and the angle of incidence. The solution for the amplitudes of the various P and S_v-waves at an arbitrary angle are given by the Zoeppritz Equations [Zoeppritz, 1919]. For normal incidence, the energy is in the reflected or transmitted P-waves and hence no S-waves are generated. As the incidence angle increases, a part of the energy transforms into reflected and transmitted S-waves [*Sheriff and Geldart*, 1995].

In this introductory treatment the solutions of the equations are displayed in curves in figure 2.12 for a fluid-solid case. Studying the variation of energy partitioning as a function of incident angle of an incident P-wave many parameters can be varied: P-wave velocity ratio, density ratio, and S-wave velocities in each medium. In general, when the shear wave velocity of the lower medium is higher than the P-wave velocity in the upper medium an efficient conversion occurs.

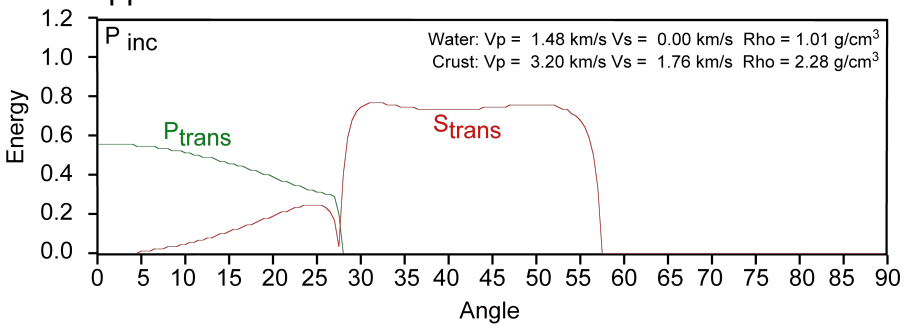

Fig. 2. 12 Partitioning of energy for transmitted waves as a function of the angle of incidence for a certain case of parameters.

The most plausible interface for the generation of converted shear waves in marine refraction experiments is the interface between the sedimentary layer and the crystalline basement. However, sediments are missing at the young mid-ocean ridges or are negligibly thin. Thus, the conversion interface has to be another one. Two possible places are the seafloor and the interface between layer 2A and layer 2B. Since no jump in velocity is expected at the transition from layer 2A to layer 2B, only a change in the velocity gradient, the seafloor is preferred for the conversion boundary. The viability of a P-S conversion at the seafloor has been studied in the following three-case scenario (Figure 2.13). To calculate the synthetic seismograms, a Fortran77 program based on a layered halfspace earth model was used [*R. Wang*, 1999]. The source depth was chosen similar to our data at a depth of 10 m in the water column. A half-sinusoid wavelet was applied with duration of 0.0025 s. A low gradient resolution was chosen because no layers in the gradient layer were of interest. A Vp-Vs-ratio of 1.8 were taken to convert the values for the shear wave velocity of each boundary.

Tab. 3 Interfaces used as input for the synthetic data modelling. Three cases are presented to observe the appearance of shear wave conversion.

Case (a)

Layer	Depth (km)	v_p (km/s)	v_s (km/s)
1	0	1.5	0
2	2.9	1.5	0
3	2.9	2.9	0
4	3.3	3.0	1.65
5	4.9	5.8	3.2
6	7.0	7.1	4.0
7	7.0	7.4	4.1

Case (b)

Layer	Depth (km)	v_p (km/s)	v_s (km/s)
1	0	1.5	0
2	2.9	1.5	0
3	2.9	2.9	1.6
4	4.9	5.8	3.2
5	7.0	7.1	4.0
6	7.0	7.4	4.1

Case (c)

Layer	Depth (km)	v_p (km/s)	v_s (km/s)
1	0	1.5	0
2	2.9	1.5	0
3	2.9	2.0	1.2
4	3.4	2.2	1.3
5	3.4	3.2	1.8
6	5.4	5.8	3.2
7	7.5	7.1	4.0
8	7.5	7.4	4.1

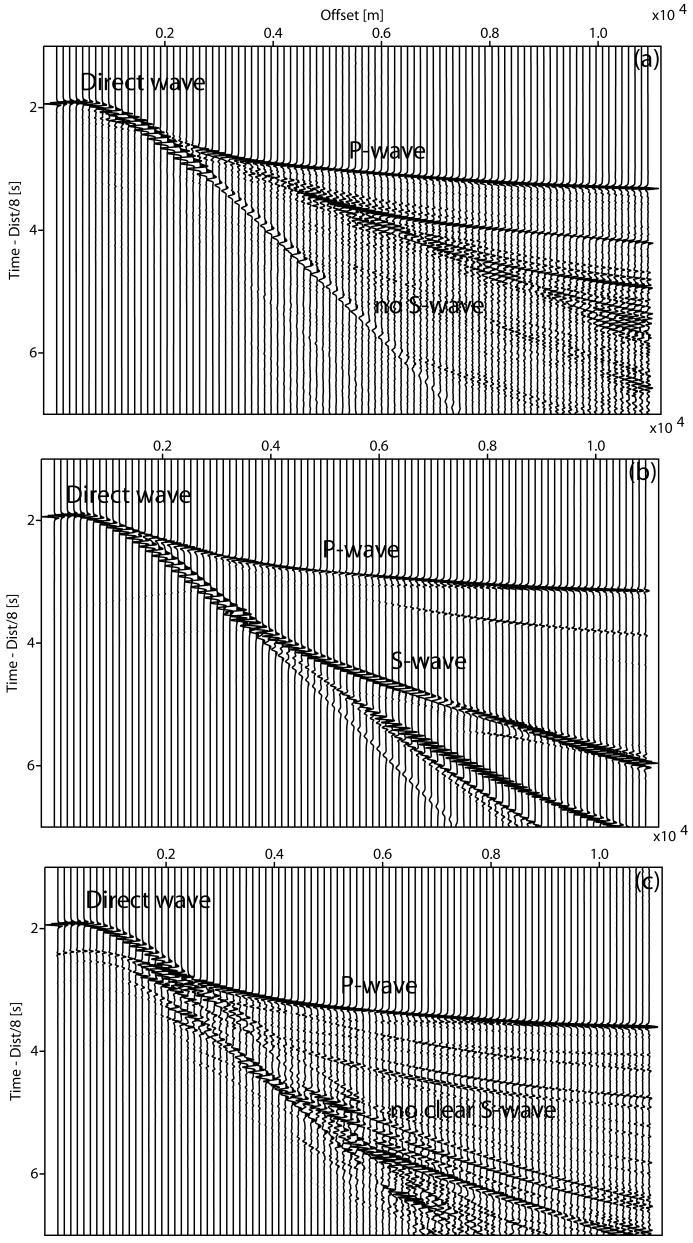

Fig. 2.13 The synthetic wavefield of the three different cases are shown: a) presents the resulting wavefield for the upper crust for the segment ends (gained from the seismic tomography results in section 4). b) Shows the clear S-wave arrivals as they occur in the central part of the segment, c) A sediment layer of 500 m has been added to the crustal model resulting in the disappearance of clear S-wave arrivals.

Table 3 presents the model parameters for all three cases. Case (a) represents the conversion taking place at the Layer 2A-2B interface. However, it results not in the clear shear wave arrival as observed in the real data. Thus, the conversion at the seismic interface between Layer 2A and 2B can be excluded. Furthermore, the detailed study in Figure 2.13-b and 2.13-c shows that conversion at the seafloor is strongly dependent on the seismic velocities of the uppermost structure. P-to-S conversion at the seafloor is possible for the calculated case (b), representing young

oceanic crust as it occurs along the ridge axis. The results in (c) assume only a thin sediment layer of 500 m with a velocity of 2.0 km/s at the seafloor, which is already quite high, but still no conversion of seismic energy from P- to S-wave occurs directly at the seafloor.
Another important fact is the roughness of the interface. If the topography in this case of the seafloor is too rough, the converted waves will be radiated incoherently from the interface resulting in weak converted shear waves. Thus, the absence of shear waves in the ridge-axis crossing profiles could be due to scattering.
The resolution of the very upper part beneath the station is reduced in marine seismic refraction experiments because of the disturbance through the water wave. Thus, shear wave arrivals as later arrivals are disturbed to even larger offsets and less information about the uppermost layers is available. This makes it difficult to model shear waves gained from refraction data. Assumptions have to be made.
The Poisson's ratio v is the ratio of transverse contraction to longitudinal extension strain in the direction of the stretching force. It is related to the P-wave velocity v_p and S-wave velocity v_s by:

$$v = \frac{(\frac{v_p}{v_s})^2 - 2}{2((\frac{v_p}{v_s})^2 - 1)} \qquad (2.1)$$

High Poisson's ratio results from a high porosity in the rocks. If the ratio or the v_p/v_s -ratio is very constant, changes in velocities are connected to changes in temperature rather than to changes in fluid content or material.

2.2.5 Appearance of crustal magma chambers in seismic data

Axial magma chambers (AMC) have been observed by seismic reflection and refraction experiments [*Canales et al.*, 2005; *Collier and Sinha*, 1992]. The occurrence of AMCs is not limited to fast spreading ridges but also observed at the slow spreading Mid-Atlantic ridge [*Detrick et al.*, 1987; *Singh et al.*, 2006]. If melt is present, the resulting velocity contrast will cause a negative polarity reflection in seismic reflection data [*Sheriff and Geldart*, 1995]. Thus, the top of the axial magma chamber could be displayed in seismic reflection data. Hotter or partially molten zones in larger AMCs will result in a decrease of seismic velocities. The study of *Collier and Sinha* [1992] modelled a melt lens with a seismic velocity of 3 km/s that is consistent with laboratory velocity measurements of an andesite melt [*Murase and McBirney*, 1973].
The significantly lower velocities can be imaged using travel times of seismic waves travelling through the magma chamber compared to those passing the magma chamber beside. However, this is difficult to get reasonably constrained low velocity anomalies in refraction experiments. Another problem is that the inversion method applied in this study is unable to resolve those abrupt changes in velocity (4.8 km/s above and up to 5.5 km/s below the 3 km/s body). After inversion using an initial

model containing the melt lens, it becomes laterally and vertically smoothed by the inversion smoothing operator.

Depending on the spreading rate, AMCs show distinct differences in their appearance. At slow spreading oceanic ridges they are of shorter life and non-stationary [*Sinha et al.*, 1998] compared to the ones at fast spreading ridges.

Not every low velocity zone is connected to an active magma chamber. The observations of the Famous area (37° N) interpreted a low velocity zone by an intrusion zone through which magma passes [*Whitmarsh*, 1973]. However, observing shear waves they excluded the presence of a larger magma chamber. Furthermore, a low velocity zone at deeper crustal levels beneath the axis or parallel has been interpreted as evidence for along-axis redistribution of melt [*Magde et al.*, 2000].

The Lucky Strike segment is situated at 37° N at the Mid-Atlantic ridge. It is an example of where it was possible to image an axial magma chamber beneath a slow-spreading ridge. The rough seafloor topography and the associated seafloor scattering makes it difficult to map such magma chambers compared to fast or intermediate spreading centres [*Singh et al.*, 2006]. They observed the reflection of the top of the magma chamber at a depth of 3 km beneath the Lucky Strike volcano. At the Juan de Fuca Ridge, in a comparable study environment [*Menke et al.*, 2002], they needed magma velocities of 3 km/s to fit the prominent delay in their arrival times. This scenario has been used to create a synthetic seismic dataset to study the appearance in seismic refraction data. For this purpose, the Fortran77 program *MSEIS* [*R. Wang*, 1999] was used again. A low velocity layer of 500 m thickness has been used to simulate the magma lens. In Table 4, the layers used as input are listed with their interface depths and velocities. The existence of a low velocity zone results in a shadow zone in the crustal arrival (Pg) (Fig. 2.15).

Tab. 4 Interfaces used in the synthetic data modelling to study the seismic wavefield behaviour for an axial magma chamber.

	Normal oceanic crust		**Magma chamber**	
Layer	Depth (km)	v_p (km/s)	Depth (km)	v_p (km/s)
1	0	1.5	0	1.5
2	2.9	1.5	2.9	1.5
3	2.9	2.9	2.9	2.9
4	4.9	5.8	4.7	4.8
5	7.0	7.1	4.7	3.0
6	7.0	7.6	5.3	3.0
7			5.3	5.5
8			7.0	7.1
9			7.0	7.6

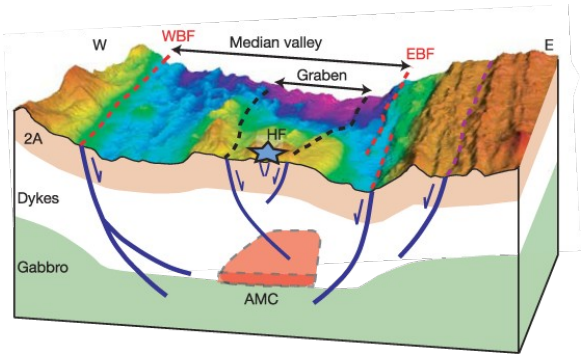

Fig. 2.14 A three-dimensional schematic diagram of the Lucky Strike AMC [*Singh et al.*, 2006]. Beneath the volcano layer 2A is about 1 km thick and a large AMC is present and extends up to 7 km in length and 4 km in width.

The delay in the Pg phase is clearly visible. In addition, a reflection (PamcP) of the low velocity zone is created. Those phases are rather weak and may be below the noise level. However, the shadow zone should be clearly visible if an AMC exists. The

mantle reflection (PmP) and the mantle first arrival (Pn), the latter rather weak, still occur, however, slightly later. Tracking to the real data of profile 2 such features are not visible (Fig. 2.9 and Appendix A).

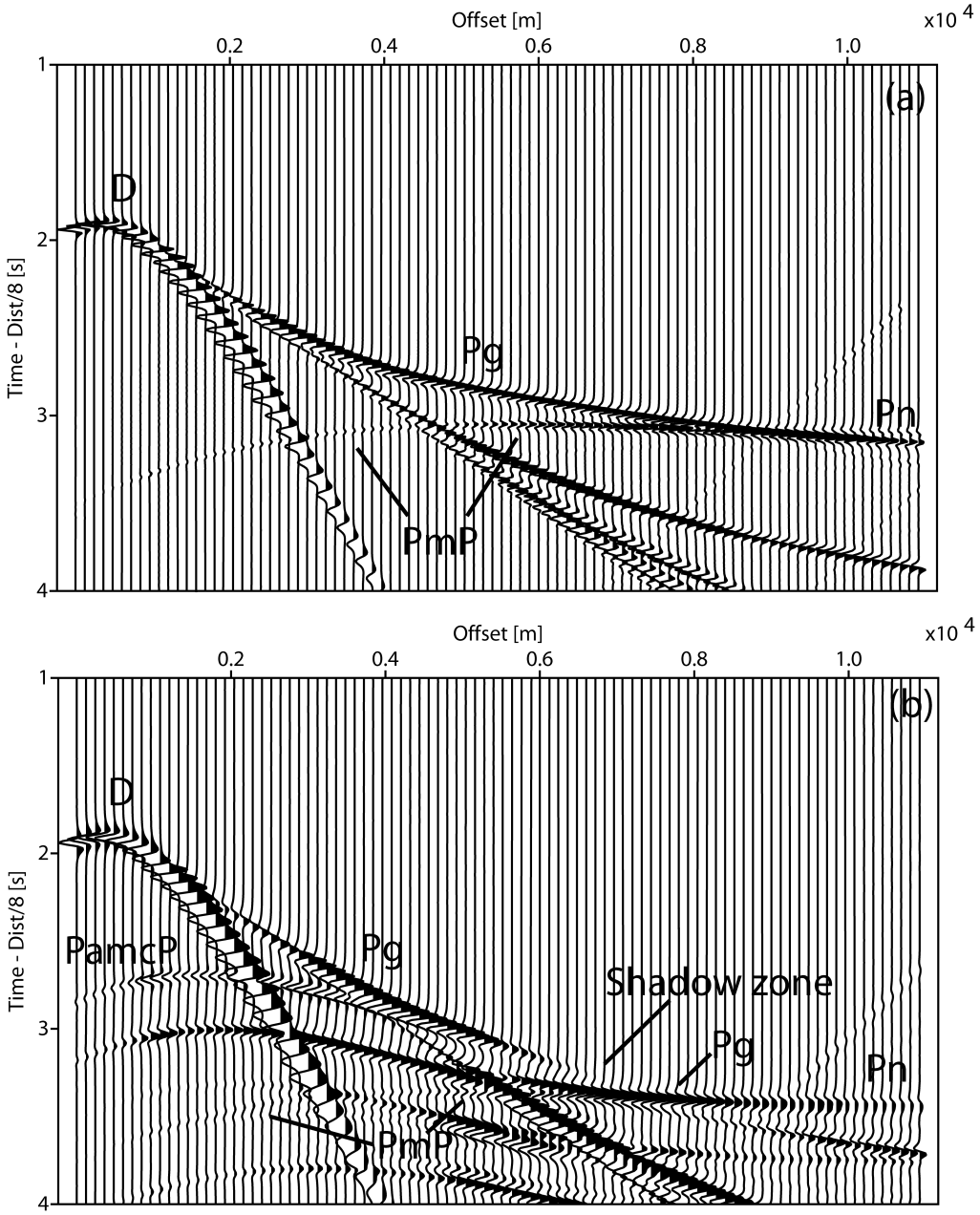

Fig. 2.15 Comparison of synthetic data for normal (a) oceanic crust and (b) oceanic crust with a low velocity zone of 500 m thickness at the layer 2 / 3 transition. The presence of a low velocity zone with a constant velocity of 3 km/s as expected from laboratory measurements results in a shadow zone and a delay in the first crustal arrival. D…direct water wave; Pg…crustal first arrival; Pn…mantle first arrival; PmP…mantle reflection; PamcP…melt lens reflection (reversed polarity).

2.3 Gravity data from the study area

The observation of the Earth's gravitational acceleration g provides information about the mass distribution in the subsurface. The value of g depends upon the latitude, elevation, and time-dependent distortions (tidal forces). Changes caused by geodynamic processes during generation and reduction of ocean seafloor can be detected. The mean value of gravity at the surface of the Earth is approximately 9.8 m/s^2. The flattening of the Earth affects the variation of the gravity from 9.78 m/s^2 at the equator to approximately 9.83 m/s^2 in the Polar Regions. To compare gravity measurements worldwide they are referred to a geoid that is a surface on which the gravitational potential is equal at any point (approximately the mean sea level).

The first data of the gravity field over oceans came from pendulum experiments on islands in the oceans. The next step came when the first instrument used at sea was built by Siemens in 1876 [*Jones*, 1999]. It was built to measure the water depth. Thinking that the less dense water replaces the rock, it was assumed that the water depth could be calculated from the decrease in gravity. However, two important facts were disregarded: the change of gravity with latitude and the more important fact that the differences in water depth are compensated below the seafloor to reach a state of equilibrium. During the 1920s and 1930s, the first serious gravity measurements came from submarines using pendulum apparatus on unstable ground where not only the pendulum length and the value of g but also the movement of the support had to be taken into account. Calibrations were carried out in shallow water using conventional land gravimeters in diving bells. Those time consuming measurements by *V. Meinesz* were applied until the 1950s.
A new stage and the beginning of a rapid development were reached by the construction of continuously recording gravimeters that had been invented in the mid-1950s. The first continuous shipboard measurement was made in 1957 [*Jones*, 1999]. Three types of gravimeter systems exist nowadays: spring gravimeter, vibrating gravimeter, and forced-feedback instruments.
Two types of gravitational measurement exist. The first one corresponds to the determination of the absolute magnitude of gravity at any place and the second is the measuring of a change in gravity from one place to another. In marine gravity surveys, the relative variation is determined and can be converted to absolute values by calibrating the instrument with existing absolute measurements on land [*Jones*, 1999].

2.3.1 Instrumentation

The gravity data of the study area were gained with a KSS30 Bodenseewerk gravimeter [*Maia and Gente*, 1998]. From the provided free-air gravity grid, the 5 profiles have been tracked and used for seismic modelling. The data are shown in Figure 2.13 for each profile (a-e). While b and d show relatively low variation in the gravity data, the anomalies in the other profiles cannot be simply explained by topography effects.

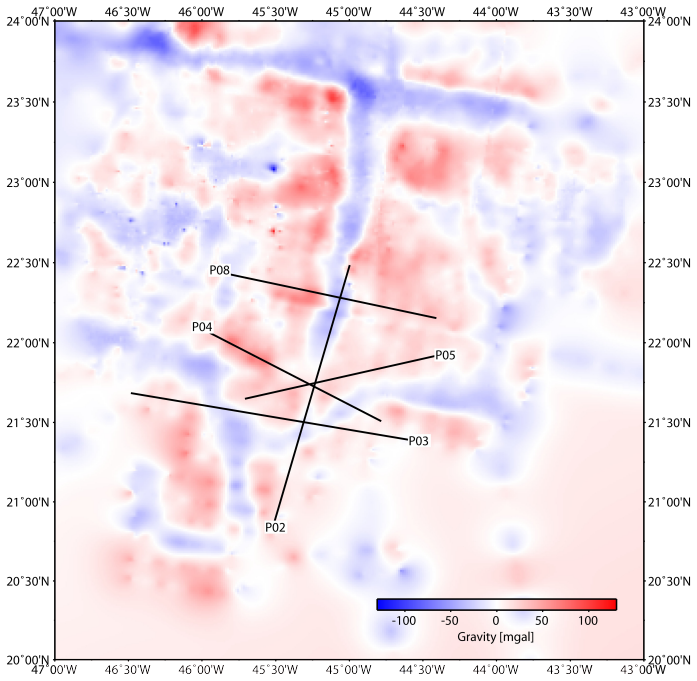

Fig. 2.16 Grid of free-air ship towed gravity data collected by *Maia and Gente* [1995].

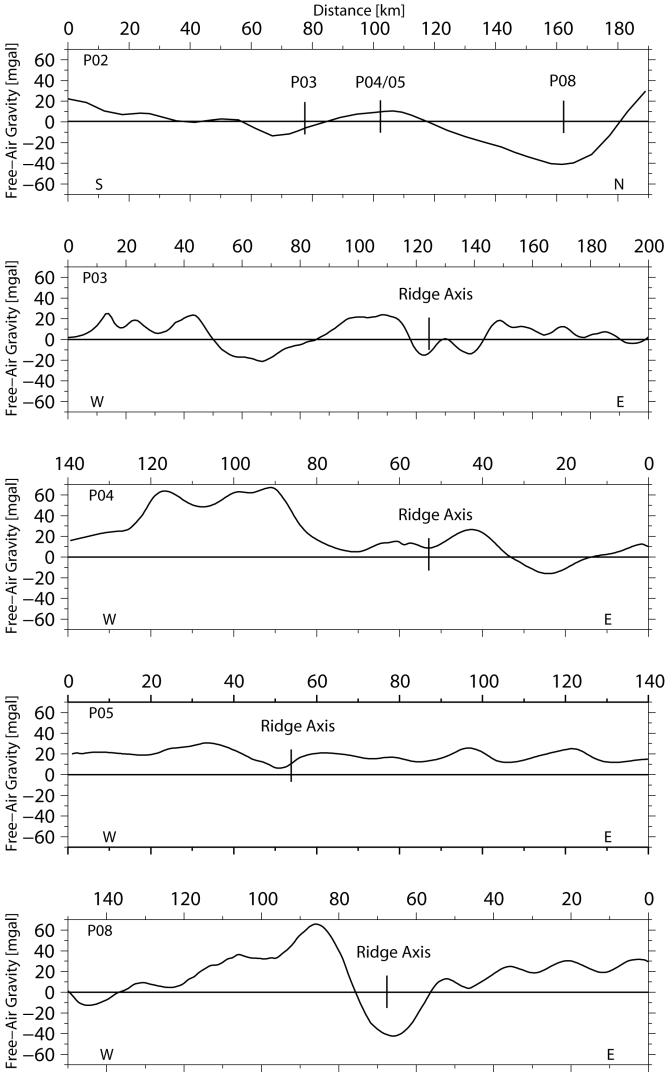

Fig. 2.17 Gravity along the seismic lines.

3 Seismic traveltime forward and tomographic modelling

The 2-D modelling of seismic refraction and wide-angle reflection traveltime data began at the end of the 1970's starting with ray tracing algorithms [*Zelt*, 1999]. Iterative traveltime inversion algorithms came up in the mid 1980's with rising computational capability. The development of inverse approaches was driven by the ability:

- To quickly obtain a final model
- The possibility to model larger data sets
- To derive simpler models for a given level of fit
- To fit data according to a specific norm → no over-fitting
- To generate a final model in terms of errors, resolution and non-uniqueness

The primary objective of wide-angle data is to obtain a velocity model that predicts the observed traveltimes. A model developed by the analysis of traveltime data is only as good as the picks [*Zelt*, 1999]. Amplitude modelling or full wavefield studies are more sensitive to vertical velocity gradients and velocity discontinuities than traveltime modelling.

Due to the complexity of the study area different modelling techniques, seismic tomographic inversion, ray trace modelling, and gravity modelling, have been used to resolve the structures. However, in regions where the crust/mantle boundary is not controlled by PmP arrivals, forward modelling of gravity and Pn travel times was used to constrain mantle structure and the geometry of Moho.

3.1 Forward method

The interpretation of the seismic refraction data was generally carried out using a trial-and-error forward modelling approach based on two-dimensional ray tracing using *Zelt's* [1992] rayinvr or *Luetger's* [1992] Macray.
The fundamental feature of this routine is the simple layered, large-block velocity model parameterisation [*Zelt and Ellis*, 1988]. Ray families have been selected to

model simple features and expand the flexibility of the modelling. This includes S-wave propagation and multiples.

3.1.1 Velocity model parameterisation

The parameterisation for the model of the rayinvr routine is described [after *Zelt's* documentation for the rayinvr code and modelling observations] in the following and similar to the one of the Macray software. The medium is assumed to be isotropic with lateral homogeneity in the normal direction to the plane of the model. The model is composed of quasi-horizontal layers with boundaries that must be consistent over the complete model without crossing another boundary. If a layer thins out the upper and lower boundaries run together to the same depth to the profile end. Each boundary is defined by a number of points connected by a straight line segment having any dip. Within each layer the P-wave velocity structure is defined at the top and the bottom of the layer. These velocities can vary laterally and discontinuities are allowed. Each layer is broken up by vertical boundaries that separate the layer into large trapezoidal blocks (cells). This irregular cell network defines the topography of the layers and is necessary to change the upper and lower velocities in one layer. The velocity at a point within a trapezoid is determined by linear interpolation between its four corners. By that a vertical as well as a horizontal velocity gradient can exist within a trapezoid. Velocity steps can be implemented between trapezoids and therewith between layers. The S-wave velocity is converted by the use of the Poisson's ratio that can vary throughout the model but is defined for one trapezoid and constant within.

3.1.2 Ray tracing

The source can be positioned anywhere in the model and the ray take-off angles can be in any direction or be determined by the user for each ray group. The receivers are always on top of the model. Thus for marine wide-angle studies the source and receivers are transposed. Each type of ray can be traced including multiple conversions of P- and S-waves, reflected and refracted waves, head waves, each possibly containing multiples.

The ray tracing itself is performed by numerically solving the ray tracing equation (a pair of first order differential equations) for 2-D media using the Runge-Kutta method [*Sheriff and Geldart*, 1995] with error control [*Červený et al.*, 1977]. The travel times, their partial derivatives and the travel time residuals are calculated.

The ray step length is selected automatically for each point in the model: if the local derivative of the velocity field is large the corresponding step length will be small and vice versa [*Zelt and Ellis*, 1988]. This is based on the fact that strong ray bending will be the result if the ray passes through an area with a high velocity gradient whereas the ray path is almost a straight line in areas with a gradient near zero. The travel times are calculated by numerical integration along the ray paths using the trapezoidal rule.

3.2 Inverse method

The tomography algorithm tomo2d of *Korenaga* [2000] has been applied for inversion of the traveltime data. For the picks an uncertainty has been assigned that changes with different phases to allow an up and down weighting to the solution from relatively certain to uncertain picks. Ideally an overall normalized X^2 traveltime misfit of 1 should be achieved [*Bevington*, 1969]. Accepting a X^2 larger than one a still well-resolved but relatively coarsely parameterised model is accepted.

3.2.1 Model parameterisation

The two-dimensional velocity model gained by forward modelling or just created from a standard input model has to be parameterised as a sheared mesh that hangs beneath the seafloor [*Korenaga et al.*, 2000]. The seafloor topography is included into the model. The nodal spacing of the mesh can be variable in horizontal and vertical directions. To avoid any bias the nodal spacing is conditional chosen to be finer than the expected velocity variation. Too coarse grid spacing can also result into inaccurate solutions of the graph theory. For the high velocity gradients connected to normal oceanic crust a very dense mesh with nodal spacing of a few hundreds of metres or less is necessary [e.g. *Toomey et al.*, 1994]. Using an irregular grid in having a denser mesh in areas of strong velocity or geologic variations and a less dense in simpler areas can save computational time. In this study the mesh has a constant horizontal nodal spacing and an increasing vertical nodal spacing for all profiles. The amount of data is fairly small and computational facilities are large enough to process that dataset.

Only one reflector is supported in the tomo2d code. But since there is no sediment cover in the investigation area, no sharp velocity contrasts in the crust are expected or seen in the data, and only rarely PmP phases are visible, this fulfils the requirements of this dataset. The reflector is represented as an array of linear segments. While the horizontal coordinate of each node is fixed, it will be varied in the vertical direction. Although there is a need of a velocity discontinuity to generate a PmP phase such a sharp interface is not adopted to the modelling. Instead a so called floating reflector that is updated without changing the adjacent velocity nodes is employed [*Korenaga et al.*, 2000].

3.2.2 Forward problem

The calculation of the ray paths and the resulting travel times in the tomo2d code [*Korenaga et al.*, 2000] is achieved by means of a hybrid method based on the graph method [*Moser*, 1991] and the ray-bending method developed by *Papazachos and Nolet* [1997].

The graph method, known as shortest path method, can calculate the shortest connections between an origin node and all the other nodes of a network. Thus, seismic travel times between nodes, used as a nodal distance, this method can be used to generate a set of first arrival travel times and corresponding ray paths [*Nakanishi and Yamaguchi*, 1986]. The search for the shortest ray path is restricted by

a forward star [*Moser et al.*, 1992]. Using a higher order forward star means a denser sampling resulting in a higher resolution but elongates the computation time. In the environment of an oceanic ridge a star that prefers the downward directions is more efficient because of the high vertical velocity gradient [*Van Avendonk et al.*, 2001]. In this work a fifth/eighth order forward star is applied. The path restricted by the forward star describes a zigzag of the seismic ray and the travel times tend to be overestimated.
Instead of using a higher-order forward star the ray-bending method [*Moser et al.*, 1992] is applied. The ray-bending method requires a good initial model, which is given by the graph solution, to better and faster converge to a global minimum. So there is a trade-off in between the computation time of the graph solution and the ray-bending.
The ray-bending method as developed by *Moser* [1992] employs the conjugate gradient method to minimise the travel time along a ray path. The rays are parameterised as beta splines [*Korenaga et al.*, 2000] using the nodes of the graph solution as initial control points in the conjugate gradient search. The calculated path will be optimised to find the nearest path with a stationary traveltime. By beta splines a broad variety of curves can be described by a relatively small amount of control points.
Other types of finite difference methods and graph methods than shortly described here can be found in *Zhang* [1998].

3.2.3 Inverse problem

An initial velocity model is given and the travel time residuals δT_j can be mapped into slowness perturbations δu along the ray path Γ_j using the following integral [*Korenaga et al.*, 2000]:

$$\delta T_j = \int_{\Gamma_j} \delta u d\Gamma \qquad (3.1)$$

This is for the refraction travel time residuals. It works similar for the reflection travel time residuals and vertical changes in reflector depth are added:

$$\delta T_j = \int \delta u d\Gamma + \frac{\partial T}{\partial z}|_{x=x_j}\ \delta z(x_j) \qquad (3.2)$$

x_j is the reflecting point of the jth ray. By discretisation these two equations can be written into one matrix equation:

$$\mathbf{d}=\mathbf{G}\,\delta\mathbf{m} \qquad (3.3)$$

with d as the traveltime residual vector, δm is the unknown model perturbation, and G is the Fréchet derivative matrix containing a velocity sensitive part (the path lengths distributed to relevant velocity nodes) and a depth sensitive part which is given by the incident angle of the ray, the slope of the reflector, and the velocity at a reflecting point as derived by *Bishop et al.* [1985]. The matrix equation (3.3) forms the foundation of this travel time tomography. The continuation in the detailed description of the

mathematical background can be found in *Korenaga et al.* [2000]. Here only the main features will be summarized shortly in the following.

This is an iterative method thus if the starting model is too far from the true model it has to be applied several times until the model converges. Pick uncertainties will be given to each hand-picked travel time to correlate them to some extent. To obtain a unique solution of the underdetermined equation (3.3) smoothness constraints, one each for horizontal and vertical directions, are applied [*Toomey et al.*, 1994] with respect to the data resolution. To avoid instability of the iteration (if the starting model is to far from the true solution) the inversion can be repeated without the outliers (too large residuals). Additionally damping constraints for velocity and depth nodes are introduced.

Now there are four parameters that have to be chosen. The correlation length parameters have been chosen by the limits of the working memory capacity of the computer. Larger values are preferred as these results in a smoother model on the cost of computation time. A suggested strategy is to further determine the smoothing weights by systematically testing velocity and depth smoothing in a single-step inversion [*Korenaga et al.*, 2000] and fix them afterwards through all subsequent iterations. A large set of smoothing weights has been plotted in diagrams with model roughness versus the predicted X^2 (Fig. 3.1).

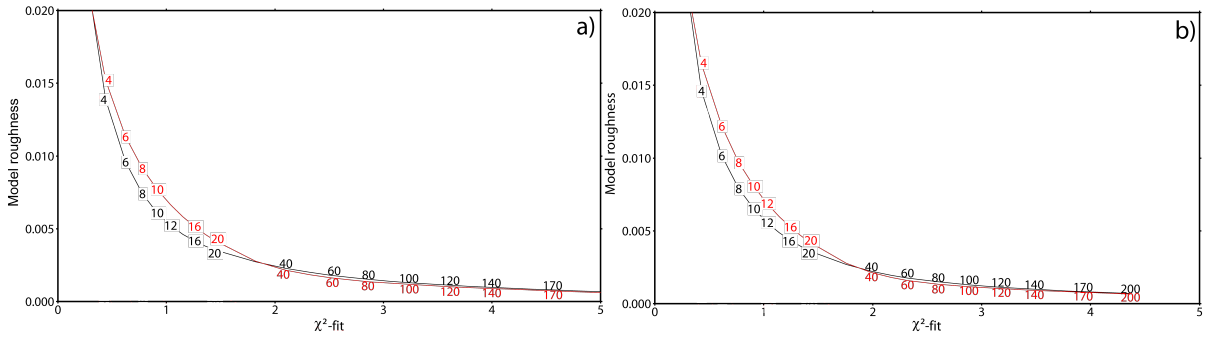

Fig 3.1 a) L-curve for inversions including Pg-phases within 20 km offset from each station and b) all picked Pg-phases. Black line is representing the horizontal model roughness and the red line the vertical one.

Even in the refraction and reflection tomography there exists non-uniqueness regarding the depth of a reflector because lower crustal velocities are mainly resolved by reflection traveltimes. Different ray coverage, strongly heterogeneous velocity structure, and a variable interface topography results in a velocity-depth ambiguity. A depth kernel weighting parameter (w) is used to investigate the velocity-depth ambiguity. A value of w=1 corresponds to the equal weighting of velocity and depth nodes [*Stork and Clayton*, 1991], and increasing the weighting parameter leads to larger depth perturbations with smaller velocity perturbations. Thus the velocity-depth ambiguity can be tested systematically. A general trend is that when the ray coverage is sparse the inversion with a lower w shows an insufficient recovery of the reflector depth and compensates this with velocity perturbations.

A regularized linear system can then be written as

$$\begin{bmatrix} d_t \\ 0 \\ 0 \\ 0 \end{bmatrix} = \begin{bmatrix} G_v & wG_d \\ \lambda_v L_{Hv} & 0 \\ \lambda_v L_{Vv} & 0 \\ 0 & w\lambda_d L_d \end{bmatrix} \begin{bmatrix} \delta m_v \\ \frac{1}{w}\delta m_d \end{bmatrix}, \tag{3.4}$$

where subscripts v and d denote the velocity and depth components, respectively, and λ_v and λ_d control the relative importance of the smoothing constraints with respect to the data resolution. L_{Hv}, L_{Vv}, and L_d are the smoothing matrices for horizontal, vertical, and depth perturbations, respectively.

3.3 Gravity modelling

3.3.1 Joint seismic and gravity inversion in general

Gravity modelling has been common in studies of deep crustal structure. The benefit of a joint seismic and gravity modelling is to gain the structure of deeper areas that are not so well resolved by seismic refraction only. The crust-mantle-boundary can be constrained by using the gravimetric data. The inversion problem becomes less non-unique. A further advantage to apply a joint modelling with both datasets are that gravity data are sensitive to lower and higher density values compared to seismic velocities that tend to be more sensitive to high-velocity zones.

3.3.2 The method of joint seismic and gravity inversion

Seismic inversion method by Korenaga is described in section 3.2. The formulation of the inverse problem is similar to the seismic joint refraction and reflection tomography by adding a Fréchet derivative matrix for the gravity anomalies and the residual gravity anomalies. Using the same annotations equation (3.4), a regularized linear system can then be written as

$$\begin{bmatrix} d_t \\ \lambda_g d_g \\ 0 \\ 0 \\ 0 \end{bmatrix} = \begin{bmatrix} G_v & wG_d \\ \lambda_g F_v & \lambda_g wF_d \\ \lambda_v L_{Hv} & 0 \\ \lambda_v L_{Vv} & 0 \\ 0 & w\lambda_d L_d \end{bmatrix} \begin{bmatrix} \delta m_v \\ \frac{1}{w}\delta m_d \end{bmatrix}, \tag{3.5}$$

where subscripts d_t and d_g are residual travel times and residual gravity anomalies respectively. G and F are Fréchet derivative matrices for travel time and gravity anomalies, respectively. The L matrices are for the smoothing constraints (equation 3.4). The *δm* vectors are for model perturbations. The mathematical background of the joint seismic traveltime and gravity inversion in more detail is described by *Korenaga et al.* [2001].

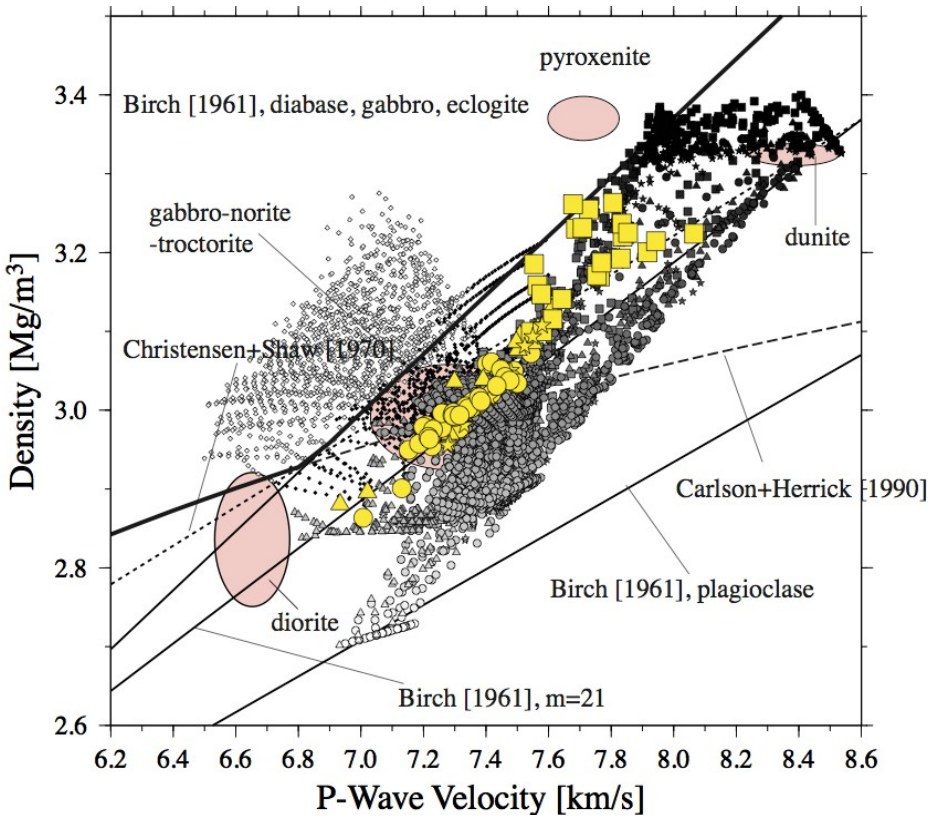

Fig 3.2 This figure is taken from *Korenaga et al.* [2001] presenting the covariation of P-wave velocity and density of mafic and ultramafic rocks at 1000 Mpa and 25° C. Three solid lines are taken from *Birch* [1961]. Dashed dotted lines are for normal oceanic crust based on ODP/DSDP core data [*Carlson and Herrick*, 1990] and on samples dredged from the Mid-Atlantic ridge.

A starting model is the velocity model gained from the joint refraction and reflection seismic travel time tomography. The correlation length functions for velocity and depth nodes are the same. Also the depth kernel weighting parameter w has still to be chosen. That will be higher, *w > 1*, than used in the seismic traveltime tomography since the velocity model that is the starting model should be well constrained. Mainly changes of the depth of the Moho are the main goal of this joint modelling.
The decision to choose the gravity-kernel weighting parameter λ_g was done by running five 2-step iterations for different λ_g-values that varied between 0.1 and 1. The RMS traveltime residuals and the RMS gravity residuals are plotted as a function of the gravity weighting parameter similar to figure 3.1.
A crucial step is to choose the velocity depth relation. Figure 3.2 presents common co-variations of P-wave velocity and density of mafic and ultramafic rocks [*Korenaga et al.*, 2001]. The velocity-density relationship adopted in this study is shown as the thick solid line. Birch's law [*Birch*, 1961] is applied for diabase and gabbro:

$$\rho = 0.375 + 0.375 v_p , \qquad (3.6)$$

This conversion law can serve as an upper bound for the density of primary gabbroic rocks (6.8 - 7.0 km/s). For velocities below the empirical relationships for oceanic crust of *Carlson and Herrick* [1990] has been chosen:

$$\rho = 3.81 + 6 / v_p , \qquad (3.7)$$

However gravity modelling has several problems as described by *Korenaga et al.* [2001]. The velocity-density relation can have large uncertainty even for a single rock type, due to compositional and porosity effects. The velocity model itself has also estimation errors. The derived density distribution has a large non-uniqueness.

3.3.3 Off-axis gravity modelling as a combined forward modelling

The above described joint seismic and gravity inversion method has been also applied for the seismic line across the MAR, profile 8. However this resulted in no trustable results. Big effort was made in changing the parameterisation and applying a thermal factor. The failing could be caused by a too small number of PmP picks, which means that the velocity model and Moho geometry are not well constraint all over the profile, and the very high lateral variation in velocity and density resulting in a complex geology as described by a detachment fault system. Possibly density variations in the mantle over the ridge-axis cross section could be a further reason for the failing. One velocity-density relation is used for one layer along the entire profile not taking into account that there could be changes in that as seen in the amagmatic western flank of the ridge-axis compared to the normal magmatic crustal generation on the eastern flank as described in Chapter 1.2.

3.4 Modelling strategy

3.4.1 Picking

The picking is the most crucial step in seismic traveltime interpretation. The first arrivals and clear later arrivals are used to develop a preliminary model. Identifying of other first and later arrivals can be done by using the predicted traveltimes and overlay them on the data. Coincident reflection data can often be used as a guide to picking the near offset reflection phase in the refraction data. But for the study area no streamer data exist. Due to noise, changes in the waveform, spatial aliasing, and weak signal the use of fully automated picking is not helpful particularly for later arrivals.

For some stations a correction for the seafloor topography has been applied. A data example from station OBH66 at line P08 in figure 3.3 shows the advantage of this approach for the identification of the later PmP-phase. The topography is corrected to a horizontal datum. A static shift correcting for the water depth has been applied to each trace using a constant P-wave velocity of 1.5 km/s for the water layer.

A more accurate solution would be a wave equation datuming. This method gives better results within areas with significant lateral changes in elevation between the starting and the final datum or in the presence of dipping reflectors where the raypath deviates strongly from vertical. However, in this study the static shift has been applied and gave satisfying results.

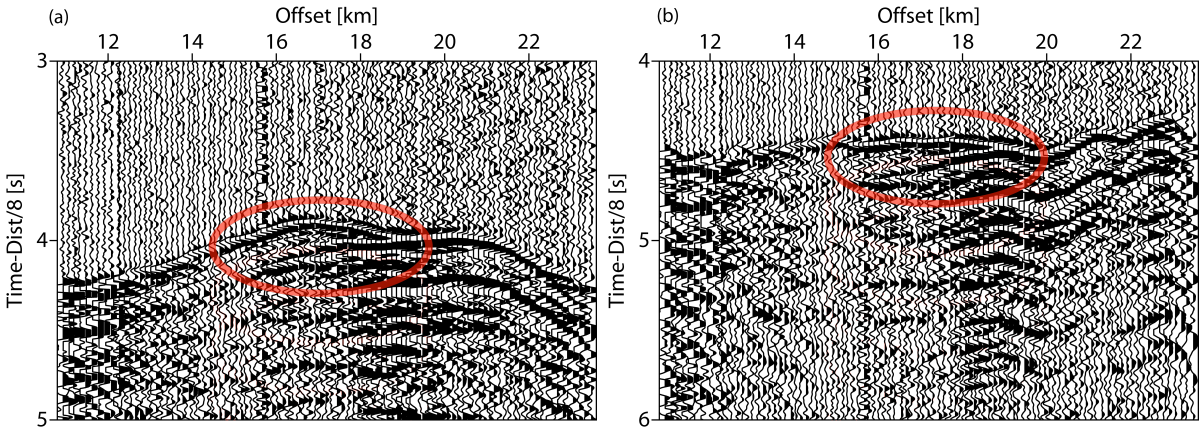

Fig 3.3 Original data (a) have been corrected for the seafloor topography (b). After the datuming it is easier to distinguish the PmP-phase from other phases.

3.4.2 Data uncertainties and traveltime reciprocity

To avoid an over- or underfitting of the data it is necessary to assign pick uncertainties to the arrival picks [*Zelt*, 1999]. The uncertainty depends on signal-to-noise ratio and the frequency content thus for each picked phase a constant uncertainty is applied. This is most important for inverse modelling.

A reciprocity test can be performed to check the arrival picks before modelling. Depending on the source-receiver geometry pairs that are reciprocal the corresponding traveltimes of any phase must be the same, regardless of Earth structure. In marine data where the shots are in the top of the water column and the receivers at the ocean bottom this reciprocal test works only for a flat seafloor with no large undulations or the traveltimes have to be corrected for the water depth. Thus this test has been performed for flat sections of the profiles.

Before starting the modelling the picked traveltimes have to be corrected for errors caused by filtering, signal delay, wrong water depth. The inversion algorithm assumes that the positions of shots and receivers within the model space are accurately known. But in reality this is not the case, and each traveltime residual uncertainty has a contribution from uncertainty in both shot and receiver positions. The true OBH positions were determined using the direct water wave. For each deployment position ray-tracing through the known water column was performed and compared to the direct water wave picks. From that a constant time shift has been applied to all shots. For all profiles and stations this shift lies between 7 and 15 ms.

3.4.3 Forward versus inverse modelling

A choice between interactive forward or inverse modelling must be made. Also a combination of both is possible. The main advantage of interactive forward modelling is to ensure a more geologically meaningful result. The reasons to apply an inverse method have been stated in the beginning of section 3. The probably most important fact is the fitting of a data set, especially a large data set, using the forward approach is realistically not possible without introducing unnecessary structures into the model. Forward modelling is very time-consuming compared to the inverse technique to

satisfy all shots after a parameter update. In the forward method a trial-and-error modelling is done. However, the understanding of the model space and the constraints of the data is maybe better.
With wide-angle and refraction data sets containing many shots it is maybe difficult to fit the data at the level required according to the pick uncertainties. Forward modelling tends to adjust parts of the current model in the way necessary to reduce the data misfit. And it becomes unique depending on the dataset and the modeller. The modeller has to be aware of those problems while interactive forward modelling. In this work both methods have been done. The aim of the forward modelling was to gain a starting model for the traveltime inversion. This starting model has been changed significantly to ensure the non-uniqueness of the problem.

3.4.4 Initial model and choice of inversion parameters

It is important that the initial velocity model is a good representation of the gross structure of the modelled area. A number of models are considered for each profile. As a starting point the crust has been divided into two layers as worked out in section 1.1.4 and described by *Houtz and Ewing* [1976] and *Bratt and Purdy* [1984] with distinct velocity gradients. The layer boundaries where constructed parallel to the seafloor.
The first initial model representing the gross structure was refined in order to better represent the known velocity structure and to identify and eliminate model artefacts.
For inversion the node spacing of the forward grid should be sufficiently small to allow the first arrival traveltimes to be calculated with an accuracy that is reflected by the traveltime residual uncertainties. If the cells are too large in their vertical exaggeration there is a danger of the inversion smoothing the vertical structure especially where the velocity gradients are high (layer 2). Smaller horizontal cell size does not introduce artefacts beyond the resolving power of the inversion method but produced a smoother final model. However, smaller cell size is computing capacity consuming.
Starting with a standard 1-D model for young oceanic crust the gross structure has been identified. Afterwards a broad variety of starting models with different velocity gradients and over all velocities has been used. Figure 3.4 shows calculations of two significant different starting models. Model (a) starts with very low velocities over the entire profile and over depth while model (b) has much higher seismic velocities than standard young oceanic crust shows [*White et al.*, 1992]. The velocity gradient does not change between the two starting models. Both runs of the inversion converge rapidly after 5 iterations to a low X^2 value. The main difference between both final velocity models is the ray penetration depth that is significant larger at (b). This can be explained by the fact that the slower model reaches less model updates during the iterations. The resulting upper velocity structure in the centre of the profile is similar in both cases. That is the model region where high ray coverage occurs and many rays cross each other. At the profile ends and in greater depth both models differ. However, the gross structure of higher velocities in the west, low velocities in the axial valley, and velocities of average young oceanic crust are gained by inversion starting from two strongly anomalous velocity fields.

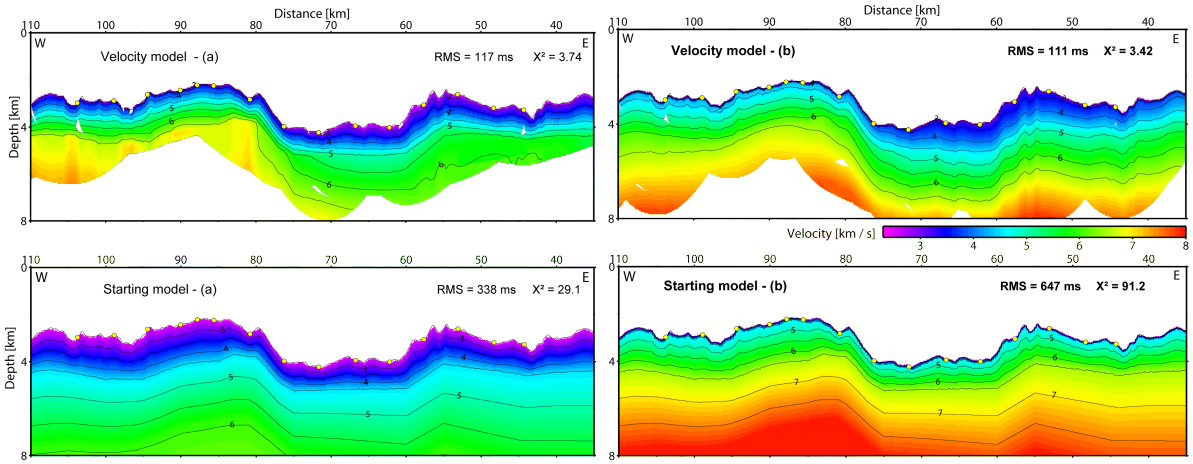

Fig 3.4 Two extreme different starting models have been chosen to demonstrate the convergence of the applied seismic travel time inversion as two examples for the variability of tested models. Model regions with good ray coverage and many crossing rays recover the velocity structure well independent on the starting model. However, a good gross structure should exist in the starting model.

3.5 Data misfit and resolution

The resolution of a model gained from seismic travel time tomography depends on the signal bandwidth that is recorded, signal-to-noise ratio, ray coverage, in detail the crossing ray coverage, and the cell size chosen for the velocity mesh. Ray density calculations, checkerboard test, derivative weight sum calculation, and sharp anomaly recovery tests are methods to test the model resolution. Ray density (cell hits) and sharp anomaly tests have been used in this work and will be described in the following.

In order to calculate the ray density the number of rays passing a cell has to be counted. This gives a fast impression where the model is well resolved by rays. However the number of crossing ray paths is more important for the velocity in a cell.

The checkerboard test and sharp single anomaly tests try to recover the anomalies of a predefined size and amplitude in a certain part (sharp anomaly) or distributed over the entire model (checkerboard). The perturbations are added to the best fitting velocity model. Rays will be traced through this perturbed velocity model and noise is added to the resulting synthetic traveltimes. The now generated traveltimes will be used as an input to another inversion run. The forward calculation and the velocity model recovered after this additional inversion will be compared and an evaluation of the degree of recovery of these anomalies can be given. If it is assumed that the synthetic ray path through the final model closely follows the true ray path, then the results of checkerboard tests on the final model should give a good indication of the size of structure that might have been resolved by the inversion process. But it also indicates where and in what manner blurring and smearing out of the structures might be expected.

4 Results

The final results of the joint reflection and refraction traveltime tomography are presented in the following sections of Chapter 4. The models are plotted at the same depth scale independent of their length. The same velocity colour table is used for all tomographic velocity models presented in this work. To examine the quality and the reliability of the models, the summation of the ray hits per individual cell of the inverse grid is plotted. A few example stations showing the seismic data can be found in Chapter 2. More seismic sections and picks with the fits from the modelling can be found in the Appendices A to D. The modelling strategy has been described in Chapter 3.

4.1 Results for profile 2

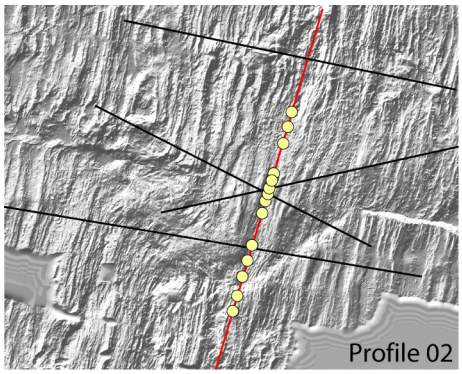

This line is aligned normal to the spreading direction on top of the ridge axis. This along-axis profile shows the lateral variation of the crust at a propagating ridge segment. Most stations have a high signal-to-noise ratio that allowed a clear identification of the different phases of P-wave arrivals. Even at large offsets, up to 70 km and partly limited by the profile length, some of the seismic records imaged the mantle. Three out of six central stations of the original deployed line did not work properly. Thus, no data or very low quality data were recorded. Therefore, an additional redeployment and shooting was performed along P06. Those stations have been added to P02, however, the re-shot profile is much shorter and offsets of only 40 km are common for the resulting seismic sections.

Primary phases at the onset of the first positive amplitude peak from the crust (Pg) and the mantle (Pn) and secondary arrivals with high amplitudes from the crust-mantle boundary (PmP) were picked manually and are presented in the seismic sections (Fig. 2.9) from three stations of the profile.

Unfortunately, the PmP-phase appears not at all stations as clear arrivals with strong amplitudes. This could be caused by a smaller crust-mantle velocity contrast or zones of lower velocities in the crust. The critical distance shows a strong variation along the

ridge-axis. The offset where the critical distance can be recognized ranges from 10 km in the north to 35 km in the segment centre. Northern stations show high velocities interpreted as mantle phases at small offsets (~10 km), while at the segment centre, mantle phases occur at much larger offsets.

4.1.1 Forward ray tracing

First velocity models were constructed using the forward traveltime modelling procedure by Zelt and Smith (1992) rayinvr due to its possibility to easily handle not only the P-waves, but also their multiples and converted S-waves. A minimum of depth and velocity nodes was used to describe the final forward model (Fig. 4.1) including crustal first arrivals and mantle reflections. The velocity model shows that the upper crust seems to have a constant thickness, while the lower crust varies in thickness between 7 km at the segment centre and 4 km at the northern segment end. The crust at the southern ridge tip has a thickness of 5.5 km. The gross structure of the segment could be resolved well by this approach.

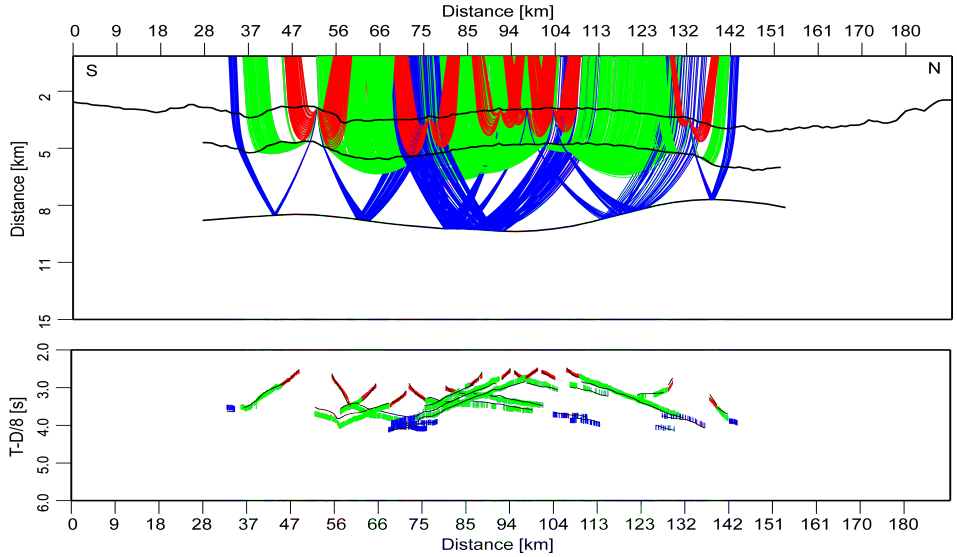

Fig 4.1 Forward model gained from the ray tracing method rayinvr [*Zelt and Smith*, 1992]. The crust is thickening in the segment centre. The northern segment end has less thick crust compared to the southern ridge tip.

4.1.2 Joint refraction and reflection tomography

To yield the velocity structure from observed travel times, a traveltime tomography [*Korenaga et al.*, 2000] was used. Several starting models were taken and tested to yield a robust final model of the velocity structure. Changes in the velocity and in the gradients from simple to more complex starting models were inverted. To begin with downward stripping of the layers was performed, inverting first for the upper crustal arrivals (see example in Figure 4.4) and applying afterwards all crustal arrivals. Step by step, and by fixing the upper part of the model, the first arrival picks of larger offsets were added. After the inversion converged rapidly to a X^2 value of about one, the mantle reflection picks could be added to the modelling. A kind of floating reflector was

added to the starting model. The inversion of the PmP travel time picks preferentially updates the depth to the reflector.
A sheared mesh with parallelogram shaped cells hangs beneath the seafloor. The velocity field is continuous everywhere. The interpolation of the velocity field within each cell and the tomographic inversion are described in section 3.2.
Figure 4.2 shows the tomography results of the first arrival picks within an offset of 20 km from each station. Shown, is a calculation using a constant velocity gradient in the starting model. The ray coverage expressed by the derivative weight sum (DWS) is continuous between 35 and 145 km in distance along the profile. The velocities in the uppermost crust, a few hundred metres below the seafloor, vary strongly. In the central part of the segment they reach the highest values of 3.2 km/s, while towards the segment ends the seismic P-wave velocities decrease to about 2.8 km/s. This observation is consistent with the results from the forward modelling (Figure 4.1). Down to approximately two kilometres beneath the seafloor the velocity gradient of 1.6 1/s is very large. It changes suddenly to a velocity gradient of less than 1 1/s. This means layer 2 is well resolved by the rays that penetrate through the subsurface within 20 km from the OBH's while only the uppermost section of seismic layer 3 is resolved. The deeper part is penetrated by some single rays that do not cross each other; thus, this region of the model is not well constrained by this kind of near offset modelling and underlies changes in the following inversion steps. Another important feature in figure 4.2 is the lower gradient, about 1 1/s, in layer 2 between 60 and 80 km in distance along the profile. This is the area of the ridge tip.
The seafloor was parameterized at a spacing of 1 km, while the regular grid has gird cells with a uniform horizontal spacing of 200 m and a vertical increasing spacing from 50 to 170 m. The velocity and depth smoothing and damping parameters were chosen as 20 and 10 for velocity and depth, respectively. A weighting factor of w=1 was used for weighting the depth and the velocity nodes equally. A larger weighting factor should lead to larger depth perturbations [*Korenaga et al.*, 2000].
A strong variation in the deeper part of the starting model and changes of the depth of the Moho resulted in very similar final models. The calculated traveltimes and their residuals to the observed traveltimes are calculated and resolution tests were performed to verify the reliability of the resulting velocity model (Figures 4.3a-d).
Profile 2, with the results of the traveltime tomography, is represented in Figure 4.4. It shows a strong variation in crustal thickness. The main compensation of the topography occurs in Layer 3, while Layer 2 almost follows the ocean floor topography. The ridge tip displays slower crustal velocities. The upper crust has a high velocity gradient with velocities increasing with depth from 2.7 km/s to 6.0 km/s and an average thickness of ~1.5-2 km. Layer 3 varies from ~2 km beneath the northern basin to 6 km in the segment centre with in depth slowly increasing velocities to about 7.4 km/s.

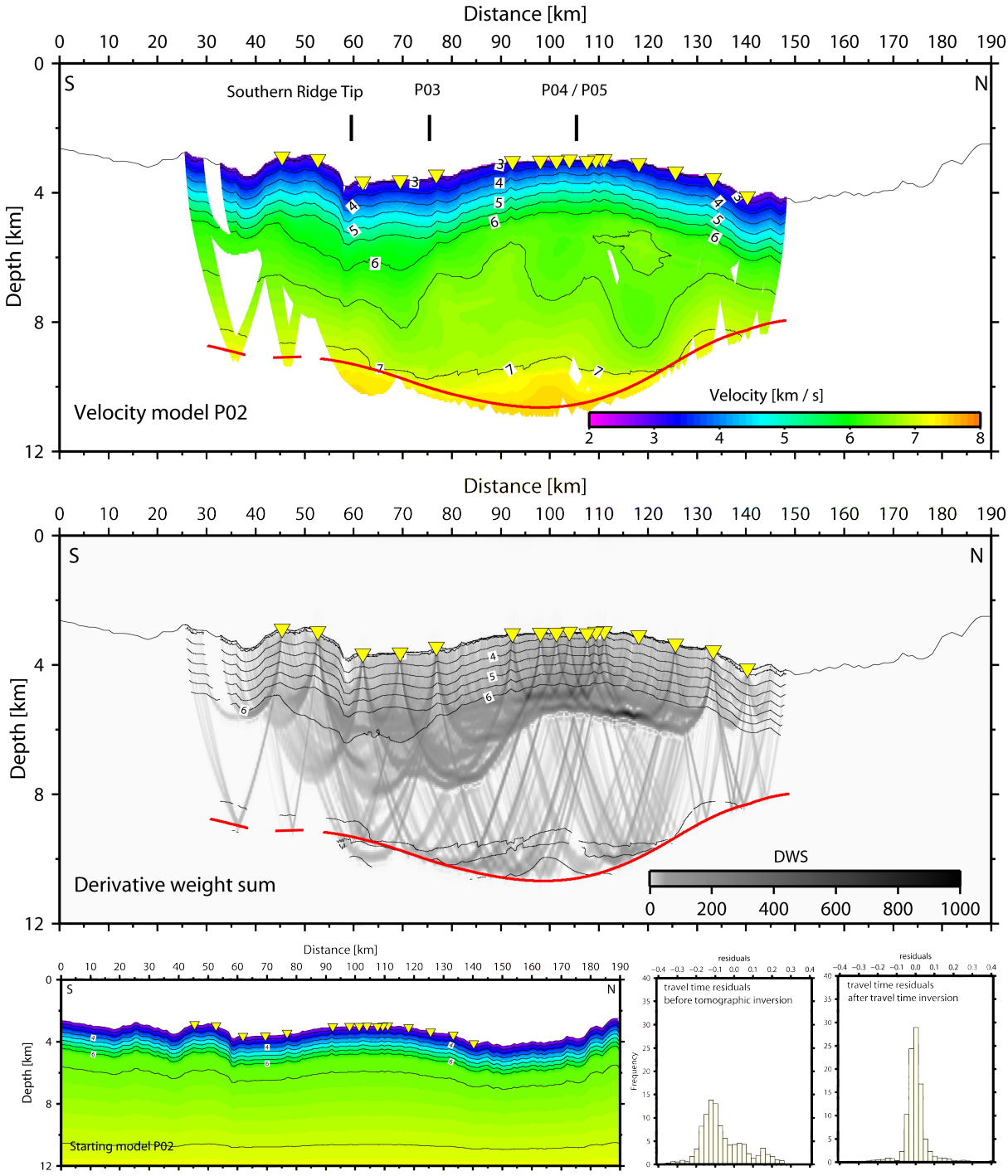

Fig 4.2 Results of the travel time tomography for profile 2 for all picks including crustal first arrivals (Pg) and wide-angle mantle reflections (PmP).

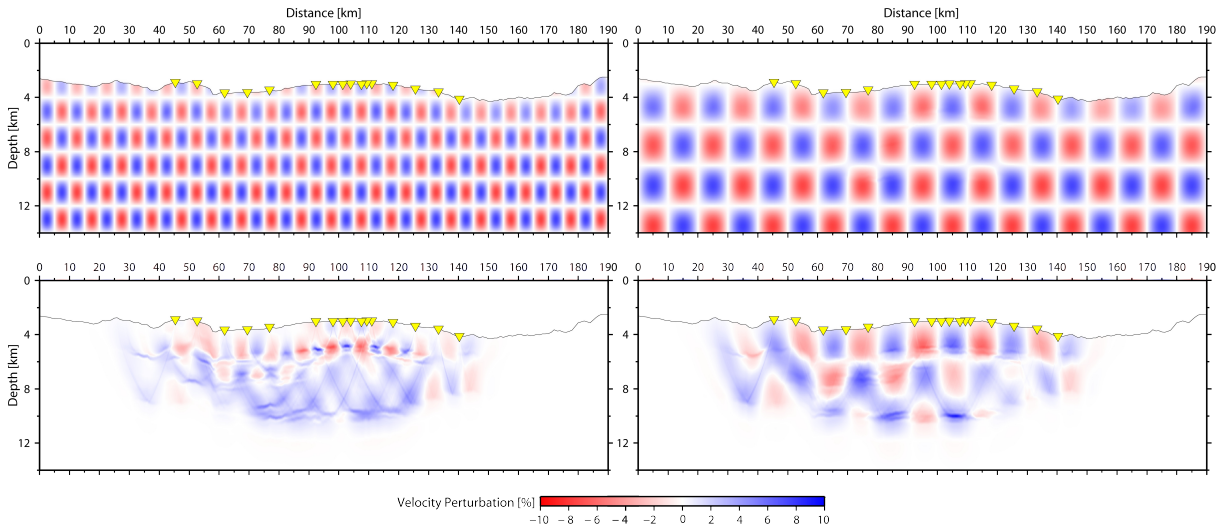

Fig 4.3 Resolution test with two different sizes of anomalies.

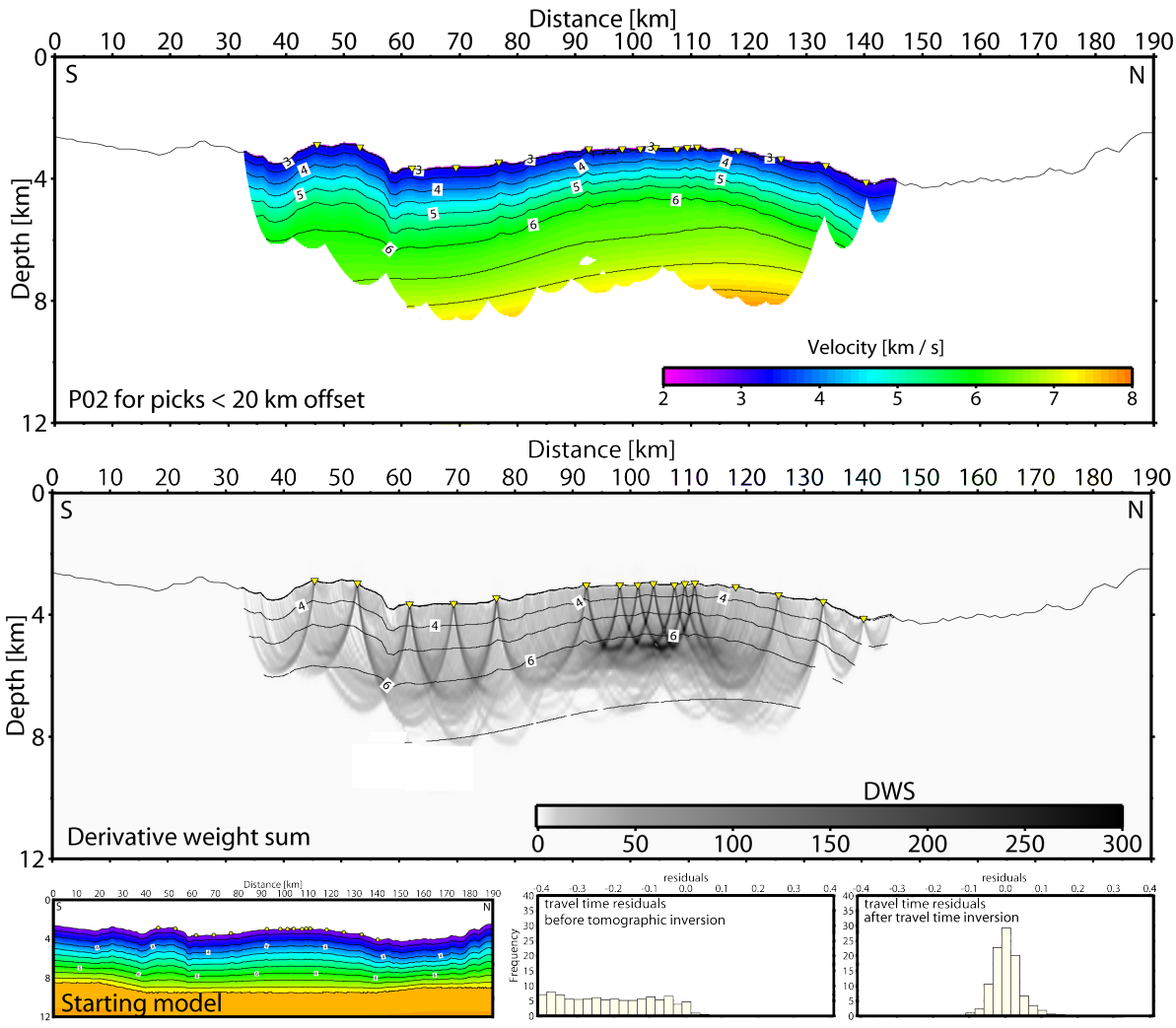

Fig 4.4 Results of the travel time tomography for profile 2 for near offset crustal picks (Pg). a) seismic velocity field; b) DWS imaging the ray coverage c) starting model, traveltime residual from the ray tracing before and after inversion (left and right, respectively).

The different offsets of the PmP arrivals (see seismic sections in Appendix A) are a result of variation in the crustal thickness, which increases at topographical highs and decreases at depressions at the northern end of the profile. This is coincident with the results from a gravimetric study of this area that figured out that the segment centres are associated with crustal thickening while depressions are marked by bands of thin crust [*Maia & Gente*, 1998]. Figure 4.4 shows the reflector at a depth of 8 km to 11 km below sea level which was interpreted as the depth of the Moho. It is better to start with a deeper, rather than shallow Moho because it seems that the inversion method is not able to calculate the ray paths correctly within too high velocities or a too high velocity gradient.
For this profile, a total of 3883 picks could be achieved. While there are 3379 crustal arrivals, 504 mantle reflections could be picked at most of the stations. The ray coverage (Figure 4.4b) is good in the central part and poor towards the model ends. The model was received after 8 iterations with X^2=1.45 and a misfit of 72 ms.

4.1.3 Converted shear waves

Along this line, prominent shear wave energy was observed (Figure 2.7 and Appendix A) on shot gathers of the central stations. The recorded S_v-waves were generated by conversion, since the source acts in the water. There are conditions to be fulfilled to have conversion of compressional waves to shear waves.
Strongest energy occurs at offsets of 10 to 25 km at the stations OBH03 to OBH11 where P-wave velocities are slightly higher than at the segment ends. That is perhaps one reason to explain the existence of S-waves. This seems to be an area of higher density and less fracturing. Thus, the S-wave velocity also rises compared to the segment ends. Therefore, the shear wave velocity of layer 2 is larger than the compressional wave velocity of the water. The centre of the segment shows a P-wave velocity of v_p=3.2 km/s. Assuming a v_p / v_s of 1.8 this results in a v_s of 1.77 km/s. Shear wave modelling showed that velocities larger than 1.6 km/s are needed to result in P-to-S conversion at the seafloor and to reach some higher amplitude S-converted phases in the seismic sections of the seismic instruments.
Strong S-wave arrivals could be identified on source gathers recorded at the central stations located between x > 70 km and x < 140 km, corresponding to approximately the segment centre. A total of 1133 picks served as input for the S-wave inversion. After 5 iterations, the model (figure 4.5) converged to a value of $X^2 < 1$ with a residual traveltime misfit of 80 ms.
The ratio of the V_p to V_s velocity was computed by velocity grid-by-grid division of the final P- and S-velocity models for the first-arrival picks. The crustal v_p/v_s-ratio is about 1.8 (Poisson's ratio of 0.28), without large variation in the central part. To the west it becomes slightly less, which could be the result of stronger fracturing of the area at the ridge tip. The resolution of the v_p/v_s-ratio is primarily determined by the resolution of the less well-resolved S-wave velocity model, as fewer and more irregularly distributed S-wave traveltime data with a larger uncertainty than P-wave traveltime data are available.

The occurrence of S-waves with a constant v_p/v_s-ratio constrains the absence of larger molten areas or magma chambers at shallow crustal levels since shear waves do not propagate through fluids. Commonly, fractures affect the bulk elastic properties and consequently, the seismic velocity. The existence of fluids significantly influences the P-wave velocity in the rocks while S-wave velocities are hardly affected. No major changes in the v_p/v_s-ratio occur. Both, P-wave velocity and S-wave velocity increase gradually.

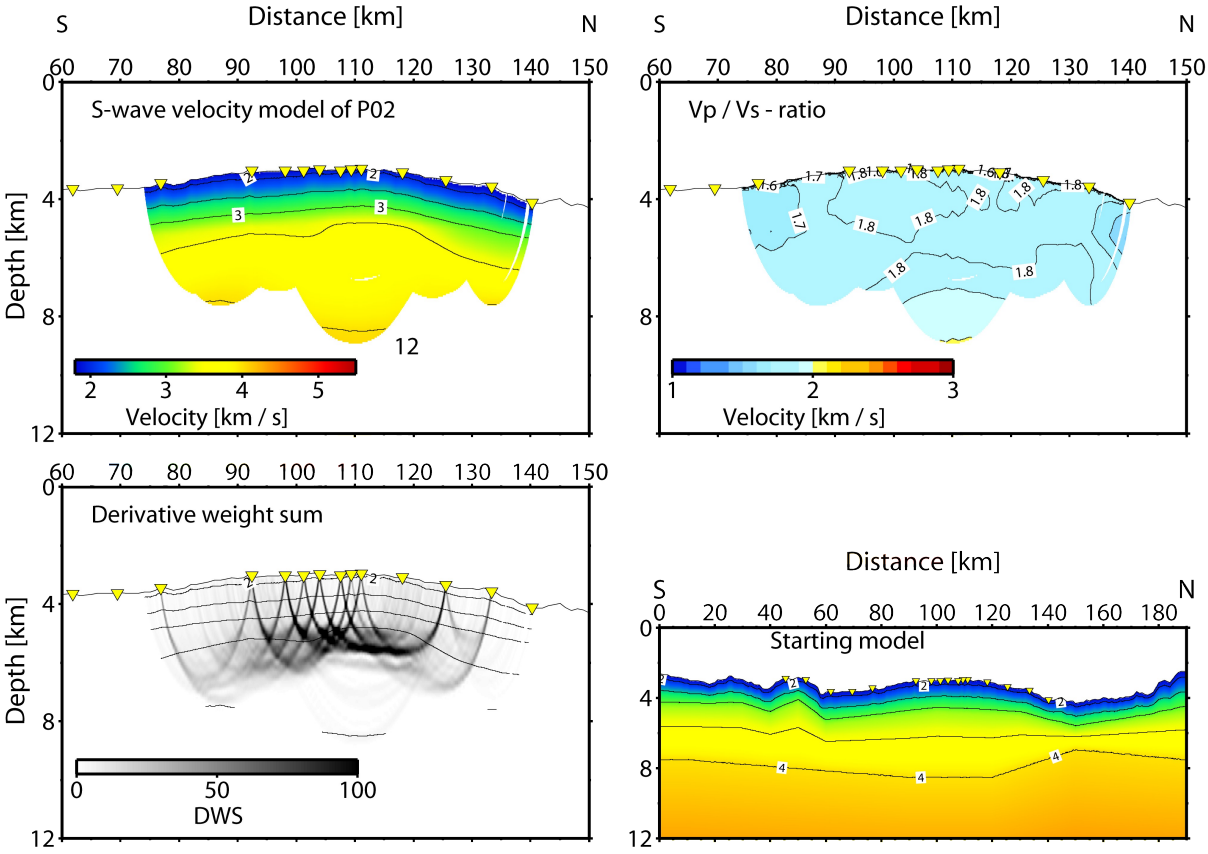

Fig 4.5 Result of the seismic travel time tomography using converted shear waves. a) seismic velocity field for shear waves; b) DWS imaging the ray coverage; c) v_p/v_s-ratio showing a relative constant ration of 1.8; d) starting model.

4.1.4 Joint seismic and gravity inversion

A joint seismic travel time and gravity data inversion was performed (Fig. 4.6). The final model of the travel time inversion was used as a starting model for the joint inversion. Since the velocities of the crust are well constrained by the seismic modelling, the weighting factor between velocity and depth notes has been chosen rather high to suppress major changes to the crustal velocity field induced by the gravity inversion (weighting factor W=10). The goal of this joint seismic and gravity inversion is to better constrain the depth of the Moho. The deeper part of the model is less resolved and more dependent on the starting model, as can be seen in the checkerboard test (Fig. 4.3). The gravity measurement is a potential field method and resolves the subsurface less sharply than the seismic method. After a series of single-inversion tests, the weighting factor between gravity and seismic data of ZW=0.6 was

chosen, giving the seismic travel times the higher weight during the inversion. For this along axis profile, a high temperature gradient of 150° C/km has been assumed [taken from models of *Gac et al.*, 2006] as a parameter in the inversion. The earth average geothermal gradient is about 30° C/km.

Further input parameters and the velocity-density relation have been discussed in section 3.3. Seismic velocities were converted to a density model using different empirical relationships for upper and lower crust: $\rho=3.81-6/v_p$ [*Carlson and Herrick*, 1990] for the upper crust; $\rho=0.375+0.375*v_p$ [*Birch*, 1961] for gabbroic rocks found in the lower crust. The result of the joint inversion (Fig. 4.6) shows an improvement of the gained model in the deeper central part. A better fit of the calculated travel times to the observed travel times was achieved (Fig. 4.7). As a result, the Moho becomes deeper at the segment centre. However, it becomes even shallower at both segment ends resulting in an increase of the travel time misfit. The seismic Moho possibly is an overestimation of crust at the segment ends and an underestimation at the segment centre. For the segment centre, this effect could be minimised by the additional data from the free-air gravity. The final model explains both the travel time data and the gravity anomaly.

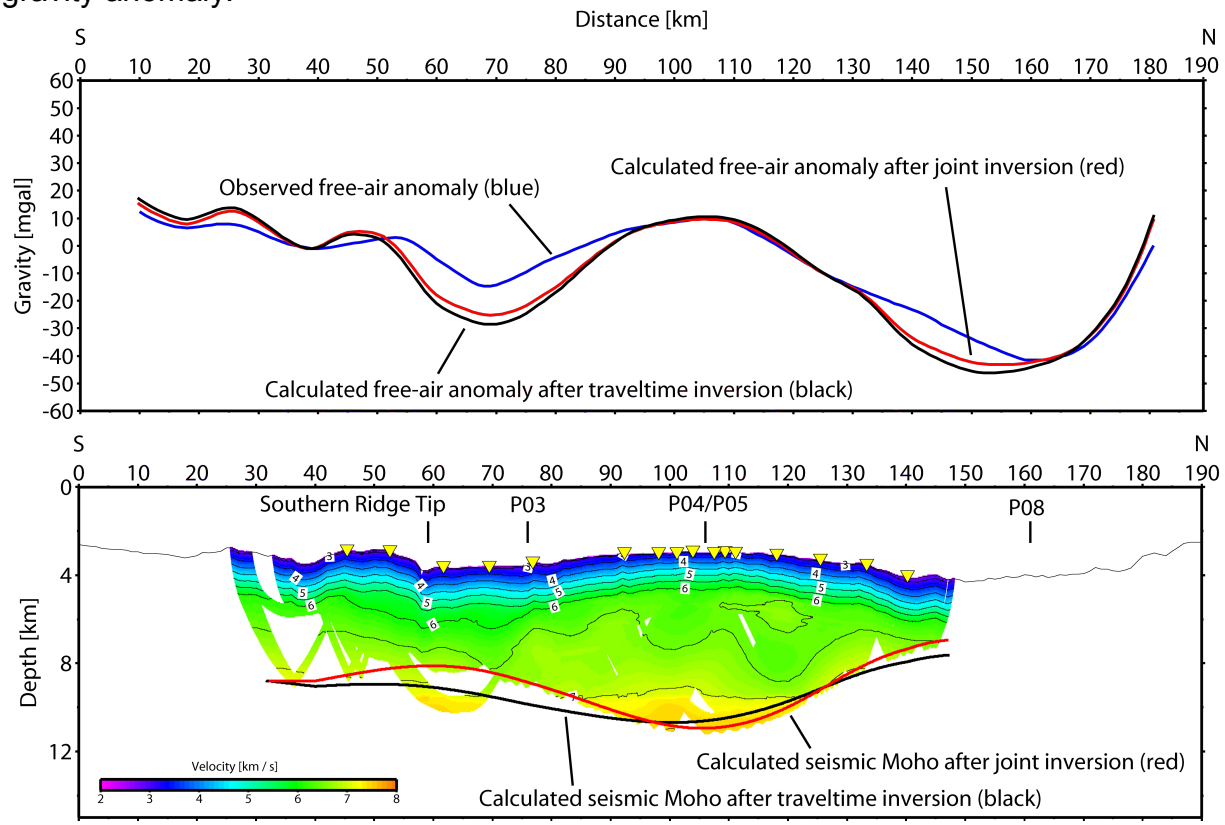

Fig 4.6 Joint seismic and gravity inversion. The upper figure presents the misfit between observed (blue solid line) and the calculated (red and black lines) free-air anomaly. The lower figure shows the velocity field gained by the joint inversion of travel time data and gravity data. The black line presents the starting model from the joint inversion which is the final velocity field of the travel time inversion. The red line is the resulting Moho after joint inversion. The crust becomes thinner at the segment ends, however, the travel time misfit rises in those areas. A better fit could be reached in the segment centre in both RMS gravity misfit and travel time misfit.

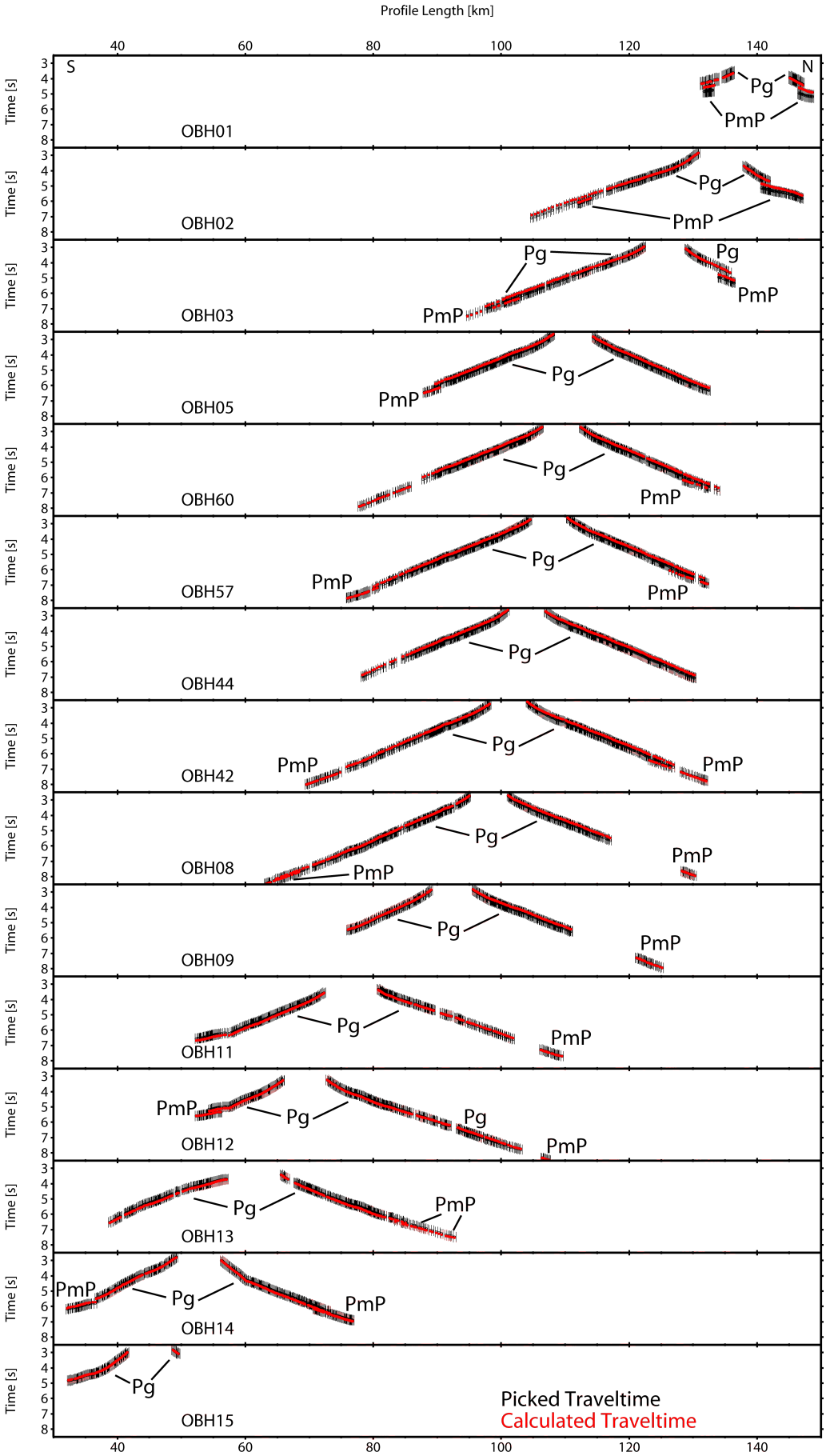

Fig 4.7 Traveltime fits for all stations along profile 2, after joint seismic and gravity inversion.

Both the travel time misfit and the gravity residual became smaller with each inversion step. The inversion was stopped after 5 iterations when the change in the model from the fourth to the fifth inversion became very small. The RMS misfit is about 13 mgal. Although a decrease in travel time RMS misfit was observed for the entire profile, model updates at the segment ends lead to a higher travel time data misfit hinting to the described effect of crustal overestimation.
The impact of the velocity-density relation is intensively studied in the next chapter for the lines P04 and P05. However, this relation is assumed to be rather constant over the entire along axis profile because the crust was generated from the same source and at approximately the same time. Thus, no change in the velocity-density relation due to time or a change in crustal material is expected.
Nevertheless, a critical discussion of this approach has to be made. The mantle is assumed to have a constant density of 3.3 g/cm³. No variation in the mantle due to serpentinisation or temperature is allowed. The gravity, as a potential field method, shows 3-D effects of the structures. For this along-axis profile it might be a strong tool to better constrain the depth of the Moho. For the spreading parallel profiles this approach failed.

4.2 Profiles 4 and 5

Both lines cross the ridge axis near the segment centre and were shot giving an overview about the temporal evolution of the segment. Thus, both lines have been placed to trace the mid-segment during ridge propagation. Changes in the crustal thickness with offset to the spreading centre are connected to changing magmatic activity over the past million years. Both seismic profiles cover crustal ages ranging from 0 to 5 ma on both sides of the ridge axis.

4.2.1 Results of profile 4

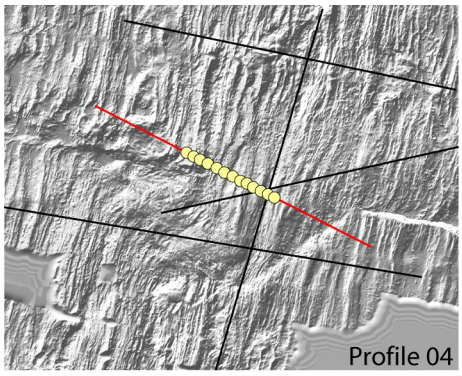

Most of the ocean bottom instruments of this profile are placed on the North American Plate. One station is on top of the ridge axis and another on the opposite ridge flank. The shooting from east to west covers a total length of 140 km. Fourteen out of fifteen stations provided data of high signal-to-noise ratio. Due to the geometry and strong lateral variations in young oceanic crust, only the area beneath the stations could be resolved. The outer 30 km to the edges of the profile show good data quality but rays towards the profile ends do not intersect with possible rays from reversed observations. Because the time a ray needs to path the subsurface is a summation, one has to estimate the upper most layers correctly to minimise errors for the lower layers. Mantle reflections could be picked at some stations. However, only picks that were absolutely well- constrained and consistent over the entire profile were used for the inversion.

The results of the seismic travel time modelling (Figure 4.8) show an increase in P-wave velocity for layer 2A with age as shown elsewhere [*Grevemeyer and Weigel*, 1996; *Grevemeyer et al.* 1998]. Overall, seismic Layer 2 is of a relatively constant thickness. Layer 3 shows a velocity reduction beneath the axial valley. The crustal thickness decreases with offset from the ridge axis from about 7 km to normal crustal thickness of 6 km. The Moho lies at a depth of ~ 10 km below the sea surface. Crustal P-wave velocities reach normal mid-oceanic crustal velocities as described in section 1.1.4. Layer 2 has a very high velocity gradient. The velocities rise rapidly from 2.9 km/ s at the ocean floor to 6.0 km/s at a depth of approx. 2 km. Beneath, values increase gently to velocities of 7.1 km/s at a depth of 6-7 km beneath seafloor. Near the Moho, crustal velocities increase rapidly from 7 to 7.4 km/s. Moho depth decreases to the west, which is also expressed in the gravity response, while this is not so well constrained by the seismic experiment because of less dense ray coverage to the west. The seismic energy was strongly scattered, possibly due to the seafloor roughness. The modelling results of the velocity structure at the ridge axis fit well with the results of the along axis profile P02 (compare to Figure 4.2).
The ray coverage (Fig. 4.8b) is good over the eastern part of the profile down to the depth of the Moho, while deeper rays are missing at the western edge. A total of 4061 picks with 455 mantle reflections were picked manually. The model was received after 5 iterations with X^2=1.39 and a RMS misfit of 65 ms. This presents a rapid convergence from the starting model to a reliable 2D velocity structure.

4.2.2 Results of profile 5

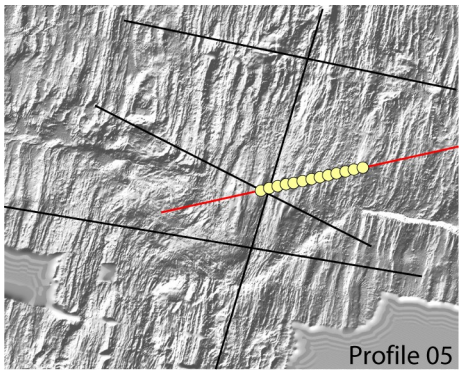

In Figure 4.9a the tomographic results for the ridge crossing profile to the east are presented. The observed structures show layer 2 with a very high velocity gradient and a relatively constant thickness of about 2 km. The estimated velocity of the upper crust rises from 2.7 km/s at the top to 6.0 km/s at a depth of approx. 2 km beneath the seafloor. The P-wave velocity of this uppermost crust increases systematically with offset to the ridge axis from 2.7 km/s to 3.2 km/s at a distance of 50 km to the spreading centre.
A rapid change in the velocity gradient determines the boundary to seismic layer3. Thus, the lower crustal layer has a very low velocity gradient. The lower crust shows slightly rising velocities from 6.0 km/s to approx. 7.2 km/s over approximately 5 km depth. Along this profile, turning ray arrivals from rays through the mantle could be picked consistently at all OBH's. Thus, they have been applied in the tomographic modelling to gain information on the upper most mantle velocities.

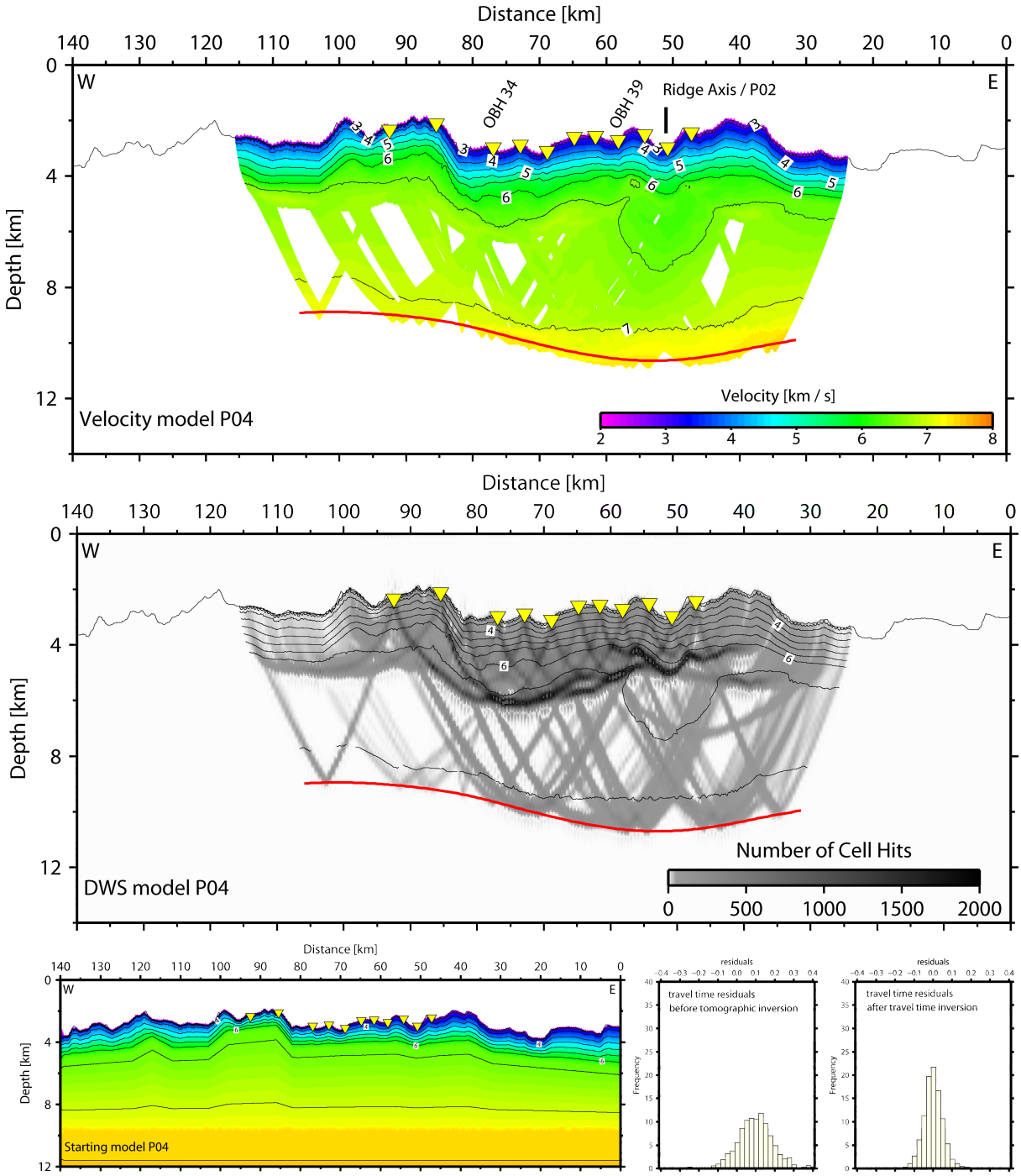

Fig 4.8 Results of the traveltime inversion of profile 04. The uppermost model presents the velocity field in the area that is covered by rays. The DWS model expresses how many rays path one cell of the grid. In the lower left part the starting model is presented. To the right the travel time residuals before and after the inversion are displayed.

The more rapid increase in seismic P-wave velocities, increasing from 7.1 km/s to 7.4 km/s over a depth interval of a few hundred metres, is interpreted as the Moho. The fact that no sharp velocity jump between lower crust and the upper mantle could be detected may be caused by the smoothing operator used in the tomographic inversion code. There is a smooth topography in the Moho reflecting a slightly thickening crust towards the ridge axis. The same was observed for the opposite profile P04 but less

strongly pronounced, which suggests the coverage of a rather magmatic robust part of oceanic crust.

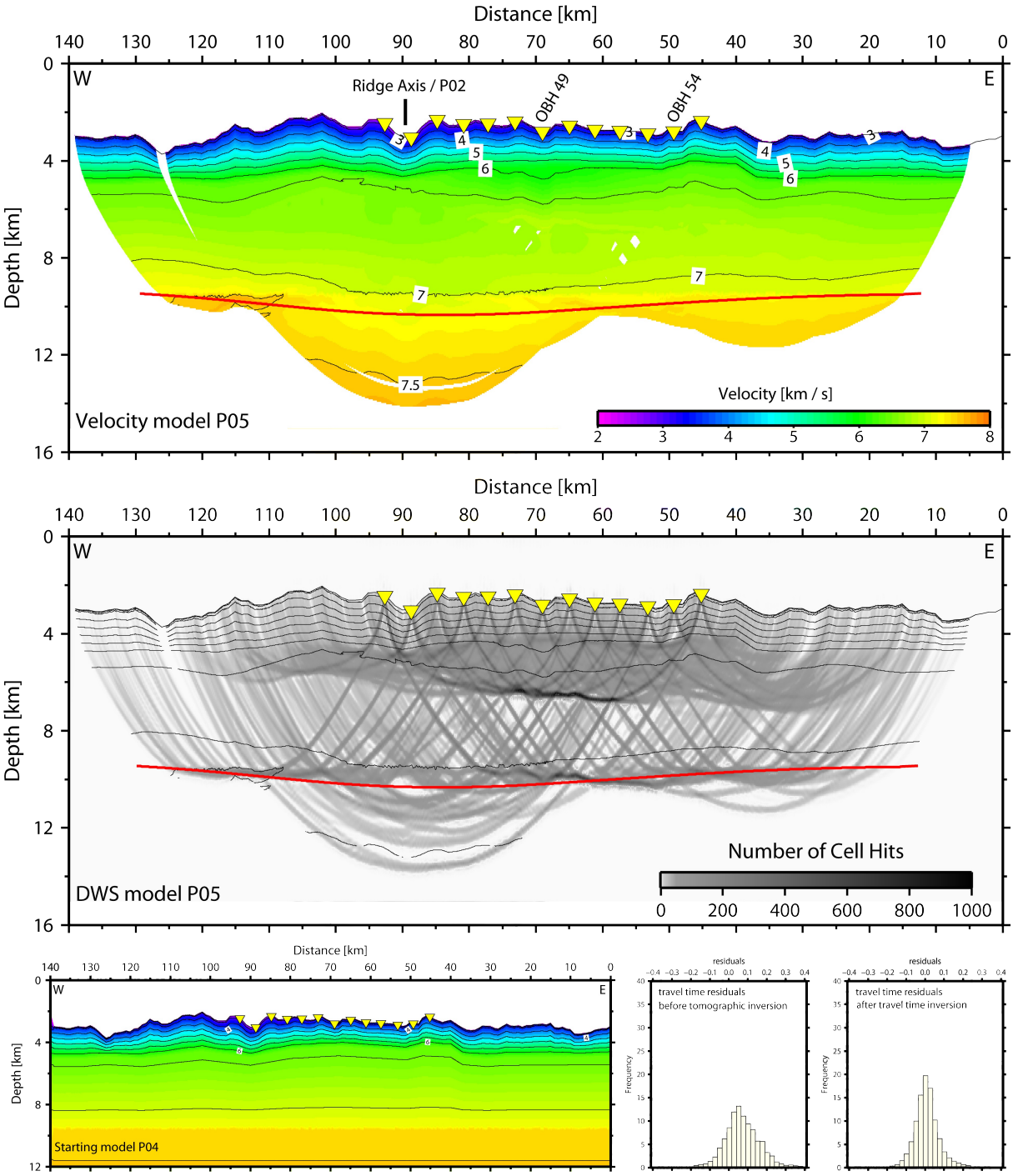

Fig 4.9 Final velocity model of profile 5. The uppermost model presents the velocity field in the area that is covered by rays. The DWS model expresses how many rays path one cell of the grid. In the lower left part the starting model is presented. To the right the travel time residuals before and after the inversion are displayed.

The ray coverage (Fig. 4.9b) is very high over the entire profile and down to the depth of the Moho. The ray penetration of the crustal turning rays reaches greater depths with distance to the ridge axis. This is caused by the higher crustal velocities in the

upper crust. A total of 7401 picks with 5807 picks from crustal first arrivals (Pg), 802 mantle first arrivals (Pn), and 792 mantle reflections (PmP) were picked manually. A pick uncertainty of 0.03 s for the near offset picks and 0.05 for the farer offset picks were applied for the inversion step.

The model was received after 5 iterations with X^2=0.94 and a misfit of 73 ms. This presents the rapid convergence from the starting model to a reliable 2D velocity structure. The reliability of these results is fairly well imaged in the resolution test in Figure 4.10. In section 4.2.3, the results of resolution tests for P04 and P05 are presented.

4.2.3 Resolution tests for P04 and P05

A kind of Monte Carlo approach has been used to study the convergence of a variety of starting models. The standard deviation of these models is shown in figure 4.10. To calculate the standard deviation the observed travel times as well as the starting model were varied. Eight travel time data sets were created including the observed travel times: by adding a positive or negative constant shift of 10 to 30 ms, a rising shift with offset from the station from 0 to 30 ms, and a random shift between plus-minus 30 ms were applied.

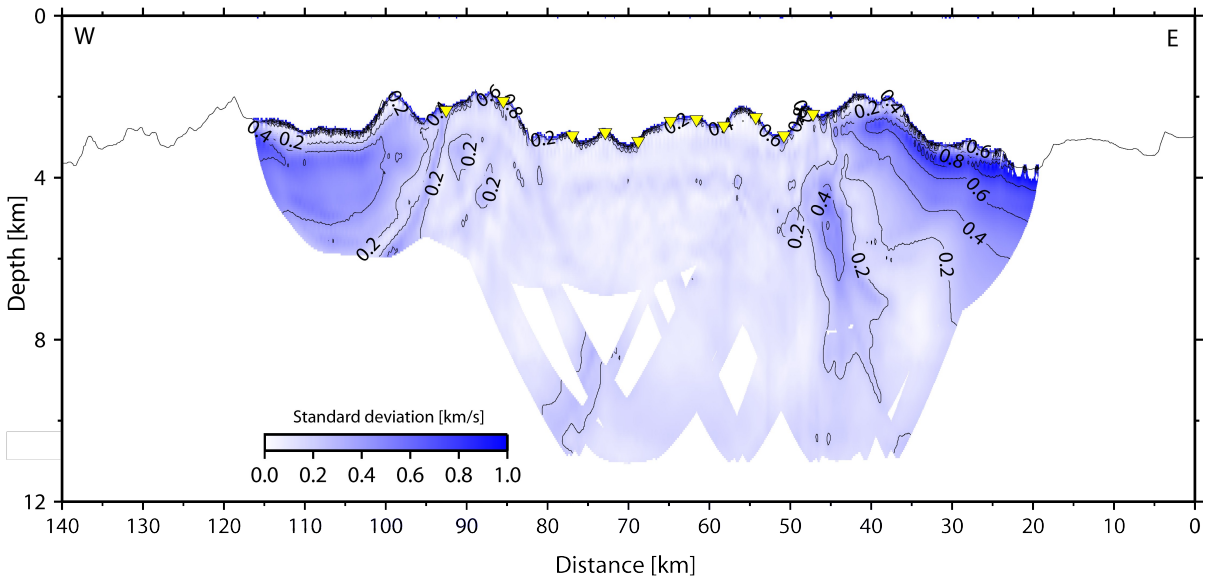

Fig 4.10 Standard deviation of profile 4. The model is well constrained beneath the stations but strongly dependent in the areas that are not covered by the ocean bottom hydrophones.

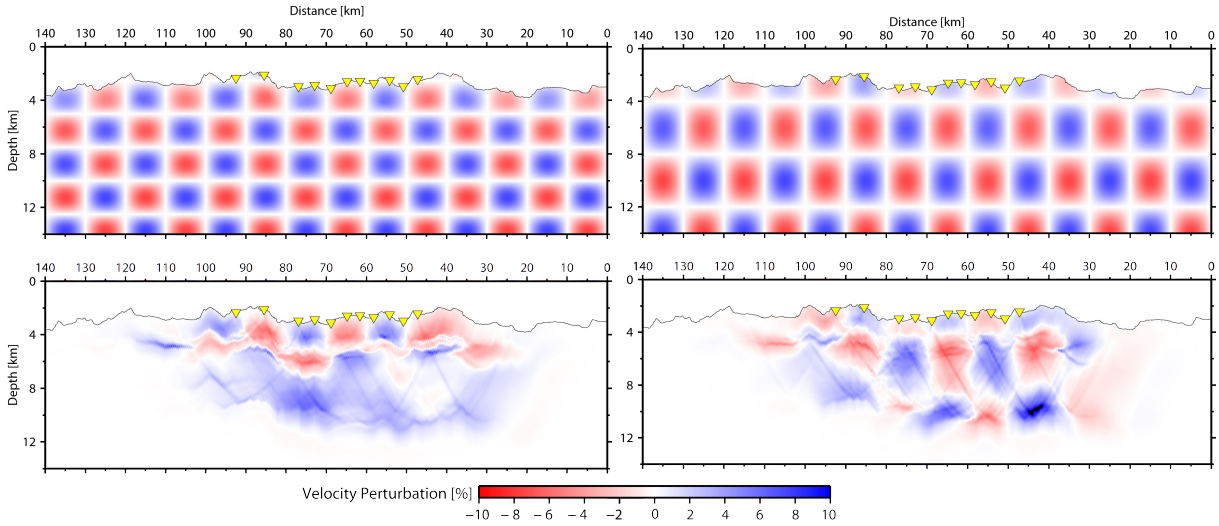

Fig 4.11 Results from a resolution test for P04. The upper two models present the initial perturbations for the test with different large velocity perturbations of plus and minus 0.5 km/s. The lower two figures show the reproduced perturbations for each respective case. Blue is a negative anomaly, red a positive one.

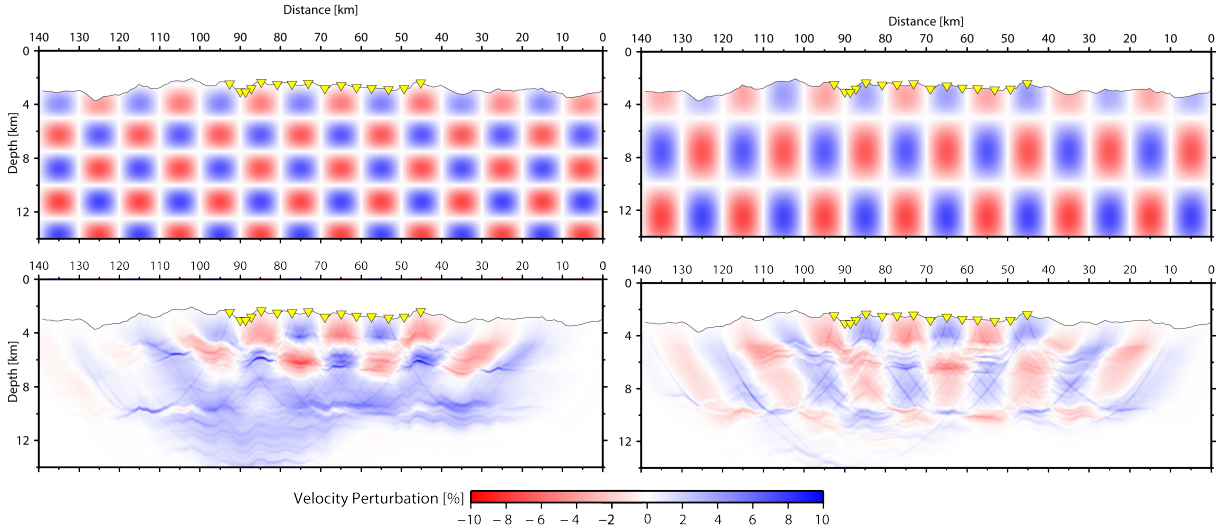

Fig 4.12 Results from a resolution test for P05. The upper two models present the initial perturbations for the test with different large velocity perturbations of plus and minus 0.5 km/s. The lower to figures show the reproduced perturbations for each respective case. Blue is a negative anomaly, red a positive one.

It is clearly visible that the regions in the models that are not covered by stations are strongly dependent on the starting model, while the central part of the profile (50 km to 90 km) is almost independent. This shows also that the structure of lower velocities beneath the ridge axis is independent of the starting model.

Alternating positive and negative Gaussian anomalies with an amplitude of 5%, a horizontal exaggeration of 10 km and vertical exaggeration of 2.5 km, were used. Two resolution tests of opposite polarity were run to ensure that no bias was introduced. The initial perturbations can be seen in the upper two models of Figure 4.11, while the lower two models show the reproduced anomalies by inversion of the synthetic travel times (P04 in Fig. 4.11 and P05 in Fig. 4.12). The region beneath the stations, from 45

km to 95 km, shows a good reproduction to a depth of about 8 km below the sea level. Deeper than this, they smear in a horizontal direction and beside this region they smear vertically because these are the dominant ray propagation directions or are not reproduced at all. Referring to the DWS figure of the model (Fig. 4.8) the area of good reproduction of the anomalies is congruent with the area where many turning rays exist that cross each other.

4.2.4 Gravity modelling

The velocity structure is only reliably resolved for the upper 5 km of the crust (Fig. 4.11 and 4.12). Since there is a trade-off between velocity and layer thickness, the depth of the Moho is dependent on the starting model. Thus, different solutions fit the seismic traveltimes. However, gravity data, as a second dataset, can help to minimize the non-uniqueness of this model.
The gravity code of *Korenaga et al.* [2001] was used to convert the seismic P-wave velocity field to densities. Since the joint inversion of the seismic and the gravity dataset did not result in improved reliable models (this issue is discussed in section 5.2.2) a study of the gravitational behaviour of the two profiles P04 and P05 has been done.

A final velocity mesh was interpolated to a grid file which was then converted to a density grid. The conversion law can be chosen. A constant density for a complete layer or a velocity dependent density using conversion laws after *Birch et al.* [1961] for diabas and gabbro or the relationship of *Carlson and Herrick* [1990] were used for the upper crust (section 3.3). The resulting gravity is calculated along the profile.
Results of this study are shown in Figures 4.13 and 4.14 for profiles P04 and P05, respectively. Especially along profile 5, the responses of the different cases are easy to distinguish because of the smooth topography. Case (a) shows the response for a constant crustal thickness of 6 km with a density of 3.0 g/cm³. The ridge axis is situated at a distance of 88 km along P05. The residuum gets larger with rising distance to the ridge axis. Thus, topography at the Moho is applied in the next step (b). The general trend fits better to the measured gravity data. However, still a rising difference between predicted and observed gravity data occurs. Dividing the crust into upper and lower crust (c) leads to even better prediction of the observed gravity data near the ridge axis. A constant density of 2.7 g/cm³ was applied for the upper crust. In case (d) the velocity-density relationship after *Carlson and Herrick* [1990] was used and in case (e) for the lower crust the *Birch* relationship [1961] was added. This results in a reasonably good fit in the part that is covered by the seismic stations. Thus, the velocity field converted to densities can also explain fairly well the gravity measured along the profile. It can also be shown that the depth of the Moho is well constrained by both the seismic travel times and the free-air gravity data. Case (f) presents a Moho that is raised by one kilometre resulting in a larger misfit between predicted and observed gravity data. The densities of the upper crust subsequently increase with offset to the ridge axis, along with the crustal age. This reflects the already in the

seismic velocities observed infilling of cracks and pores via hydrothermal deposition [*Grevemeyer and Weigel*, 1996].

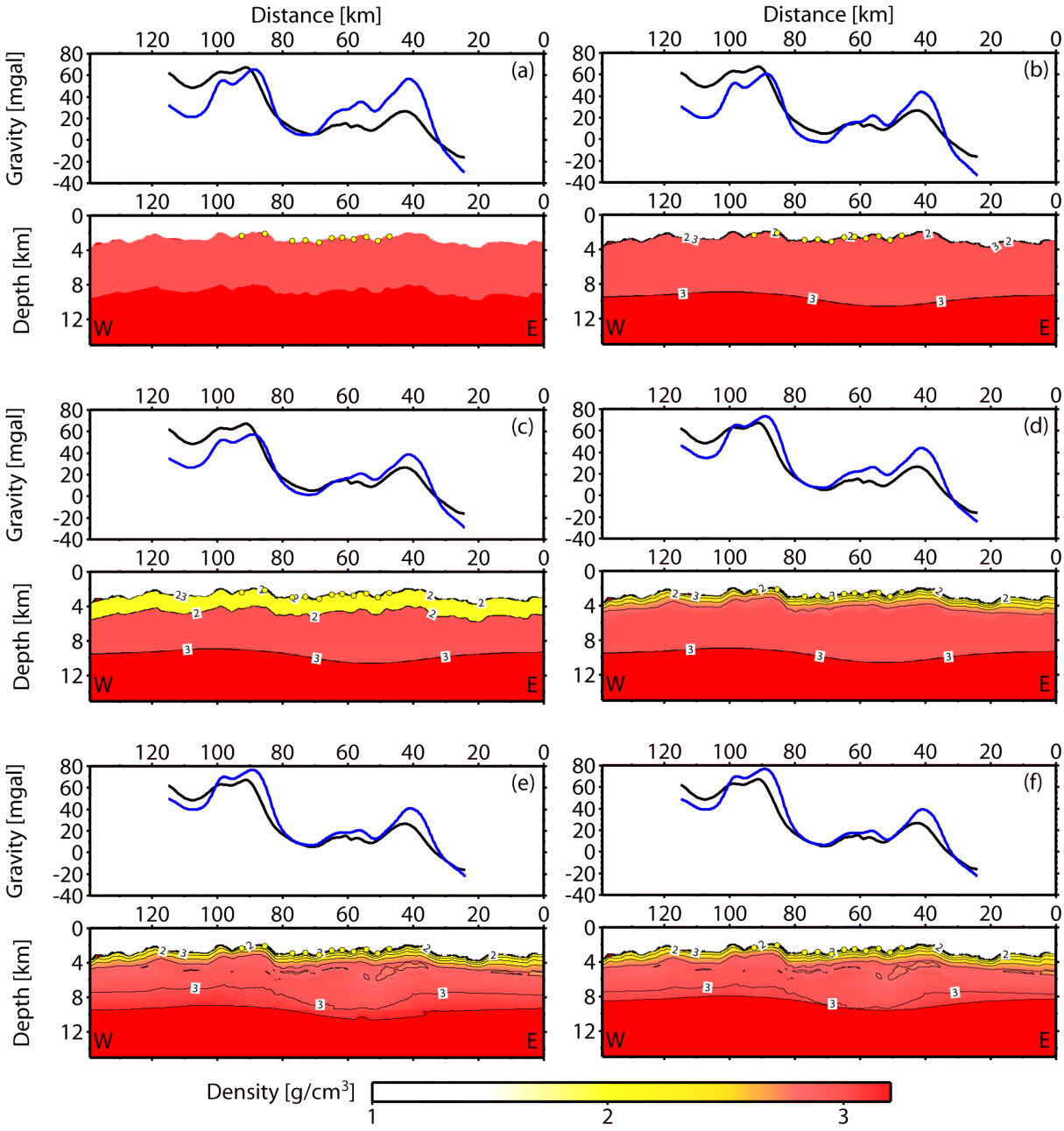

Fig 4.13 Profile 4: Observed free-air gravity anomaly is plotted with the predicted free-air gravity anomaly based on the different layer density models. The six-case-study points out the consistency of the seismic model with the free-air gravity measurements. Details on the figures a-f are explained in the text.

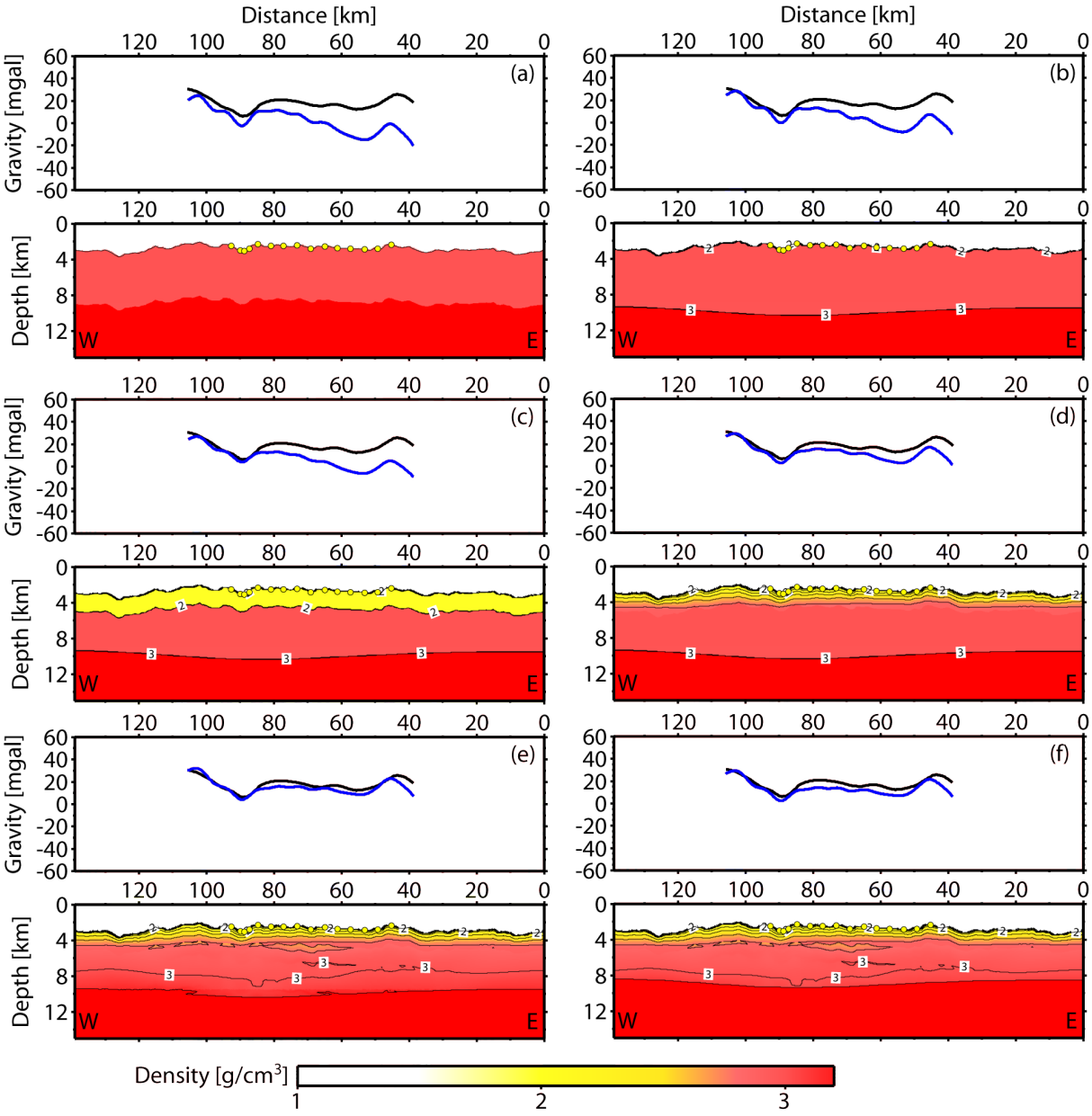

Fig 4.14 Profile 5: Observed free-air gravity anomaly is plotted with the predicted free-air gravity anomaly based on the different layer density models. The six-case-study points out the consistency of the seismic model with the free-air gravity measurements. Details on the figures a-f are explained in the text.

4.3 Profile 8

4.3.1 Tomographic model

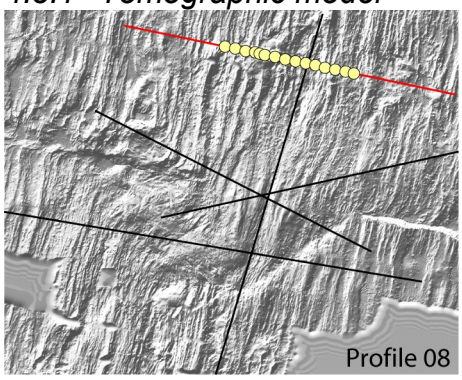

Due to the complexity of the area, different modelling techniques like seismic tomography, ray trace modelling, and gravity modelling were used to resolve the crustal and upper mantle structure. Even though Pg and Pn data are of excellent quality, the rough seafloor topography causes a weak trace-to-trace correlation for phases of the crust-mantle boundary (PmP) reflection. Thus, only portions of the profile with flat seafloor topography show good PmP data.

The recorded data at small offsets of up to 30 km have a high signal-to-noise ratio (Fig. 2.11 and Appendix D), allowing a clear identification of the first-arrival travel times from the crust (Pg). Only a few record sections show crust-mantle boundary reflections (PmP) as clear secondary arrivals in a credible manner that they can be used for the inversion modelling. The onset of mantle first arrivals (Pn) is not clearly observed at the most of the stations. However, fast apparent velocities at large offsets indicate rays turning within the uppermost mantle. Due to the fact the PmP occurs only at a few portions along the lines, it is difficult to derive a well imaged Moho along the entire profile.

The 2305 hand-picked travel times show a strong scattering in time at the equal shot-receiver distance. This strong variation in these observed travel times suggests a strong variation in the shallow seismic structure along the profile.

The described joint refraction and reflection tomographic method (Section 3.2) of *Korenaga* [2000] was used to invert P-wave travel times for the upper seismic structures of the profile.

Starting from different velocity gradients for the layers resulted in a similar final model. This shows that the final solution depends only weakly on the starting model. The resulting model supports a similar strong variation of the upper 1 to 2 kilometres of the crust.

Nevertheless, several different starting models were used to test the robustness of the inversion result. A regular grid with uniform horizontal grid cells of 200 m and a vertically increasing spacing from 50 to 170 m hangs below the seafloor that was parameterized at a spacing of 500-600 m. Downward stripping of the layers, inverting first for the upper crustal arrivals, near offset picks, and then proceeding with the larger offset picks, lead to a robust model of the refracted data for the crust as shown in Figure 4.15.

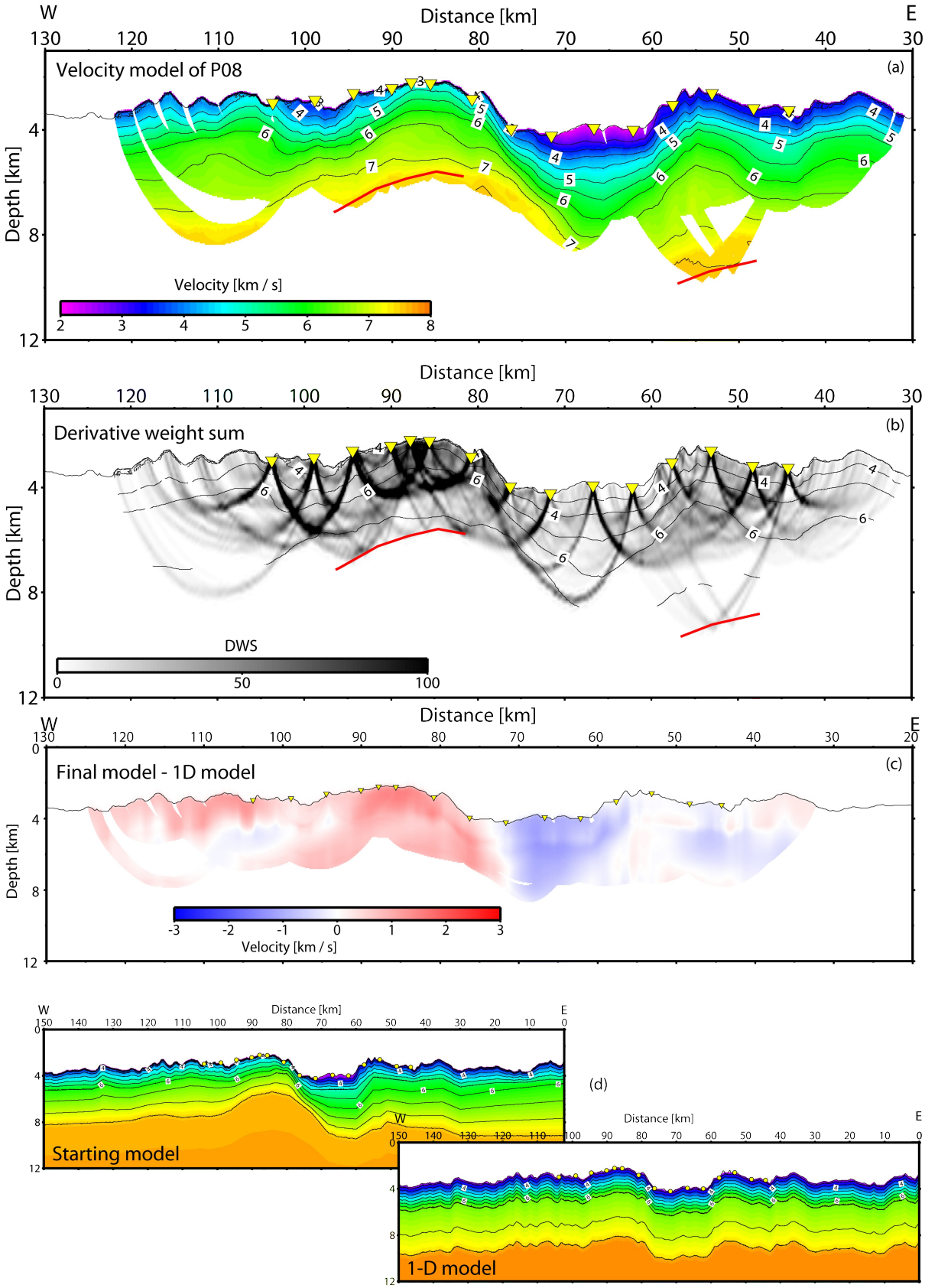

Fig 4.15 Final results of the travel time tomography for profile 8. a) Final seismic velocity model; b) DWS imaging the ray coverage along the profile; c) Final velocity model subtracted from the 1-D model in figure d; d) starting model for the inversion algorithm, and 1-D model for comparison of the result.

The expected strong variation in the crustal structure is very well displayed in the seismic velocity model (4.15a). The eastern flank of the ridge shows typical features of normal oceanic crust with a high velocity gradient in Layer 2 and a relatively constant thickness of 1.5-2.2 km. The calculated velocities rise from 3.2 km/s at the seafloor to about 6.5 km/s at 2 km below the seafloor. The lower crust has a lower gradient and velocities increase slowly to 7.0-7.2 km/s near the expected bottom of the crust. The median valley, with velocities of 2.3-2.4 km/s, exhibits the slowest velocities along the profile. Those low velocities were observed in the eastern part of the valley in the upper few hundred metres. These velocities reach 6.5 km/s at a depth of 4 km below seafloor giving a markedly lower velocity gradient compared to the eastern ridge crest. Following the seafloor of the median valley to the west, the seismic P-wave velocities rise to 3 km/s, and approaching the core complex they increase rapidly to values of about 4.4 km/s. The uppermost crust is characterised by a steep vertical velocity gradient. Lower crustal velocities of 7 km/s were imaged even at 1.5 km below the subsurface. To the west of the core complex, the crust becomes more similar to the eastern flank. The upper crust, layer 2, is characterised by a high velocity gradient, while the seismic velocities in the lower crust moderately increase to velocities of 7.1-7.2 km/s at 4 km depth.

4.3.2 Forward Model including Pn-phase and gravity data

The benefit of using a ray tracing forward method was the application of a joint modelling approach using observed travel times, including mantle arrivals (Pn), and the marine free-air anomalies. The program MacRay [*Luetgert*, 1992] has been used to generate a model satisfying both gravity and seismic data, where Pn arrivals and gravity data provide useful constraints on the crustal thickness and structure of the uppermost mantle.

Seismic velocities were converted to a density model using different empirical relationships for the upper and lower crust: $\rho=3.81-6/v_p$ [*Carlson and Herrick*, 1990] for the upper crust; $\rho=0.375+0.375*v_p$ [*Birch*, 1961] for gabbroic crust found in the lower crust. The mantle was initially assumed to have a constant density of 3.3 g/cm³. The uppermost oceanic crust, with velocities less than 4 km/s, was assumed to have higher densities than can be reached by the *Carlson and Herrick* [1990] relationship (Fig. 4.16). A value of 2.4 g/cm³ was used, using constraints from an ocean bottom gravity study at the Juan de Fuca Ridge [*Stevenson et al.*, 1994.] Figure 4.16 shows that there is not only a strong lateral variation in the density and velocity field at crustal levels, but also density variations in the mantle. Owing to 934 picks of Pn arrivals distributed along the entire profile, we could image both the geometry of the seismic Moho and the velocity structure of the mantle. The modelling strategy was to start with a flat Moho. However, profound changes had to be introduced to fit both Pn arrivals and free-air data. Away from the ridge crest, velocities of 7.8 km/s fit the Pn branches best. Below the median valley and the western ridge flank velocities decrease to 7.5 km/s.

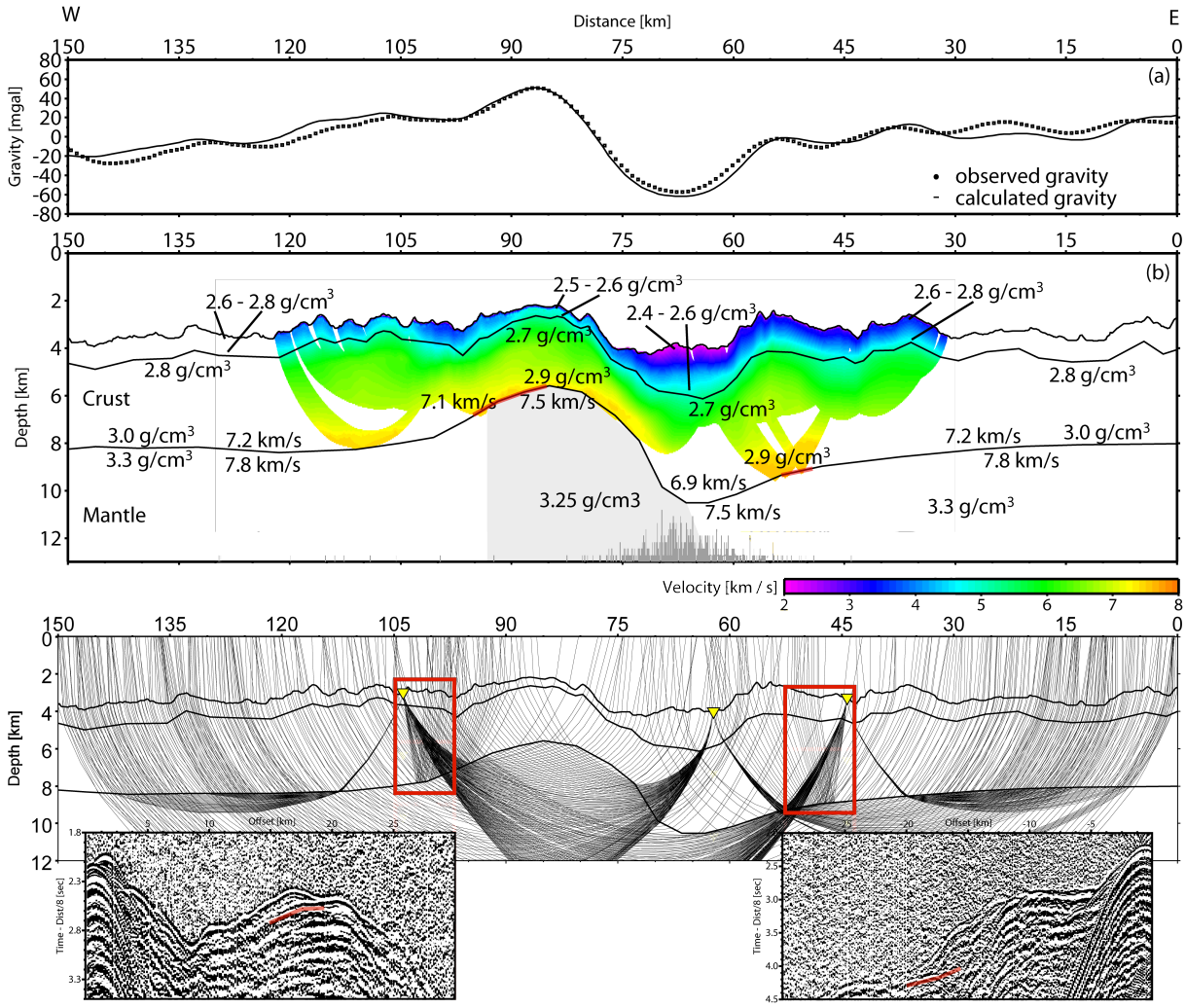

Fig 4.16 Final result of the seismic and gravity forward modelling for profile 8. Using free-air data and the Pn-phases the shape of the Moho could be modelled. Result of the inversion is included. Red parts of the Moho are areas where the Moho is additional constraint by inverted PmP arrivals. At the bottom of the diagram box the distribution of earthquakes is displayed. The lower part shows two examples of PmP phases used for modelling (OBH66 and OBH80).

Potential field methods are non-unique and the interpretation of seismic results may suffer from the trade-off between seismic velocity and the thickness of a layer. Nevertheless, a high density contrast both at the water/seabed interface and the Moho caused profound lateral variations of about 100 mGal in the observed gravity field. The topographic effect alone could not explain the observed anomaly over the massif, supporting a shallower mantle (higher density material) underlying the core complex. The final model (Fig. 4.16) shows reduced velocities and density in the mantle below the median valley and the core complex and reduced crustal thickness under the detachment fault, indicating crustal thinning caused by faulting. The rms residual for the gravity modelling is 5.22 mgal. The observed and calculated travel times are plotted and compared in Figure D-2 in the Appendix.

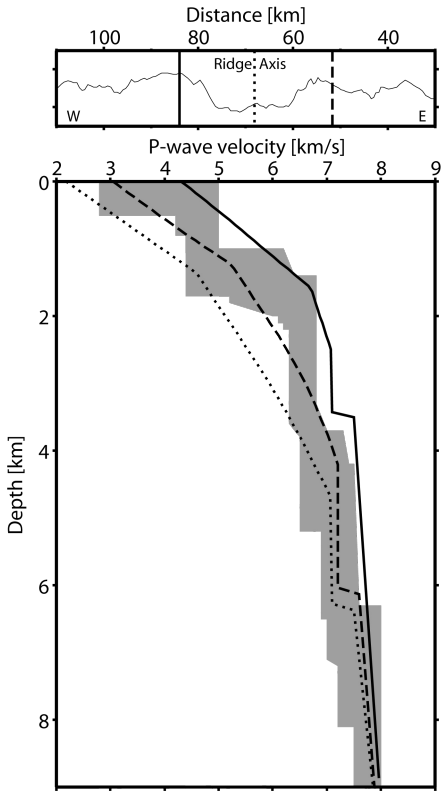

The comparison of the 1D velocity structure from other studies of the MAR and at different offsets in the study area is presented in Figure 4.17. The velocity-depth profiles clearly show the huge differences between the central valley, the eastern, and the western flank. The velocities of the upper crust and the velocity gradients change significantly.

Fig 4.17 Three velocity versus depth profiles at the western and eastern ridge flank, and from the axial valley have been plotted and compared to the v-d sections of *White et al.* [1992], represented by the grey area.

4.3.3 Observed PmP reflections

A few clear PmP branches (Fig. 4.18) were observed and were used to constrain the final model derived from ray tracing and gravity modelling. It is interesting to note that a few PmP branches sampled both the normal roughly 6 km thick crust away from the core complex and the portion of thinner crust under the core complex, supporting crustal thickness variations from the forward modelling. In addition, the occurrence of PmP arrivals suggest that a well defined Moho has been developed to both sides of the ridge axis, indicating ongoing magmatic accretion during detachment faulting and hence supporting the model of *Dick et al.* [2000], suggesting that the detachment fault is rooted in a zone of magmatic accretion at ~1.5-2 km depth.

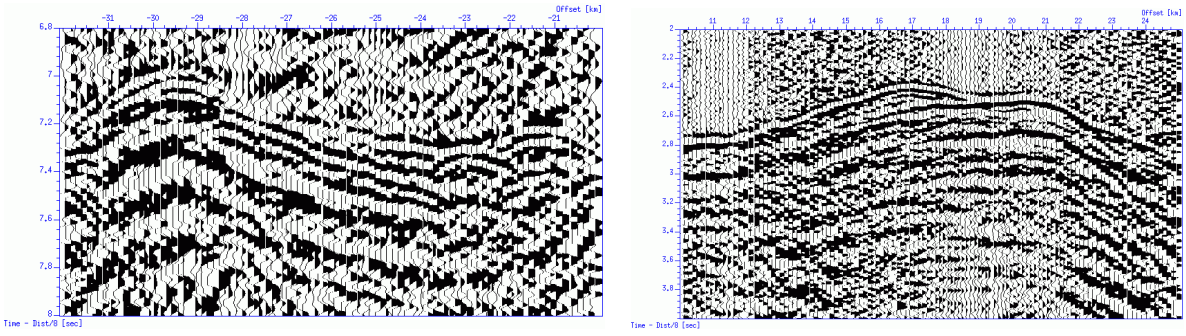

Fig 4.18 Zoom into seismic section of OBH66. To the left: image of the multiple of the western branch of the station. To the right: The PmP observed on the eastern branch of OBH74 towards the core complex.

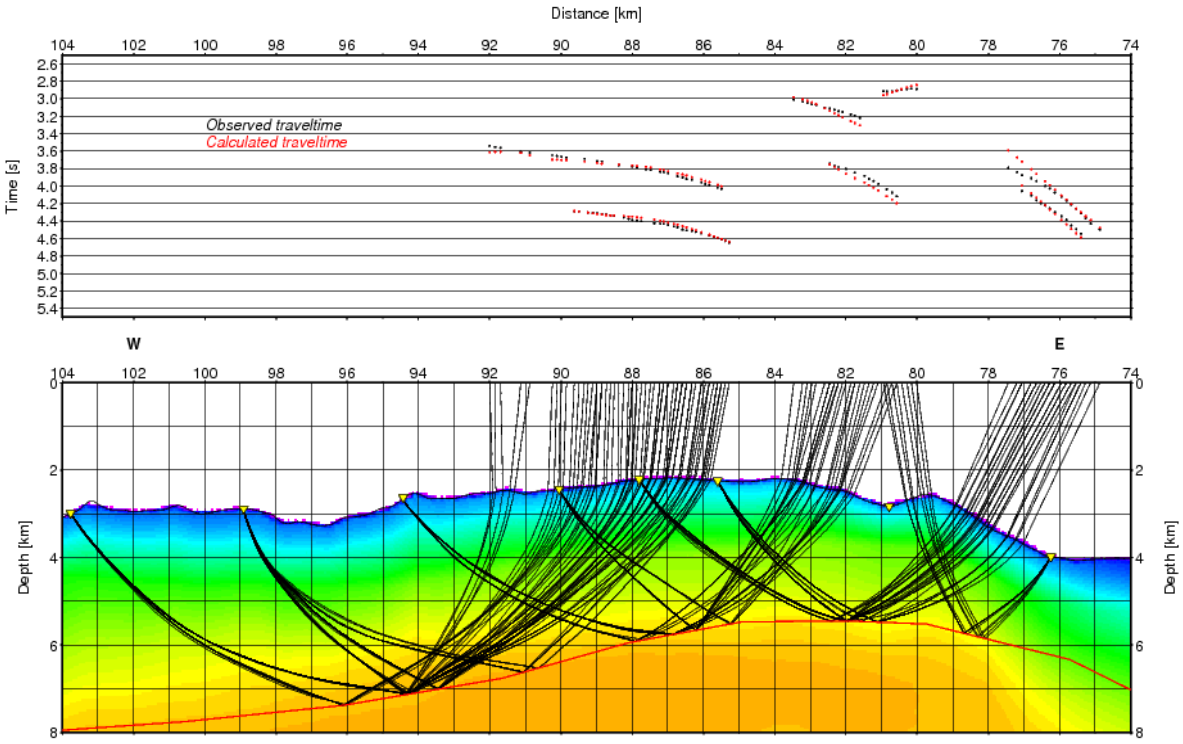

Fig 4.19 Ray path of the PmP from stations 66 to 71 and 73 through the velocity model gained from seismic tomographic modelling.

4.3.4 Intracrustal reflections

On the inner valley stations, near offset reflection phases could be observed. OBH74 is one example with the strongest reflections shown in Fig. 4.20b. The gained final velocity model was used to locate the reflector that must be a steep one since the reflection in the seismic section (Fig. 4.20b) is asymmetric. By using the raytracer of the Korenaga package, the data fit best for a shallow fault presented in Fig. 4.20a. The fault fits well with the topographic structure and cuts the upper crust into the lower crust. The total length could not be followed because the direct wave is disturbing the weaker near offset reflections. With decreasing reflection angle (beneath the station) a reduction of energy that is reflected by the fault surface is observed.

This could be the presently active fault that accommodates the plate separation during an interval of starved magmatism. The fault dips at an average angle of about 54°.

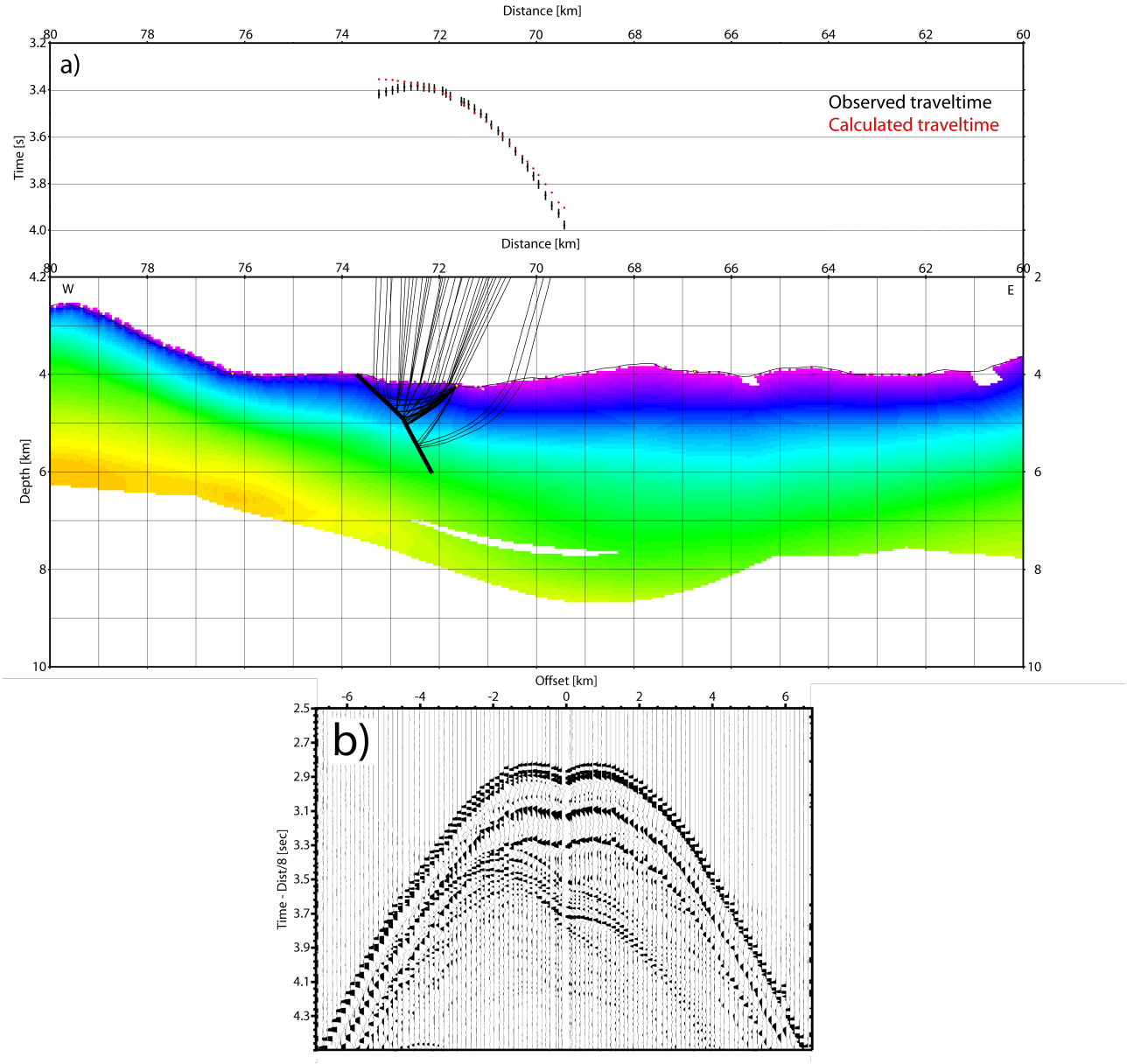

Fig 4.20 Reconstruction of a fault plane by means of a) raytracing in the upper part the observed and calculated traveltimes are displayed. b) seismic section of OBH74 with the reflection phase within the direct wave arrival.

5 Interpretation and discussion

5.1 Along-axis variation

The most profound feature in the along-axis structure of the TAMMAR segment is that the crustal thickness varies from a maximum of about 8 km at the segment centre to a minimum of ~4 km at the northern and ~5.5 km at the southern segment end. Rising steeply from about 3.0 km/s to ~6.0 km/s and further down more gently to ~7.0-7.2 km/s, the seismic velocities along all three profiles are typical for oceanic crust [*White et al.*, 1992]. The compressional wave velocity of layer 2 reflects the porosity of this basaltic layer rather than the melt supply [*Minshull et al.*, 2006]. The decrease of porosity with depth is caused by decreased pore space with depth through crack closure with increasing confining pressure.

If the variation in crustal thickness is interpreted as variations in melt supply, a focused magmatic accretion beneath the segment centre is indicated. However, due to this asymmetry in the crustal thickness, more magma is distributed from a central injection point to the southern segment end. The crust at the northern segment end seems to be even thinner than at the southern ridge tip, where the axial valley is much wider compared to the southern end axial valley (light blue lines in Fig. 5.1). Thus, the data favour that melts are preferentially transported towards the south.
The region to the south of the TAMMAR segment shows higher seismic activity. It seems to be a “cold” regime compared to the TAMMAR segment. Tectonism is dominating accretion in the northern bounding segment as well. Indeed, a reduction in seismicity is not a general feature of propagation. An example of a seismically active propagating ridge segment can be seen near 20° N at the Mid-Atlantic Ridge imaged in Figure 1.12. Thus, seismic activity is rather an indicator of the recent thermal state of a segment, i.e., whether it is in an active magmatic or in a tectonic phase of crustal accretion.
Instead of only propagating to the south, the TAMMAR segment is lengthening towards both ends. The southern tip is penetrating into old crust because the next segment has an offset discontinuity and these prominent wake shapes are created. The northern tip grows into the northern segment. However, because of this non-offset discontinuity, the impact of propagation is less pronounced in the bathymetry. By connecting the summits of a row of abyssal hills on the African plate north of the

ancient fracture zone (compare to figure 1.14) a rhomb shaped pattern is indicated and drawn in Figure 5.1. This can be done on the western plate as well, however, the summits are even less pronounced. The dark blue lines indicate the main structure and therefore the evolution of the segment, but do not have to be interpreted as real former segment boundaries. The old discontinuity should be the row of nodal basins which are less clearly visible in the bathymetry immediately north of the marked lines across the summits. The segment grew from approximately 30 km in length to what it is nowadays, 90 km.

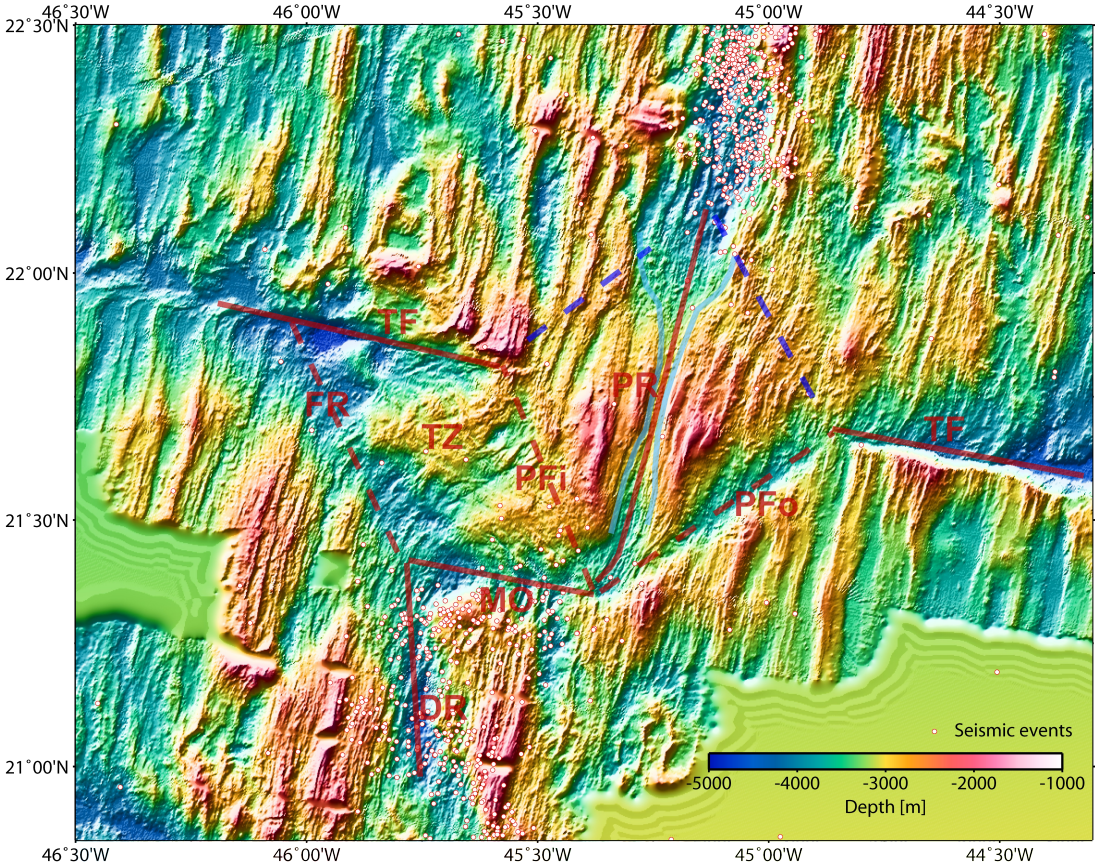

Fig 5.1 Modification of the map of section 1 (Fig. 1.7). The northern blue lines indicate that the segment is not only propagating southwards but it is growing into both directions. The major tectonic elements are indicated in the bathymetric map of the propagating ridge system. Shown are propagating ridge (PR), doomed ridge (DR), failed ridge (FR), ancient transform (TF), migrating offset (MO), sheared zone of transferred lithosphere (TL), inner pseudofault (PFi) and outer pseudofault (PFo). In light blue the axial valley is marked.

5.1.1 Shallow crust

The TAMMAR segment (about 95 km in length) is one of the longest segments along the Northern Mid-Atlantic Ridge. The average segment length along the MAR between 15° and 35° N is about 50 km [*Smith et al.*, 2003]. Figure 5.2 presents three velocity-depth profiles of the along-axis line P02. The grey curve represents the segment centre at 104 km distance along the profile. The red velocity-depth curve has been tracked near the northern segment end at 141 km. At the southern segment end, the black curve represents the velocity-depth function at 63 km. They differ profoundly between the segment centre and its ends. The velocity gradient of the upper crust is

slightly smaller at the segment ends compared to the centre where seismic velocities as high as 3.2 km/s have been found.

Converted shear waves

The along-axis profile shows prominent shear wave arrivals on several stations with stronger phases in the centre of the segment. For mid-ocean ridges, this is a very rare observation. Since the source generates the wave field in the water column, only P-waves were generated that have to be converted to S-waves while travelling through the subsurface. This conversion interface is most likely the seafloor itself because a strong contrast in velocities is needed and a sediment layer is absent. To be effectively converted from compressional to shear modus, the transmitted S-wave velocity v_s has to be larger than incoming P-wave velocity v_p from the layer above (section 2.2.4). Higher P-wave velocities have been observed in the central part of the TAMMAR segment compared to its tips. A reasonable explanation could be that the basalt in the segment centre is more homogeneous and consolidated than in the ends. Piled lava flows are predominant in the centre of the segment while pillows exist at the end [pers. communication *J. Dyment*]. Tectonic disruption of the basaltic layer may also be more pronounced at the ends than at the centre.

A v_p/v_s ratio of 1.8 has been obtained that rises slightly with depth. This is a high Poisson's ratio above 0.3 in the upper crust and is typical for young oceanic crust due to its high porosity in the form of cracks, fissures, breccias and talus [*Hyndman*, 1979].

Anisotropic effects in the shallow crust

The seismic velocities of the presented refraction profiles show different values at the intersections. For example, the crossing of P02 and P05 has a v_p of ~ 3.2 km/s ridge axis parallel while v_p of ~ 2.9 km/s has been observed for P05 at seafloor level. The propagation directions are almost perpendicular to each other. Thus, this is evidence for a significant anisotropy within the upper crust. For vertical cracks, seismic P-waves have an azimuthal velocity variation, with the fastest direction in the plane of the cracks. S-waves generally split into a fast and a slow component, with particle motion in and normal to the plane of cracks, respectively. The faster component is aligned parallel to the ridge axis. Thus, the anisotropy is a result of cracks and fractures generated during the plate separation. Anisotropy of ~10 % has been observed for the upper crust.

Refraction studies give a poor resolution of the shallow-most crust because the turning ray arrivals are masked by the direct water wave. Also, refraction data can not resolve a single, thin, fluid-filled crack; it is sensitive to an area of several fluid filled cracks. However, P-wave velocity variations have been observed in several studies in oceanic environments [*Shearer and Orcutt*, 1985; *Detrick et al.*, 1998; *Dunn and Toomey*, 2001; *Barclay and Toomey*, 2003] with the common result being that crustal anisotropy is restricted to the upper 3 km with cracks aligned perpendicular to the spreading direction. Our observations are consistent with those studies. More insights into the anisotropy in this segment can be derived from the interpretation of the small

OBH-network, P71 to P74 of the Costmar-Cruise, which goes beyond the scope of this thesis. However, the aspect of anisotropy has to be kept into mind while looking at the velocity fields gained from the tomographic traveltime inversion.

Several observations indicate that the upper 3-4 km of crust is cool and brittle [*Thibaud et al.*, 1998; *Barclay et al.*, 2001; *Dunn et al.*, 2005]. In the shallow crust, seismic anisotropy has been detected that is an indicator of widespread ridge-parallel extension cracks in the upper 2 km [*Barclay et al.*, 2001; *Barclay and Toomey*, 2003]. Already described by *Gente et al.* [1995], the axial valley floor at the segment centre is smooth and dominated by sheet flows with no sediment cover and very few tectonic features. The segment ends have undergone significant tectonic stretching and they correspond to a region of minimum melt injection. This implies a thin crust perhaps overlaying serpentinites [*Mével et al.*, 1991]. The serpentinisation would be a result of thin magmatic crust and extensive fracturing, and therefore easy penetration of seawater to mantle rocks. At the southern ridge tip, the seismic velocity gradient shows a less distinct change at the boundary of layer 2 and 3 compared to the segment centre. *Detrick et al.* [1993] detected also an anomalously linear velocity increase with depth at the segment end. They interpreted this seismic structure as intensely fractured and altered crust overlying serpentinised peridotite. This could be constrained by *Canales et al.* [2000] for a non-transform ridge offset discontinuity near 34°30’ N at MAR.

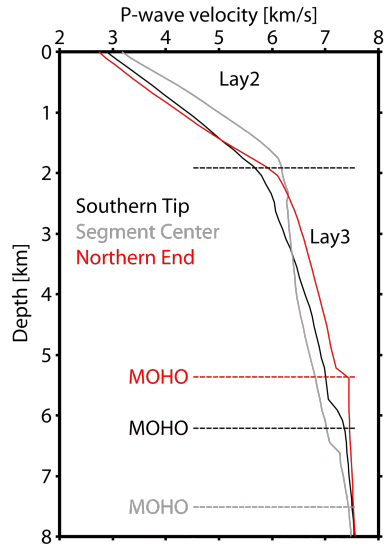

Fig 5.1 Velocity versus depth profiles representing the segment centre (grey), the northern (red) and the southern (black) segment end of the TAMMAR segment.

Axial magma chamber

Early works of *Orcutt et al.* [1976] and *Rosendahl et al.* [1976] provided first observations of a low velocity zone beneath the East Pacific Rise, enhancing the search for comparable features beneath the MAR. Seismic evidence for a shallow axial magma chamber has been found in the Lucky Strike segment [*Singh et al.*, 1998]. Anomalously low seismic velocities have been found beneath the Snake Pit neovolcanic zone in the MARK area, to the north of our study area, [*Calvert*, 1995; *Canales et al.*, 2000] with clear indications of crustal melt.

Synthetic seismograms have been generated (section 2.2.5), including a low velocity zone, and compared to the observed seismic data. No shadow zone, as expected, has been detected in the seismic section neither in the stations above the segment centre nor in the arrivals from stations at the end of the profile. Furthermore, no phase delay as detected at the Juan de Fuca Ridge [*Menke et al.*, 2002] caused by much lower seismic velocities of the magma chamber, or a phase shift in the near offset reflections caused by the top of the magma lens [*Canales et al.*, 2006], could be observed in the seismic refraction and wide-angle reflection profiles shot during the survey. Also, profiles with some offset to the ridge axis have been studied for this purpose. However, they did not provide any evidence for an axial melt zone.
Thus, the seismic lines presented here do not provide evidence for seismic low-velocity zones associated with crustal magma chambers comparable to the studies of *Sinha et al.* [1998], *Canales et al.* [2000], or *Menke et al.* [2002]. Indeed, the observation of converted shear waves contradicts the presence of a substantial magma body. Shear waves do not propagate through fluids because they shear the particles (particle movement perpendicular to the propagation direction) only P-waves do (particle movement along propagation direction). A traveltime tomography with shear waves was performed and the subsurface of the central part of the TAMMAR segment could be resolved to a depth of 4 km.
Because of limited resolution of refraction experiments, interstitial partial melt beneath the segment cannot be excluded. Some attenuation has been observed at stations on top of the axial high from shots from North and South. The only place along P02 where seismic velocities are anomalously low compared to average MAR values is towards the southern segment end. Velocities as low as 6 km/s have been found at 3 km depth. The velocity gradient reaches almost 1 s^{-1} below the upper crust which is rather high compared to average Atlantic crust. This is interpreted to result from increased porosity due to fracturing and subsequent filling by extrusive lavas. This process is comparable to other segments along the MAR [*Hooft et al.*, 2000] that might be enhanced by the southward propagation of the segment and a change in the regional stress field may be related to tectonic rotations of the crust between the propagating and the dying ridge associated with the migrated offset [*Pockalny et al.*, 1994].

There is no evidence for a shallow axial magma chamber in the style of the Lucky Strike segment [*Singh et al.*, 2006] at the current time. The top of it should be at the interface seismic layer 2/3 (diabas/gabbro), expected to be at 2 to 2.5 km depth. An AMC of a reasonable size would also influence the seismic data.
Profiles P04 and P05 may suggest that there is evidence for a magmatic robust phase in the recent past. *Gente et al.* [1996] observed young magmatic activity with an event in the median valley lasting over 100 000 - 300 000 years, supporting the high magmatic activity along the TAMMAR segment. Traveltime modelling (section 4.2) shows a lowering of the seismic velocities in the segment centre that is interpreted as a zone of focussed melt supply and lateral redistribution at crustal levels. Velocities might be lowered by higher temperatures of the subsurface which is also confirmed by

the low seismicity of the segment [*Smith et al.*, 2003]. *Sinha et al.* [1998] found that AMCs at the MAR are short-lived. Magma chambers at the MAR are transient and successful seismic imaging of them at a slow spreading ridge, like in the Lucky Strike area, is difficult. The AMC is connected to a young and active volcano and to active hydrothermal venting.
However, the tomography method tends to under-predict low-velocity zones (compare to the checkerboard test in figure 4.3). Given that the resolution of the imaging is no better than 2 km, partial melt in isolated pockets may exist.

5.1.2 Lower crust and mantle

The faster velocities in the segment centre and the enlargement of the critical distance in the seismic sections show that the crust is thickened at the segment centre (Fig. 5.3). Gravity measurements constrain that a large component of the gravity data is due to a substantial thickening of the crust at the segment centre. Constraints on a thick crust but thin lithosphere resulting in a “hot segment” environment are also supported from results of passive seismic studies and the mantle Bouger anomaly. The achieved data sets have been plotted into a diagram. Figure 5.3 shows conformity over all the received results. The seismic events from PMEL/NOAA’s experiment [*Smith et al.*, 2003], the mantle bouger anomaly (MBA) published by *Gente et al.* [1995], the topography, and the crustal thickness, derived from the seismic traveltime modelling, are plotted. A lower seismic activity in the segment centre between 21.4° N and 22° N occurs while the MBA shows a negative anomaly and the crustal thickness rises to the segment centre as well. The previous gravity measurements by *Maja and Gente* [1998] suggest that the crust at the shallow centre is ~2 km thicker than usual, which is consistent with the data acquired in this project.
The shallow water depth at the segment midpoint, crustal thickening from seismic refraction data, relatively low velocities at the Moho (crust-mantle boundary), an anomalously large mantle Bouger gravity anomaly low centred on the segment, and the seismic gap have all been attributed to enhanced and focused mantle upwelling and magmatism near the segment centre [*Detrick et al.*, 1995; *Thibaud et al.*, 1998; *Dunn et al.*, 2005]. This is comparable to results at the OH-1 ridge segment at 35° N at the MAR [*Barclay et al.*, 1998; *Hooft et al.*, 2000; *Magde et al.*, 2000; *Dunn et al.*, 2005].

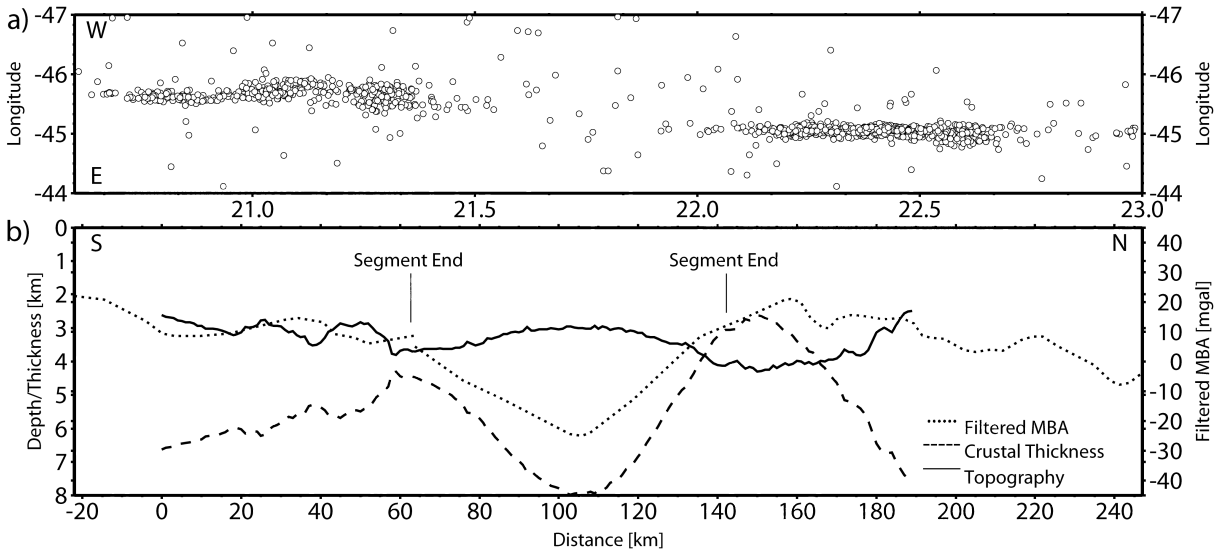

Fig 5.3 a) Seismic small scale events along the MAR. b) Filtered Mantle Bouger anomaly (dotted line), topography (solid line), and crustal thickness (dashed line) of P02.

The seismic results of this study support the idea of focused mantle upwelling and melting with vertical melt delivery to the crust [*Niu et al.*, 2001]. The viscosity of gabbros is higher compared to basalts, leading to more deposition of gabbroic crust beneath the segment centre. Because of the higher viscosity, higher forces are needed to transport the melt through dikes towards the segment ends. The less viscose basalts are distributed in a more balanced way. While more magma seems to be transported towards the southern segment end the northern segment end shows an even higher degree of crustal thinning. Because of the penetration into older lithosphere, the crust at the southern end experiences different stresses and may become weaker.

The central part of the segment shows higher velocities at the bottom of seismic layer 3. The P-wave velocity rises up to 7.4 km/s, which is too fast for gabbros but too slow for mantle rocks. These observed velocities in the Moho transition zone are consistent with partially serpentinised peridotites [*Christensen*, 1966]. However, it is unlikely that seawater penetrates in a mid-segment setting to such great depths causing serpentinisation in this area. The low seismicity [*Smith et al.*, 2003] suggests a rather ductile lower crust and implies low tectonism and therewith no deep fractures into the deeper crust or down to the mantle.

The seismic Moho represents a rapid increase from crustal velocities to upper mantle velocities in excess of 8 km/s [*Purdy and Ewing*, 1986].These high velocities above 8 km/s are characteristic for both, ultramafic cumulates and residual harzburgits, making it impossible to distinguish between them with seismic velocities only [*Karson and Elthon*, 1987]. *Karson and Elthon* [1987] described the oceanic lithosphere as a generalized columnar section depicting various geologic and geophysical features. They divide the lithosphere into two parts, the magmatic section (basaltic carapace, gabbroic, and cumulate ultramafic rocks) as a product of crystallisation of basaltic liquids and the residual mantle section (dominated by tectonised harzburgit,

interpreted as peridotite that has been depleted by the extraction of basaltic liquids now represented as crust). Thus, the seismic Moho and the petrologic Moho differ. Connecting the seismic Moho to lithology, as is often done for ophiolites [*Kelemen et al.*, 1997 – Oman ophiolit; *Karson et al.*, 1984 – Bay of Islands], it is interpreted as the boundary between the interlayered gabbroic and ultramafic rocks and the ultramafic cumulates. The petrologic Moho is the boundary between the magmatic section and the residual mantle [*Karson and Elthon*, 1987].

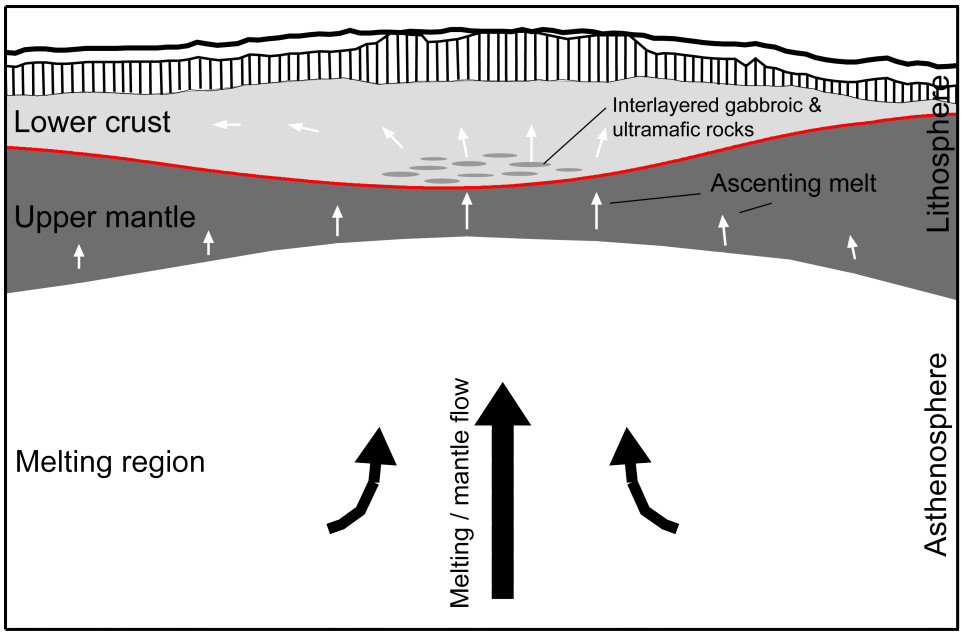

Fig 5.4 Sketch showing a geological interpretation of the results. The main features are discussed in the text.

Similar to the OH-1 segment at 35° N [*Canales et al.*, 2000], this zone of higher velocities could be interpreted as an alternating sequence of gabbro sills and dunites. The seismic Moho derived by the travel time modelling would then represent the base of this transition zone composed of gabbros alternating with dunites.

The large RMS misfit of calculated and observed free-air anomalies may support serpentinisation near the segment ends. Serpentinisation reduces the density, resulting in a negative anomaly in the free-air gravity. The joint seismic and gravity inversion results in an even shallower Moho at the segment ends than gained from the travel time inversion.

Rather than an important lithological boundary, the seismic Moho might represent the lateral variation of the igneous structure of the lithosphere, while it possibly crosses major lithologic contacts [*Karson and Elthon*, 1987]. Apparently continuous reflections might be generated by different geologic contacts at different points along the seismic line. Thus, it possibly represents the top of the ultramafic cumulates at the segment centre and the boundary between fractured and hydrothermally altered ultramafics and unaltered upper mantle near the segment ends [*Sinha and Louden*, 1983].

Figure 5.4 represents a reconstruction of the internal structure of the TAMMAR segment as interpreted from the seismic velocities. Not resolved, but from description of the seafloor [*Gente et al.*, 1995; 1996], a small layer of pillows covers the intrusive

zone. In the segment centre, the seafloor is covered by old and young lava lakes. The thickness of the magmatic section of the lithosphere might be underestimated, however, layer 3, which is interpreted as gabbroic rocks, thins towards the segment ends. In the centre, a zone of higher seismic velocities is interpreted as an interlayered zone consisting of gabbros and dunites.
PmP arrivals are not very strong along the whole profile, however, at the ends of the segment the critical distance is very short and high velocities of about 8 km/s occur at small offsets (compare to OBH01 in figure 2.9). Thus, mantle is very shallow beneath the seafloor. The northern end reveals the thinnest crust (3 - 4.5 km) observed along the seismic profile 2 and the seafloor topography is characterised by a wide basin.
The southern ridge tip shows rather thicker crust of 5 km. The axial valley is smaller compared to the northern end, thus the melt supply seems to be slightly higher. More magma is transported at crustal levels towards the south. Thicker crust in the south indicates preferred magma supply to the south – a feature perhaps related to ridge propagation.
To explain the near-bottom magnetic structure of the segment, it requires a 2.3 km thick serpentinised peridotite at the segment ends [*Honsho et al.*, 2009]. They observed a relative low at the segment centre (10 A/m), a very strong high (30 A/m) at the southern, and a weaker high (18 A/m) at the northern segment end. A possibly larger serpentinisation at the southern segment end could be confirmed by rather smooth velocity gradients below the upper crust which suggest a gradual change in velocity with depth. This could be caused by fracturing and ongoing serpentinisation to a shallow depth level in a weak lithosphere. The magnetic observations can be indirectly confirmed by the joint seismic and gravity modelling.

5.2 Off-axis structures – a temporal evolution

5.2.1 Seismic interpretation

The off-axis structures are studied and imaged by the seismic lines P04 and P05. A survey of the off-axis structures outlines the history of this part of the spreading centre. Both profiles show a minor thickening from larger offsets towards the ridge axis. An average crustal thickness of 6.5 km suggests a magmatically robust segment. Profile 5 images a subsequent increase of the upper crustal thickness, reaching the thickest point near the ridge axis. Thus, a slight increase in magmatic activity, during the past million years, is expressed in the part covered by the seismic stations. The central valley structure is not well constrained because only one station was placed on the western plate and the coverage of crossing rays in the central valley is too small (compare to figures 4.11 and 4.12).
While P05 is aligned along a magmatically robust and possibly tectonically more or less undisturbed area, P04 seems to cut sections that are lithologically different. The westernmost stations (OBH31-OBH33) have been placed on top of a topographical high that might be connected to the ancient transform at 21°40' N. The eastern end of this profile cuts the outer pseudofault caused by the propagation of the ridge segment.

The axial valley, again, is poorly covered by crossing rays. Thus, the deeper axial valley structure is not so well resolved. Therefore, the depth of the Moho has large uncertainties. However the depth of the Moho beneath the seismic array looks very similar on both conjugated ridge flanks.

P04 shows reduced mid-crustal velocities beneath the ridge crest. This may be caused by higher temperatures beneath the central valley. The zone extends to both sides of the ridge axis. As described, the eastern side of the ridge axis represents a poorly constrained structure. The shape of this reduced velocity area is not well constrained. However, reduction of the P-wave velocity has been observed in all inversion runs. The model uncertainty here is very high (compare to Fig. 4.10). Profile 5 shows very smooth velocities and a clear reduction of seismic velocities beneath the ridge axis has not been observed. This could be due to the resolution problem or it may have a physical meaning. The two different flow lines could explain the resulting structures by seismic anisotropy. P-waves are only sensitive to changes in their propagation direction. Thus, it is suggested that the velocity variations are largely due to horizontal rather than vertical velocity changes. The most likely cause of the anisotropy in this young oceanic crust is the presence of near-vertical, sub-parallel cracks or dikes in the mid-shallow crust.

This could be caused by a very active magmatic period that is also expressed in the bathymetry. The median valley in that area is not as well expressed as it is at the segment ends. At the topographical high, the valley is only 2 km wide and has a depth of 600 m, i.e. very shallow. The ridge peaks are separated by less than 10 km. They represent an old volcanic ridge that has been separated by the plate motion. *Gente et al.* [1996] suggested that half a million years ago, an active magmatic phase, lasting for about 100000 to 300000 years, was followed by a tectonic period. If this active time resulted in a stronger along-axis diking, the seismic velocities may be lowered in the shallower crust because of the possible existence of partial melt. At the seafloor it might erupt in fissure volcanism that tends to show higher seismic velocities than the porous pillow lava directly beneath the seafloor. Mid-segment higher velocities in the axial valley have been obtained along both profiles, P04 and P02. Profile P04 shows lower velocities compared to P02 (studied in section 5.1.1 about the upper crust anisotropy). Two percent of anisotropy can be generated by 50% melt fraction in dikes that make up 6% of the crust or the vice versa [*Dunn et al.*, 2005]. Assuming that the dikes remain frozen, they still lower the seismic velocity normal to their alignment. A two-stage process has been suggested by *Gente et al.* [1996]: 1) an important magmatic event generates a dome structure and 2) a tectonic event cuts across this dome and creates the half-dome structures which are later moved away to the ridge flanks.

The reduction in seismic P-wave velocity has not been observed along profile 5, which is aligned SSW-NNE. Thus, the possible dike intrusion zone does not influence the wave propagation in the along profile direction. This might suggest that the lower crust is intruded by dikes with a trend that is not perpendicular to the spreading direction but rotated by about 40-50°. In the study area, an estimate of the velocity

vector of ridge motion over the mantle in a hot spot reference frame can be found from the HS3-NUVEL-1A plate motion model [*Gripp and Gordon*, 2002]. This might result in stresses different than those that would be caused by the plate separation leading to seismic anisotropy in the crust with the faster direction aligned with the direction of the ridge motion.

The P-wave velocity of the uppermost crust increases systematically with offset to the ridge axis. This age dependent velocity rise is related to secondary alteration products filling the pore space, as found by *Grevemeyer and Weigel* [1996]. The P-wave velocity rises from 2.7 km/s to 3.2 km/s over a distance of 40 km from the ridge axis away. This results in a slight seismic velocity increase of 0.5 km/s over a period of 3.1 m.y., taking a half spreading rate of 13 mm/y into account.
However, aside from all crustal velocity variations, the magma budget seems to be very constant over the past million years since no significant crustal thickening has been observed.

5.2.2 Gravity modelling

Only a hand full of reliable models could be gained from the joint gravity inversion itself. Thus, the general use did not lead to better constraint models. Much effort has been made to run the joint inversion with different weighting factors between the gravity and seismic, the velocity depth weighting factor, and damping of the velocity field. Also, the temperature gradient has been varied. At “hot” mid-ocean ridges, the temperature gradient of the subsurface is much higher compared to the world average value of 30° C. Taking the NMARL model [*Shaw and Lin*, 1996] as a reference model, the temperature gradient ranges in the segment centre from about 180° C at the ridge axis to approx. 50° C at 20 km off-axis. It also decreases towards the segment ends. Since serpentinisation is expected towards the segment ends, the mantle density is expected to vary as well. Thus, simple modelling of both datasets independent of the profile flow line in this mid-ocean ridge environment is difficult and beyond the scope of this work. Changes to the inversion code would be necessary to allow for horizontal variation in mantle density and the treated velocity gradient. However, this is an objective that was not in demand during the generation of the inversion tomography code by *Korenaga* et al. [2000; 2001].
This study also demonstrates that there is no hidden model space that might have been missed in the previous modelling procedure. If there where such a model space no change in travel time fits should be observed while the gravity fits are improved.

5.3 Origin of oceanic detachments

This is the first time both ridge flanks have been imaged with a single profile, covering hanging wall and footwall of a core complex. We obtained a strong variation in seismic velocities within the upper 2 km across the ridge axis. Velocities near the seabed vary by more than ±1.1 km/s. A profound feature is a very rapid increase in P-wave velocity

where the median valley approaches the western ridge flank. Velocities increase from about 2.3 km/s to 4.5 km/s over a distance of 5-7 km and are fastest below the dome-shaped core complex. Towards the east, however, seismic velocities increase more gradually (Figure 4.15).
Seismic velocities may increase as the crust ages. This phenomenon is related to hydrothermal precipitation of secondary alteration products into open pore spaces and cracks, decreasing the porosity and hence increasing seismic velocities [e.g., *Grevemeyer and Weigel*, 1996; *Carlson*, 1998; *Grevemeyer et al.*, 1999]. The impact of hydrothermal activity on the seismic structure causes a gradual change in seismic velocities [*Grevemeyer et al.*, 1999; *Nedimovic et al.*, 2008]. A rapid change, however, may support a change in lithology. Sampling supports this interpretation. Dredges from the median valley floor and the eastern ridge shoulder recovered basaltic seafloor, while sampling provided a wide range of rock types, including serpentinites and gabbroic rocks from the core complex (Fig. 4.17). Thus, the structure of the core complex seems to be laterally heterogeneous, as has been evidenced at other core complexes [*Karson et al.*, 2006; *Canales et al.*, 2008; *Dick et al.*, 2008].

The interpretation of seismic refraction data yielding lithology from seismic velocities is difficult, as seismic P-wave velocity decreases with increasing degree of serpentinisation. Velocities higher than 8 km/s characterise un-altered peridiotites, while 100% transformation of peridotite to serpentinite cause velocities to decrease to 4.5 km/s [*Carlson and Miller*, 2003]. Thus, serpentinisation may turn velocities of mantle peridiotites into velocities typical for lower crustal or upper crustal rocks. Fracturing may even further decrease seismic velocities. Gabbroic rocks have velocities of 6.7 to 7.1 km/s, depending on the relative abundance of plagioclase, pyroxenes and olivine and of their alteration products. Fracturing, however, may also decrease values significantly. Thus, based on seismic velocity data alone it is difficult to discriminate between different rock types. Nevertheless, *Canales et al.* [2008] found a correlation between seismic velocities and lithology. They found that areas where serpentinites have been dredged were characterised by P-wave velocities below 3.5 km/s, while velocities above 4 km/s generally occur where gabbros have been found. Our data at the 22°19'N core complex support fast velocities close to the seabed (3-4 km/s), reaching ~7 km/s at 1.5 km below the seafloor. In context of the *Canales et al.* [2008] interpretation, our seismic data suggest that lower crustal rocks have been brought to shallow depth; thus, the core complex is suggested to be dominantly composed of gabbroic rocks.

5.3.1 Models of core complex formation

For a long time it has been known that the most likely place to dredge lower crustal and upper mantle rocks is at topographic highs near ridge-transform intersections and along fractures zones [*Blackman et al.*, 1998]. Given the classic structure of oceanic crust, as described in section 1.1.4, the exposure of deep-seated rocks would require 4 to 6 km of unroofing. Near transform faults the crust is thinner [*Detrick et al.*, 1993; *Tolstoy et al.*, 1993], thus, 3-4 km would be enough.

Recent studies show that those places are not only limited to topographical highs at segment ends with large-offset discontinuities [*Canales et al.*, 2008]. Therefore, a more general mechanism is needed to expose those deep seated rocks.
A big variety of models exist that try to explain this:
- An early model suggests that the oceanic crust at slow spreading centres is very homogeneous and shows plutonic material even at shallow levels [*Hess*, 1962; *Dick et al.*, 1991; *Cannat et al.*, 1995], thus, relatively little extension would be needed to expose plutonic material.
- Another early model suggests that plutonic material rises upwards by the lower-density serpentine diapirs that have been created by incoming water through major faults that penetrate into the mantle [*Cann and Funnell*, 1967; *Bonatti*, 1976]. These diapirs may than fail by landsliding of the weak serpentinite.
- A more recently discussed model explains the exposure as a result of extension of normal oceanic crust on faults that throw down from the inside corners toward the outside corners near the ends of spreading ridge segments. Two end-members of this model are described as follows: 1) Extension is on a planar, low-angle fault that extends beneath the seafloor of the median valley and separates entirely the lower crust from the upper crust during amagmatic periods [*Dick et al.*, 1981; *Karson*, 1990]. Lower crust is transported to the inside corners, while upper crust is transported to the outside corners. 2) The other variant, based on *Buck* [1988] and *Wernicke and Axen* [1988], envisages steep normal faults, bottoming in the brittle-ductile boundary at the spreading axis and rotating to lower angles as they are spread away [*Tucholke and Lin*, 1994]. It can carry rider blocks of upper crust.

5.3.2 Data from drilling and dredging

Aside from the topography and the gravitational anomaly a third reason to shoot this seismic line was the fact that peridotites have been found at the topographical high during the TAMMAR Dive-21 (section 1.5.2) on the southeastern scarp of the massif. In addition, the results of a study from *Cannat* [1995] can be used in this work to become another view on the origin of these structures and combine both, seismic methods and petrology.
Figure 5.5 shows all rock samples of that area, the flow line of dive21, and our seismic refraction line. Basalts only have been found in the axial valley and east of that. The core complex itself provides everything from upper and lower crust to serpentinised mantle. In the central dome mainly basalts have been found, while the southern footwall shows serpentinised peridotite.
Drilling efforts at a number of oceanic core complexes generally drilled gabbroic rocks [*Dick et al.*, 2000; *Blackman et al.*, 2006; *Ildefonse et al.*, 2007]. For example, hole U1309D penetrated roughly to a depth of 1.4 km and sampled dominantly gabbroic rocks of a highly primitive nature at the Central Dome of the Atlantis Massif to the north of the Atlantis transform fault boundary of the Mid-Atlantic Ridge. Dredges from a rifted inside corner high at the MAR near 5° S found that serpentinites have been smeared as fault gauges along the corrugated slip surface, while the core complex internally was largely plutonic [*Reston et al.*, 2002]. Drilling into the Atlantis Bank at the

Southwest Indian Ridge also provided mainly gabbroic rocks from the core complex [*Dick et al.*, 2000]. *Dick et al.* [2000] proposed a detachment fault rooting at or near a melt-rich zone near the ridge axis, where a continuous magmatic crust may have formed during detachment faulting, which exposes mainly gabbros. In such a scenario, a Moho boundary is formed and therefore constrains our interpretation that lower crustal material forms the oceanic core complex, while upper mantle has not been exposed. In other scenarios of core complex formation, where extension occurs during amagmatic extension [*Tucholoke et al.*, 1998] or where the detachment fault is rooted in the shallow lithosphere [*Escartin et al.*, 2003], we would not expect the formation of a pronounced density or velocity contrast at Moho depth. Thus, hydrothermal circulation in exposed and fractured mantle may cause an alteration front [*Escartin et al.*, 2003; *Python et al.*, 2007]. However, alteration would cause a gradual change in velocity and density instead of a sharp contrast, as derived from the joint forward modelling of mantle refractions and gravity field data. Furthermore, the occurrence of PmP reflections supports a significant velocity contrast at depth and hence magmatic formation of the crust.

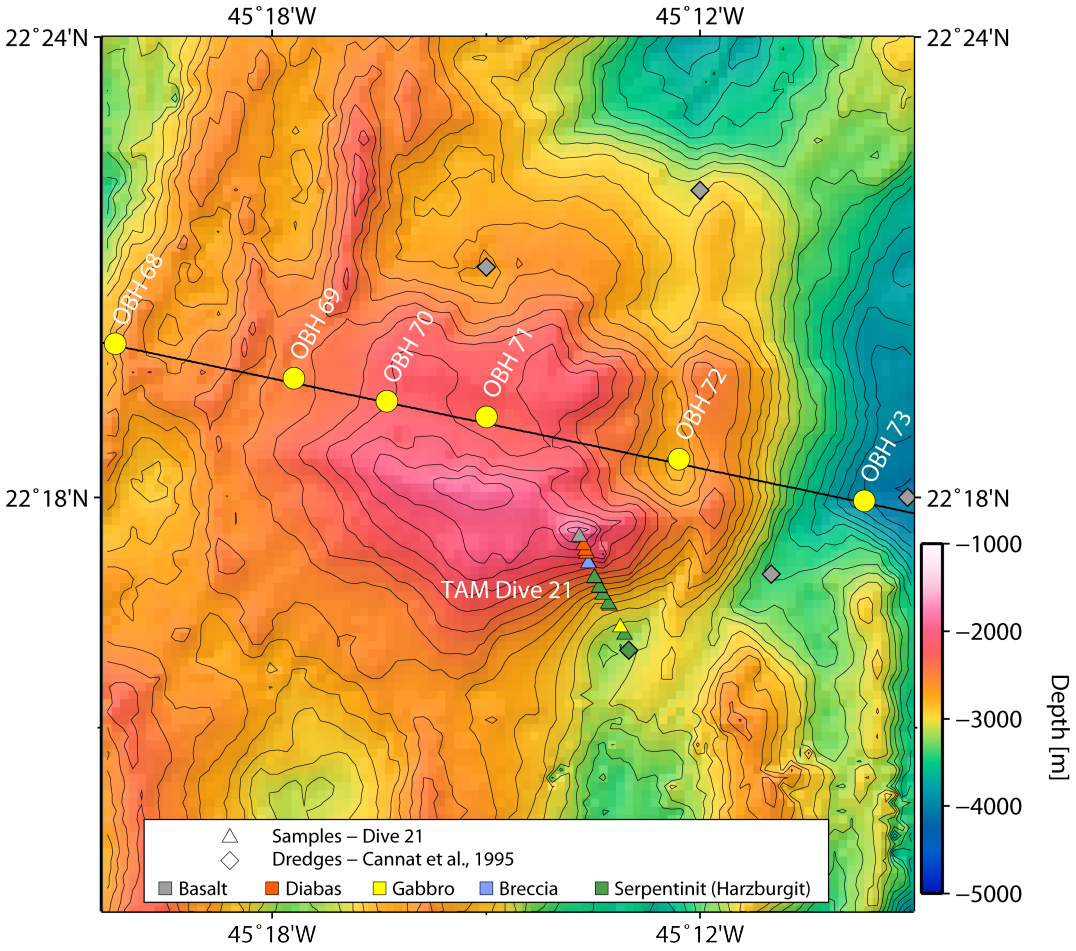

Fig 5.5 Bathymetric map of the massif showing the location of the TAMMAR Dive-21 and the seismic line P08.

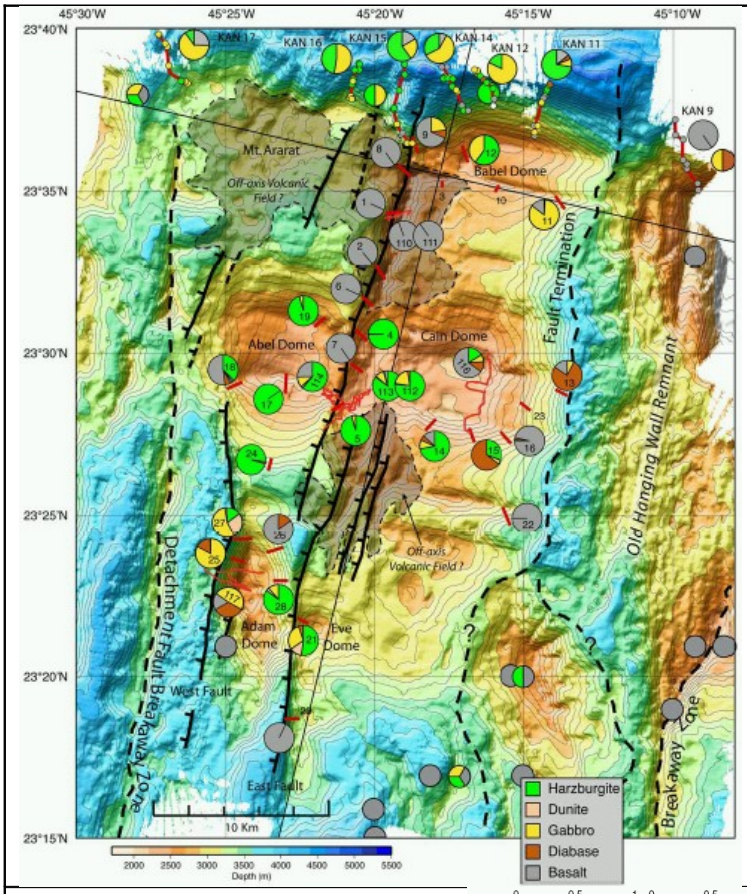

Fig 5.6 Figure from *Dick et al.* [2008] to show another core complex that has been studied. Basalts have been found on top of the dome while ultramafic rocks could be detected at the steep flanks facing the discontinuity (Kane fracture zone).

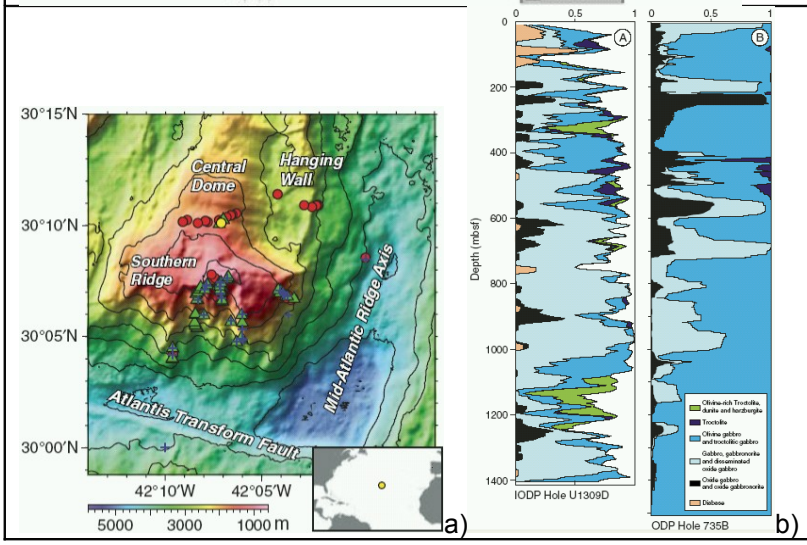

Fig 5.7 a) Bathymetric map from the Atlantis massive. The figure is taken from *Ildefonse et al.* [2007]. b) Drilling results of IODP hole U1309D and ODP Hole 735. Mainly gabbroic rocks have been found.

Most geophysical observations including seismic lines and drilling are conducted along spreading parallel lines over the central part of the OCC's in a less complicated structure, while dredging and submersible dives studies the steep flanks of those massifs probably due to less sedimentation and simpler sampling. Thus both observation areas reflect different lithology. Rock sampling along the steep walls of OCC's show serpentinised peridotite mostly in the foot of the walls at segment ends (compare to figure 5.6 [*Dick et al.*, 2008]). Basalts and gabbros have been drilled and dredged along the surfaces of those massifs and in the upper part of steep walls. The study of the Atlantis Massif (Figure 5.7a) shows dredging of the southern flank

provides a high amount of serpentinites while the drilling site IODP Hole U1309D (Figure 5.7b) situated in the central dome explored gabbroic rocks [*Ildefonse et al.*, 2007]. Same results have been obtained in a study by *Dick et al.* [2000] where the ODP Hole 735B at the West Indian Ridge went though gabbroic structures only Fig.5.7b).

5.3.3 Interpretation for the OCC-study

To the east normal oceanic crust can be found. The axial valley is shaped by basalts and pillows. At the western flank the valley seafloor is intersected by a large fault (Fig. 1.13) followed by further faults towards the central valley, the plate tectonic strain is accommodated by faulting. Instead of a horizontal crustal transfer from the western side to the eastern side of the axial valley the plate boundary is assumed to be the detachment fault or in detail the active normal fault. With the North American Plate limited beneath the detachment fault and the African plate as the hanging wall. This normal fault is active as long as the rotation exceeds a certain angle. Than the Mohr circle comes to intersect the line representing shear stress required to cut a new fracture [*Buck*, 1988], described in section 1.2.9. This results in generating a new normal fault. The ‘old’ fault segment is transported as a rafted block on the detachment fault. Those ancient faults are still visible in the bathymetry. The bathymetric data (Fig. 1.13) display also that the faults in the south of the core complex and in the north curve into the OCC. The axial volcanic chain is disrupted. This suggests that the plate boundary has been moved to the west in that part of the Mid-Atlantic ridge.

High seismicity [*Smith et al.*, 2003] and low magmatic activity [*Gente et al.*, 1995] imply a rather short and 'cold' segment. However, the along axis thermal structure also in short segments expect a permanent hot zone in the segment centre and a temperature reduction towards the segment ends [*Gac et al.*, 2006]. Based on our petrologic data the detachment fault is possibly rooted in an active intrusive zone, a former magma body, which also accommodates shearing at high temperature. Similar observations were made at the Atlantis Massif [*Grimes et al.*, 2008] and at the Atlantis Bank [*Baines et al.*, 2008].

In the centre of the segment gabbroic crust is accreted and transported off axis. While at the segment ends less crust is produced the crust thins significantly [*Cannat et al.*, 1995]. During the rotation through detachment faulting upper and lower crust is transported along and with the detachment fault. Because of the amount of new accreted crust no mantle will outcrop while at the sides of the massif, because the thin crust mantle will be unroofed, resulting in the observed 'cold' contact separating serpentinites from diabas dikes and basalts (section 1.5.3). The unroofing of mantle in the steep walls is possibly also backed by the geometry of the rotation in this upside-down half-graben like structure.

Figure 5.8 presents a visualisation of a faulted bathymetry model calculated by *H. Schouten (Woods Hole Oceanographic Institute)* that lies along the seismic line above the core complex. The bathymetry is shown with a bold line. They modelled the bathymetry as caused by normal faulting at the edge of the rift valley floor, assuming a

flexural fault rotation with increasing extension on the fault using an effective elastic thickness of Te=0.5 km. Variable fault extension results in variable throw of the fault and rotation of the top of the fault [*Schouten, pers. communtication*]. They used these properties to generate a quick model for visualisation of the relationship between faulting and bathymetry. However, it shows that they had to add some longer wavelength components that cannot be simulated with flexure. This means the total elevation of the massif cannot be explained just by flexure.
One scenario to explain the total elevation of the core complexes could be the flow of sea water into cracks that are created while the plates move apart at the spreading centre. If the cracks extends deep enough the water come into contact with mantle rocks and the minerals, mainly olivine, will interact with the seawater and form serpentine that is less dense than unaltered mantle. Respectively the surrounding rock has a higher density thus the altered portion wants to rise toward the seafloor. This may forces the elevation of oceanic core complexes.

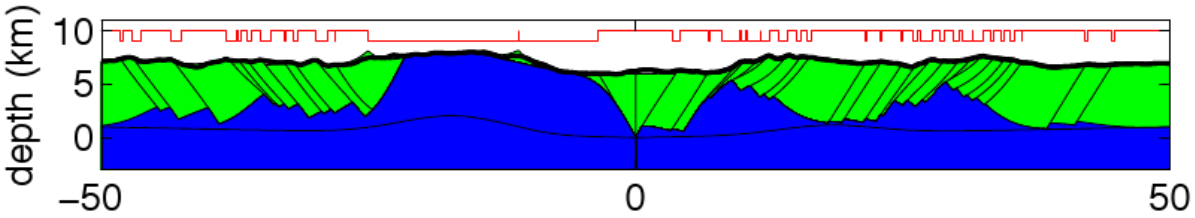

Fig 5.8 Visualisation of the bathymetry as caused by normal faulting modelled by *H. Schouten*. Blue and green do not have any physical meaning other than the base of the green represents the original level at 6 km depth. The red square wave above the model shows the extension on each fault. The rider block than is only a spike. They had to add some longer wavelength component that cannot be simulated with flexure to the model, compare to the solid black line through (0,0).

5.3.4 Constraints from the PmP-phase

The seismic P-wave velocities along the OCC's surface are too slow for serpentinised peridotite of the mantle. The identified PmP-arrivals (figure 4.19) in the seismic data at a few stations support the theory that no mantle has been exposed in the central part of the domed structure but the crust-mantle boundary is elevated and lies shallow beneath the seafloor. The presence of the PmP-phase more or less recommends a rather sharp transition from crust to mantle. Since an alteration front would tend to result in a slight change in seismic velocities no seismic reflections would be expected because of the missing contrast in acoustic impedance.
However, the lack of very strong crust-mantle boundary reflections can be explained by scattering caused by the rough seafloor but also a possibly less sharp transition from mantle to crust caused by serpentinisation of the mantle.
PmP reflections and the density contrast support crustal thinning of ~40% under the core complex, suggesting that accretion of American plate is dominated by faulting rather than magmatic construction. In contrast, crust under the eastern ridge flank and further west of the OCC is roughly 6 km thick and seafloor topography shows generally ridge parallel abyssal hill fabric. It is therefore reasonable to classify these areas as normal oceanic crust accreted by magmatic processes.

Reduced seismic velocities in the uppermost mantle might be caused to some extent by high mantle temperatures and the existence of a few percent of melt. *Grevemeyer et al.* [1998], for example, detected at the East Pacific Rise that mantle velocities increase from <7.5 km/s near the ridge crest to >8 km/s in rough 10 m.y. old crust. At slow spreading ridges, faults penetrating down to mantle depth [*Huang and Solomon*, 1988] may provide paths for seawater to reach the upper mantle. Evidence for the penetration of very high temperature hydrothermal fluids down to mantle depths has also been found in ophiolites [*Leblanc et al*., 1991; *Benoit et al*., 1999; *Python et al*., 2007]. Hydration and hence serpentinisation may therefore affect seismic velocities. However, as mantle velocities seem to increase from ~7.5 km/s at the ridge crest to 7.8 km/s roughly 60 km off-axis, we favour the interpretation that changes in the thermal regime dominate this evolutionary process.

5.3.5 Evolution of the core complex

The critical question is whether the proposed detachment fault causing the core complex is still active or inactive. Unfortunately, no fault plane solutions are available for this area. In general, however, existing fault plain solutions support that faulting occurs at normal faults dipping at 40-60° [*Huang and Solomon*, 1987; 1988]. The overall distribution of earthquakes may provide an initial assessment of the tectonic processes acting at core complexes. Hydroacoustic monitoring of the Mid-Atlantic Ridge between 35°N and 15°N [*Smith et al.*, 2003] indicated that near 22°15'N seismicity is generally concentrated below the axial valley (Fig. 4.16), while the core complex itself is almost aseismic. A similar feature has been observed in the TAG area at 26°10'N using a local network of ocean bottom seismic stations. In addition to the distribution of seismicity within the area the deployment provided earthquake hypocentres, indicating an active steep fault (~70°) that is rooted in the median valley [*deMartin et al.*, 2007]. In addition, seismic velocities derived from crustal phases provided a velocity structure similar to our tomographic inversion, suggesting that lower crustal rocks are being exhumed in a detachment fault, which appears to roll over to a shallow dip of 20° and become aseismic at a depth of ~3 km.

In contrast to the TAG detachment fault, bathymetric data from the 22°19'N core complex suggest that the inactive detachment fault is covered by rafted blocks (Figure 1.13). The occurrence of rafted blocks is supported by the diabase dykes and basalts sampled during dive21 of *Nautile* (section 1.5.3) and basalts dredged from the central part of the massif [*Cannat et al*., 1995] (Fig. 5.5). Along with our final seismic velocity and density model the observed features could generally be explained by the 'rolling-hinge' model proposed by *Buck* [1988]. Rock mechanics experiments and numerical simulations show that when a fault is rotated away from the optimum angle for shear, frictional sliding along a fault may become more difficult than creating a new fault through un-fractured rock [e.g., *Nur et al*., 1986; *Buck*, 1988]. In this scenario, a normal fault, when significantly rotated from the optimum angle of slip, relative to the crustal stress field, is replaced by a new planar fault orientated in the optimum direction. Thus, the low angle detachment fault is inactive and is covered with rafted

blocks. The high westward dip of the dykes observed with *Nautile* indicates a rotation of about 20° if we suppose that they originally emplaced in a vertical crack. The geometry of the detachment fault and uplift of the dome-shaped core complex is further affected by the low flexural rigidity of zero-aged crust.

Core complex formation at the Atlantis Bank at the Southwest Indian Ridge caused a strong asymmetry in both lithospheric structure and spreading rate. *Baines et al.* [2008] reported that 80% of plate motion was accommodated by the detachment fault, causing a northward migration of the ridge crest with respect to adjacent segments spreading symmetrically. Therefore, *Baines et al.* [2008] hypothesised that asymmetric spreading rates may be a characteristic feature of other detachment faults. Unfortunately, magnetic data from the 22°19'N core complex are not as detailed as from the Atlantis Bank. However, the existing data from *Gente et al.* [1995] suggest that lithospheric accretion at the MAR near 22°19'N occurs symmetrically with respect to the amount of lithosphere added to the African and North American plates.

Based on the seismic velocity model, bathymetry and seafloor ages from magnetic data [*Gente et al.*, 1995], an evolutionary model has been derived for the core complex formation at 22°19'N (Fig. 5.9). Roughly 1.9 m.y. ago symmetric spreading stopped and core complex formation initiated, perhaps related to a decrease in the magma production rate. In our scenario, the active fault dips at ~60° and is located in the median valley. When rotated away from its optimum dip, slip stops and a new fault is created. Ongoing activity causes crustal thinning of 40% and exposed ~20 km of gabbroic lower crust. Crustal thinning, flexural fault rotation and perhaps serpentinisation cause an uplift of the core complex, resulting into the prominent dome-shaped massif of the 22°19'N core complex. The detachment fault, however, remains inactive [*Buck*, 1988].

The observation that serpentinised mantle tends to dominate the lithology of OCC walls facing segment ends or ridge crest discontinuities may suggest that along axis variations in melt supply govern the observed pattern. High seismicity [*Smith et al.*, 2006; *Escartin et al.*, 2008] and reduced magmatic activity [*Escartin et al.*, 2008] imply that OCCs occur at rather cold settings. However, the along axis thermal structure indicates zones of upwelling at the segment centre and a temperature reduction towards the segment ends [*Gac et al.*, 2003; 2006]. Based on the petrologic data, the detachment fault possibly rooted in an active intrusive zone, a former magma body that also accommodated shearing at high temperature. Similar observations were made at the Atlantis Massif, Mid-Atlantic Ridge [*Grimes et al.*, 2008] and at the Atlantis Bank at the Southwest Indian Ridge [*Dick et al.*, 2000]. Near the hotter centre away from major ridge crest discontinuities the fault zone is rooted at mid-crustal levels in gabbroic crust, while at the cooler segment ends the lower thermal gradient promotes that the fault is rooted at lower crustal levels near the crust/mantle boundary zone. Thus, during phases of extension and subsequent flexural fault rotation lower crust is

transported along with the detachment fault where magmatic accretion keeps pace with extension and mantle is un-roofed where melt supply is too low. A post-deformation of the serpentinites samples of dive21 in low temperature conditions could not be found. Thus, serpentinite smeared as fault gauges along the corrugated slip surface, comparable to the ICH-study near 5° S [*Reston et al.*, 2002], is not preferred in this interpretation. However, a three-dimensional structure of the core complex is expected concerning all obtained results. Figure 5.10 may represents a possible model of a three-dimensional structure of an OCC.

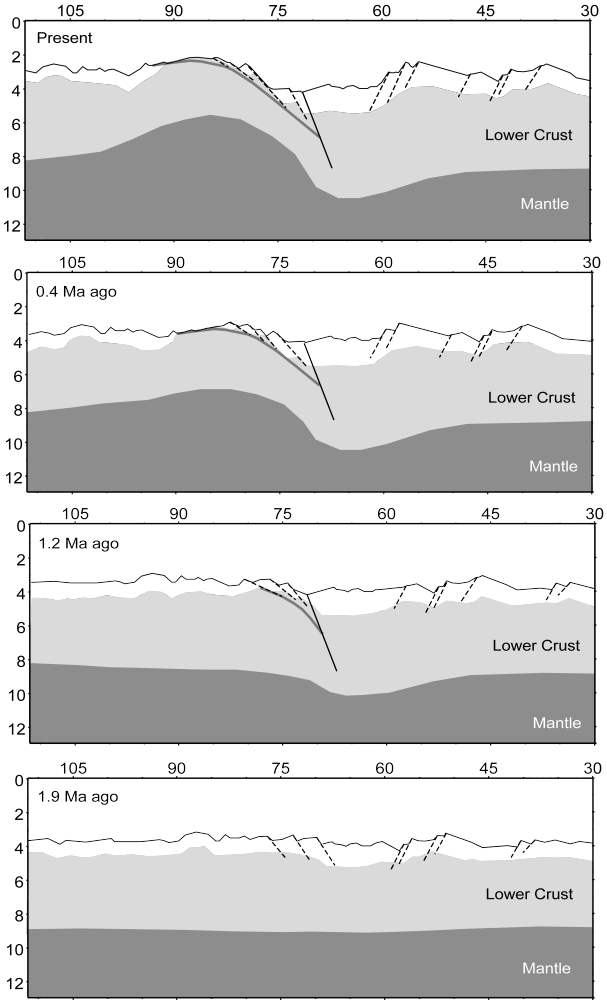

Fig 5.9 Evolutionary model of the central part of the core complex. The present state shows the geological interpretation of the seismic modelling. The sketches b-d display a possible scenario of the core complex evolution. The crust thins anomalously after initiation of the detachment fault. The mantle wells up while the detachment fault grows. To the east normal faulting occurs. The plate boundary moves from the centre westwards to the active fault of the core complex.

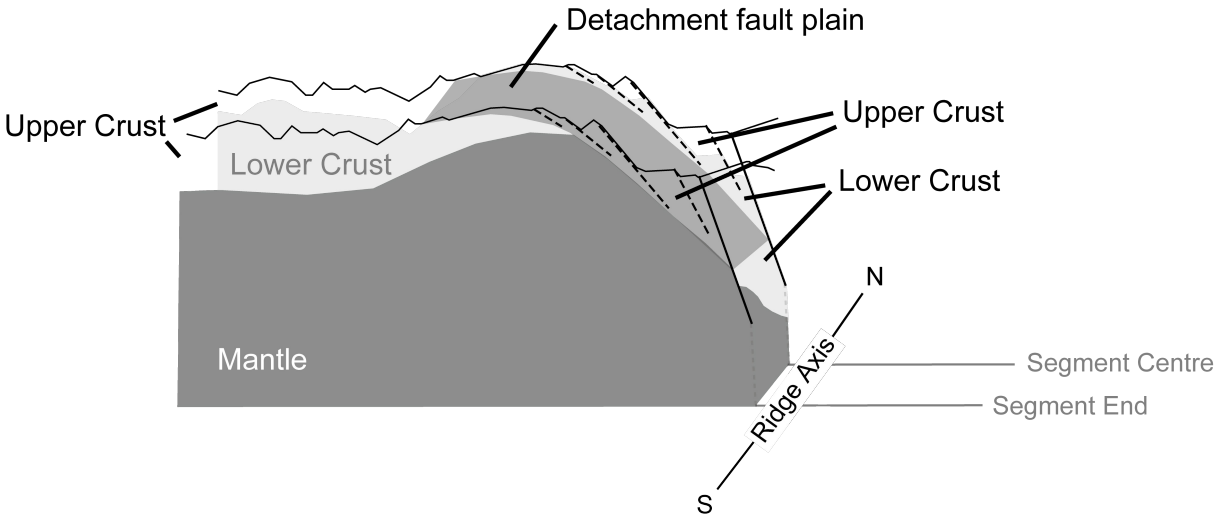

Fig 5.10 Sketch of the three-dimensionality of an OCC. Two slices have been cut through the massif. In front the segment end setting is displayed while in the back the mid-segment structures are shown. On the right in the axial valley the gabbroic layer thins extremely towards the front. The detachment fault (the medium dark grey surface) roots at different levels of the layer3.

6 Conclusions

Both segments together, the northern with the core complex and the TAMMAR segment, may represent two stages of a cycle of growing and dooming segments. While the magmatically robust southern segment reaches its maximum length the northern tectonic one may begin a more magmatically active period to grow at the expense of the TAMMAR segment.

6.1 Conclusions for the propagating ridge segment

Along the ridge axis of the TAMMAR segment, a change in crustal thickness of up to 4 km has been observed. At the northern segment end, the crust is only approx. 4 km thick, while the segment centre has a crustal thickness of up to 8 km. The southern ridge tip has a 5.5 km thick crust and is 1.5 km thicker than the northern segment end. This emphasizes the role of mantle upwelling with focused melt supply in the segment centre and prefers a transport of melts at crustal levels towards the south. The major part of the melts, however, remains at the segment centre. Basalts feeding the upper crust are distributed uniformly.

In the segment centre the lower crust is characterised by a low seismic velocity gradient and reaches seismic velocities faster than 7.2 km/s on top of the Moho. This high velocity zone is interpreted as an interlayered zone of gabbros and dunites.

The results of the joint seismic and gravimetric modelling suggest an overestimation of the crustal thickness near the segment end. The segment ends are dominated by tectonic expansion providing sea water pathways down to relatively shallow mantle rocks. The caused serpentinisation of peridotite is expressed in negative free-air anomalies above the segment end. Magnetic data collected using a submarine confirm this observation.

The seismic Moho might cross major lithologic contacts. Phases interpreted as mantle reflections (PmP) can be generated by different geologic structures.

The existence of converted shear waves and the lack of phase delay, a prominent shadow zone, or changes in the polarity of near-offset reflections, propose no larger axial magma body. There is no evidence for an active magma chamber.

The segment is lengthening towards the north and south. However, it may have reached its maximum size and stops growing. The driving force, maybe a huge magma chamber, disappeared and the force to penetrate melts through dikes along the ridge axis is no longer strong enough to break into the neighbour’s segments crust.

The earthquake distribution resulting from a seismicity study [Smith et al., 2003] hints to a magmatic active TAMMAR segment today. However, a lack in seismicity is no reasonable indication for propagation, rather evidence for the magmatic activity of a ridge segment during a small scale temporal variation between magmatic and tectonic crustal accretion. The appearance of mantle upwelling seems to have coincided with the onset of propagation 4.5 million years ago [*Kahle*, 2008]. *Kahle* [2008] figured out that spreading at the doomed ridge is taken up by mechanical rifting with minimal associated volcanism, thus, the magmatically very active segment [*Gente et al.*, 1995] is propagating into older crust of a magmatically starved segment. The thermal and gravitational differences, and the high amount of melts connected to the upwelling, may imply a driving mechanism for the migration of an earlier stable fracture zone setting.

6.2 Conclusions for the oceanic core complex

Across the Mid-Atlantic Ridge at 22°19'N seismic refraction data show large lateral variations of the upper crustal P-wave velocity structure. We observe the lowest velocities in the median valley, increasing gradually toward the east and rapidly near the western ridge flank. The western flank shows a prominent high of an oceanic core complex. Velocities of 4.5 km/s, however, indicate highly fractured rocks. Roughly 1.5 km below the seabed, seismic velocities reach 7 km/s. Fast material under the dome-shaped core complex may indicate the exposure of lower crust material, suggesting that the rapid change in seismic velocities is related to a lithological change caused by un-roofing of the crust. In contrast, seismic velocity data suggest that the lithosphere at the conjugated eastern flank was accreted by processes dominated by magmatic construction and hence show a typical velocity depth distribution expected for normal oceanic crust.

Hydroacoustic monitoring suggests that the detachment fault itself is seismically inactive, while seismicity clusters below the median valley [*Smith et al.*, 2003]. Thus, the aseismic low-angle detachment fault may turn into a steep normal fault under the rift valley. Joint raytracing and gravity modelling suggest that crust under the core complex is with respect to the conjugated ridge flank approx. 40% thinner. The velocity and density contrast as well as a few clear PmP reflections support that a Moho boundary was created during core complex formation, suggesting that the detachment fault is rooted in a zone of magmatic accretion at 2-4 km depth.

We favour the interpretation that the core complex was formed by a mechanism similar to the rolling-hinge model from *Buck* [1988]. The core complex formation started roughly 1.9 m.y. ago and is perhaps still active. Even though accretion seems to be highly asymmetric in term of the lithospheric structure of conjugated ridge flanks, accretion of North American and African plates occur at similar rates. However, while the eastern flank is composed of rocks showing the typical velocity depth profiles of magmatic crust, plate separation is accommodated by tectonic stretching and detachment faulting forming the North American plate.

No mantle rocks are exposed along the central part of the massif as can be interpreted from the seismic and gravity modelling. However collected rock samples from the southeastern steep wall revealed serpentinised peridotite that is leading to a three-dimensional structure of the core complex, where lower mantle temperatures near segment ends support thinner crust and mantle un-roofing.

Acknowledgements

First and foremost, I like to thank Ingo Grevemeyer for all the support he has given starting from my first day at IFM-GEOMAR until the very last days of this work - the discussions, advices, guidance, funding, but also the freedom in tackling the tasks.

Thanks must also go to Jason Phipps Morgan and César Ranero who initiated the project and spend time for discussions. The seismic survey was made possible by the funding of the Deutsche Forschungsgemeinschaft (grants Mo 961-5/1 Ra 925-5/1 Gr 1964-8/2+8/3) and the support of the participants of cruise M60-2. I would also like to thank Captain Kull and the crew of the R/V Meteor.

I am very grateful to Ernst Flüh for his continuous support and the many days I could spend on several and multifarious research cruises. I was able to attend many scientific meetings and got continuous financial support over the past years.

Special thanks to my parents and my brother for their support during the last few years.

Many thanks go to Andy Conn for the improvement of the manuscript. Cord Papenberg, Anne Krabbenhöft, and Jörg Petersen introduced me to the secrets of onboard works, preparing instruments and data pre-processing and the time for open questions.

Furthermore I thank to all members of the Geodynamics Department for their friendly assistance and the nice working atmosphere within the department. Special thanks belong to the inhabitants of building 12.

References

Alt, J.C. and W.C. Shanks, 1998 - Sulfur in serpentinised oceanic peridotites: Serpentinization processes and microbial sulfate reduction, *J. Geophys. Res.* **103**, 9917-9929.

Anderson, E.M., 1951 – *The Dynamics of Faulting (2nd ed.)*, Oliver & Boyd, Edinburgh, 208 pp.

van Andel, T.H., V.T. Bowen, P.L. Sachs, and R. Siever, 1965 – Morphology and sediments of a portion of the Mid-Atlantic Ridge, Science 148, 1214-1216.

van Avendonk, H.J.A., A.J. Harding, J.A. Orcutt, and W.S. Holbrook, 2001 – Hybrid shortest path and ray bending method for traveltime and raypath calculations, *Geophysics* **66**, 648-653.

Baines, A.G., M.J. Cheadle, B.E. John, J.J. Schartz, 2008 – The rate of oceanic detachment faulting at Atlantis Bank, SW Indian Ridge, *Earth Planet. Sci. Lett.* **273**, 105-114.

Barclay, A. H., D. R. Toomey, and S. C. Solomon, 1998 - Seismic structure and crustal magmatism at the Mid-Atlantic Ridge, 35°N, *J. Geophys. Res.* **103**, 17,827–17,844.

Barclay, A.H., D.R. Toomey, and S.C. Solomon, 2001 – Microearthquake characteristics and crustal vp/vs structure at the Mid-Atlantic Ridge, 35° N, *J. Geophys. Res.* **106**, 2017-2034.

Barclay, A.H., and D.R. Toomey, 2003 – Shear wave splitting and crustal anisotropy at the Mid-Atlantic Ridge, 35° N, *J. Geophys. Res.* **108**, 2378-2388.

Benz, T., 2003 – Erkundung mariner Untergrundstrukturen in Küstengebieten, *Kolloquium: Geophysikalische Methoden zur Baugrunderkundung unter der Gewässersohle*, BAW, Hannover.

Bevington, P.R., 1969 – *Data Reduction and Error Analysis for the Physical Sciences*, McGraw-Hill, New York.

Birch, F., 1961 – The velocity of compressional waves in rocks to 10 kilobars, part 2, *J. Geophys. Res.* **66**, 2199-2224.

Bishop, T.N., K.P. Bube, R.T. Cutler, R.T. Langan, P.L. Love, J.R. Resnick, R.T. Shuey, D.A. Spindler, and H.W. Wyld, 1985 – Tomographic determination of velocity and depth in laterally varying media, *Geophysics* **50**, 903-923.

Blackman, D.K., J.R. Cann, B. Janssen, D.K. Smith, 1998 – Origin of extensional core complexes: Evidence from the Mid-Atlantic Ridge at Atlantis Fracture Zone, *J. Geophys. Res.* **103**, 21 315-21 333.

Blackman, D.K., B. Ildefonse, B.E. John, Y. Ohara, D.J. Miller, and C.J. MacLeod, 2006 – *Proc. of Integrated Ocean Drilling Program* **304/305**, Texas.

Bonatti, E., 1976 – Serpentinite protrusion in the oceanic crust, *In* Emiliani, C., *The Sea* **7**: New York (Wiley), 241-283.

Bratt, S.R. and G.M. Purdy, 1984 – Structure and variability of oceanic crust on the flanks of the East Pacific Rise between 11° and 13° N, *J. Geophys. Res.* **89**(B7), 6111-6125.

Buck, W.R., 1988 – Flexural rotation of normal faults, *Tectonics* **7**, 959-973.

Calvert, A.J., 1995 - Seismic evidence for a magma chamber beneath the slow-spreading Mid-Atlantic Ridge, *Nature* **377**, 410-414.

Canales, J.P. and J.A. Collins, 2000 – Seismic structure across the rift valley of the Mid-Atlantic Ridge at 23°20' (MARK area): Implications for crustal accretion processes at slow spreading ridges, *J. Geophys. Res* **105**, 28 411-28 425.

Canales, J.P, R.S. Detrick, S.M. Carbotte, G.M. Kent, J.B. Diebold, A. Harding, J. Babcock, M. Nedimovic, E. Van Ark, 2005 – Upper crustal structure and axial topography at intermediate spreading ridges: Seismic constraints from the southern Juan de Fuca Ridge, *J. Geophys. Res.* **110**, doi:10.1029/2005/JB003630.

Canales, J.P., S.C. Singh, R.S. Detrick, S.M. Carbotte, A. Harding, G.M. Kent, J.B. Diebold, J. Babcock, M.R. Nedimović, 2006 – Seismic evidence for variations in axial magma chamber properties along the southern Juan de Fuca Ridge, *EPSL* **246**, 353-366.

Canales, J.P., B.E. Tucholke, M. Xu, J.A. Collins, and D.L. DuBois, 2008 – Seismic evidence for large-scale compositional heterogeneity of oceanic core complexes, *G³-Cube* **9**, No 8.

Cann, J.R. and B. Funell, 1967 – Palmer Ridge: a section through the upper part of the ocean crust, *Nature* **213**, 661-664.

Cann J.R., D.K. Blackman, D.K. Smith, E. McAllister, B. Janssen, S. Mello, E. Avgerinos, A.R. Pascoe, and J. Escartin, 1997 – Corrugated slip surfaces formed at ridge-transform intersections on the Mid-Atlantic Ridge, *Nature* **385**, 329-332.

Cannat, M., 1993 – Emplacement of mantle rocks in the seafloor at mid-ocean ridges, *J. Geophys. Res.* **98**, 4163-4172.

Cannat, M. et al., 1995 – Thin crust, ultramafic exposures, and rugged faulting patterns at the Mid-Atlantic Ridge (22°-24°N), *Geology* **23**, 49-52.

Cannat, M. et al., 2006 – Modes of seafloor generation at a melt-poor ultraslow-spreading ridge, Geology 34, 605-608.

Carbotte, S., S.M. Welch, K.C. Macdonald, 1991 – Spreading rates, rift propagation and fracture zone offset histories during the past 5 my on the Mid-Atlantic Ridge: 25° - 27°30'S and 31°-34°S, *Mar. Geophys. Res.* **13**, 51-80.

Carlson, R.L., and C.N. Herrick, 1990 – Densities and porosities in the oceanic crust and their variations with depth and age, *J. Geophys. Res.* **95**, 9153-9170.

Carlson, R.L., 1998 – Seismic velocities in the uppermost oceanic crust: Age dependence and the fate of layer 2A, *J. Geophys. Res.*, **103**, 7069-7077.

Carlson, R.L. and D.J. Miller, 2003 – Mantle wedge water contents estimated from seismic velocities in partially serpentinised peridotites, *Geophys. Res. Let.* **30** (5), 1250.

Ceuleneer G., 1988 - Nicolas A. and Boudier F. Mantle flow patterns at an oceanic spreading centre: the Oman peridotites record, *Tectonophysics* **151**, 1-26.

Ceuleneer G. and Cannat M., 1997 - High temperature ductile deformation of the site 920 peridotites. In : Karson J.A., Cannat M., Miller D.J. and Elthon D., Eds., *Proc. Ocean Drilling Progam, Scientific Results*, **153**, College Station, Texas, U.S.A., 23-34.

Červený, V., I. Molotkov and Pšenčík, 1977 – Ray method in seismology, Charles Univ. Press.

Chen, Y.J. and J. Lin, 1999 – Mechanism for the formation of ridge-axis topography at slow-spreading ridges: a lithospheric-plate flexural model, *Geophy. J. Int.* **136**, 8-18.

Christensen, N.I., 1966 – Elasticity of ultrabasic rocks, *J. Geophys. Res.* **71**, 5921-5931.

Christeson, G.L., G.M. Purdy, and G.J. Fryer, 1992 – Structure of young upper crust at the East Pacific Rise near 9°30' N, *Geophys. Res. Lett.* **19**, 1045-1048.

Christeson, G.L., K.D. McIntosh, and J.A. Karson, 2006 – Inconsistent correlation of seismic layer 2A and lava layer thickness in oceanic crust, *Nature* **445**, 418-421.

Collier, J.S. and M.C. Sinha, 1992 – Seismic mapping of a magma chamber beneath the Valu Fa Ridge, Lau Basin, *J. Geophys. Res.* **97**(B10), 14031-14053.

deMartin, B.J., R.A. Sohn, J.P. Canales, S.E. Humphris, 2007 – Kinematics and geometry of active detachment faulting beneath the Trans-Atlantic Geotraverse (TAG) hydrothermal field on the Mid-Atlantic Ridge, *Geology* **35**-8, 711-714.

DeMets, D. et al., 1990 - Current Plate Motions, *Geophys. J. Int.* **101**, 425-478.

Detrick, R.S., P.J. Fox, K. Karstens, W.B. Ryan, L. Mayer, and J.A. Karson, 1984 – A SeaBeam survey of the Kane fracture zone and adjacent Mid-Atlantic Ridge rift valley, *Eos Trans. AGU* **65**, 1106.

Detrick, R.S., P. Buhl, E. Vera, J. Mutter, J. Orcutt, J. Madsen, and T. Brocher, 1987 – Multi-channel seismic imaging of a crustal magma chamber along the East Pacific Rise, *Nature* **326**, 35-41.

Detrick, R.S., R.S. White, and G.M. Purdy, 1993 – Crustal structure of North Atlantic fracture zones, *Reviews of Geophysics* **31**, 439-458.

Detrick, R.S., H.D. Needham, and V. Renard, 1995 – Gravity anomalies and crustal thickness variations along the Mid-Atlantic Ridge between 33°N and 40°N, *J. Geophys. Res.* **100**, 3767-3787.

Detrick, R.S., D.R. Toomey, and J.A. Collins, 1998 - Three-dimensional upper crustal heterogeneity and anisotropy around Hole 504B from seismic tomography, *J. Geophy. Res.* **103**, 30 485-30504.

Dick, H.J.B., W.B. Bryan, and G. Thompson, 1981 – Low-angle faulting and steady-state emplacement of plutonic rocks at ridge-transform intersections., *EOS* **62**, 406.

Dick, H.J.B., H. Schouten, P.S. Meyer, D.G. Gallo, H. Bergh, R. Tyce, P. Patriat, K.T.M. Johnson, J. Snow, and A. Fisher, 1991 – Tectonic evolution of the AtlantisII Fracture zone, in Proc. ODP, Sci. Results, 118, edited by R. VonHerzen, P. Robinson, et al., 359-398, College Station, Texas.

Dick, H.J.B., J.H. Natland, J.C. Alt, W. Bach, D. Bideau, J.S. Gee, S. Haggas, J.G.H. Hertogen, A. Kingdon, P.J. LeRoux, J. Maeda, P.S. Meyer, D.J. Miller, H.R. Naslund, Y.L. Niu, P.T. Robinson, J. Snow, R.A. Stephen, P.W. Trimby, H.U. Worm, A. Yoshinobu, 2000 – A long in situ section of the lower ocean crust: results of ODP Leg 176 drilling at the Southwest Indian Ridge, *Earth Planet. Sci. Lett.* **179**, 31–51.

Dick, H.J.B., M.A. Tivey, and B.E. Tucholke, 2008 – Plutonic foundation of a slow-spreading ridge segment: Oceanic core complex at Kane Megamullion, 23°30'N, 45°20'W, *Geochem. Geophys. Geosyst.* **9**, Q05014, doi: 10.1029/2007GC001645.

Dietz, R.S., 1961 – Continent and ocean basin evolution by spreading of the sea floor, *Nature* **190**, 854-857.

Dunn, R.A. and D.R. Toomey, 1997 – Seismological evidence for three-dimensional melt migration beneath the East Pacific Rise, *Nature* **388**, 259-262.

Dunn, R.A., and D.R. Toomey, 2001 - Crack-induced seismic anisotropy in the oceanic crust across the East Pacific Rise (9°30' N), *Earth Planet. Sci. Lett.* **189**, 9-17.

Dunn, R.A., V. Lekic, R.S. Detrick, and D.R. Toomey, 2005 – Three-dimensional seismic structure of the Mid-Atlantic Ridge (35°N): Evidence for focused melt supply and lower crustal dike injection, *J. Geophys. Res.* **110**, B09101, doi:10.1029/2004JB003473.

Durand, C., P. Gente, and O. Dauteuil, 1995 – Caracteristiques morphologiques des segment axiaux de la dorsal Medio-Atlantique entre 20° N et 24° N, *C. R. Acad. Sci.* **320**, 412-418.

Elthon D., 1987 - Petrology of gabbroic rocks from the Mid-Cayman Rise spreading center, *J. Geophys. Res.* **92**, 658-682.

Escartín, J., C. Mével, C.J. MacLeod, A.M. McCaig, 2003 – Constraints on deformation conditions and the origin of oceanic detachments: The Mid-Atlantic Ridge core complex at 15°45'N, *Geochem. Geophys. Geosyst.* **4**, No. 8.

Escarin, J., D.K. Smith, J. Cann, H. Schouten, C.L. Langmuir, and S. Escrig, 2008 – Central role of detachment faults in accretion of slow spreading oceanic lithosphere -------- .

Flueh, E.R. and J. Bialas, 1996 – A digital, high data capacity ocean bottom recorder for seismic investigations, *Int. Underwater Systems Design* **18**, 18-20.

Flueh, E.R., and I. Grevemeyer, 2005 – Cruise Report SO181, TIPTEQ – from The Incoming Plate to mega-Thrust EarthQuakes, *Berichte aus dem Leibnitz Institut für Meereswissenschaften* **2**, ISSN 1614-6298, 539 pp.

Francis, T.J.G., 1981 – Serpentinisation faults and their role in tectonics of slow spreading ridges, *J. Geophys. Res.* **86**, 11616-11622.

Gac, S., J. Dyment, C. Tisseau, and J. Goslin, 2003 – Axial magnetic anomalies over slow-spreading ridge segments: insights from numerical 3-D thermal and physical modelling, *Geophys. J. Int.* **154**, 618-632.

Gac, S., C. Tisseau, J. Dyment, and J. Goslin, 2006 – Modelling the thermal evolution of slow-spreading ridge segments and their off-axis geophysical signature, *Geophy. J. Int.* **164**, 341-458.

Gente, P., D. Aslanian, A. Campan, M. Cannat, G. Ceuleneer, C. Deplus, C. Durand, C. Laverne, H. Leau, M. Maia, E. Marion, C. Mével, R. Pockalny, and M. Seyler, 1991 – Geometry of the past and present-day segmentation of the Mid-Atlantic Ridge south of Kane fracture zone *EOS* **72**, 477.

Gente, P., R.A. Pockalny, C. Durand, C. Deplus, M. Maia, G. Ceuleneer, C. Mével, M. Cannat, and C. Laverne, 1995 – Characteristics and evolution of the segmentation of the Mid-Atlantic Ridge between 20° N and 24° N during the last 10 million years, *EPSL* **129**, 55-71.

Gente, P., G. Ceuleneer, O. Dauteuil, J. Dyment, C. Honsho, C. Laverne, C. LeTrudu, N.C. Mitchell, M. Ravilly, and R. Thibaud, 1996 – On- and Off-axis Submersible Investigations on an Highly Magmatic Segment of the Mid-Atlantic Ridge (21° 40' N): the TAMMAR Cruise, *InterRidge News* **5** (2), 27-31.

Grevemeyer I. and W. Weigel, 1996 – Seismic velocities of the uppermost igneous crust versus age, *Geophys. J. Int.* **124**, 631–635.

Grevemeyer I., W. Weigel, and C. Jennrich, 1998 – Structure and ageing of oceanic crust at 14° S on the East Pacific Rise, *Geophys. J. Int.* **135**, 573-584.

Grevemeyer, I., N. Kaul, H. Villinger, and W. Weigel, Hydrothermal activity and the evolution of the seismic properties of upper oceanic crust. *J. Geophys. Res.* **104** (1999), pp. 5069–5079.

Grimes, C.B., B.E. John, M.J. Cheadle, and J.L. Wooden, 2008 – Protracted construction of gabbroic crust at a slow spreading ridge: Constraints from $^{206}Pb/^{238}U$ zircon ages from Atlantis Massif and IODP Hole U1309D (30°N, MAR), *Geochem. Geophys. Geosyst.* **9**, Q08012, doi: 10.1029/2008GC002063.

Gripp, A.E., and R.G. Gordon, 2000 – Young tracks of hotspots and current plate velocities, *Geophys. J. Int.* **150**, 321-361.

Hess, H.H., 1962 – A history of ocean basins, in *Petrological Studies: A volume in Honor of A.F. Buddington*, Geolog. Soc. Of America, 599-620.

Hey, R.N., 1977 – A new class of "pseudofaults" and their bearing on plate tectonics: a propagating rift model, *Earth Planet. Sci. Lett.* **37**, 321.

Hey, R.N., F.K. Duennebier, and W.J. Morgan, 1980 – Propagating rifts on mid-ocean ridges, *J. Geophys. Res.* **85**, 3647-3658.

Hey, R.N., M.C. Kleinrock, S.P. Miller, T.M. Atwater, and R.C. Searle, 1986 – Sea beam/deep-tow investigation of an active oceanic propagation rift system, Galapagos 95.5° W, *J. Geophys. Res.* **91**, 3369-3394.

Hey, R.N., J.M. Sinton, and F.K. Duennebier, 1989 – Propagating rifts and spreading centers, in *Decade of North American Geology: The Eastern Pacific Ocean and Hawaii*, Geological Society of America, 161-176.

Hooft, E.E.E., R.S. Detrick, D.R. Toomey, J.A. Collins, and J. Lin, 2000 – Crustal thickness and structure along three contrasting spreading segments of the Mid-Atlantic Ridge 33.5°-35°N, *J. Geophys. Res.* **105**, 8205-8226.

Honsho, C., J. Dyment, K. Tamaki, M. Ravilly, H. Horen, and P. Gente, 2009 (in press) – Magnetic structure of a slow-spreading ridge segment: insights from near-bottom magnetic measurements onboard a submersible, *J. Geophys. Res.*.

Houtz, R., and J. Ewing, 1976 – Upper crustal structure as a function of plate age, *J. Geophys. Res.* **81**, 2490-2498.

Huang and Solomon, 1987 – Centroid Depths and Mechanisms of Mid-Ocean Ridge Earthquakes in the Indian Ocean, Gulf of Aden, and Red Sea, *J. Geophys. Res.* **92**, 1361-1382.

Huang, P.Y. and S.C. Solomon, 1988 – Centroid depths of mid-ocean ridge earthquakes: dependence on spreading rate, *J. Geophys. Res.* **93**, 13445–13477.

Hyndman, R.D., 1979 – Poisson's ratio in the oceanic crust: a review, *Tectonophysics* **59**, 321–333.

Ildefonse, B., D.K. Blackmann, B.E. John, Y. Ohara, D.J. Miller, and C.J. MacLeod, 2007 – Oceanic core complexes and crustal accretion at slow-spreading ridges, *Geology* **35**, 623-626.

Jones, E.J.W., 1999 – *Marine Geophysics*, University College London, John Wiley and Sons, LTD, England.

Kahle, R.L., 2007 – A seismic investigation of the 21.5° N propagating segment on the Mid-Atlantic Ridge, Doctor Thesis, St. John's College, University of Cambridge.

Karson, J.A., J.A. Collins, and J.F. Casey, 1984 – Geologic and seismic velocity structure of the crust/mantle transition in the Bay of Islands ophiolite complex, *J. Geophys. Res.* **89**, 6121-6138.

Karson, J.A. and D. Elthon, 1987a – Evidence for variations in magma production along oceanic spreading centres: A critical appraisal, *Geology* **15**, 127-131.

Karson, J.A., G. Thompson, S.E. Humphris, J.M. Edmond, W.B. Bryan, J.R. Brown, A.T. Winters, R.A. Pockalny, J.F. Casey, A.C. Campbell, G. Klinkhammer, M.R. Palmer, R.J. Kinzler, and M.M. Sulanowska, 1987b – Along-axis variation in seafloor spreading in the MARK area, Nature 328, 681-685.

Karson, J.A., 1990 – Seafloor spreading on the Mid-Atlantic Ridge: implications for the structure of ophiolites and oceanic lithosphere produced in slow-spreading environments. In:

J. Malpas, E.M. Moores, A. Panyiotou and C. Xenophontos, Editors, *Ophiolites: Oceanic Crustal Analogues*, Geological Survey Department, Nicosia, Cyprus (1990), 547–555

Karson, J.A., and A.T. Winters, 1992 – Along-axis variations in tectonic extension and accommodation zones in the MARK Area, Mid-Atlantic Ridge 23° N latitude, *Parson, L.M., et al., eds., Ophiolites and their modern oceanic analogues*: Geolocical Society (London) Spec. Publication 60, 107-116.

Karson, J.A., G.L. Früh-Green, D.S. Kelley, E.A. Williams, D.R. Yoerger, and M. Jakuba, 2006 – Detachment shear zone of the Atlantis Massif core complex, Mid-Atlantic Ridge, 30° N, *Geochem. Geophys. Geosyst*. **7**, Q06016, doi:10.1029/2005GC001109.

Kelemen, P.B., K. Koga, and N. Shimizu, 1997 – Geochemistry of gabbro sills in the crust-mantle transition zone of the Oman ophiolite: Implications for the origin of the oceanic lower crust, *Earth Planet. Sci. Lett.* **146**, 475-488.

Kious, W.J. and R.I. Tilling, 1996 – This Dynamic Earth: the Story of Plate Tectonics: "Historical perspective", U.S. Geological Survey, ISBN: 0160482208.

Kleinrock, M. C. and B. E. Tucholke, 1997 - Fast rift propagation at a slow-spreading ridge, *Geology* **25**, 639-642.

Kong, L.S.L., S.C. Solomon, and G.M. Purdy, 1992 – Microearthquake characteristics of a mid-ocean ridge along-axis high, *J. Geophys. Res.* **97**, 1659-1685.

Korenaga, J., W.S. Holbrook, G.M. Kent, P.B. Kelemen, R.S. Detrick, H.C. Larsen, J.R. Hopper, and T. Dahl-Jensen, 2000 – Crustal structure of the southeast Greenland margin from joint refraction and reflections seismic tomography, *J. Geophys. Res.* **105**, 21 591-21 614.

Korenaga et al., 2001 – Gravity anomalies and crustal structure at the southeast Greenland margin, *J. Geophys. Res.* **106**, 8853-8870.

Leblanc M., G. Ceuleneer, H. Al Azri, and J. Jedwab, 1991 - Concentration hydrothermale de Pd et de Pt dans les péridotites mantellaires du complexe ophiolitique d'Oman, Compte Rendus Académie des Sciences, C. R. Acad. Sci. **312**, II, 1007-1012.

Lin, J., J.P. Morgan, 1992 – The spreading rate dependence of three-dimensional Mid-ocean ridge gravity structure, *Geophys. Res. Lett.* **19**, 13-16.

Lin, J., B.E. Tucholke, and M.C. Kleinrock, 1993 – Evidence from gravity and morphology for long-term variability in magmatic vs. tectonic extension at the Mid-Atlantic Ridge [abs.]: *EOS* **73**, 303.

Luetgert, J.H., 1992 – Interactive Two-Dimensional Seismic Raytracing for the Macintosh, *U.S. Geological Survey, Open-File Report* **92-356**, 44.

Macdonald, K.C., 1982 – Mid-Ocean ridges: Fine Scale Tectonic, Volcanic and Hydrothermal Processes Within the Plate Boundary Zone, *Ann. Rev. Earth Planet. Sci.*

Macdonald, K.C., P.J. Fox, L.J. Perram, M.F. Eisen, R.M. Haymon, S.P. Miller, S.M. Carbotte, M.H. Cormier, and A.N. Shor, 1988 – A new view of the mid-ocean ridge from the behaviour of ridge-axis discontinuities, *Nature* **335**, 217 - 225.

Macdonald, K. C., D. S. Scheirer, and S. M. Carbotte, 1991 - Mid-Ocean Ridges: Discontinuities, Segments and Giant Cracks., *Science* **253** , 986–994, 1991.

Macdonald, K. C., 1998 - Linkages between faulting, volcanism, hydrothermal activity and segmentation on fast spreading centres, in Faulting and Magmatism at Mid-Ocean Ridges, edited by W. R. Buck, P. T. Delaney, J. A. Karson, and Y. Lagabrielle, AGU, *Geophysical Monograph* **106**, 27-58.

Magde, L.S., R.S. Detrick, 1995 – Crustal and upper mantle contribution to the axial gravity anomaly at the southern East Pacific Rise, *J. Geophys. Res.* **100**, 3747-3766.

Magde, L. S., and D. W. Sparks, 1997 - Three-dimensional mantle upwelling, melt generation and melt migration beneath segmented slow spreading ridges, *J. Geophys. Res.* **102**, 20 571–10 583.

Magde, L.S., A.H. Barcley, D.R. Toomey, R.S. Detrick, and J.A. Collins, 2000 – Crustal magma plumbing within a segment of the Mid-Atlantic Ridge, 35° N, *Earth Planet. Sci. Lett.* **175**, 55-67.

Maia and Gente, 1998 – Three-dimensional gravity and bathymetry analysis of the Mid-Atlantic Ridge between 20° N and 24° N: Flow geometry and temporal evolution of the segmentation, *J. Geophys. Res.* **103**, 951-974.

Melson W.G. and T.H. van Andel, 1966 – Metamorphism in the mid-Atlantic ridge, 22° N latitude, *Marine Geol.* **4**, 165-186.

Melson, W.G., G. Thompson, and T.H. van Andel, 1968 – Volcanism and Metamorphism in the Mid-Atlantic Ridge, 22° N Latitude, *J. Geophys. Res.* **73**, 5925-5941.

Menke, W., M. West, and M. Tolstoy, 2002 – Shallow crustal magma chamber beneath the axial high of the Coaxial Segment of Juan de Fuca Ridge at the "Source Site" of the 1993 eruption, *Geology* **30**, 359-362.

Metha Aalok, 2007 – Oldest Known Ocean Crust Found on Greenland, *National Geographic News*.

Mével, C., M. Cannat, P. Gente, E. Marion, J.M. Auzende, and J.A. Karson, 1991 – Emplacement of deep rocks on the west median valley wall of the MARK area (M.A.R. 23° N), *Tectonophysics* **190**, 31-53.

Minshull, T.A., M.R. Muller, and R.S. White, 2006 – Crustal structure of the Southwest Indian Ridge at 66° E: seismic constraints, *Geophys. J. Int.* **166**, 135-147.

Morgan, J. Phipps and E.M. Parmentier, 1985 – Causes and Rate-Limiting Mechanisms of Ridge Propagation: A Fracture Mechanics Model, *J. Geophys. Res.* **90**, 8603–8612.

Morgan, J. Phipps and D. T. Sandwell, 1994 - Systematics of ridge propagation south of 30°S, *Earth Planet. Sci. Lett.* **121**, 245-258.

Moser, T.J., 1991 – Shortest path calculation of seismic rays, *Geophysics* **56**, 59-67.

Moser, T.J., G. Nolet, and R. Snieder, 1992 – Ray bending revisited, *Bull. Seismol. Soc. Am.* **82**, 259-288.

Muller, R.D., M. Sdrolias, C. Gaina, and W.R. Roest, 2008 – Age, spreading rates and spreading symmetry of the world's ocean crust, *Geochem. Geophys. Geosyst.* **9**, Q04006, *doi:10.1029/2007GC001743*.

Murase, T. and A.R. McBirney, 1973 – Properties of some common igneous rocks and their melts at high temperatures, *Geol. Soc. Am. Bull.* **84**, 3563-3592.

Mutter, J.C., and J.A. Karson, 1992 – Structural processes at slow-spreading ridges, *Science* **257**, 627-634.

Naar, D.F. and R.N. Hey, 1986 – Fast rift propagation along the East Pacific Rise near Easter Island, *J. Geophys. Res.* **91**, 3425-3438.

Nakamura, Y., P.L. Donoho, P.H. Roper, and P.M. McPherson, 1987 – Large offset seismic surveying using ocean-bottom seismograms and air guns: Instrumentation and field technique, *Geophysics* **52**, 1601-1611.

Nakanishi, I and K. Yamaguchi, 1986 – A numerical experiment on nonlinear image reconstruction from first arrival times for two-dimensional island arc structure, *J. Phys. Earth* **34**, 195-201.

Natland J.H. and H.J.B. Dick, 1996 - Melt migration through high-level gabbroic cumulates of the East Pacific Rise at Hess Deep: the origin of magma lenses and the deep crustal structure of fast spreading ridges. In C. Mevel, K.M. Gillis, J.F. Allan, and D. Elthon, (Eds), *Proc. of the Ocean Drilling Progam, Scientific Results* **147**, College Station, Texas, 21-59.

Nedimović M.R., S.M. Carbotte, J.B. Diebold, A.J. Harding, J.P. Canales, G.M. Kent, 2008 – Upper crustal evolution across the Juan de Fuca ridge flanks, *Geochem. Geophys. Geosyst.* **9**, Q09006, doi:10.1029/2008GC002085.

Niu, Y., D. Bideau, R. Hekinian, R. Batiza, 2001 – Mantle compositional control on the extent of mantle melting, crust production, gravity anomaly, ridge morphology, and ridge segmentation: a case study at the Mid-Atlantic Ridge 33-35° N, *EPSL* 186, 383-399.

Nur, A., H. Ron, and O. Scotti, 1986 – Fault mechanics and the kinematics of block rotations, *Geology* **14**, 746-749.

Orcutt, J.A., B.L.N. Kennett, and L.M. Dorman, 1976 – Structure of the East Pacific Rise from an Ocean Bottom Seismometer Survey, *Geophys. J. Int.* **45**, 305-320.

Papazachos, C. and G. Nolet, 1997 – P and S deep velocity structure of the Hellenic area obtained by robust non-linear inversion of traveltimes, *J. Geophys. Res.* **102**, 8349-8367.

Pratt, J.H., 1855 – On the attraction of the Himalaya Mountains and of the elevated regions beyond them upon the plumb line in India, *Transactions of the Royal Society of London* **145**B, 53-100.

Price, N.J., and J.W. Cosgrove, 1990 – *Analysis of Geological Structures*, Cambridge Univ. Press.

Pockalny, R.A., A. Smith, and P. Gente, 1994 – Spatial and Temporal Variability of Crustal Magnetisation of a Slowly Spreading Ridge: Mid-Atlantic Ridge (20°-24° N), *Marine Geophysical Res.* **17**, 301-320.

Purdy, G.M., and J. Ewing, 1986 – Seismic structure of the ocean crust, in *The Western North Atlantic Region: Boulder Colorado*, Geological Society of America, The Geology of North America, 313-330.

Purdy, G.M., 1987 – New observations of the shallow seismic structures of young oceanic crust, *J. Geophys. Res.* **92**, 9351-9362.

Purdy, G.M., J.C. Sempere, H. Schouten, D. Dubois, and R. Goldsmith, 1990 – Bathymetry of the Mid-Atlantic Ridge, 24°-31° N: A map series, *Mar. Geophys. Res.* **13**, 247-252.

Python M., G. Ceuleneer, Y. Ishida, J.-A. Barrat, and S. Arai, 2007 - Oman diopsidites : a new lithology diagnostic of very high temperature hydrothermal circulation in mantle peridotite below oceanic spreading centres, *Earth Planet. Sci. Lett.* **255**, 289-305.

Ranero, C.R., T.J. Reston, 1999 – Detachment faulting at ocean core complexes, *Geology* **27**, 983-986.

Ravilly, M. et al., 1998 - Axial magnetic anomaly amplitude along the Mid-Atlantic Ridge between 20° N and 40° N, *J. Geophys. Res.* **103**(B10), 24,201-24,221.

Reston, T. J., W. Weinrebe, I. Grevemeyer, E. R. Flüh, N. C. Mitchell, L. Kirstein, C. Kopp, H. Kopp, 2002 - A rifted inside corner massif on the Mid-Atlantic Ridge at 5° S, *Earth Planet. Sci. Lett.* **200**, 255-269.

Rohr, K.M.M, B. Milkereit, and C.J. Yorath, 1988 – Asymmetric deep crustal structure across the Juan de Fuca Ridge, *Geology* **16**, 533-537.

Rosendahl, B.R., R.W. Raitt, L.M. Dorman, L.D. Bibee, D.M. Hussong, and G.H. Sutton, 1976 – Evolution of oceanic crust 1: a physical model of the East Pacific Rise crest derived from seismic refraction data, *J. Geophys. Res.* **81**, 5294-5304.

Ross, K. and D. Elthon, 1997 – Cumulus and postcumulus crystallization in the oceanic crust: Major and trace-element geochemistry of Leg 153 Gabbroic rocks. In : Karson J.A., Cannat M., Miller D.J. and Elthon D., Eds., *Proc. Ocean Drilling Progam, Scientific Results*, **153**, College Station, Texas, U.S.A., 23-34.

Sandwell, D.T. and W.H.F. Smith, 1997 – Marine gravity anomaly from Geosat and ERS-1 satellite altimetry, *J. Geophys. Res.* **102**, 10039-10054.

Schouten, H., K.D. Klitgord, and J.A. Whitehead, 1985 – Segmentation of mid-ocean ridges, *Nature* **317**, 225-229.

Schouten, H. H.J.B. Dick, and K.D. Klitgord, 1987 – Migration of mid-ocean ridge volcanic segments, *Nature* **326**, 835-839.

Schuhmann, W., 1985 – *Der neue BLV Steine- und Mineralienführer*, BLV Verlagsgesellschaft mbH München.

Sempéré, J.C., G.M. Purdy, and H. Schouten, 1990 – The segmentation of the Mid-Atlantic Ridge, *Nature* **344**, 427-431.

Sempéré, J.C., J. Lin, H.S. Brown, H. Schouten, and G.M. Purdy, 1993 – Segmentation and morphotectonic variations along a slow-spreading center: The Mid-Atlantic Ridge (24°00'N-30°40'N), *Mar. Geophys. Res.* **15**, 153-200.

Shaw, W.J., and J. Lin, 1996 – Models of ocean ridge lithospheric deformation: Dependence on crustal thickness, spreading rate, and segmentation, *J. Geophys. Res.* **101**, 17977-17993.

Shearer, P., and J.A. Orcutt, 1985 – Anisotropy in the oceanic lithosphere - theory and observations from the Ngendei seismic refraction experiment in the south-west Pacific, *Geophys. J. R. Astron. Soc.* **80**, 493-526.

Sheriff, R.E. and L.P. Geldart, 1995 – *Exploration seismology, vol. 2; Data-processing and interpretation*, 2nd Edition, Cambridge Univ. Press.

Singh, S.C., G.M. Kent, J.S. Collier, A.J. Harding, and J.A. Orcutt, 1998 – Melt to mush variations in crustal magma properties along the ridge crest at the southern East Pacific Rise, *Nature* **394**, 874-878.

Singh, S.C, W.C. Crawford, H.Carton, T. Seher, V. Combier, M. Cannat, J.P. Canales, D. Düsünür, J. Escartin, and J.M. Miranda, 2006 – Discovery of a magma chamber and faults beneath a Mid-Atlantic Ridge hydrothermal field, *Nature* **442**, doi:10.1038/nature05105.

Sinha, M.C. and K.E. Louden, 1983 – The Oceanographer fracture zone – I. Crustal structure from seismic refraction studies, *Geophys. J. Royal Astron. Soc.* **75**, 713-736.

Sinha M.C., C. Constable, C. Peirce, A. White, G. Heinson, L.M. MacGregor, and D.A. Navin, 1998 – Magmatic processes at slow spreading ridges: implications of the RAMESSES experiment at 57°45' N on the Mid-Atlantic Ridge, *Geophys. J. Int.* **135**, 731-745.

Sinton, J.M., D.S. Wilson, D.M. Christie, R.N. Hey, and J.R. Delaney, 1983 – Petrologic consequences of rift propagation on oceanic spreading ridges, *Earth Planet. Sci. Let.* **62**, 193-207.

Skelton, A.D.L. and J.W. Vally, 2000 – The relative timing of serpentinisation and mantle exhumation at the ocean-continent transition, Iberia: constraints from oxygen isotopes, *Earth Planet. Sci. Let.* **178**, 327-338.

Smith, D.K., J. Escartin, M. Cannat, M. Tolstoy, C.G. Fox, D.R. Bohnenstiel, and S. Basin, 2003 – Spatial and temporal distribution of seismicity along the Mid-Atlantic Ridge (15 – 35° N), *J. Geophys. Res.* **108**(B3), 2167.

Smith et al., 2006 – Widespread active detachment faulting and core complex formation near 13° N on the Mid-Atlantic Ridge, Nature **442**, 440-443.

Smith, D.K., J. Escartin, H. Schouten, J.R. Cann, 2008 – Fault rotation and core complex formation: Significant processes in seafloor formation at slow-spreading mid-ocean ridges (Mid-Atlantic Ridge, 13°-15° N), *Geochem. Geophys. Geosyst.* **9**, Q03003, doi:10.1029/2007GC001699.

Solomon, S. C. and D. R. Toomey, 1992 - The Structure of Mid-Ocean Ridges, *Earth Planet. Sci. Lett.* **20**, 329-264.

Stevenson, J.M., J.A. Hildebrand, M.A. Zumberge, 1994 – An ocean bottom gravity study of the southern Juan de Fuca Ridge, *J. Geophys. Res.* 99, 4875-4888.

Stork, C. and R.W. Clayton, 1991 – Linear aspects of tomographic velocity analysis, *Geophysics* **56**, 483-495.

Thatcher, W. and D.P. Hill, 1995 – A simple model for fault generated morphology of slow-spreading mid-ocean ridges, *J. Geophys. Res.* **100**, 561-570.

Thibaud, R., P. Gente, and M. Maia, 1998 – A systematic analysis of the Mid-Atlantic Ridge morphology and gravity between 15° N and 40° N: Constraints of the thermal structure, J. Geophys. Res. **103**, 24 223-24 243.

Thibaud, R. O. Dauteuil, and P. Gente, 1999 – Faulting pattern along slow-spreading ridge segments: a consequence of along-axis variation in lithospheric rheology, *Tectonophysics* **312**, 157-174.

Toomey, D.R., G.M. Purdy, S.C. Solomon, and W.S.D. Wilcock, 1990 – The three-dimensional seismic velocity structure of the East Pacific Rise near latitude 9°30' N, *Nature* **347**, 639-644.

Toomey, D.R., S.C. Solomon, and G.M. Purdy, 1994 – Tomographic imaging of the shallow crustal structure of the East Pacific Rice at 9°30' N, *J. Geophys. Res.* **99**, 24 135-24 157.

Tolstoy, M., A. Harding, and J. Orcutt, 1993 – Crustal thickness on the Mid-Atlantic Ridge: Bull's-eye gravity anomalies and focused accretion, *Science* **262**, 726-729.

Tucholke, B.E., and H. Schouten, 1988 – Kane Fracture Zone, *Marine Geophys. Res.* **10**, 1-39.

Tucholke, B.E. and J. Lin, 1994 – A geological model for the structure of ridge segments in slow spreading ocean crust, *J. Geophys. Res.* **99**, 11 937-11 958.

Tucholke, B. E., J. Lin, M.C. Kleinrock, M. Tivey, T.B. Reed, J. Goff, and G. Jaroslow, Segmentation and crustal structure of the western Mid-Atlantic Ridge flank, 25°25' - 27°10'N and 0 - 29 m.y., *J. Geophys. Res.* **102**, 10 203-10 223.

Tucholke, B.E., J. Lin, M.C. Kleinrock, 1998 – Megamullions and mullion structure defining oceanic metamorphic core complexes on the Mid-Atlantic Ridge, *J. Geophys. Res.* **103**, 9857-9866.

Tucholke, B.E., K. Fujioka, T. Ishihara, G. Hirth, and M. Kinoshita, 2001 – Submersible study of an oceanic megamullion in the central North Atlantic, *J. Geophys. Res.* **106**, 16 145-16 161.

Wang, R., 1999 - A simple orthonormalization method for the stable and efficient computation of Green's functions, *Bull. of the Seismological Soc. of America* **89**, 733-741.

Wernicke, B. and G.J. Axen, 1988 – On the role of isostacy in the evolution of normal fault systems, *Geology* **16**, 848-851.

White, R.S., D. McKenzie, and R.K. O'Nions, 1992 – Oceanic crustal thickness from seismic measurements and rare earth element inversions, *J. Geophys. Res.* **97**, 19 683-19 715.

Whitmarsh, R.B., 1973 – Median valley refraction line, mid-Atlantic ridge at 37° N, *Nature* **246**, 297-299.

Wiener, N., 1949 – *Extrapolation, Interpolation, and Smoothing of Stationary Time Series*. New York: Wiley, ISBN 0-262-73005-7.

Wilson, D.S., R.N. Hey, and C. Nishimura, 1984 – Propagation as a mechanism of ridge rotation: A model for the tectonic evolution of the Juan de Fuca Ridge, *J. Geophys. Res.* **89**, 9215–9225.

Zelt, C.A. and R.M. Ellis, 1988 – Practical and efficient ray tracing in two-dimensional media for rapid traveltime and amplitude forward modelling, *Canadien J. of Expl. Geophys.* **24**, 16-31.

Zelt, C.A. and R.B. Smith, 1992 – Seismic traveltime inversion for 2-D crustal velocity structure, *Geophys. J. Int.* **108**, 16-34.

Zelt, C.A., 1999 – Modelling strategies and model assessment for wide-angle seismic traveltime data, *Geophys. J. Int.* **139**, 183-204.

Zhang, J. and M.N. Toksöz, 1998 – Nonlinear refraction and reflection traveltime tomography, Geophysics 63, 1726.

Zoeppritz, K., 1919 – *Über Reflexion und Durchgang seismischer Wellen durch Unstetigkeitsflächen*, Erdbebenwellen VII B, Nachrichten der Königlichen Gesellschaft der Wissenschaften zu Göttingen, Math. Phys., K1:57-84.

Eidesstattliche Erklärung

Hiermit versichere ich an Eides Statt, dass ich diese Arbeit ausschließlich unter Anleitung meiner wissenschaftlichen Lehrer und unter Verwendung der angegebenen Hilfsmittel angefertigt habe. Ferner habe ich weder diese noch eine ähnliche Arbeit hier oder an einer anderen Hochschule im Rahmen eines Prüfungsverfahrens vorgelegt.

Kiel,

Lebenslauf

Name	Anke Dannowski	
Geburtstag	15.06.1978	
Nationalität	Deutsch	
Adresse	Ackermannstr. 10 01217 Dresden	
Beruf	seit Nov. 2004	Wissenschaftliche Angestellte IFM-GEOMAR
Höhere Ausbildung	Okt. 1997 - Okt. 2004	Geophysik an der TU Bergakademie Freiberg
	Aug. 1999 - Juli 2000	NTNU Trondheim, Norwegen
Schulische Ausbildung	Aug. 1992 - Juni 1997	Vitzthum-Gymnasium
	Sept. 1991 - Juli 1992	Robert Schumann Gymnasium
	Sept. 1985 - Juli 1991	46. POS Soja Kosmodemjanskaja

Appendix

A – Profile 02

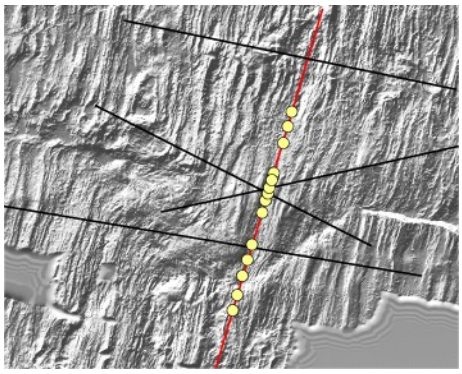

Figure A-1: Location map for profile 02 with ocean bottom instruments.

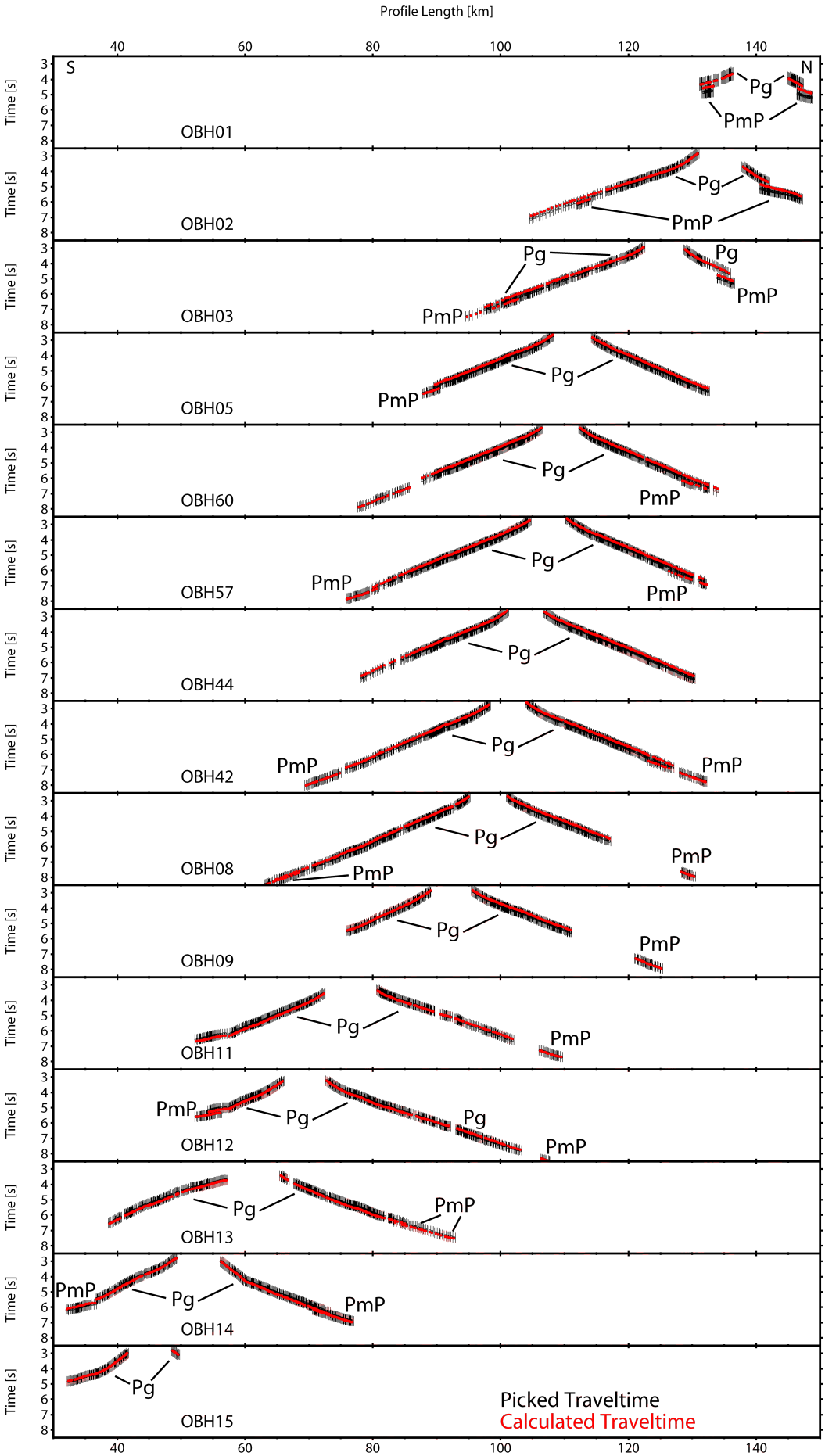

Figure A-2: Observed and calculated travel times of P-wave arrivals for P02.

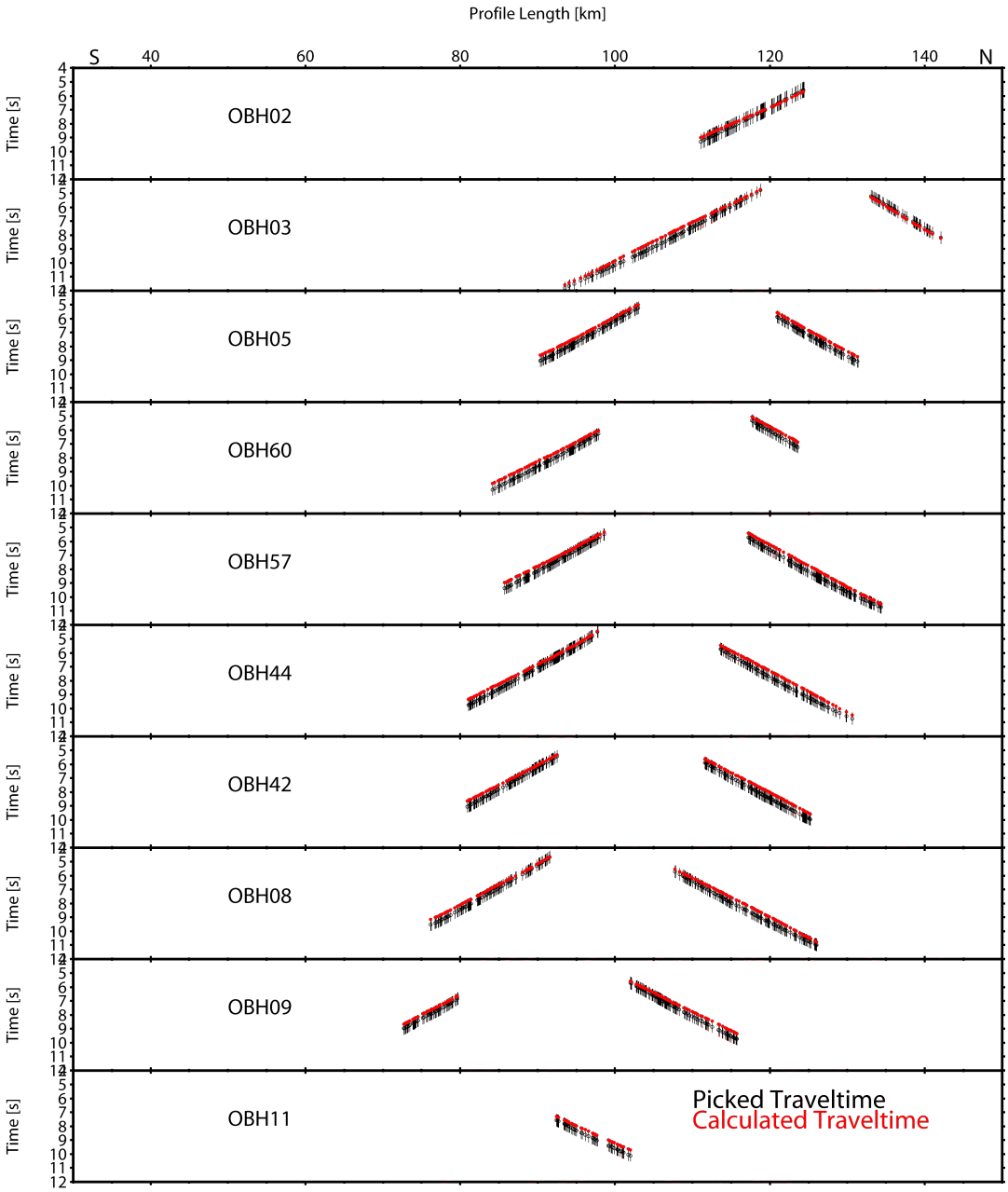

Figure A-3: Observed and calculated travel times of S-wave arrivals for P02.

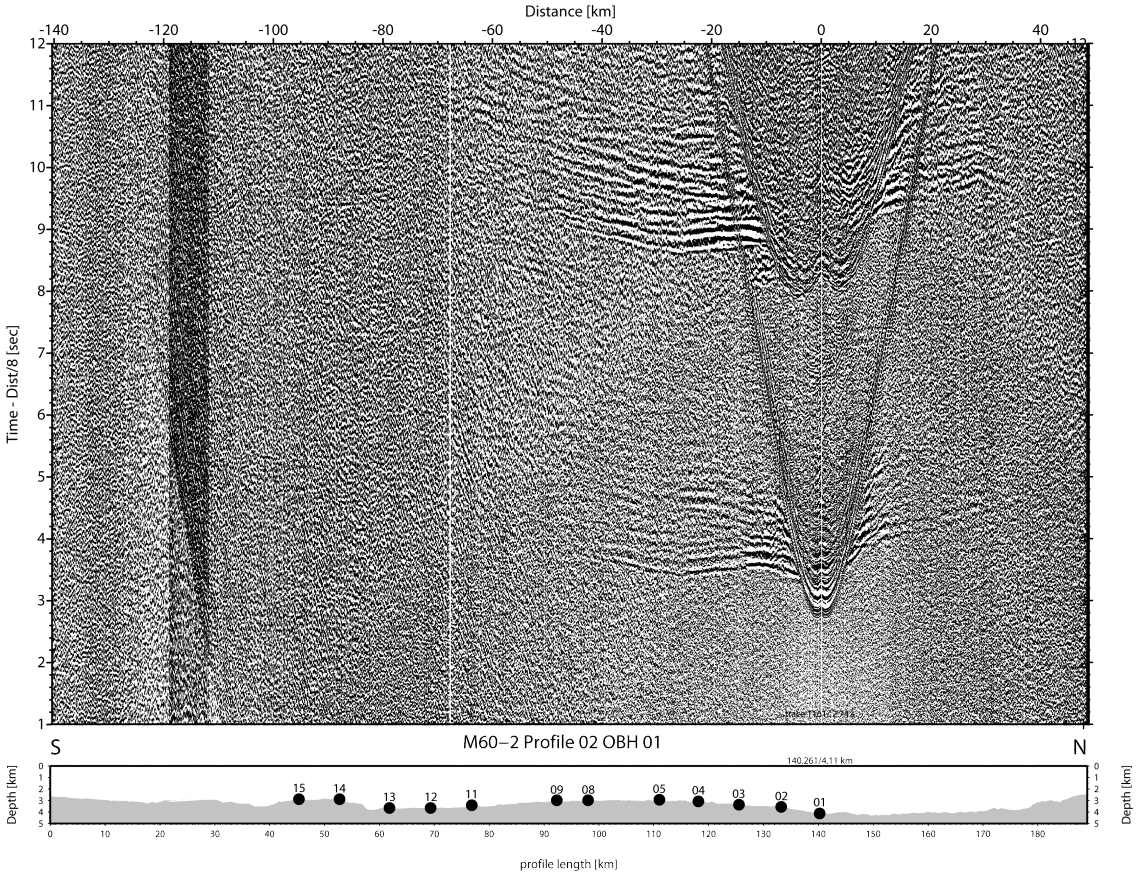

Figure A–4: Record section from OBH 01.

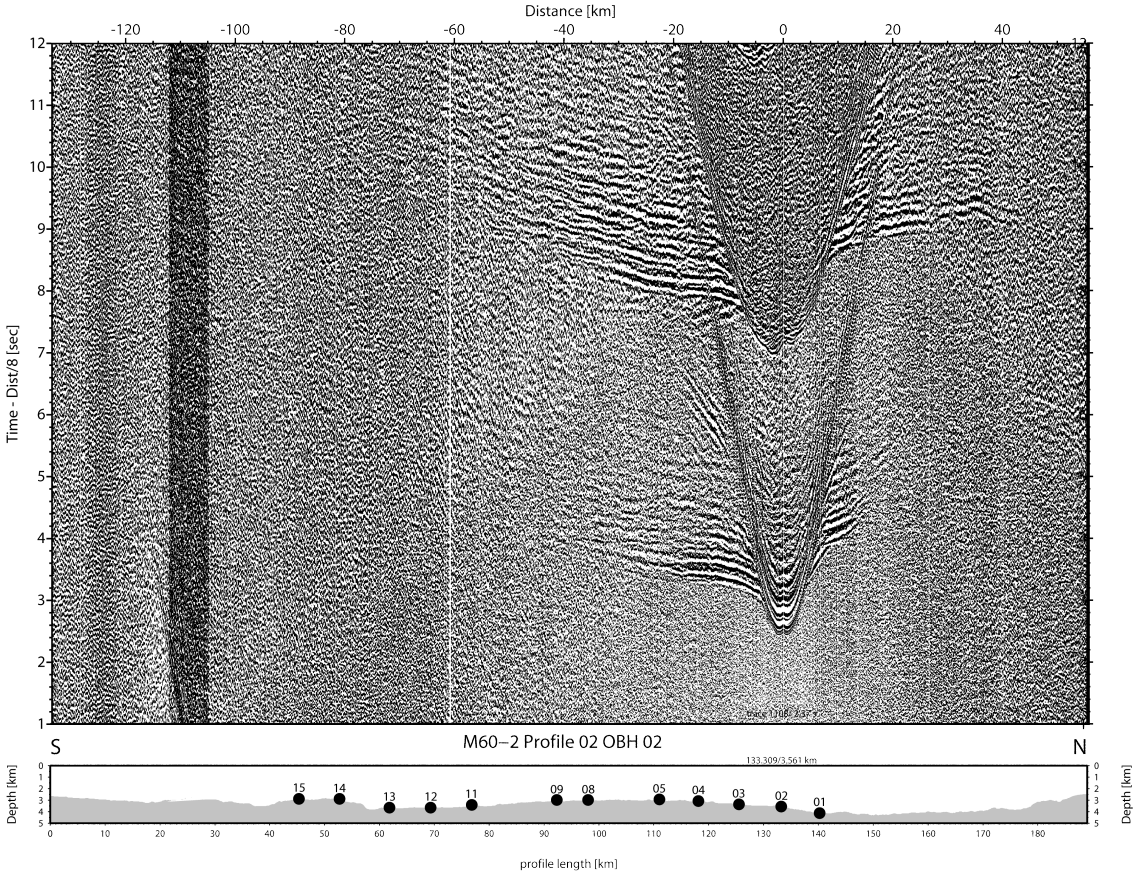

Figure A–5: Record section from OBH 02.

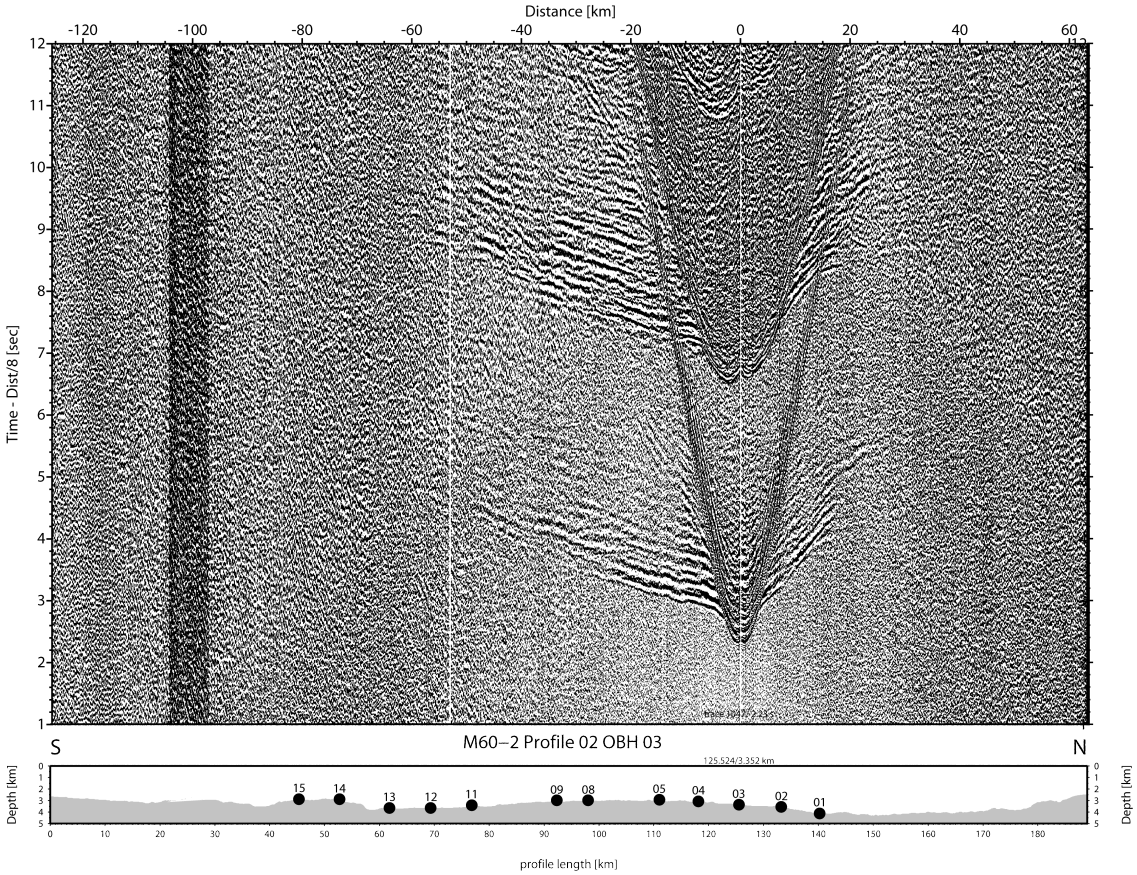

Figure A–6: Record section from OBH 03.

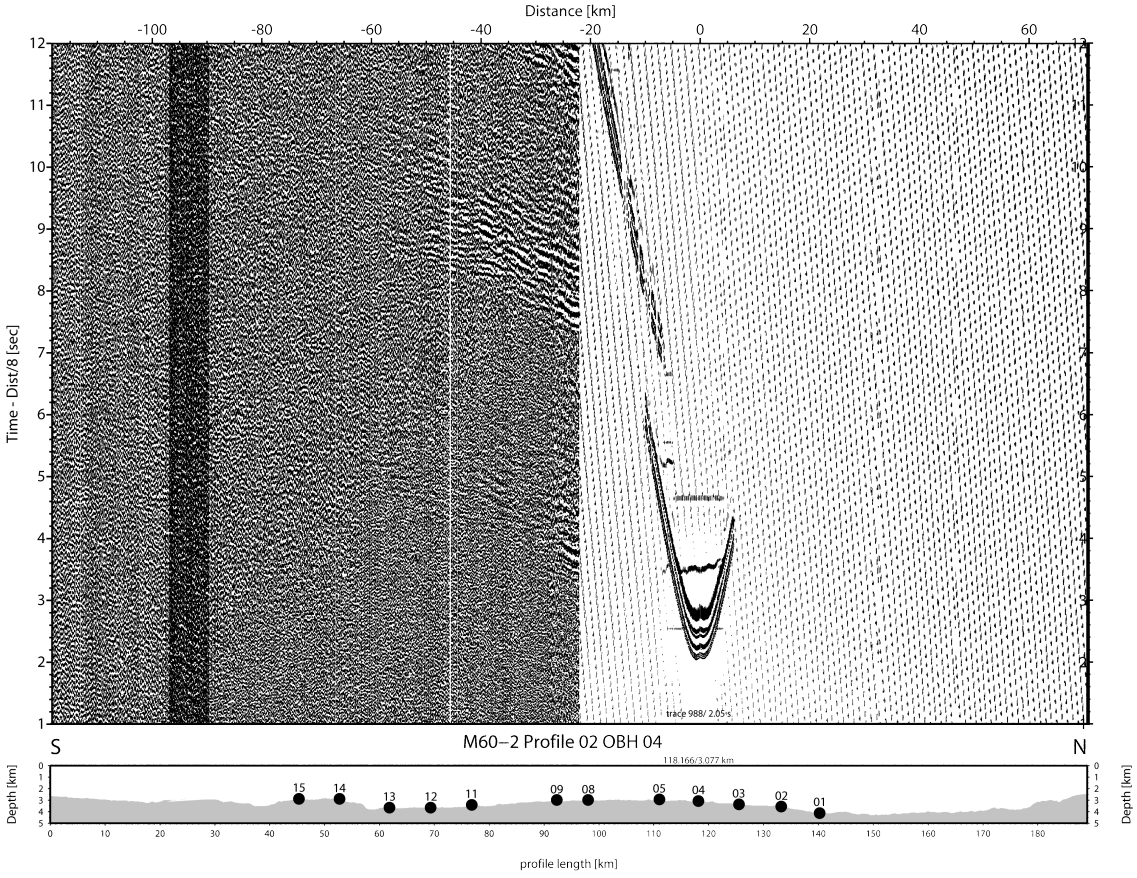

Figure A–7: Record section from OBH 04.

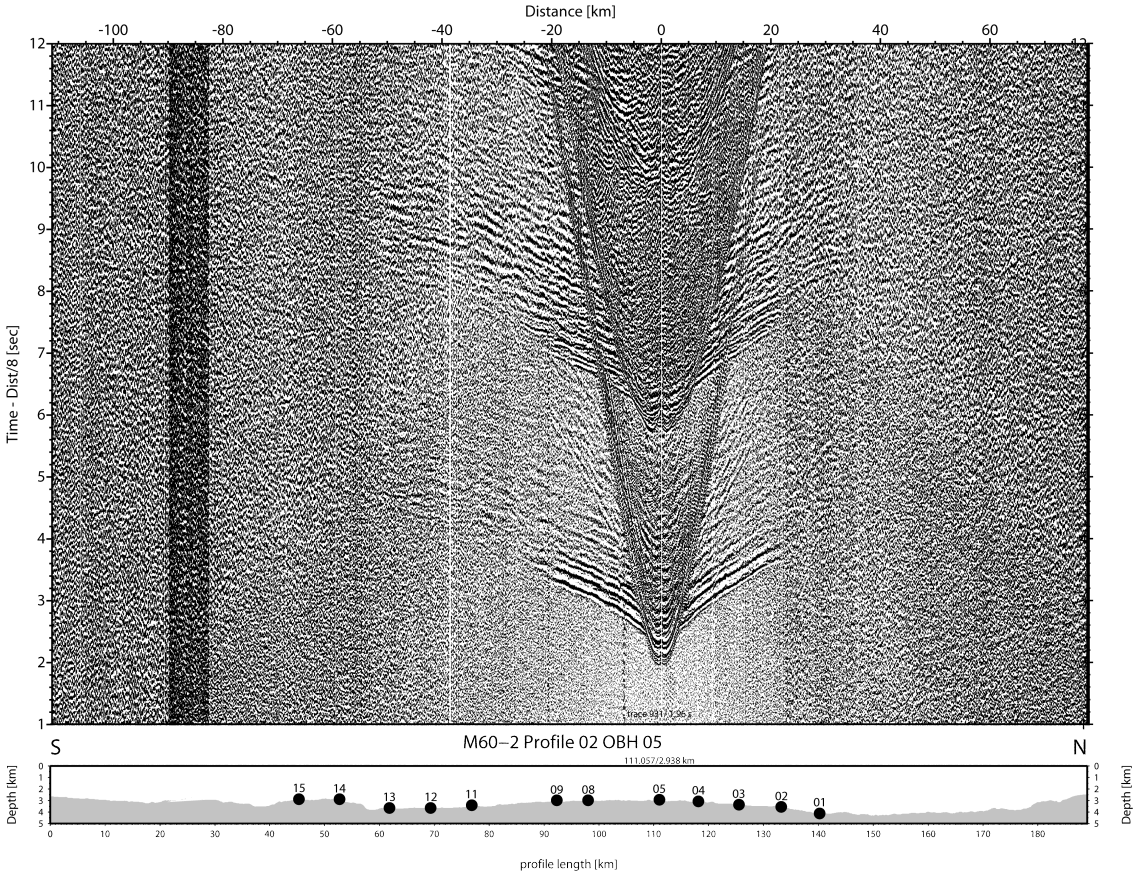

Figure A–8: Record section from OBH 05.

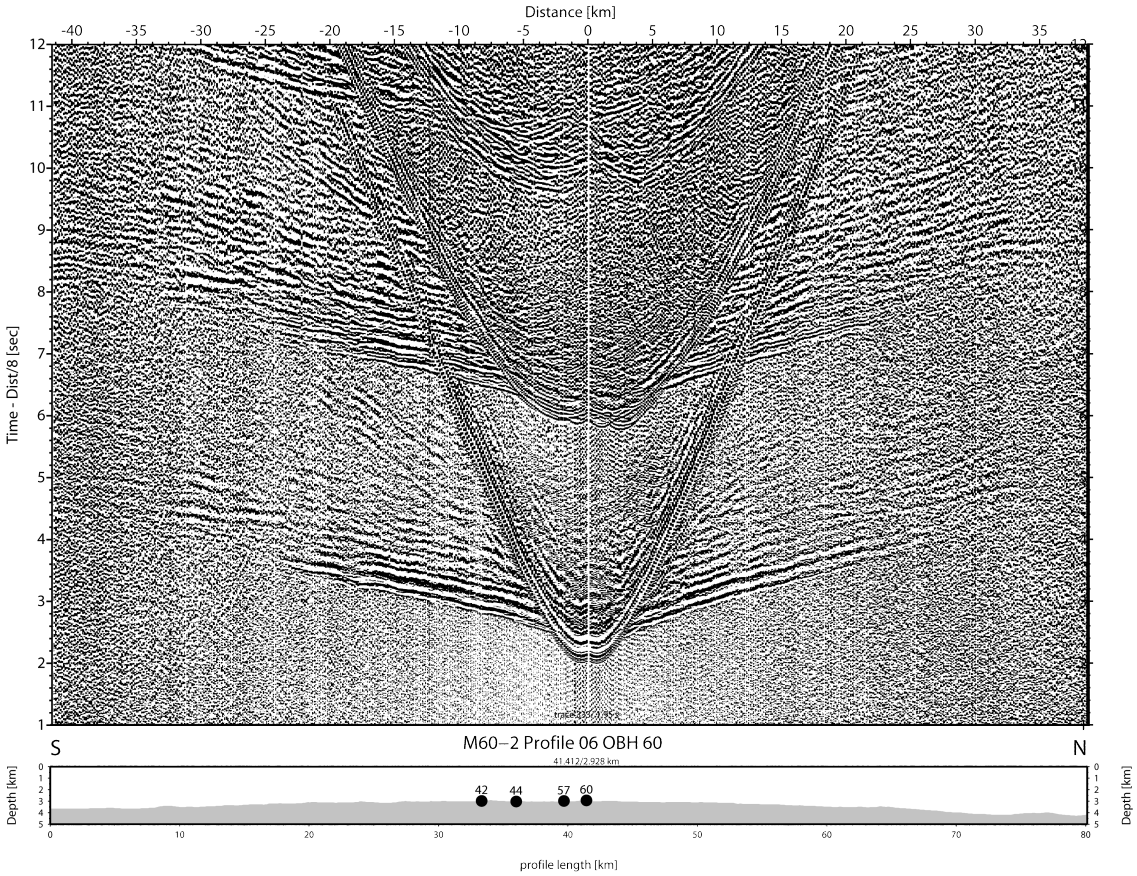

Figure A–9: Record section from OBH 60.

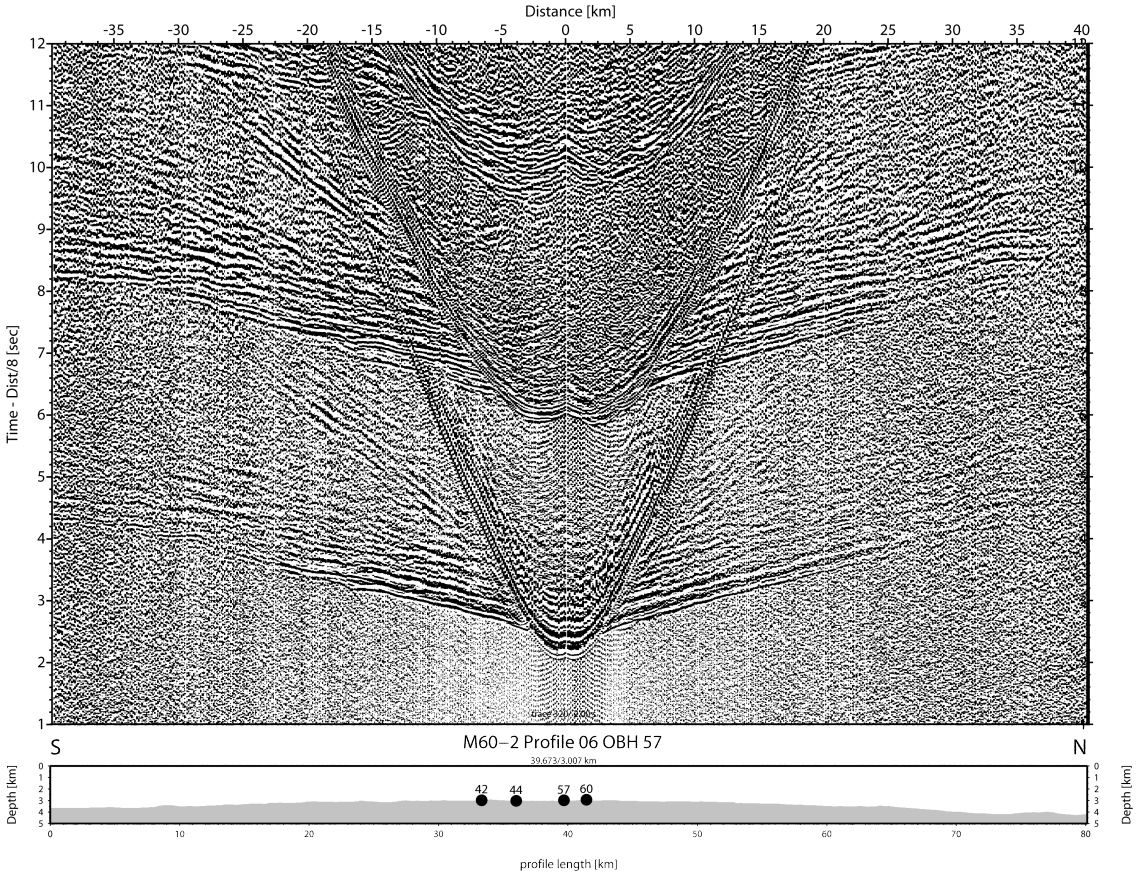

Figure A–10: Record section from OBH 57.

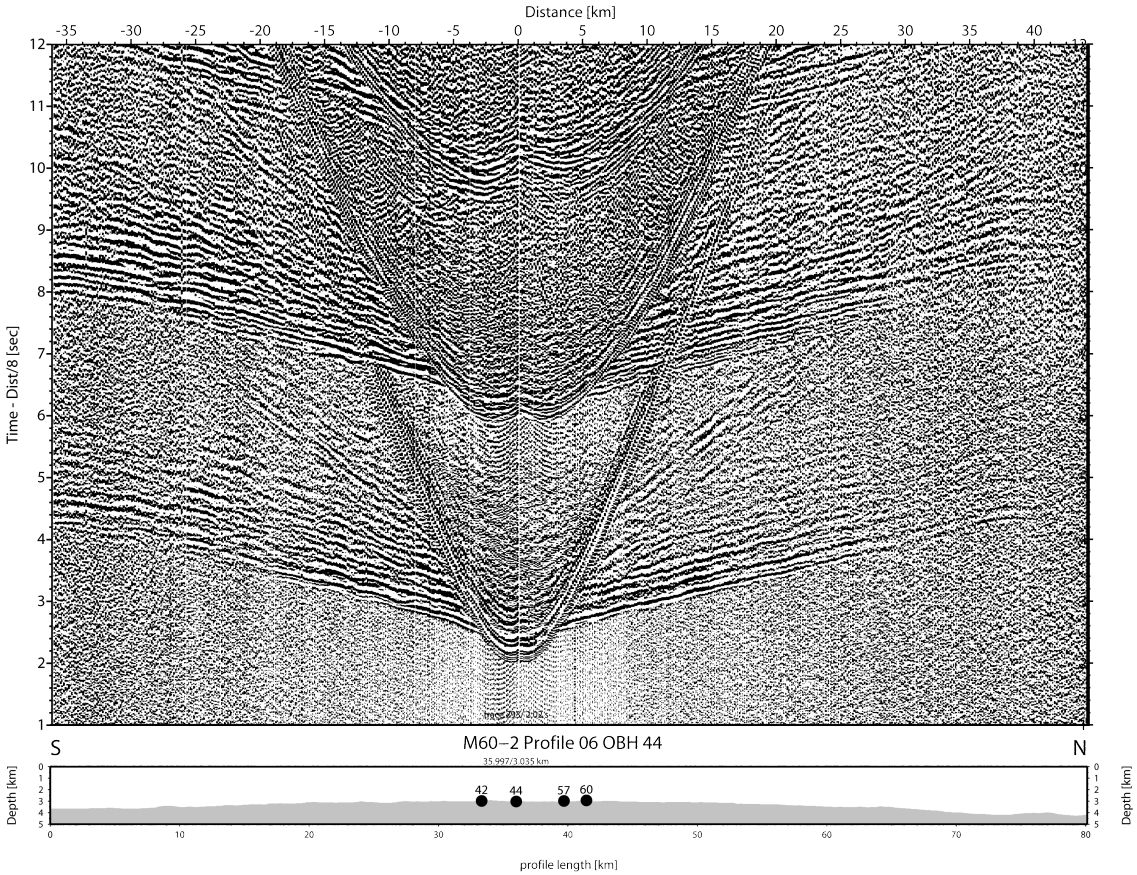

Figure A–11: Record section from OBH 44.

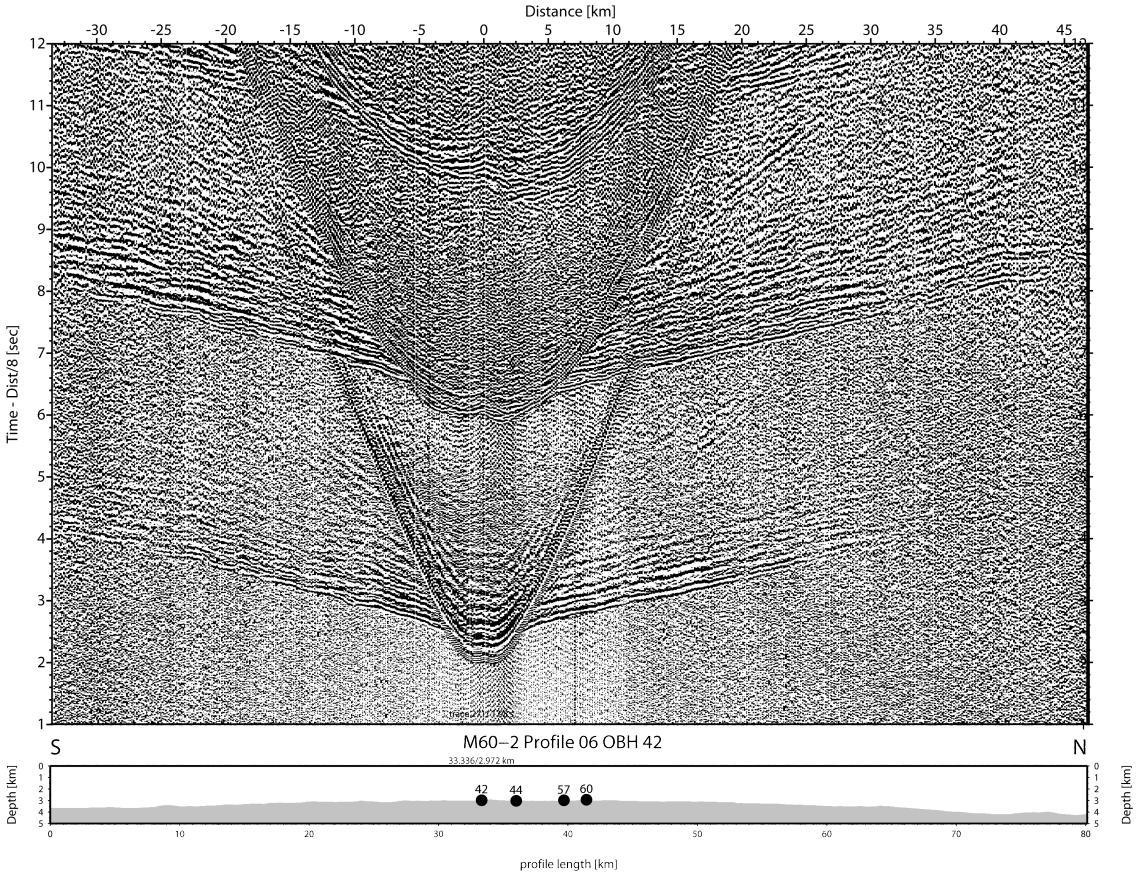

Figure A–12: Record section from OBH 42.

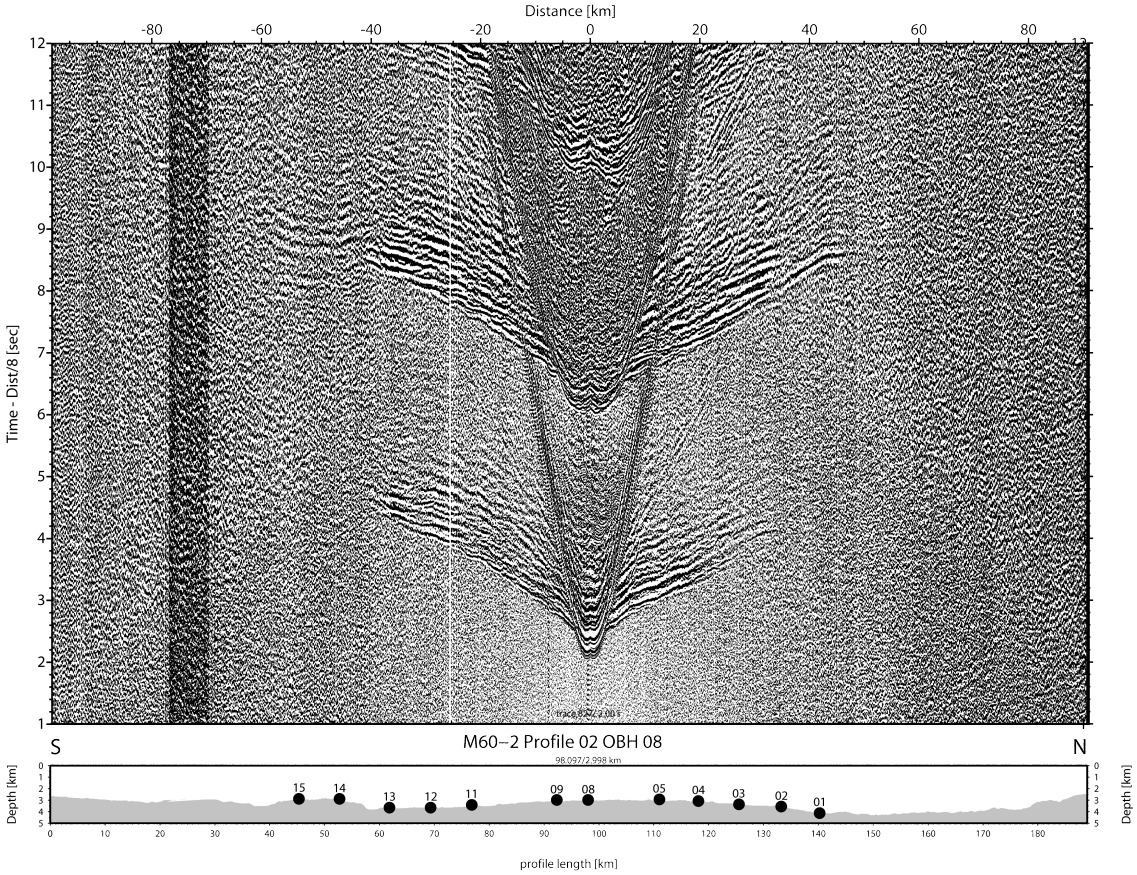

Figure A–13: Record section from OBH 08.

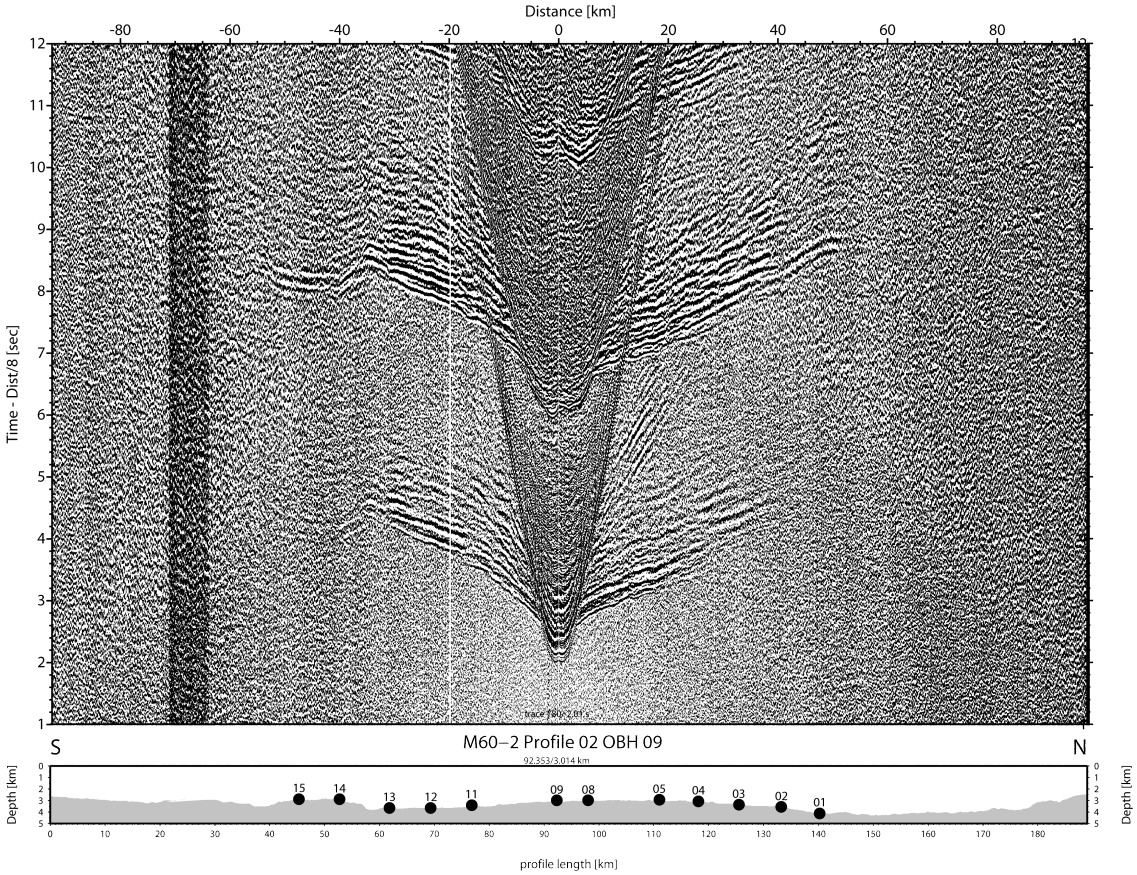

Figure A–14: Record section from OBH 09.

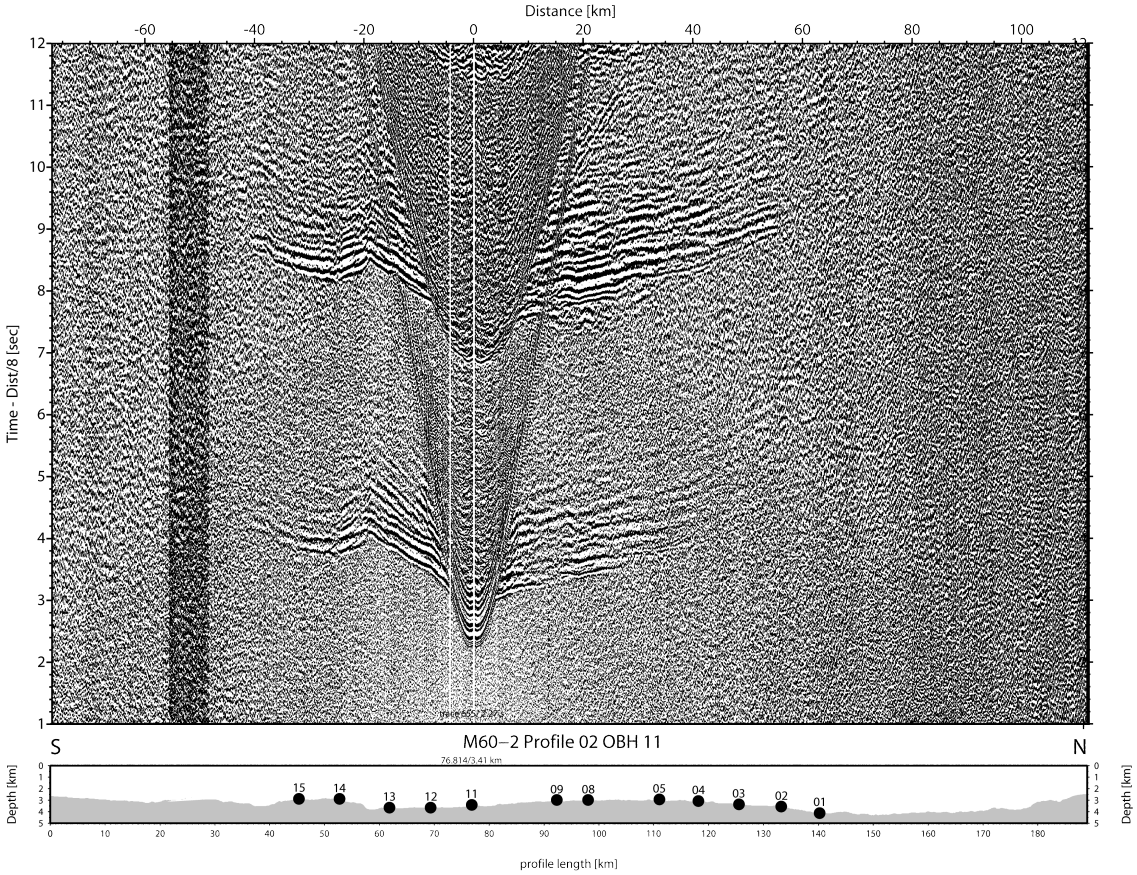

Figure A–15: Record section from OBH 11.

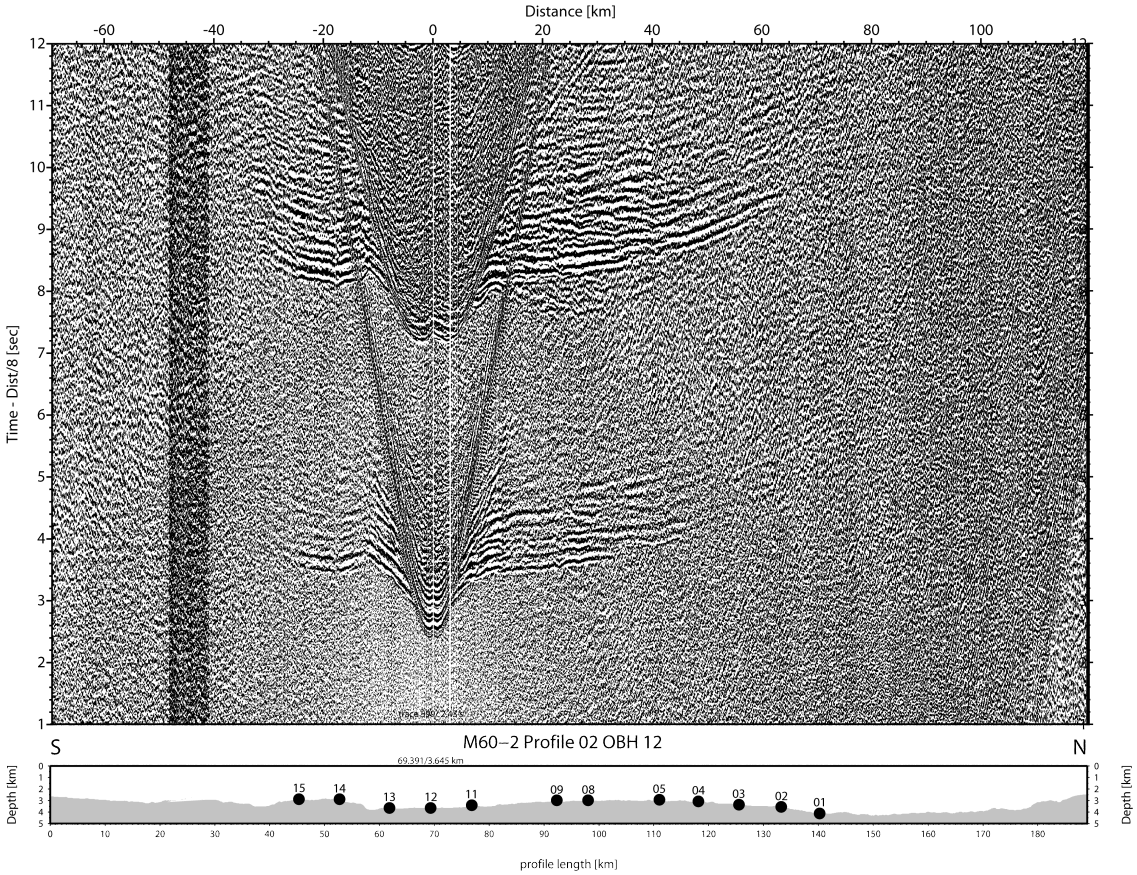

Figure A–16: Record section from OBH 12.

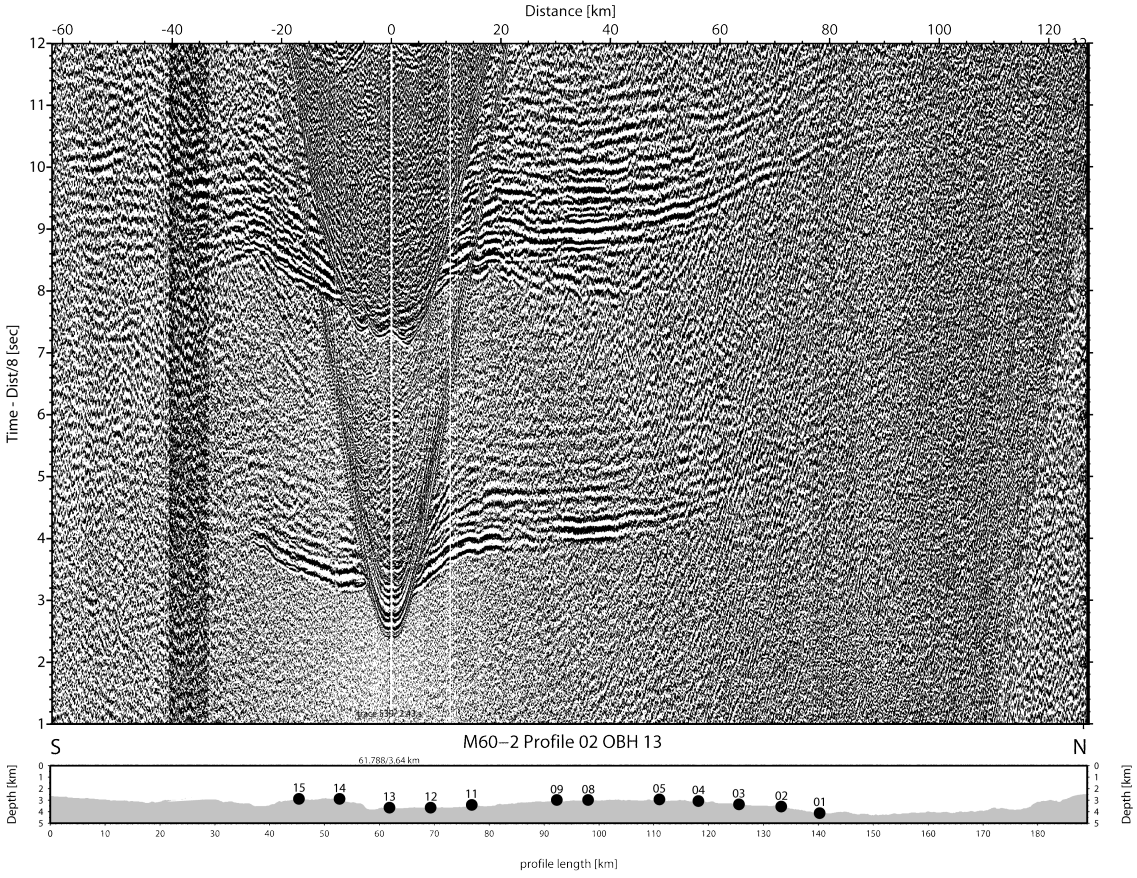

Figure A–17: Record section from OBH 13.

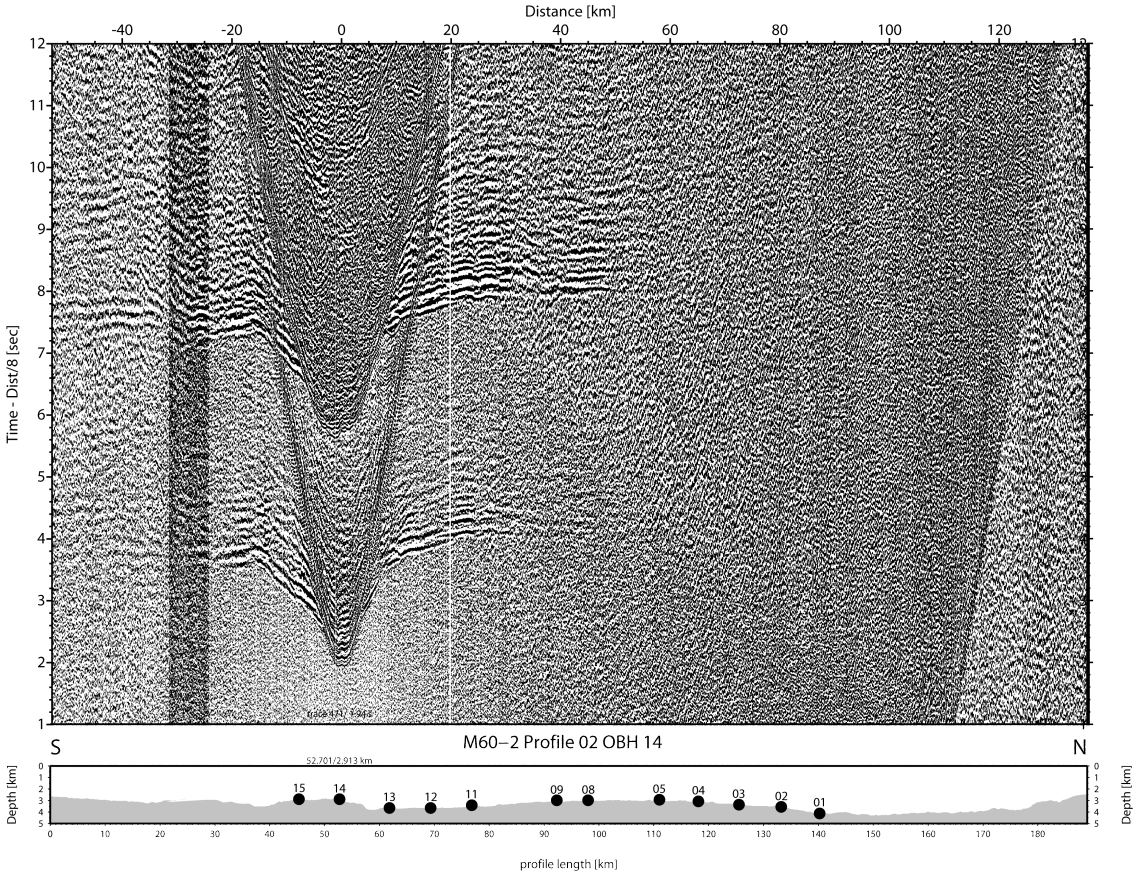

Figure A–18: Record section from OBH 14.

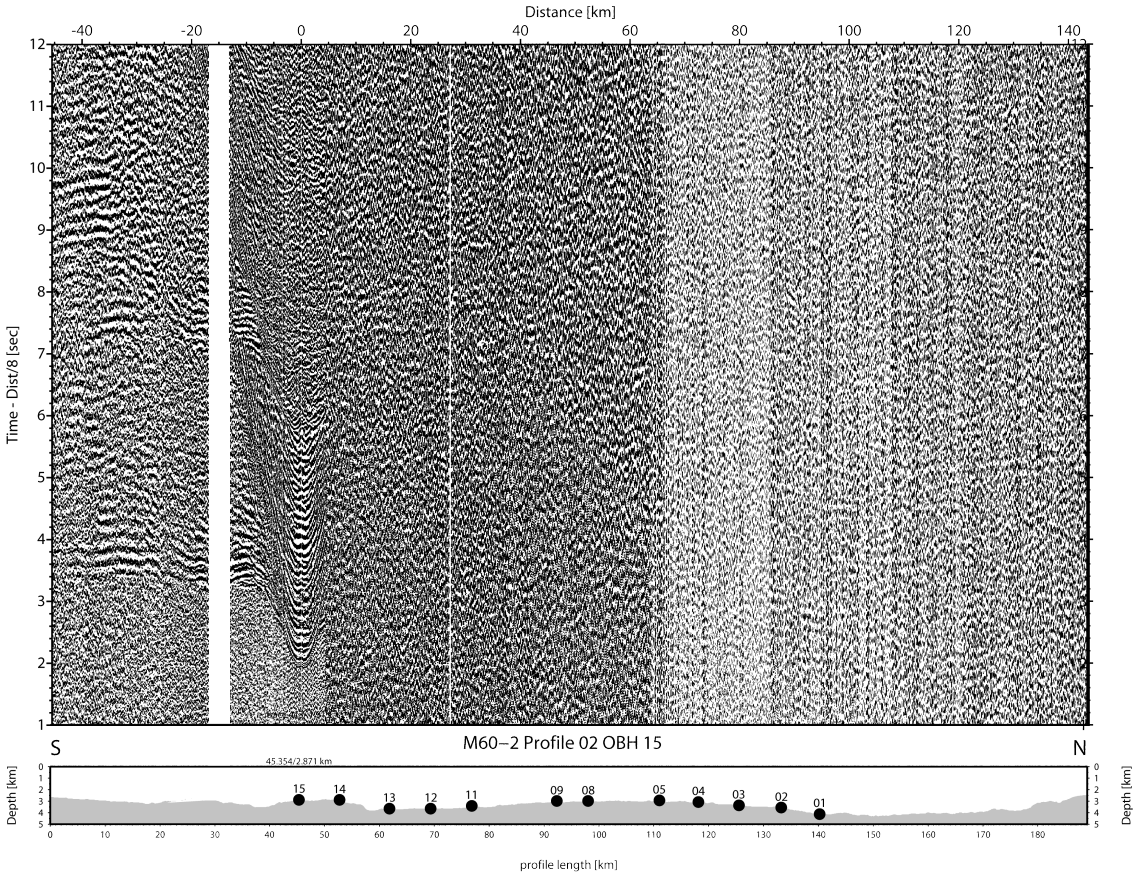

Figure A–19: Record section from OBH 15.

B – Profile 04

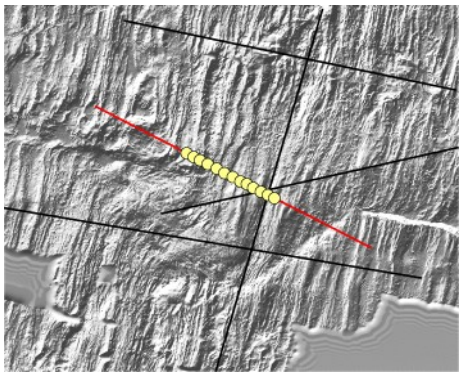

Figure B-1: Location map of profile 04 with stations.

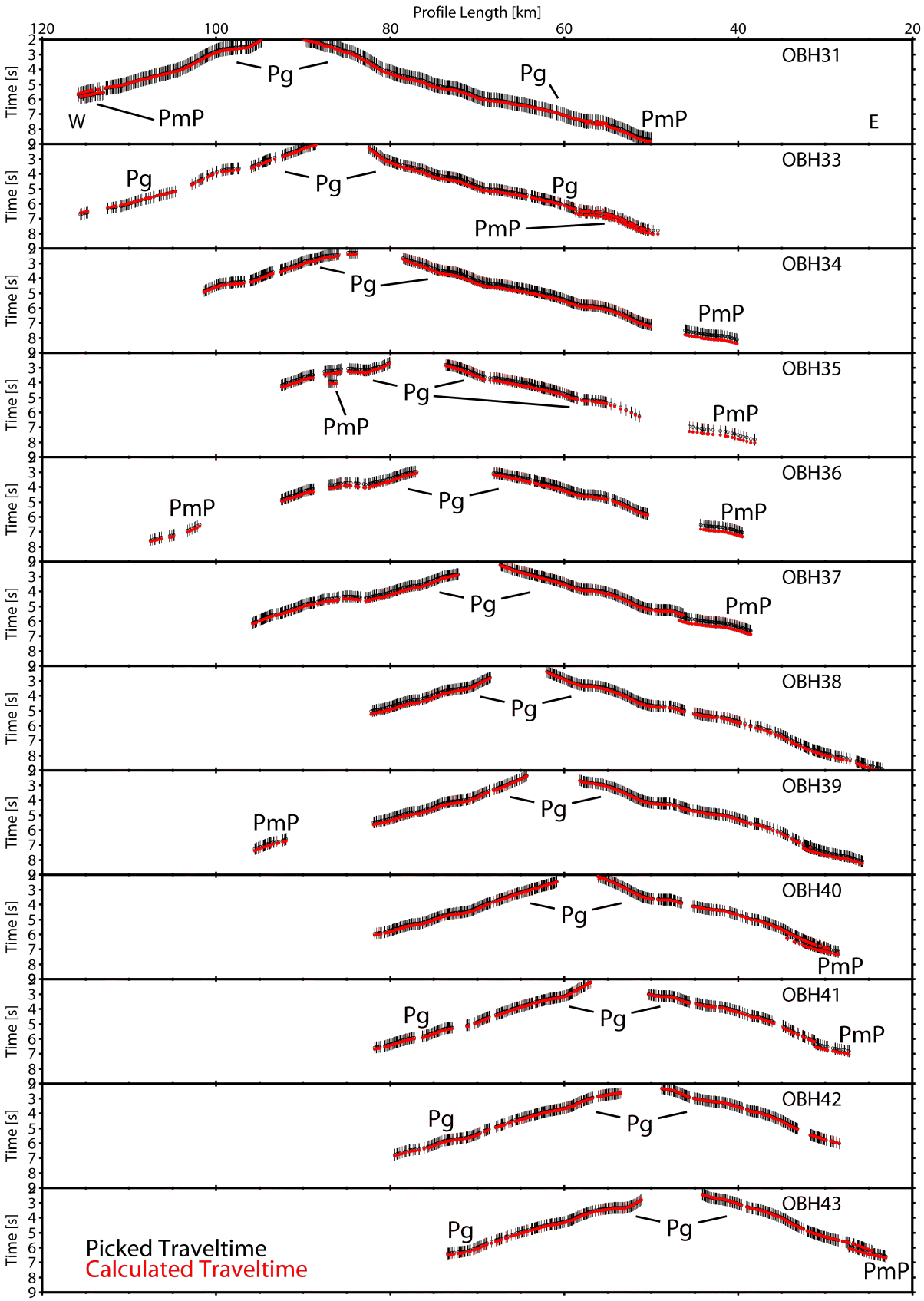

Figure B-2: Observed and calculated travel times for P-wave arrivals of P04.

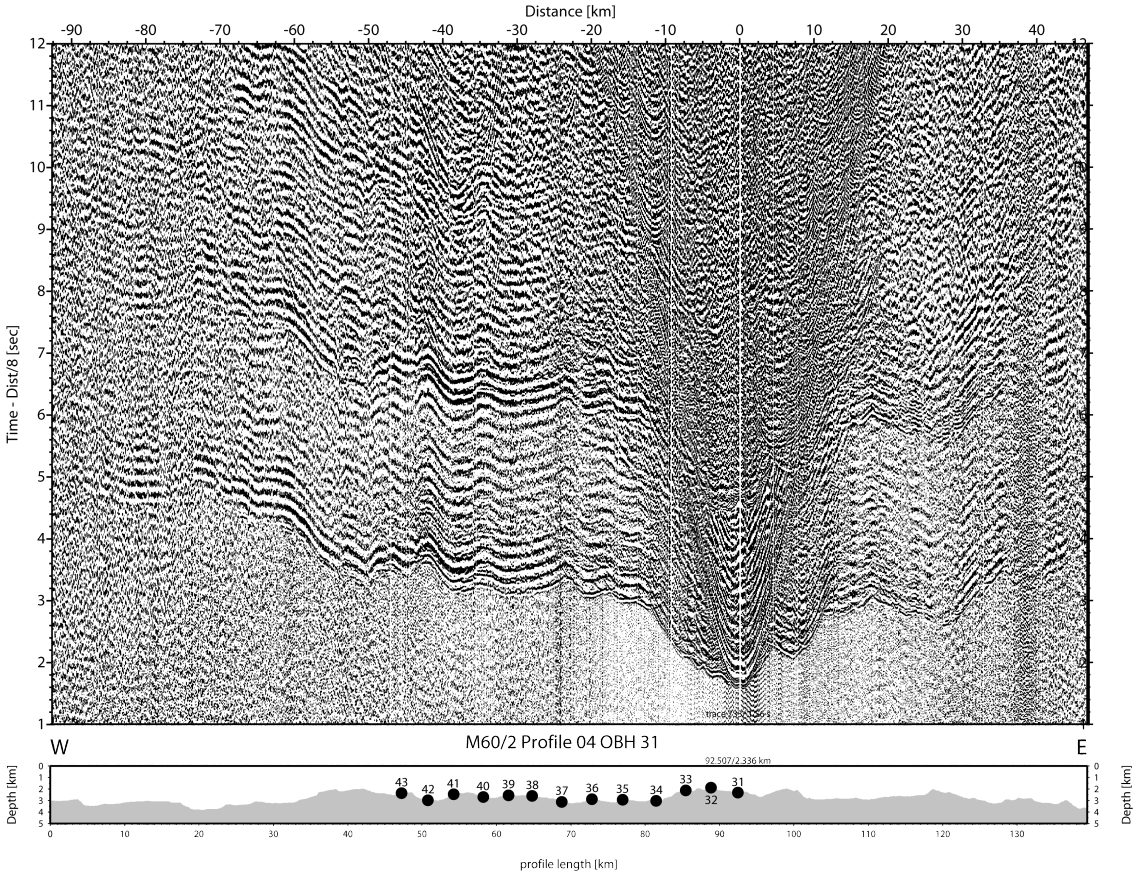

Figure B–3: Record section from OBH 31.

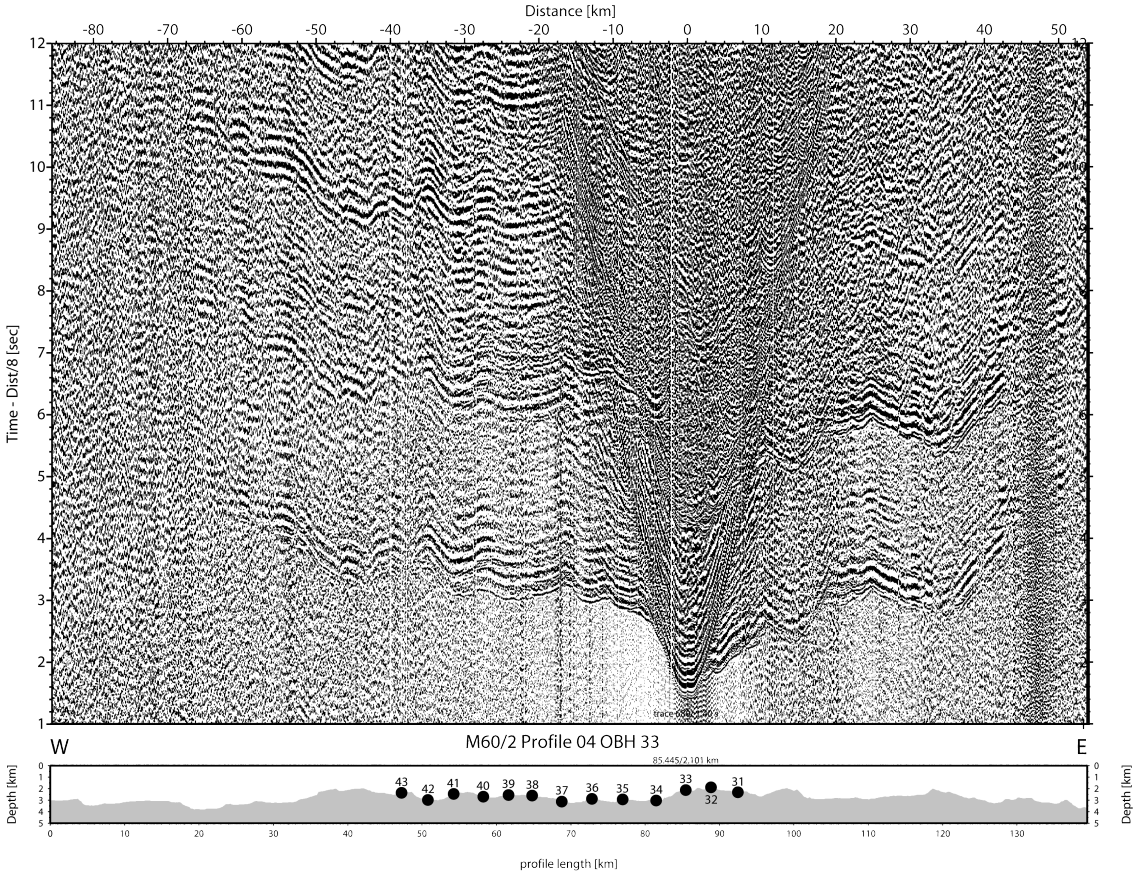

Figure B–4: Record section from OBH 33.

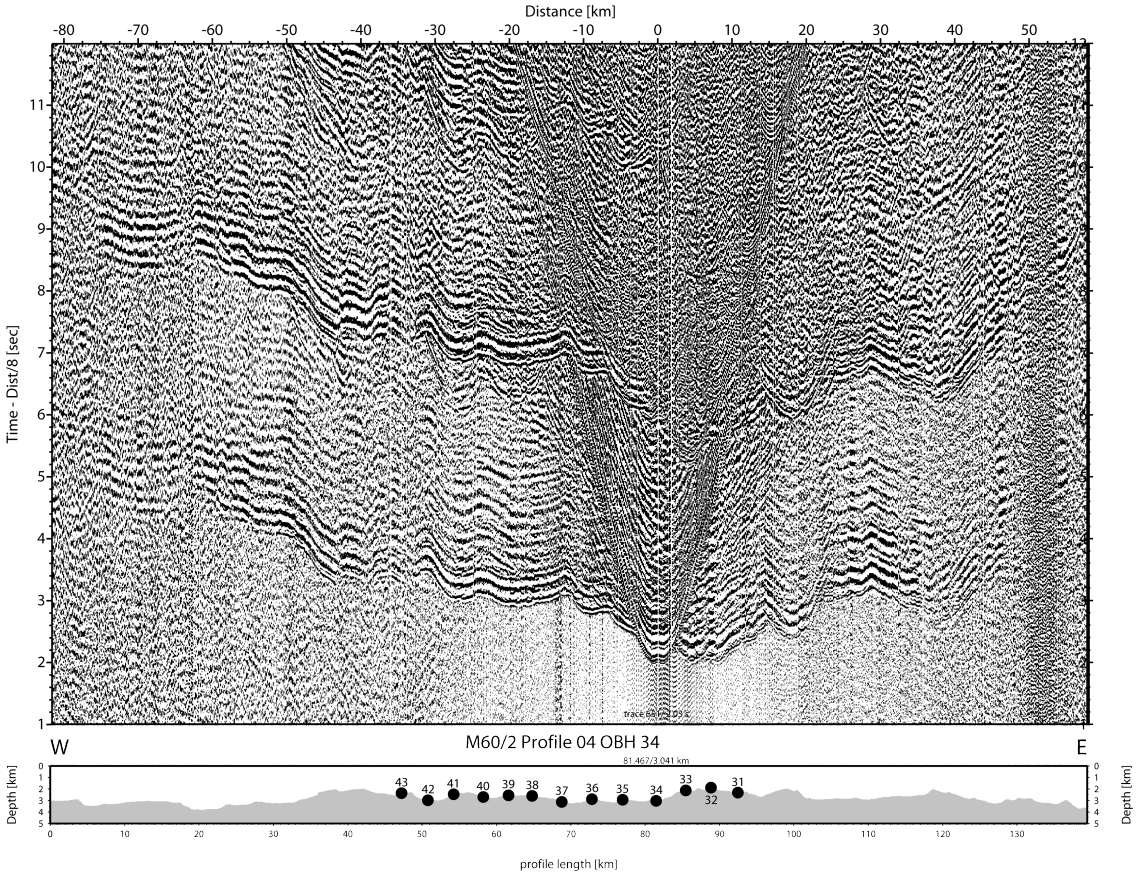

Figure B–5: Record section from OBH 34.

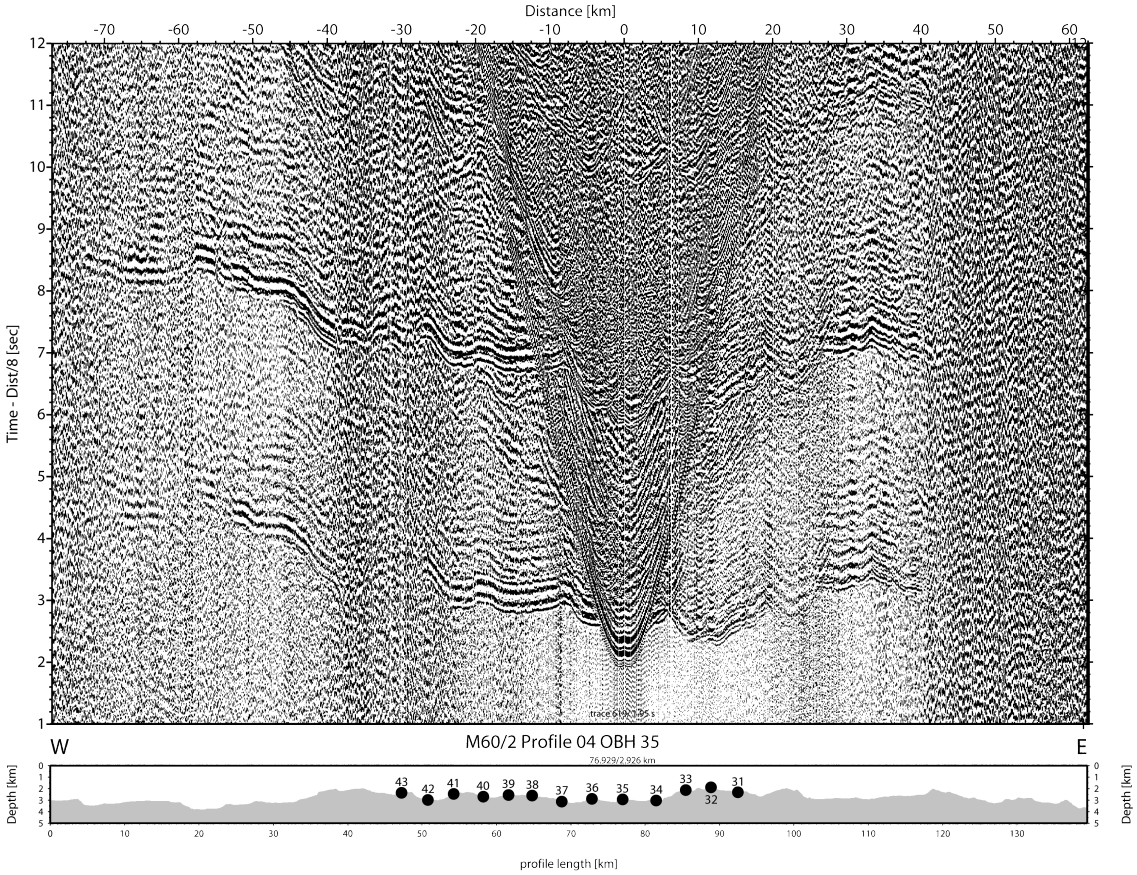

Figure B–6: Record section from OBH 35.

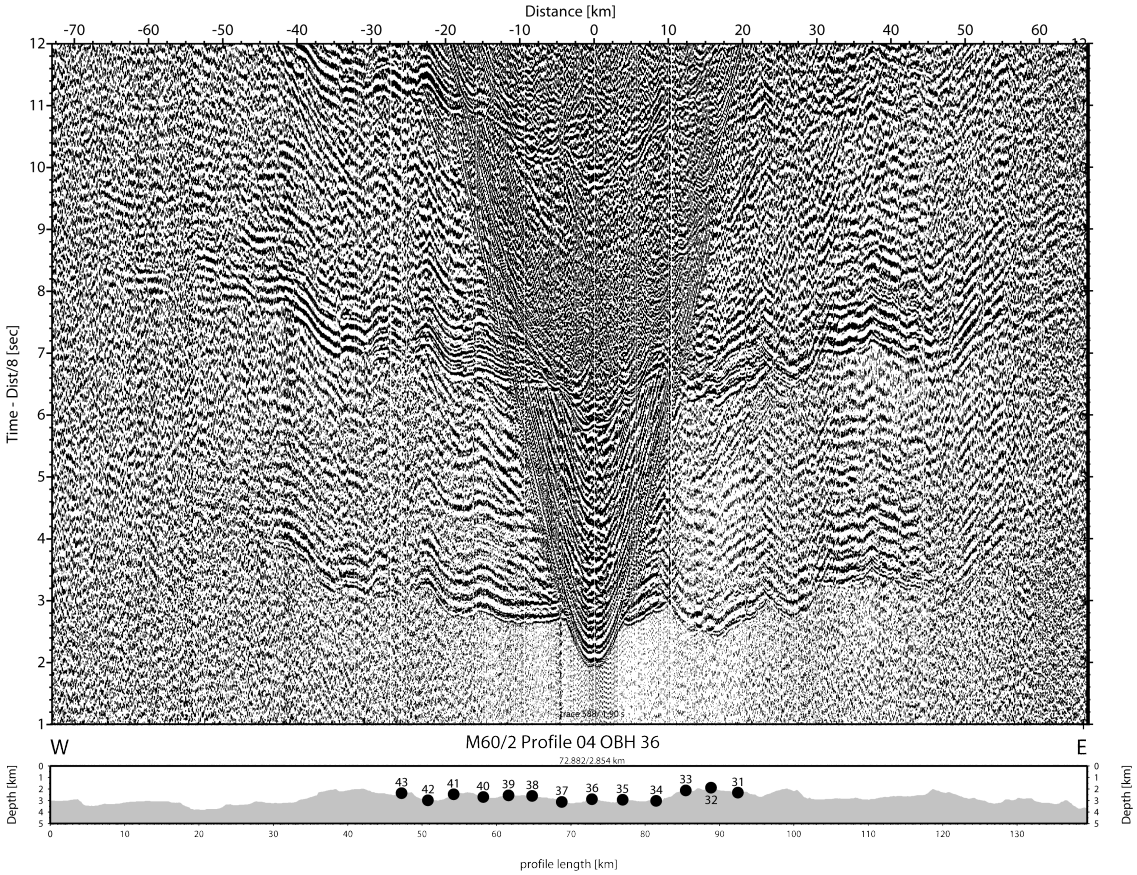

Figure B–7: Record section from OBH 36.

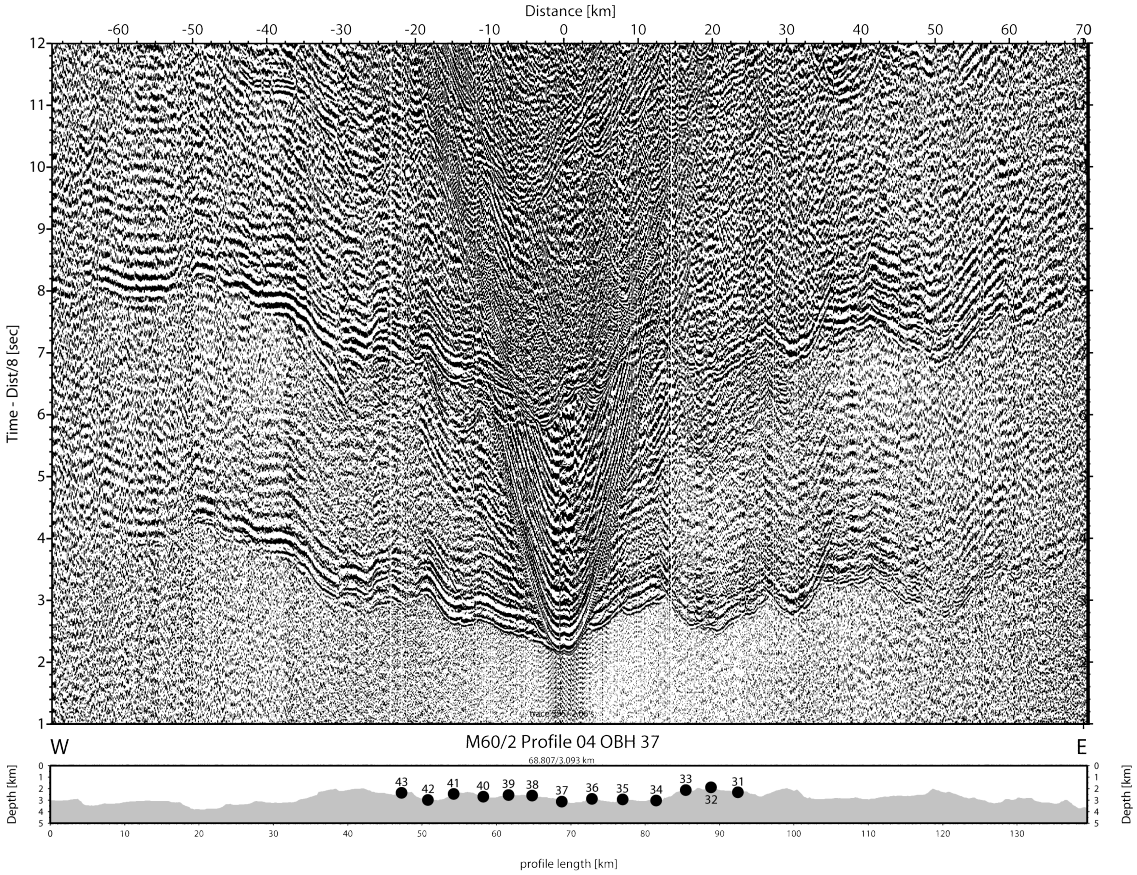

Figure B–8: Record section from OBH 37.

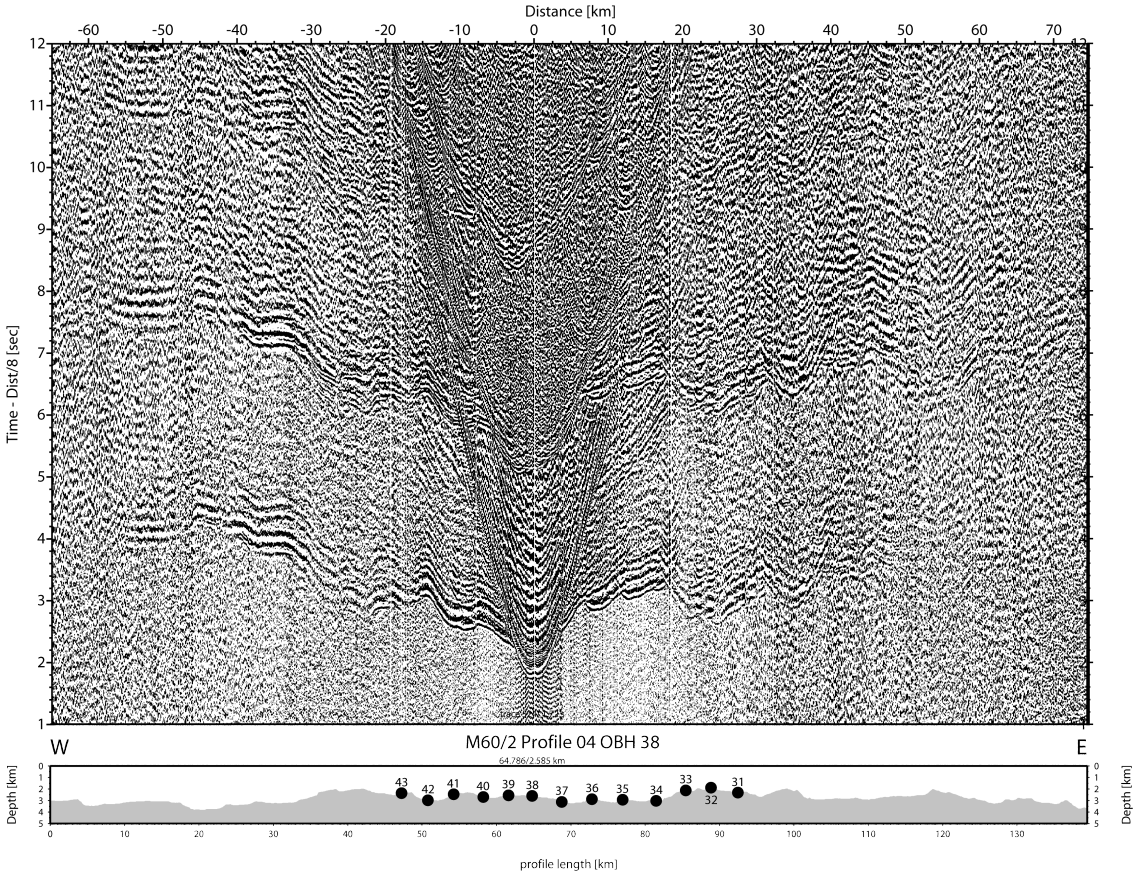

Figure B–9: Record section from OBH 38.

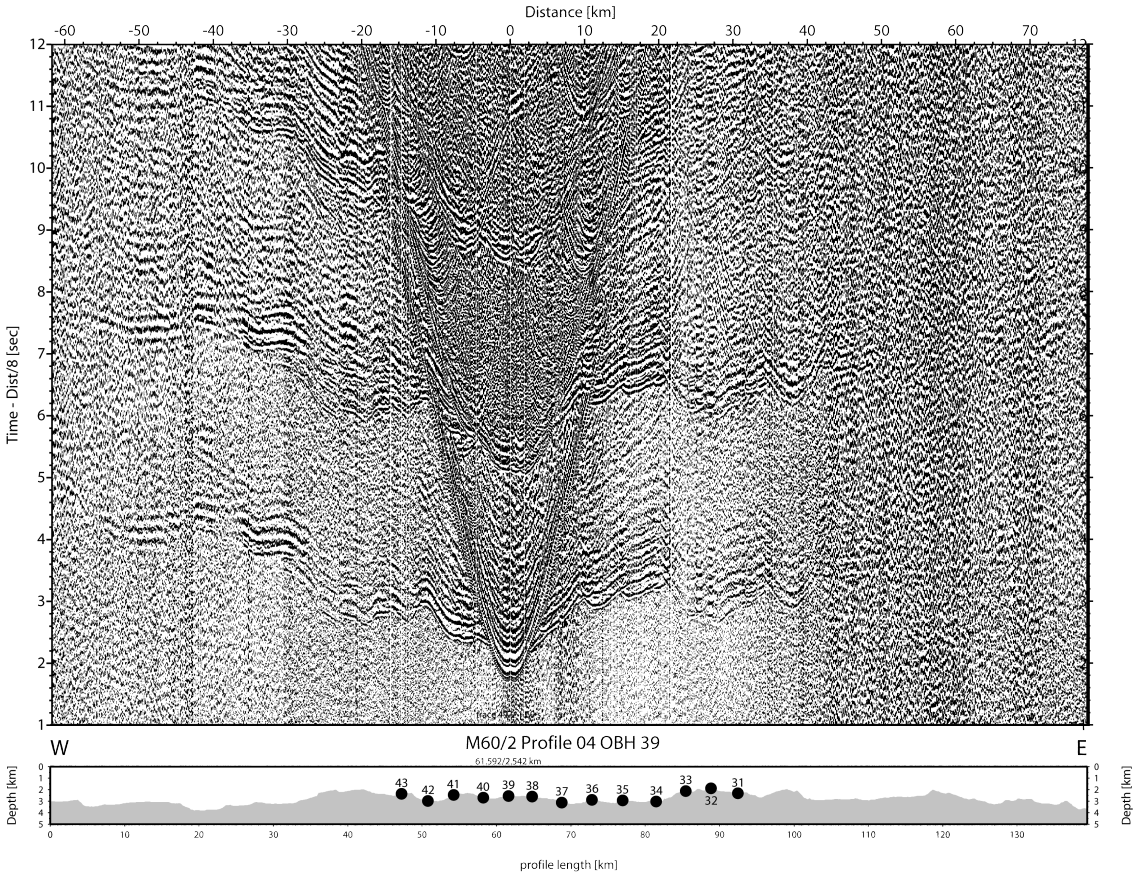

Figure B–10: Record section from OBH 39.

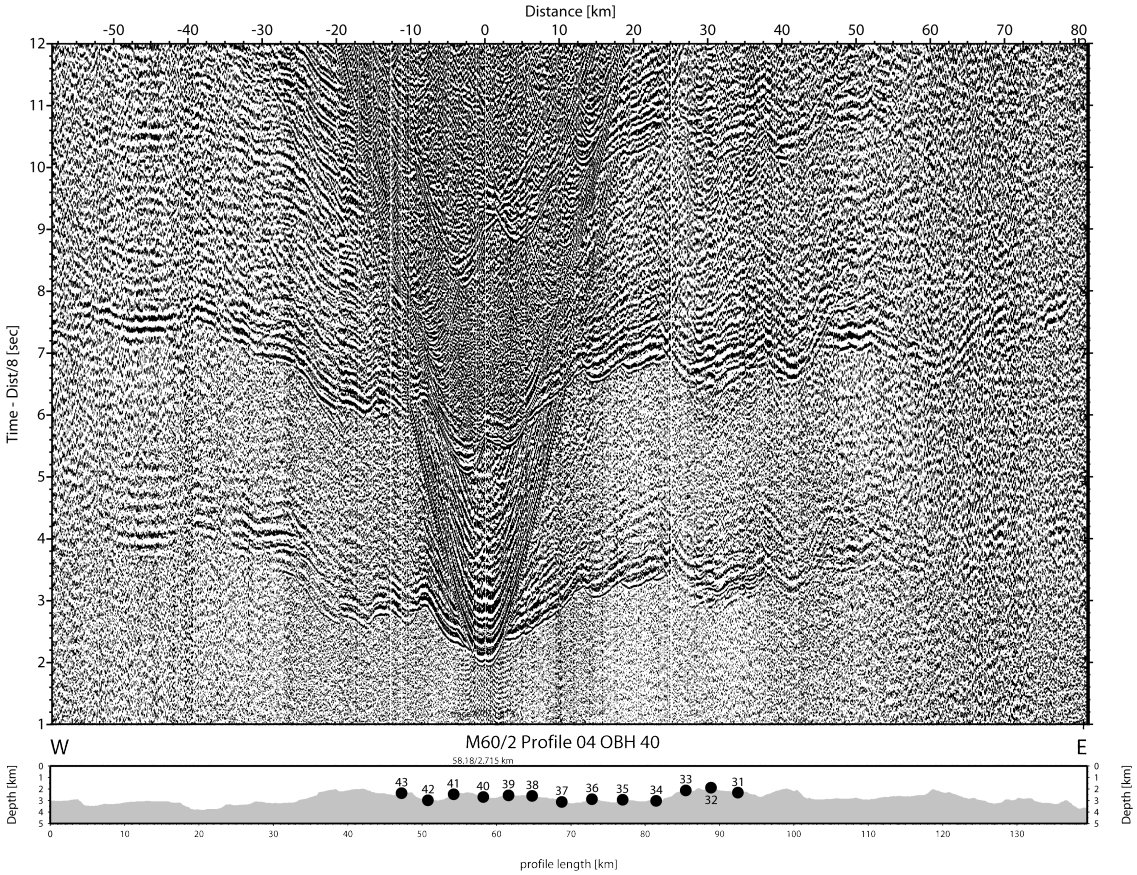

Figure B–11: Record section from OBH 40.

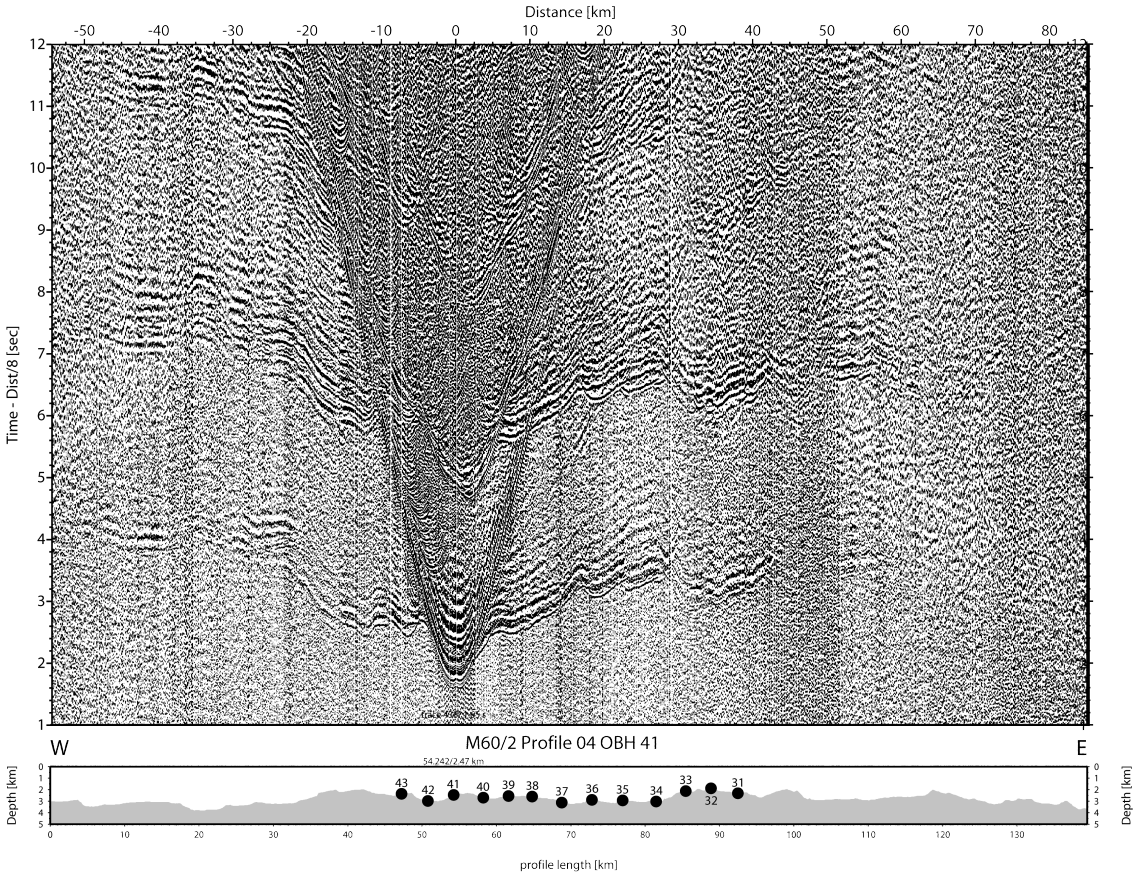

Figure B–12: Record section from OBH 41.

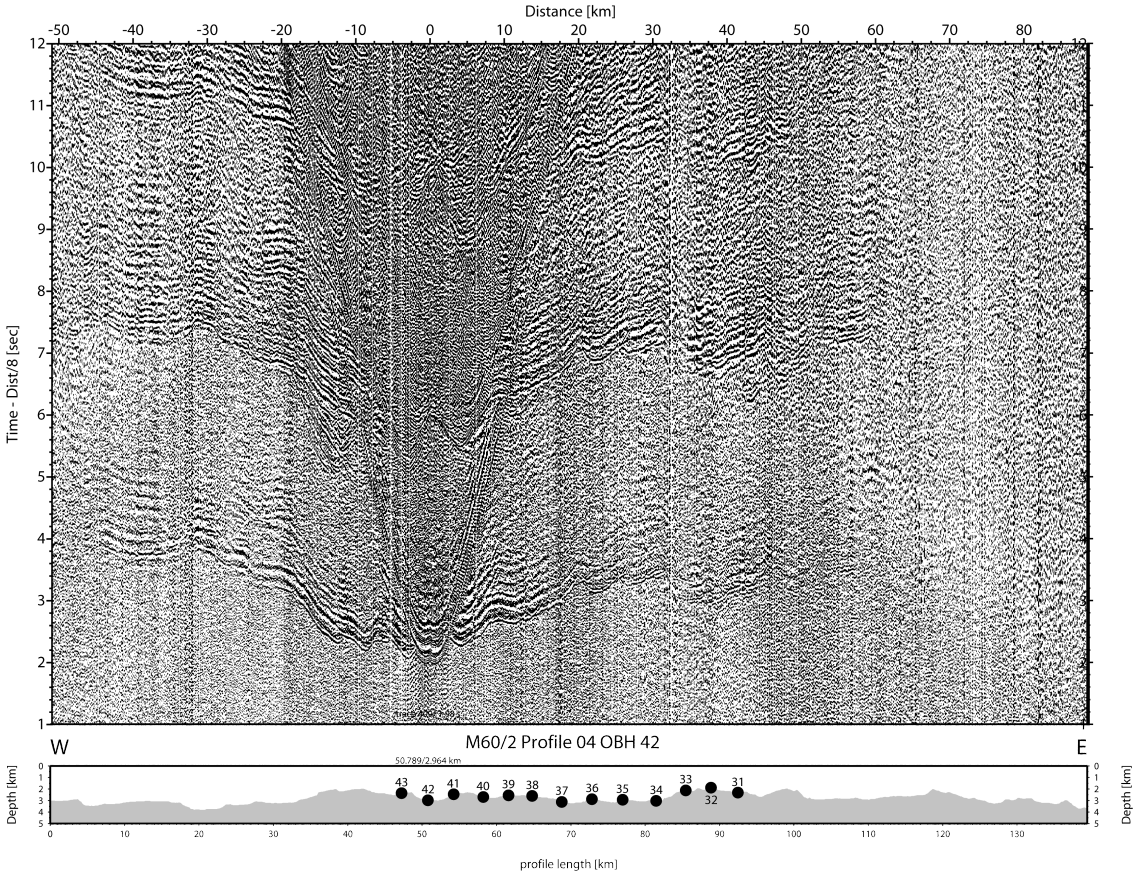

Figure B–13: Record section from OBH 42.

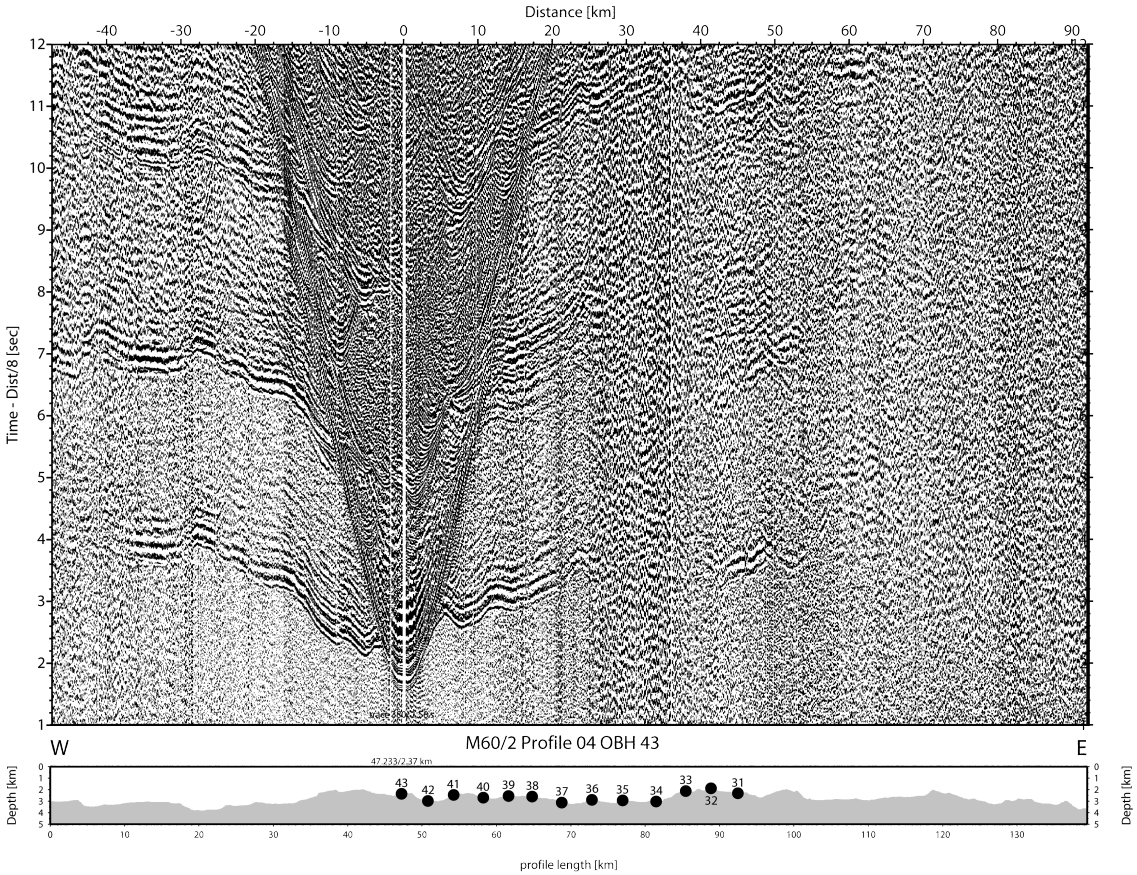

Figure B–14: Record section from OBH 43.

C – Profile 05

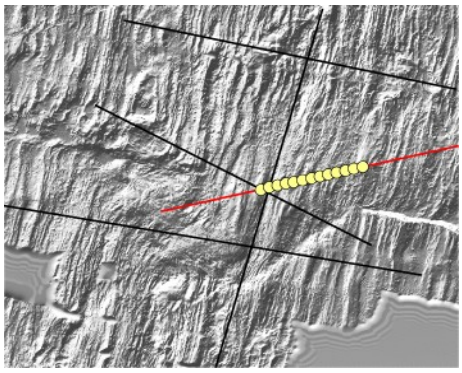

Figure C-1: Location map for profile 05 with instruments.

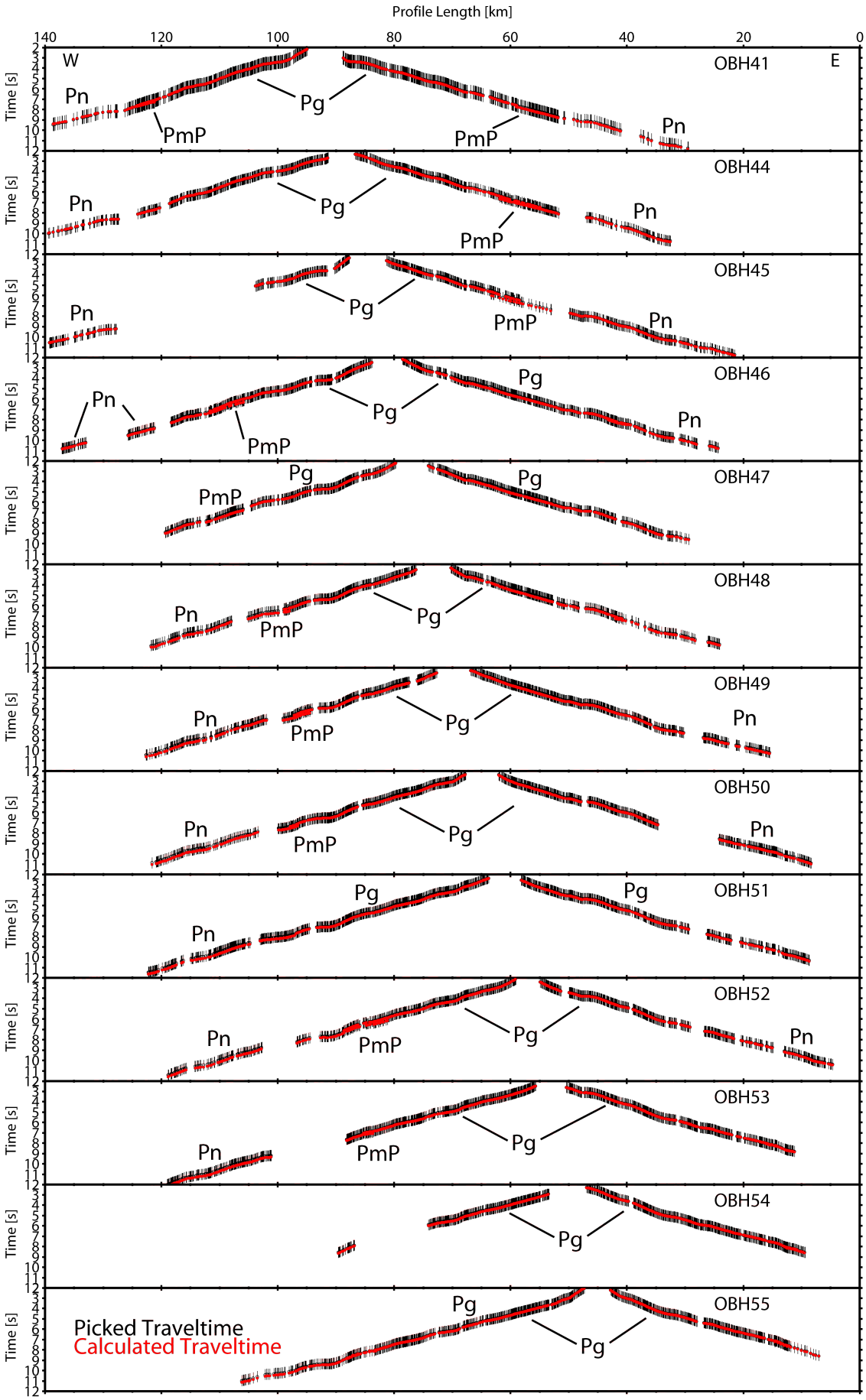

Figure C-2: Observed and calculated travel times for P-wave arrivals of P05.

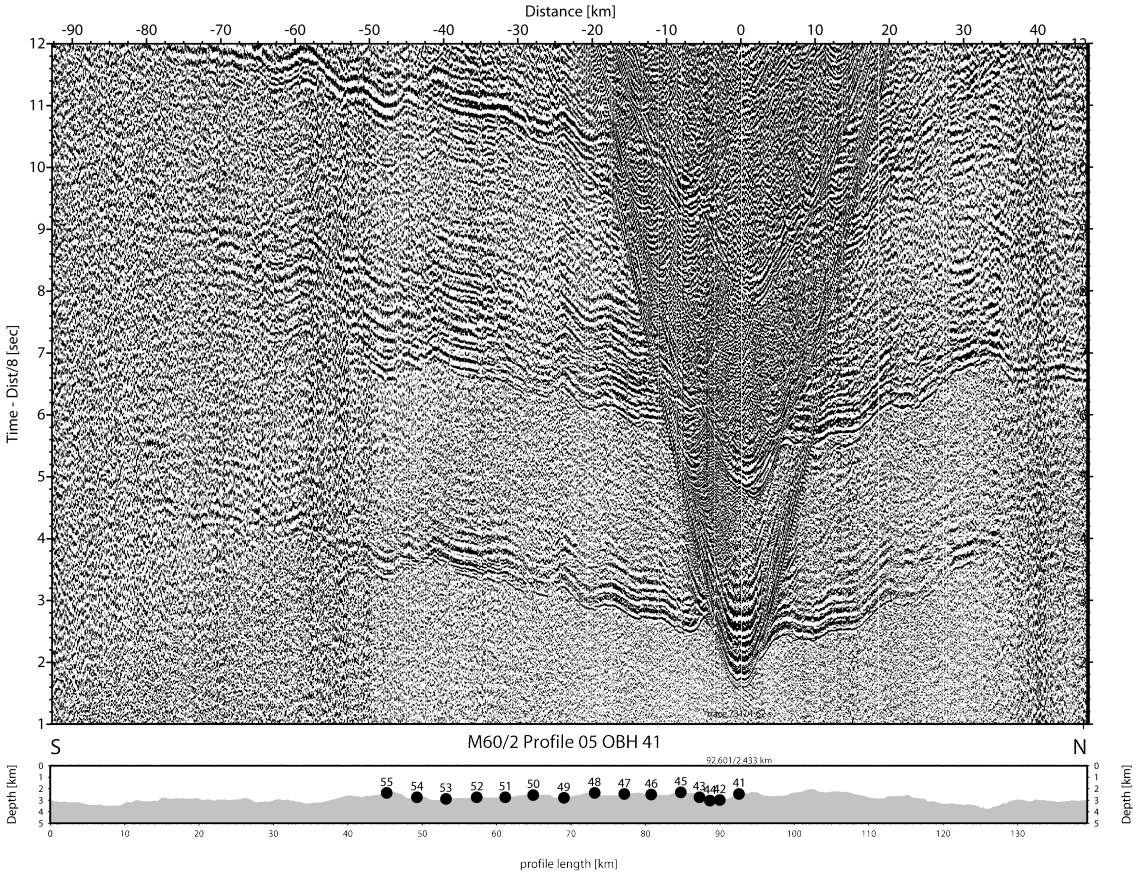

Figure C–3: Record section from OBH 41.

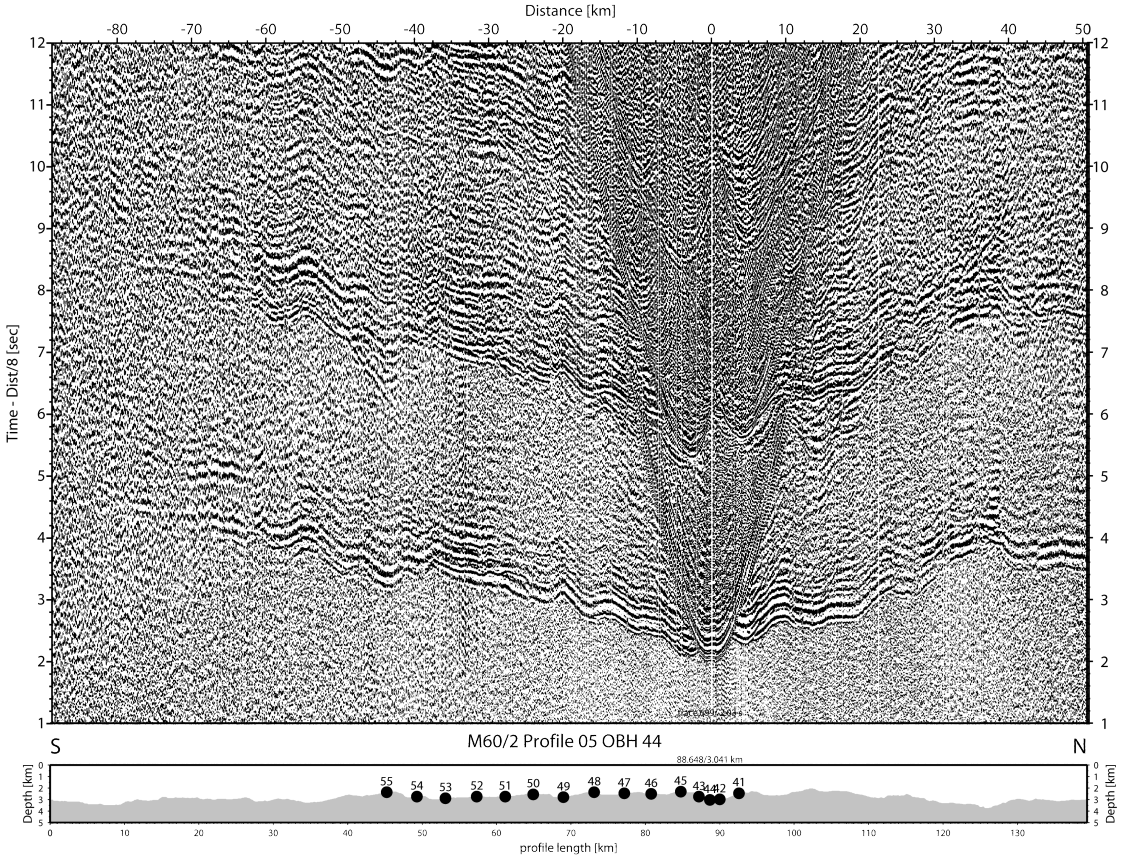

Figure C-4: Record section from OBH 44.

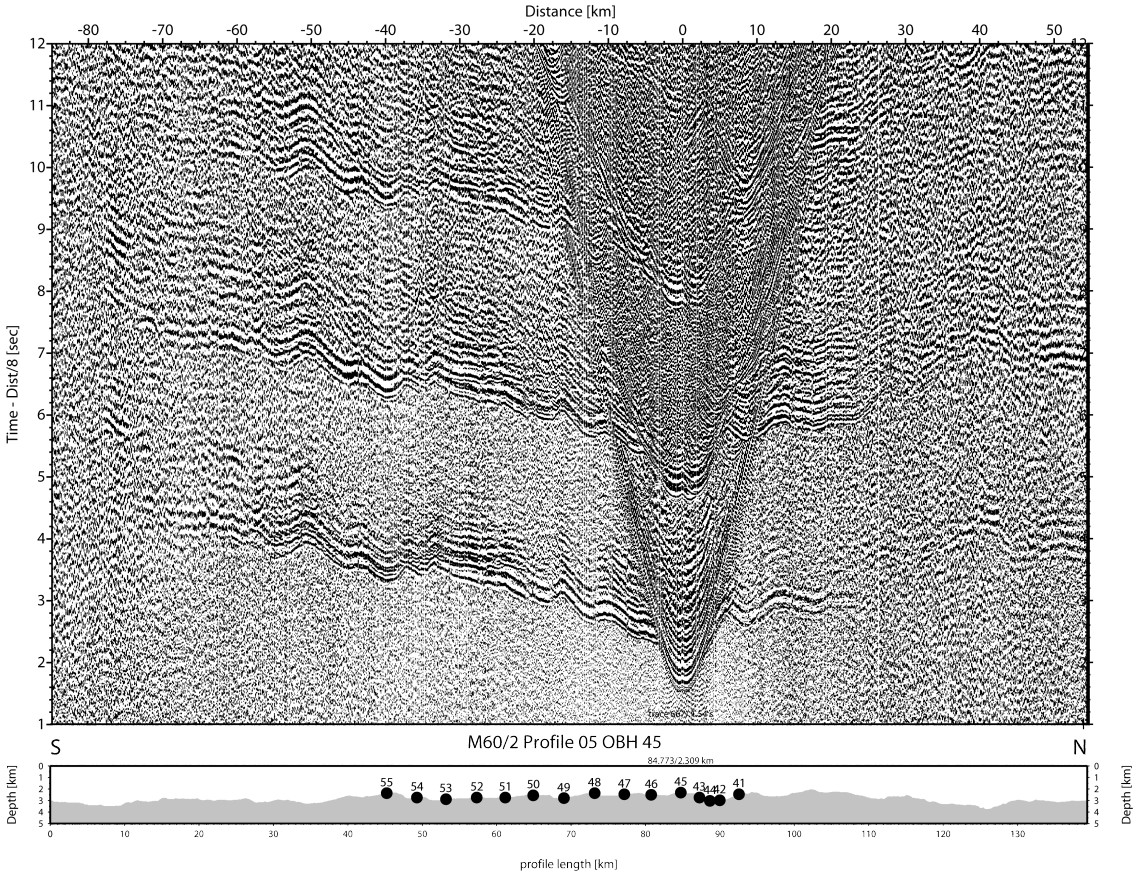

Figure C–5: Record section from OBH 45.

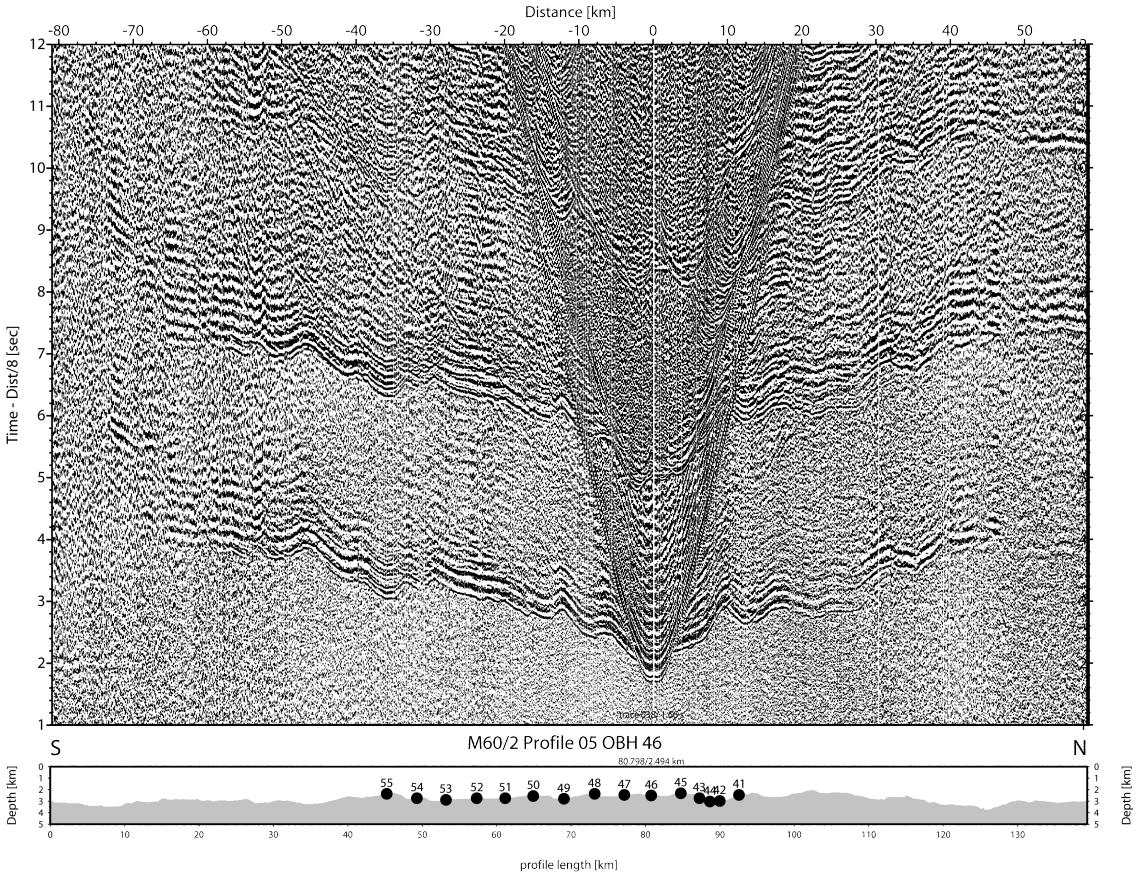

Figure C–6: Record section from OBH 46.

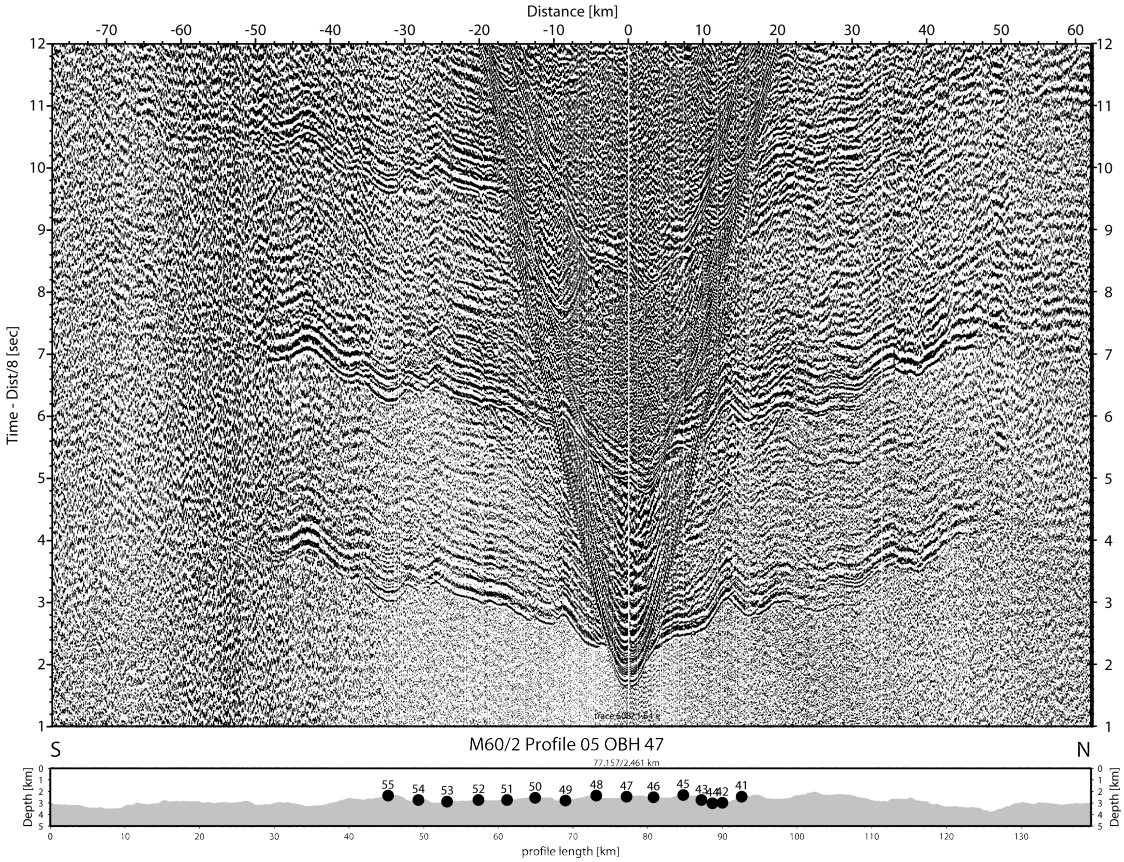

Figure C-7: Record section from OBH 47.

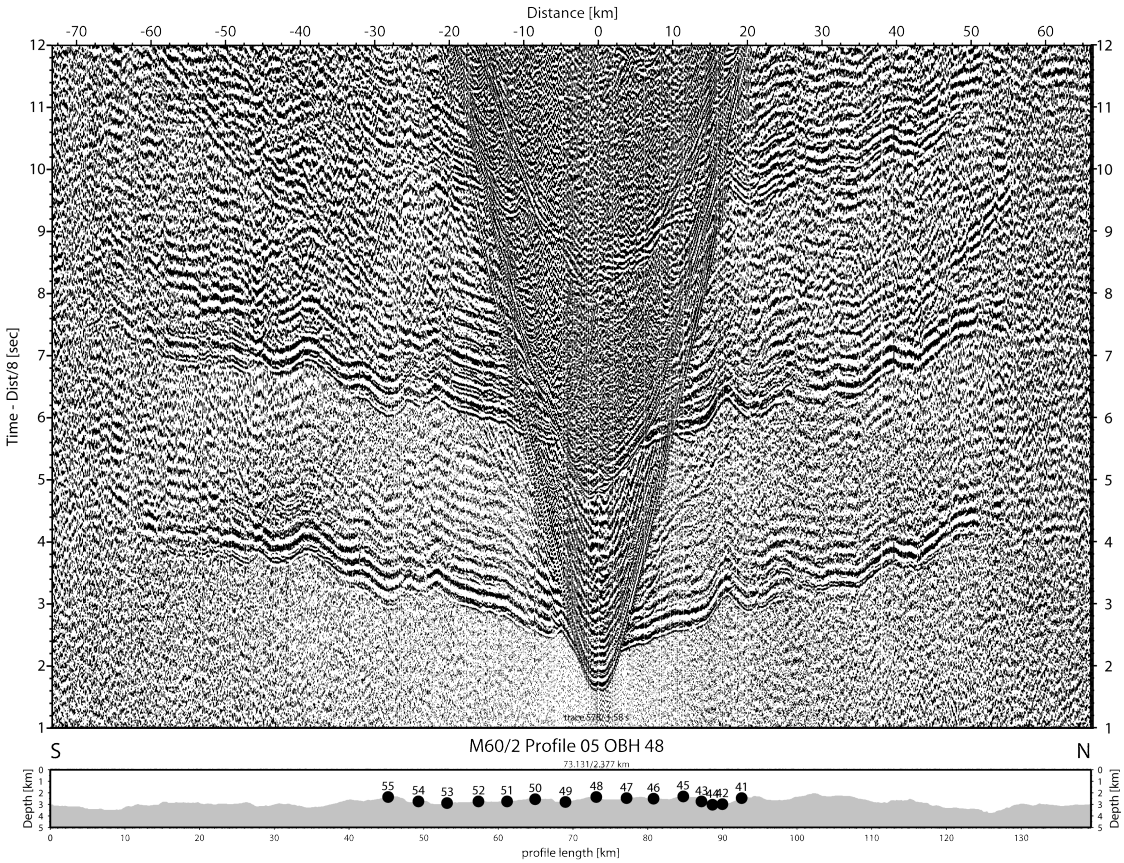

Figure C-8: Record section from OBH 48.

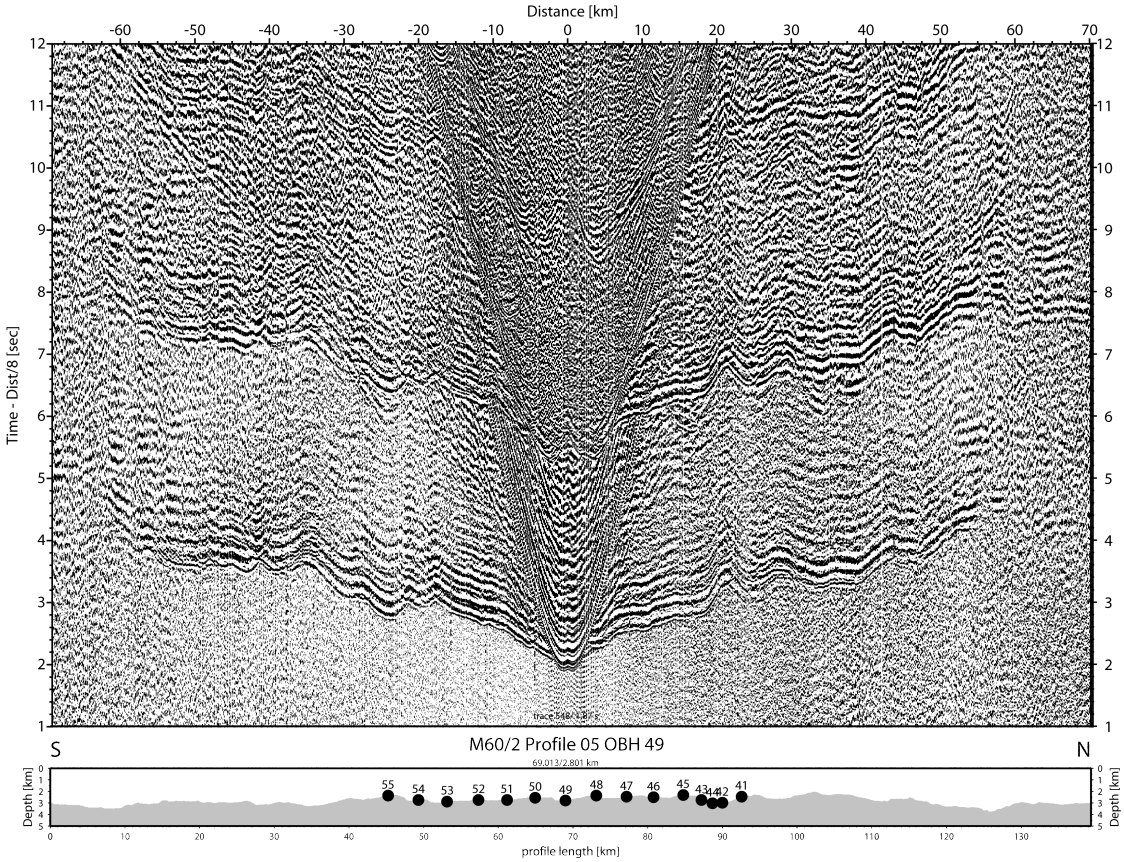

Figure C-9: Record section from OBH 49.

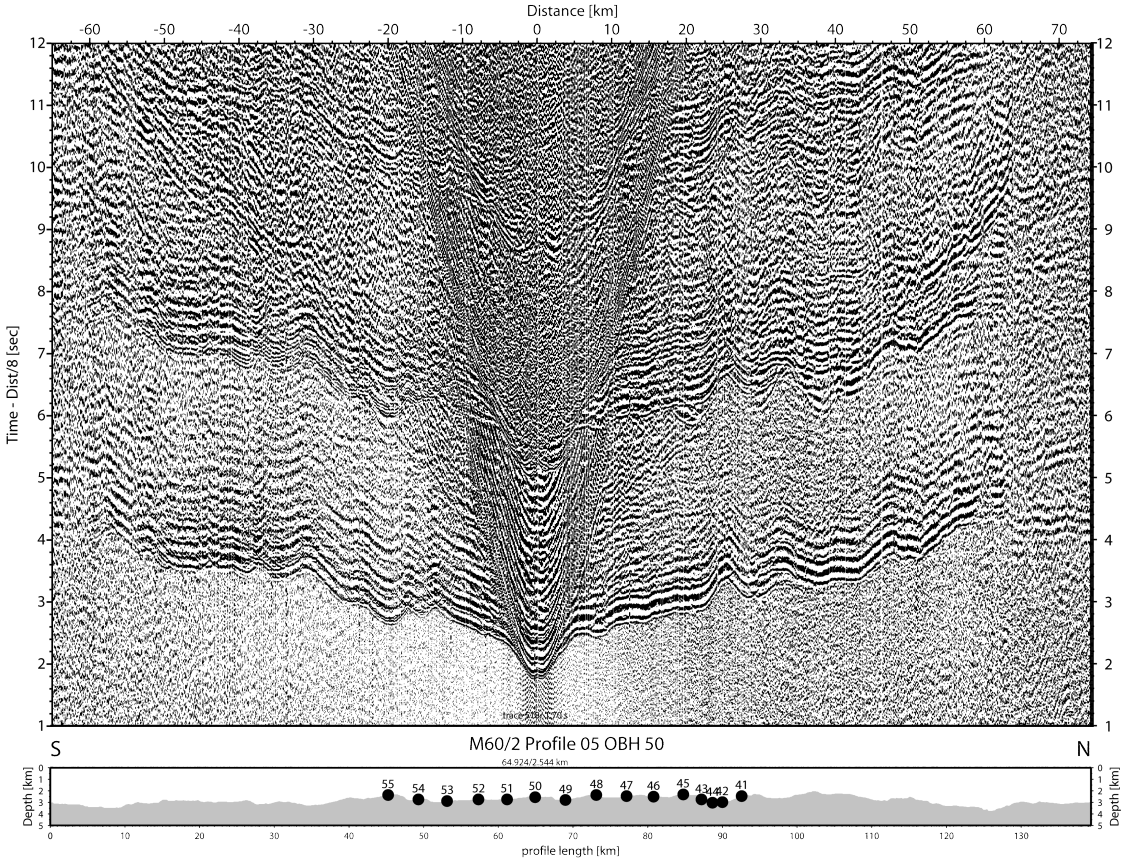

Figure C-10: Record section from OBH 50.

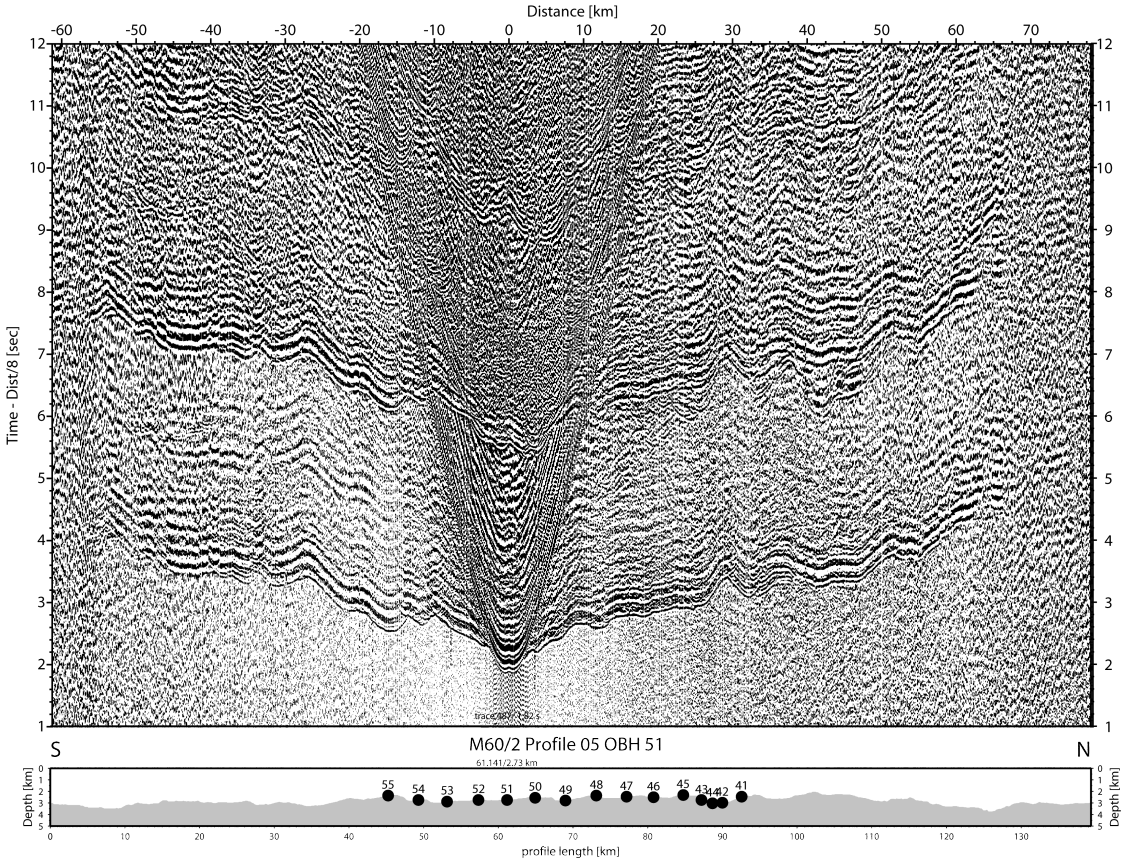

Figure C-11: Record section from OBH 51.

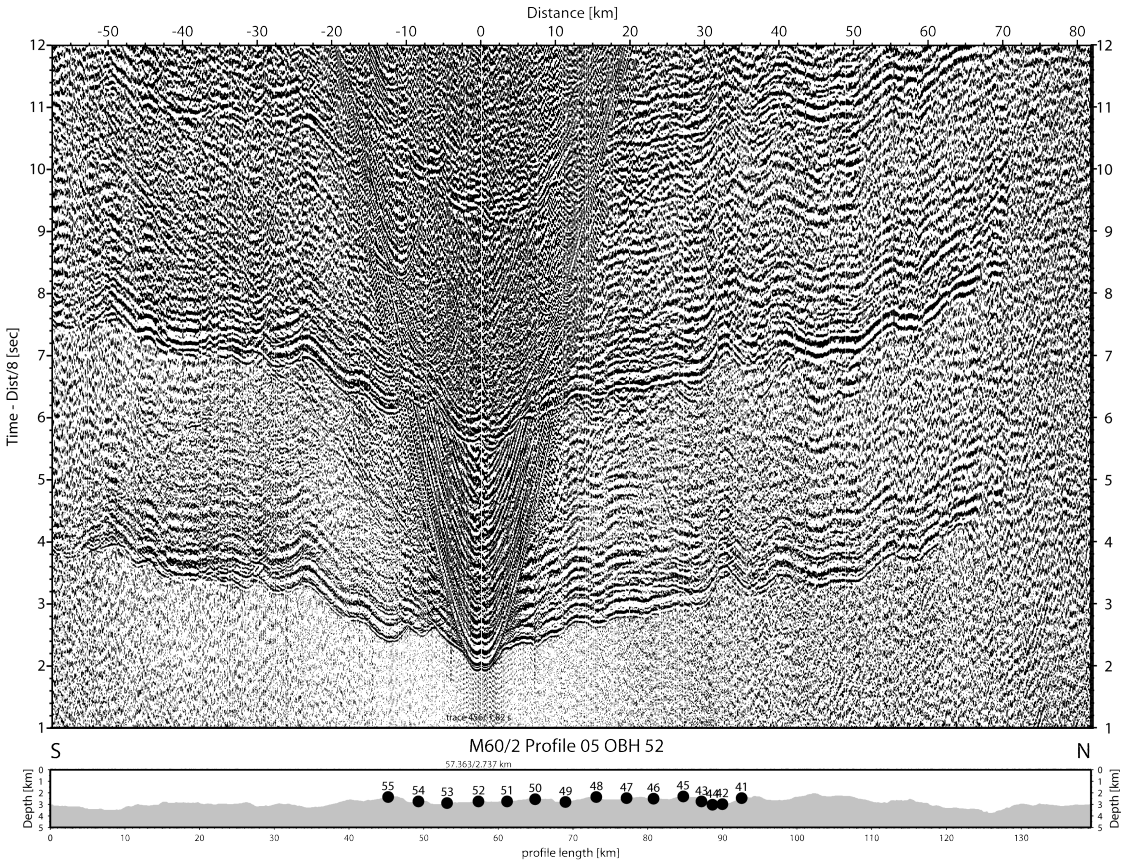

Figure C-12: Record section from OBH 52.

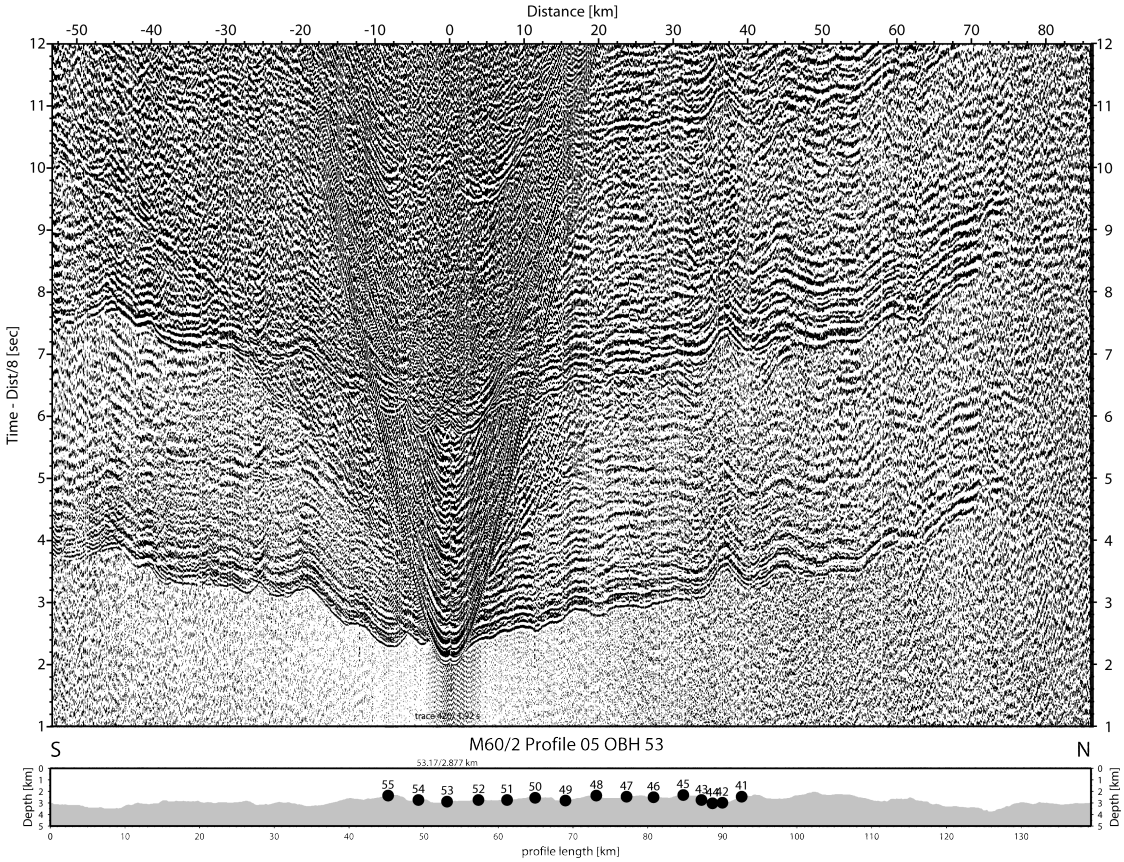

Figure C-13: Record section from OBH 53.

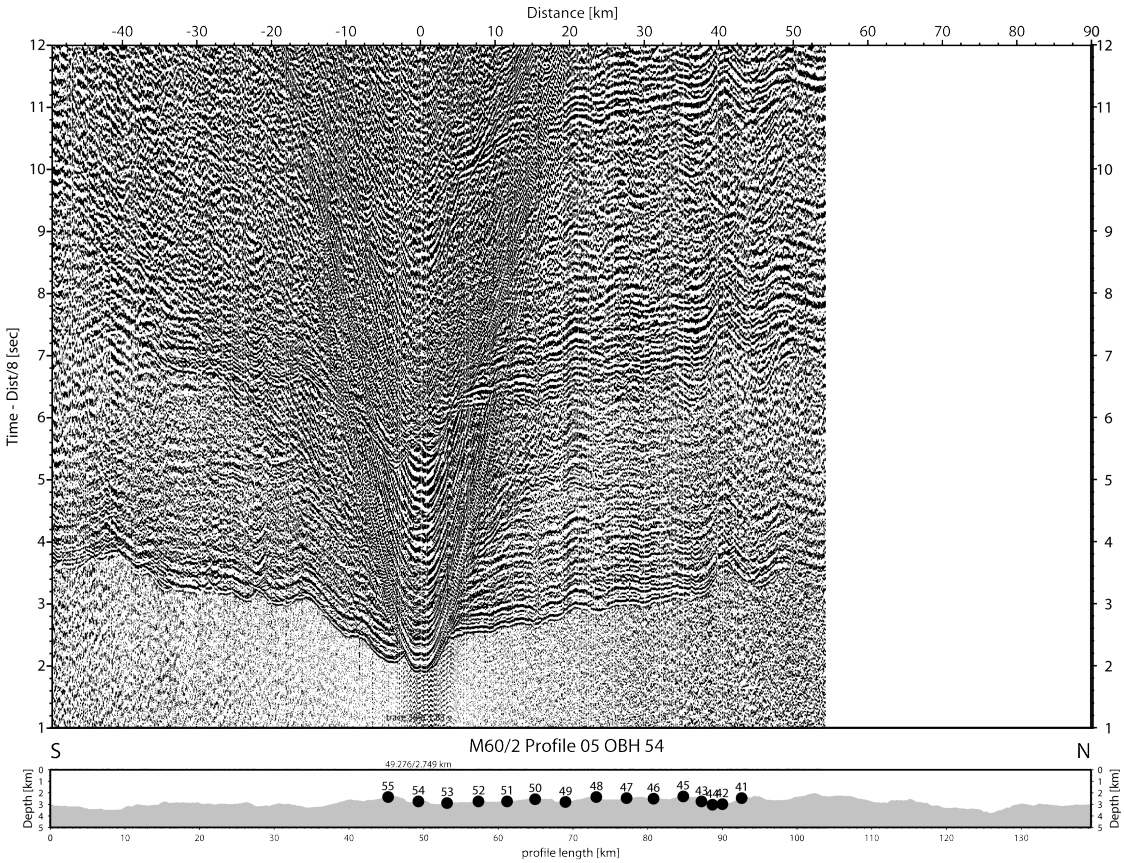

Figure C-14: Record section from OBH 54.

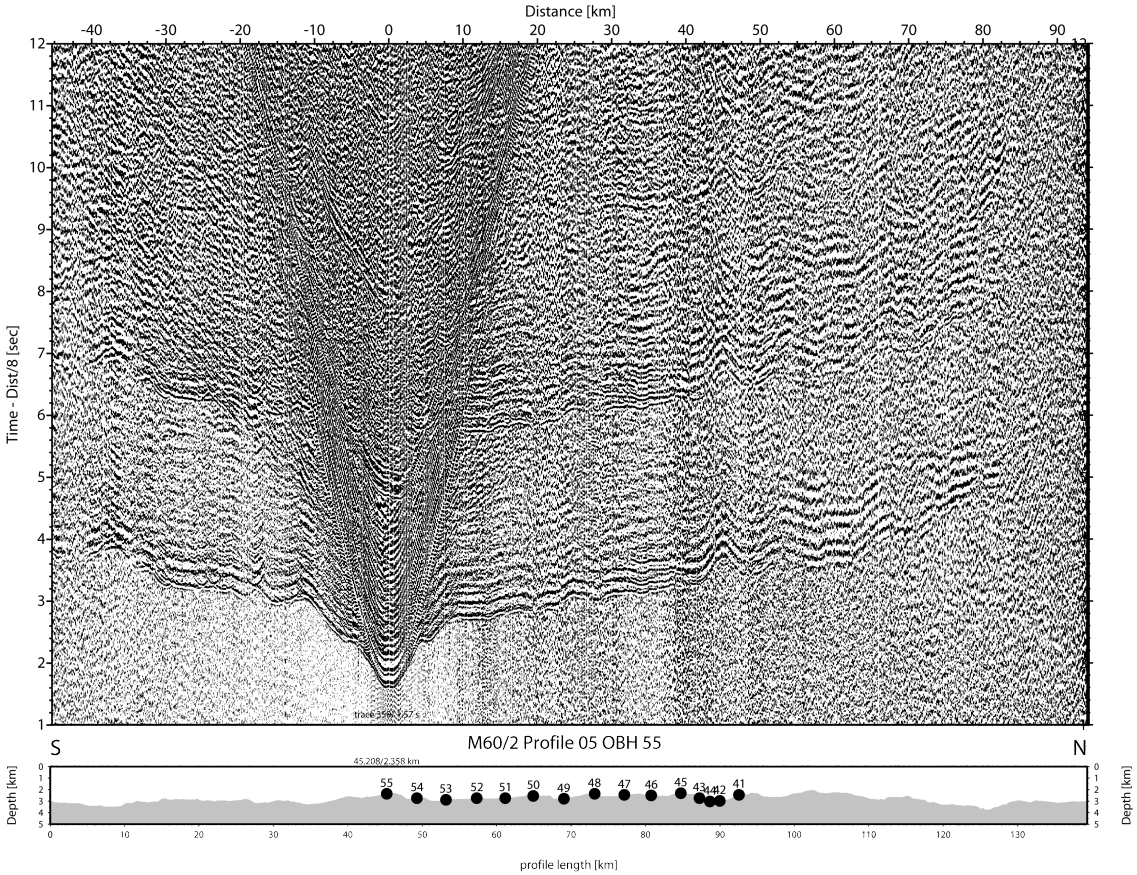

Figure C–15: Record section from OBH 55.

D – Profile 08

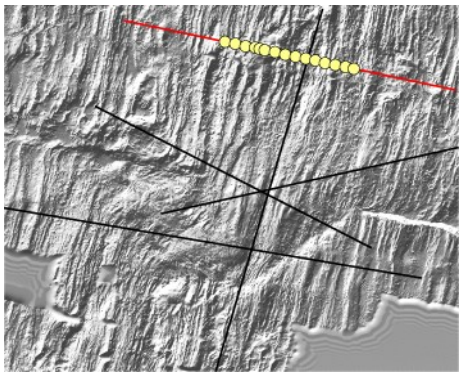

Figure D-1: Location map for profile 08 including the instruments.

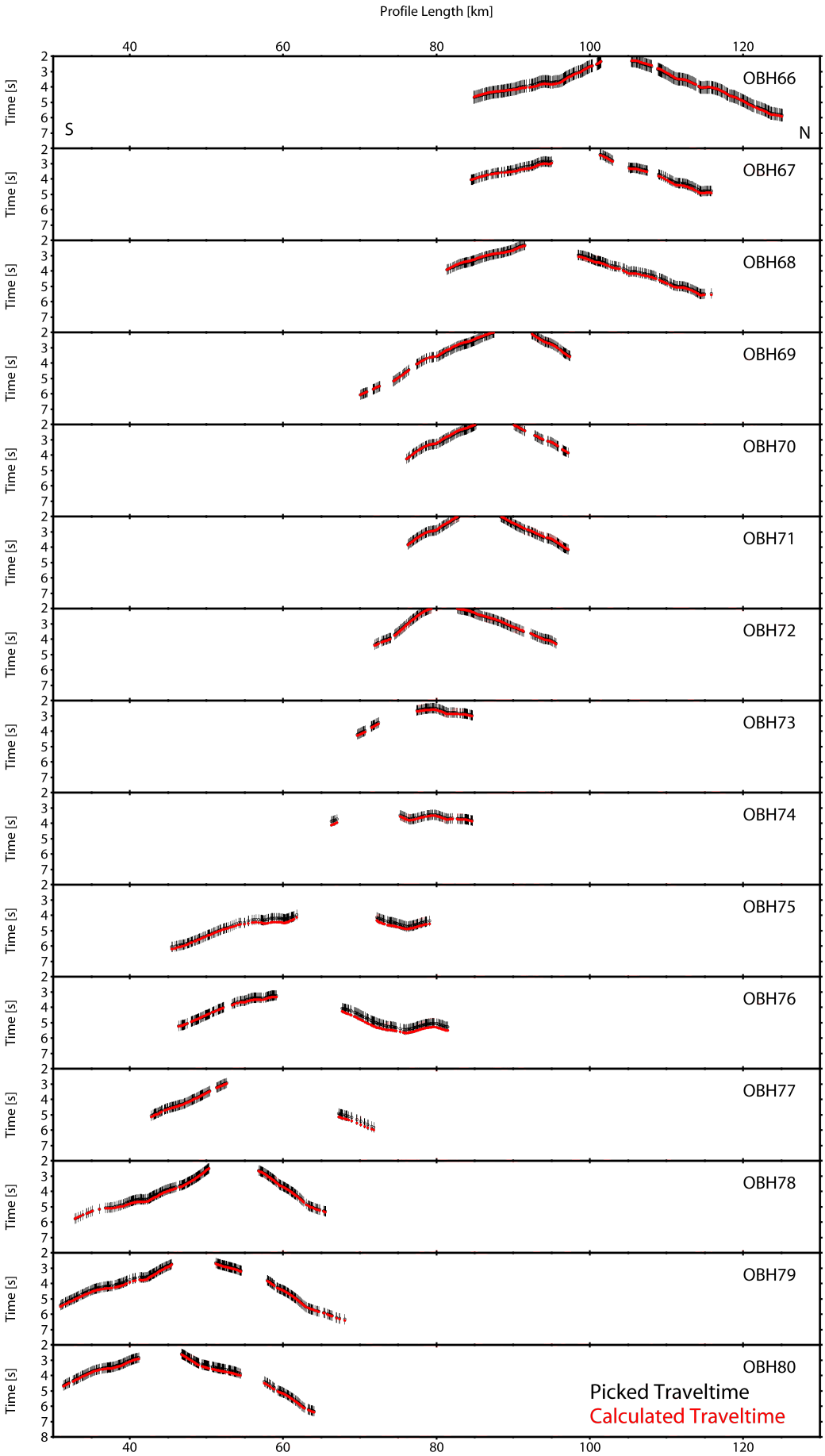

Figure D-2: Observed and calculated travel times of P-wave arrivals for P08.

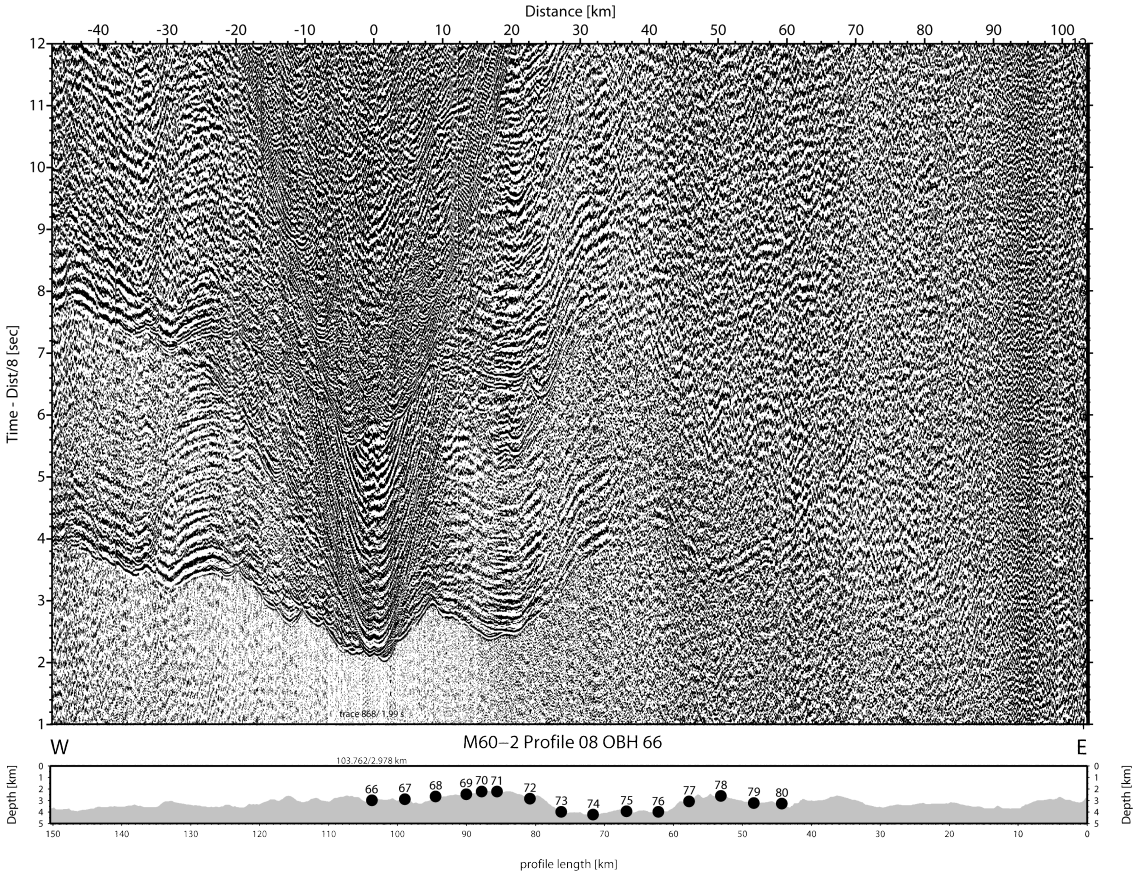

Figure D–3: Record section from OBH 66.

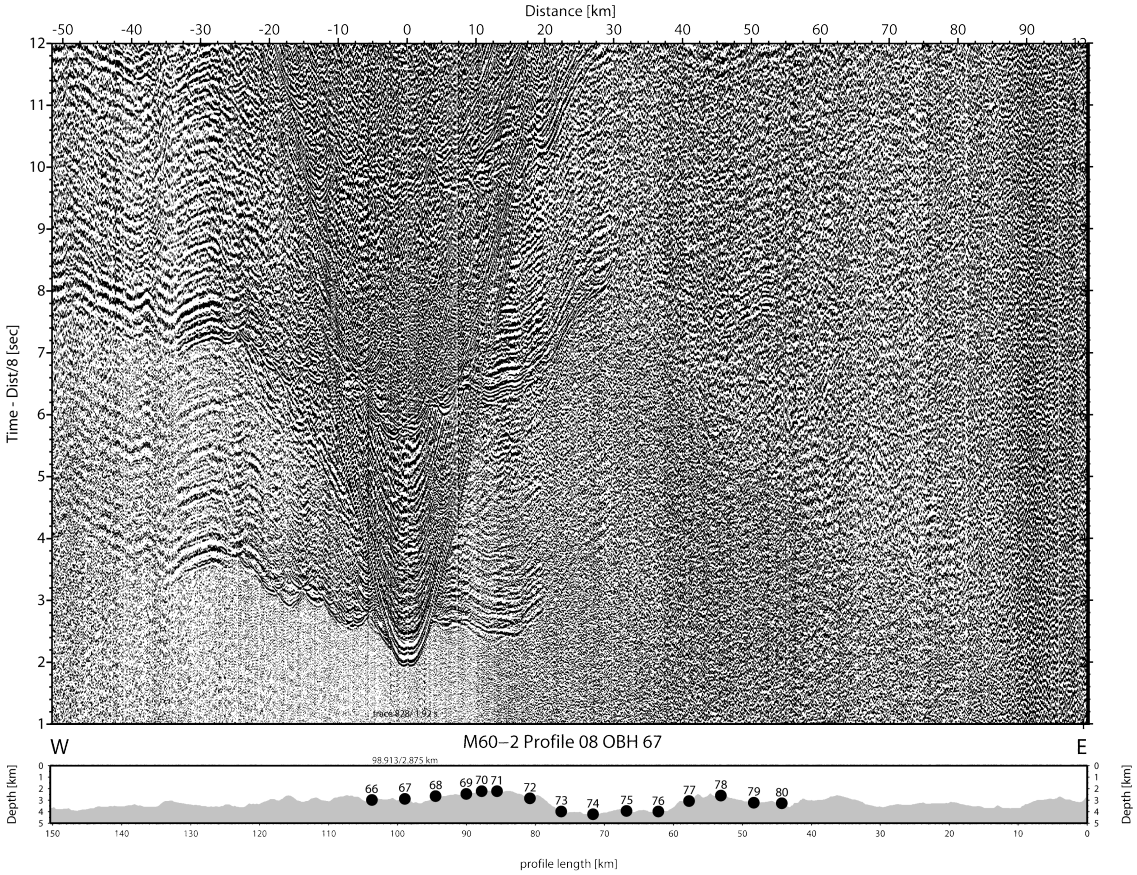

Figure D–4: Record section from OBH 67.

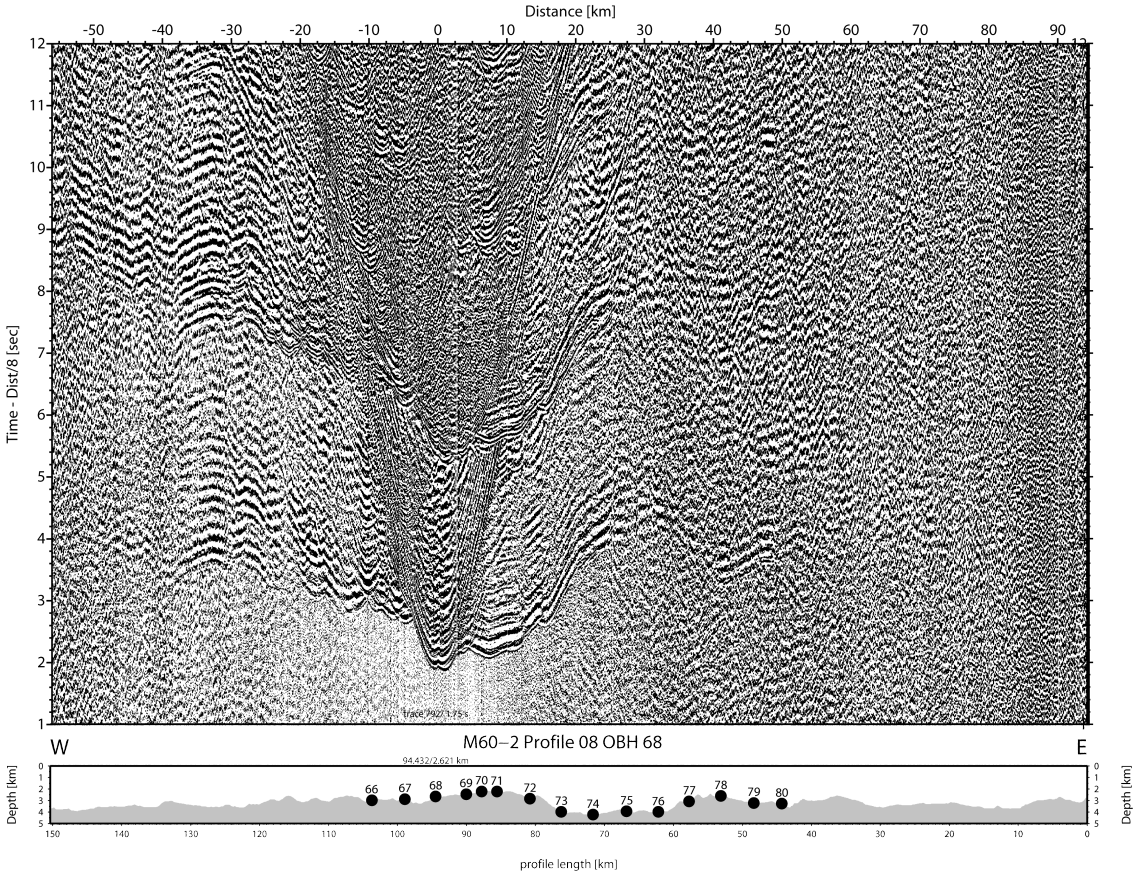

Figure D–5: Record section from OBH 68.

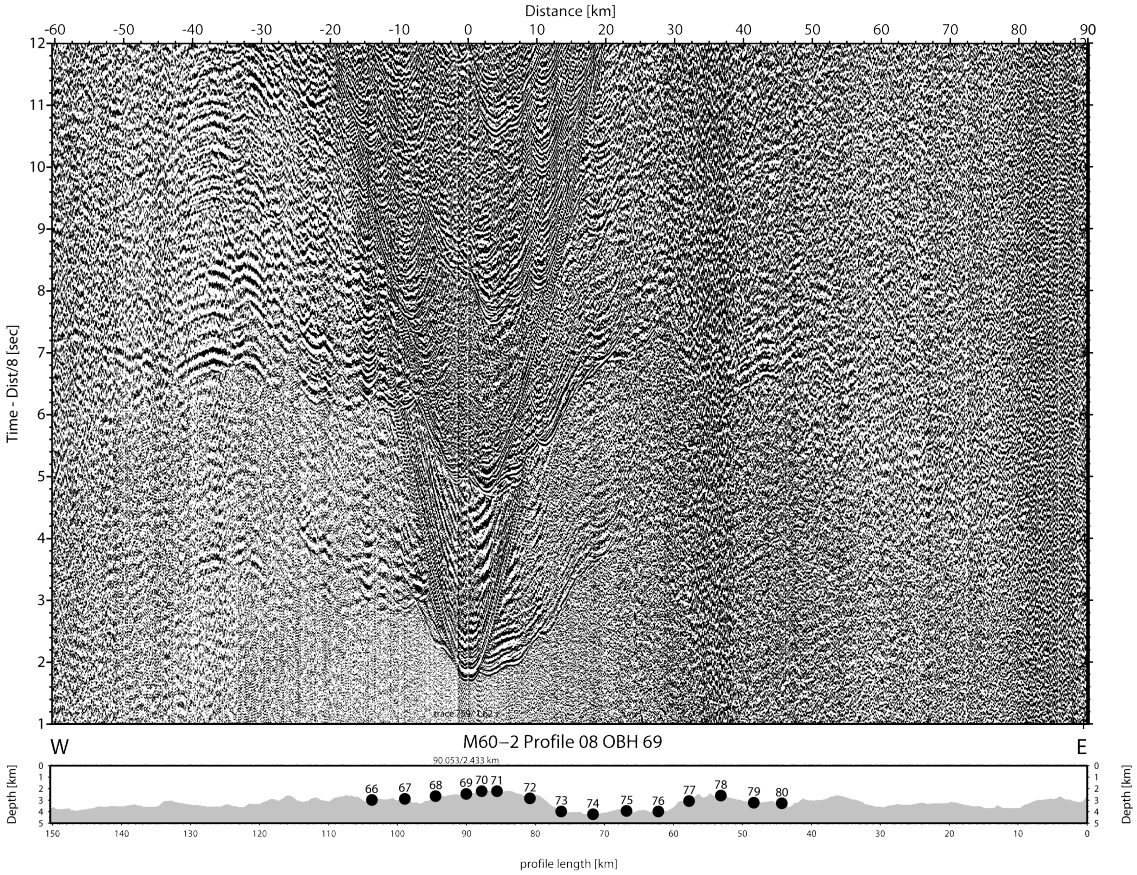

Figure D–6: Record section from OBH 69.

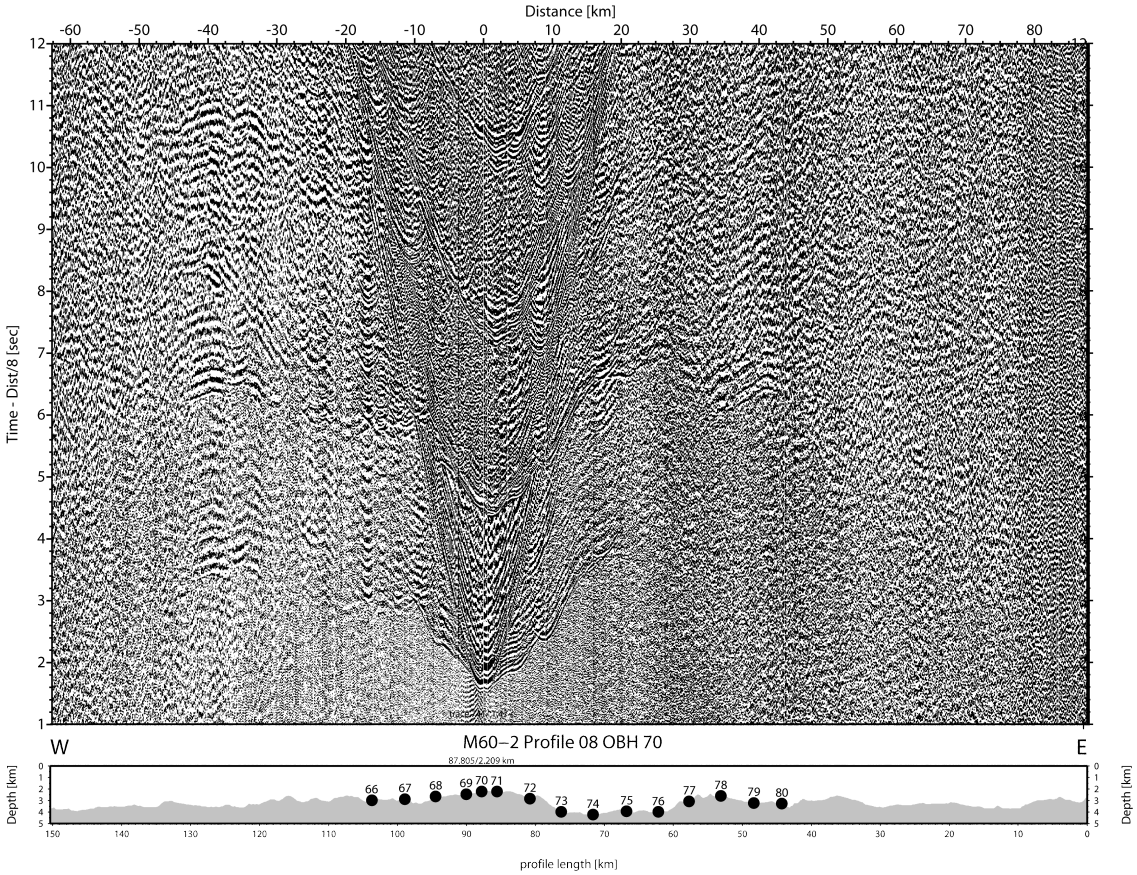

Figure D–7: Record section from OBH 70.

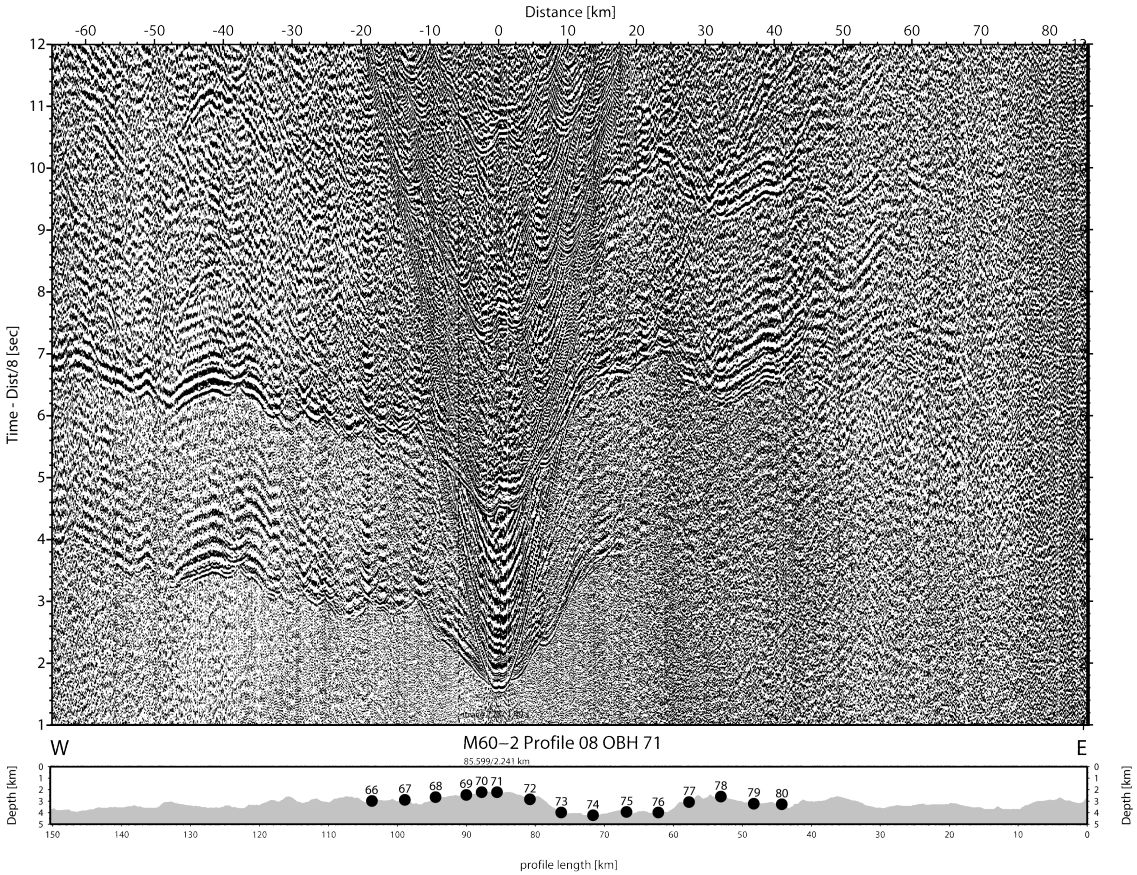

Figure D–8: Record section from OBH 71.

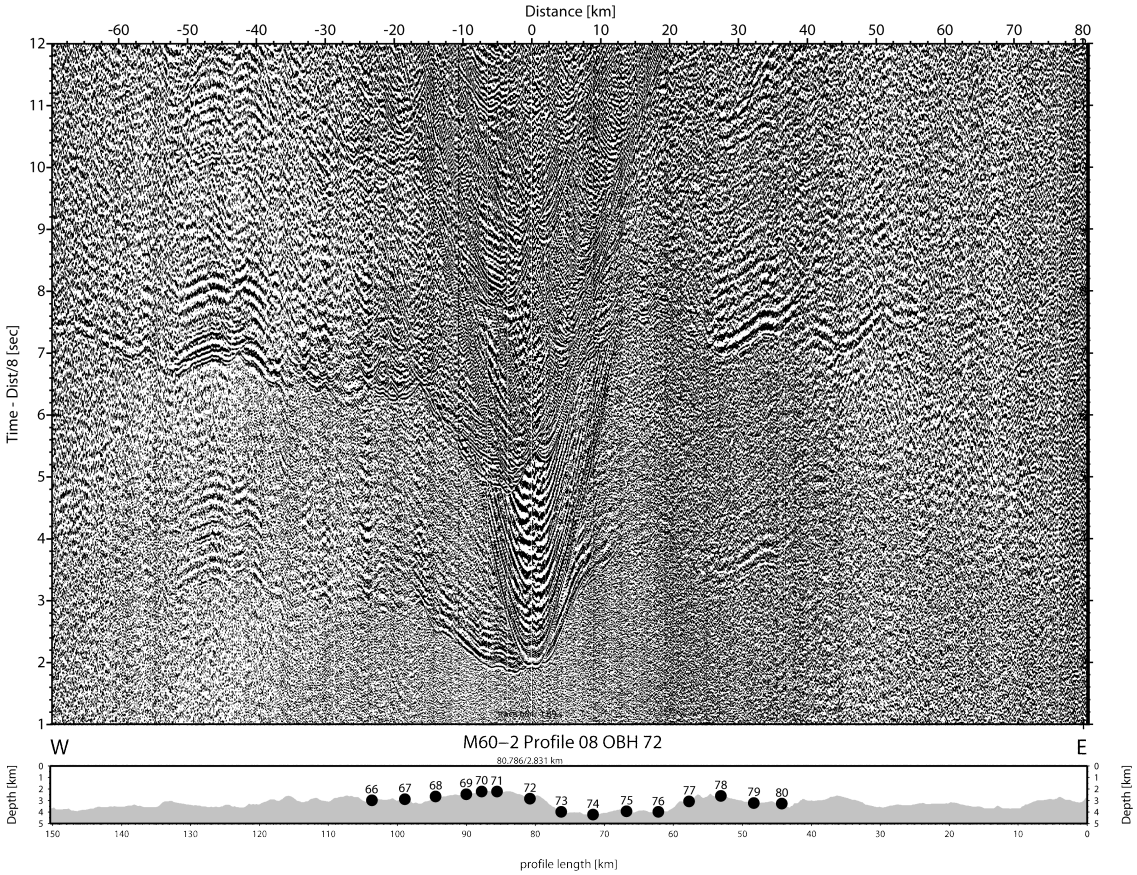

Figure D–9: Record section from OBH 72.

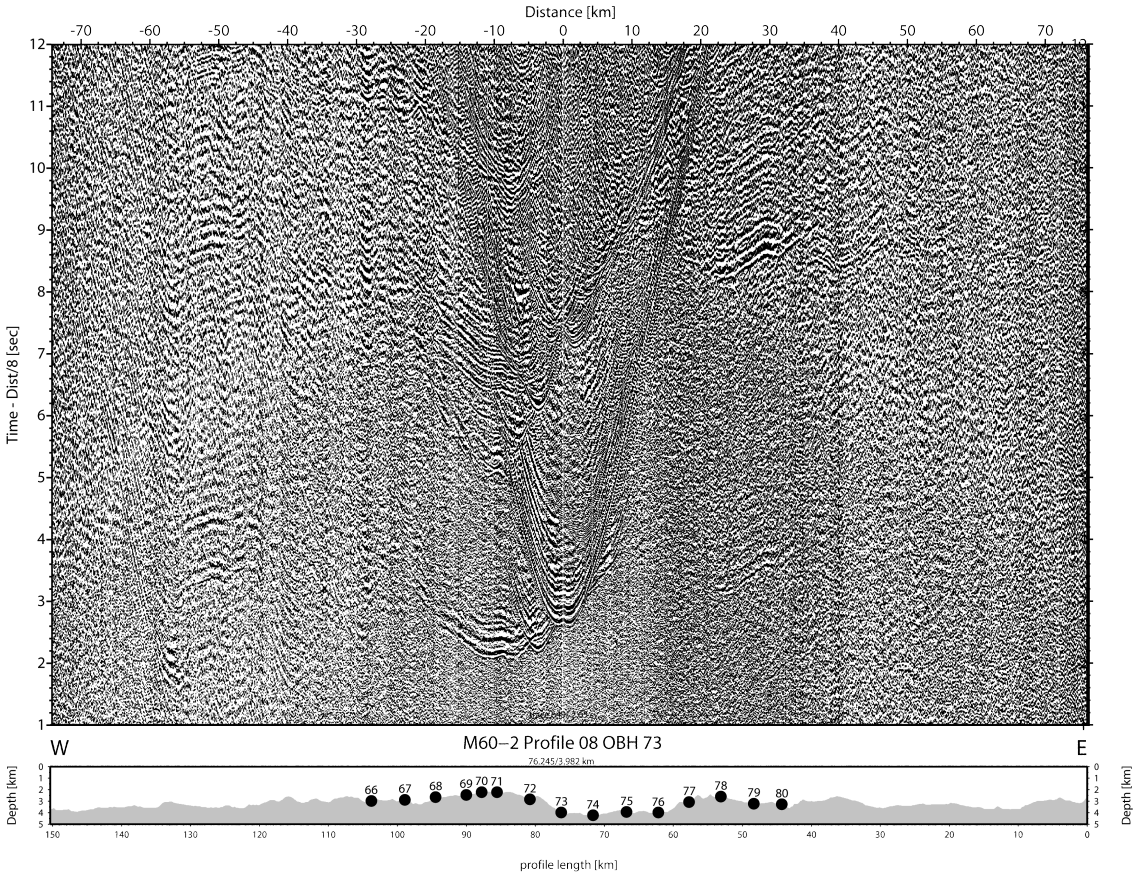

Figure D–10: Record section from OBH 73.

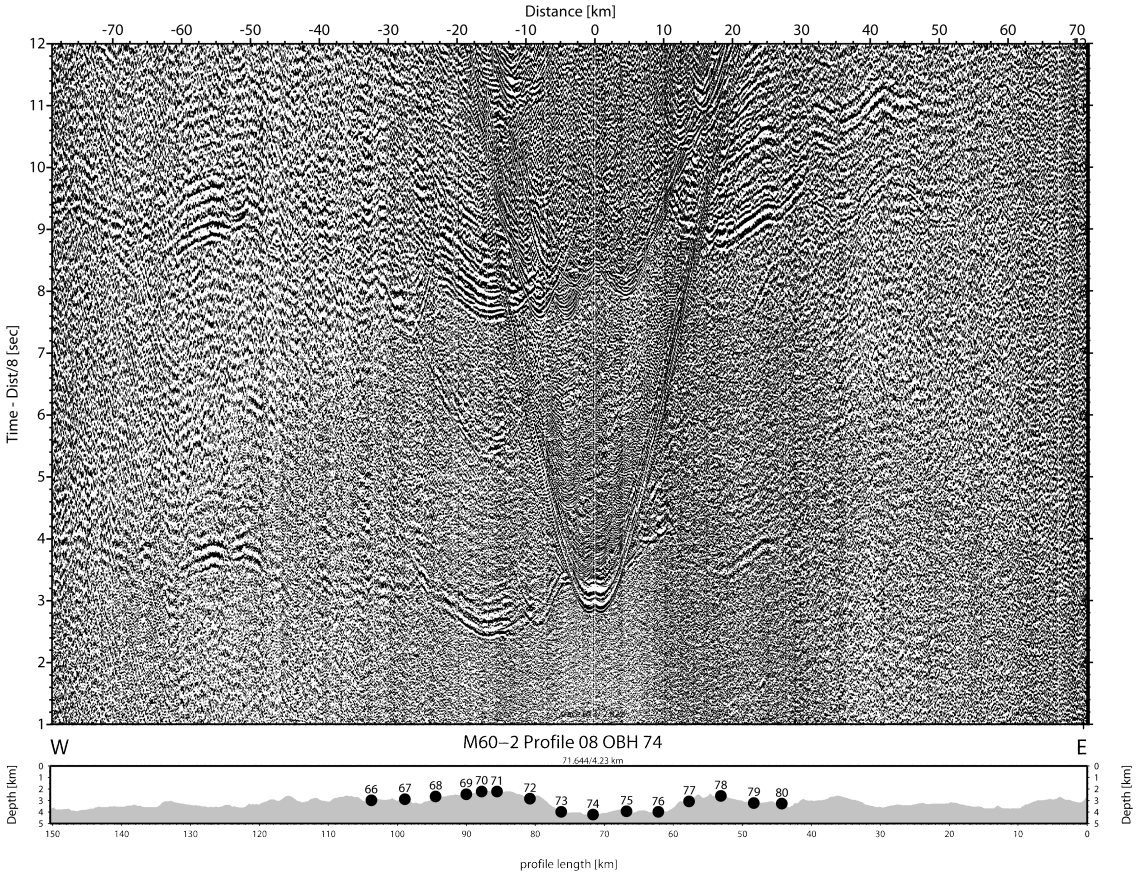

Figure D–11: Record section from OBH 74.

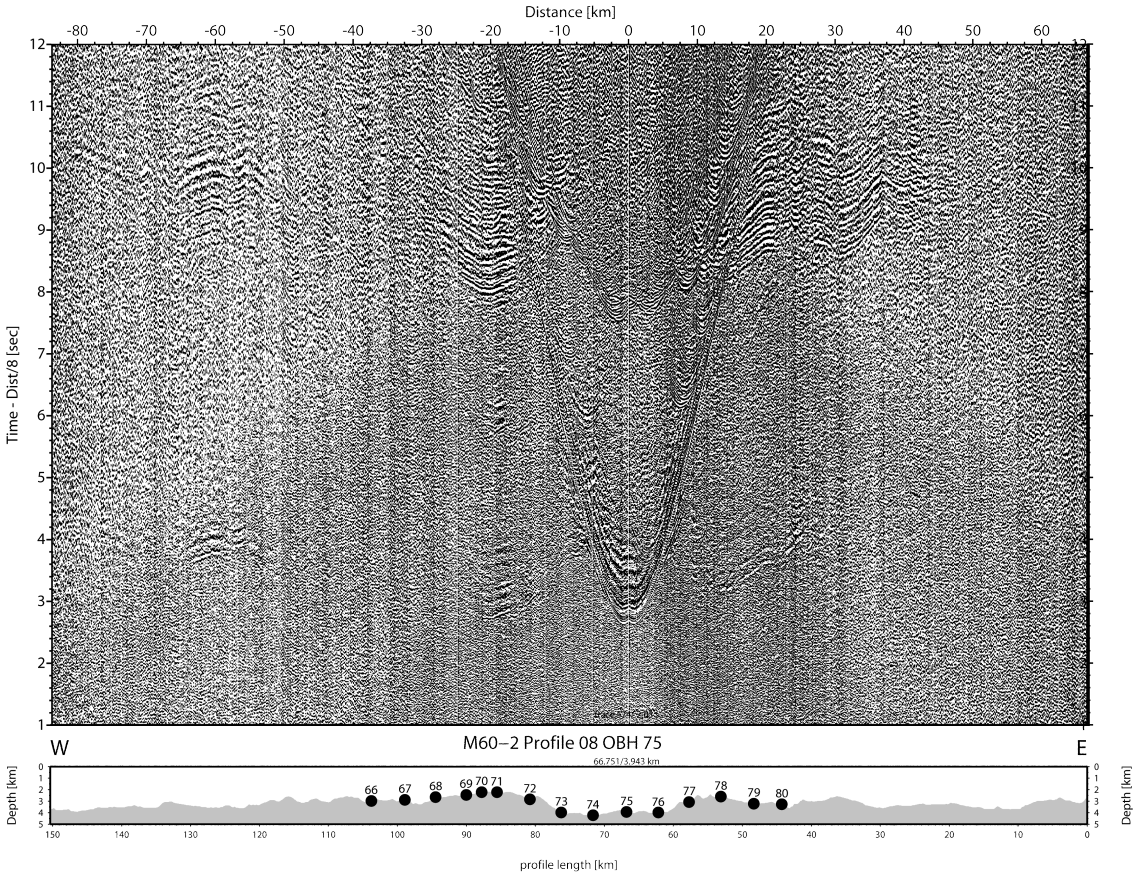

Figure D–12: Record section from OBH 75.

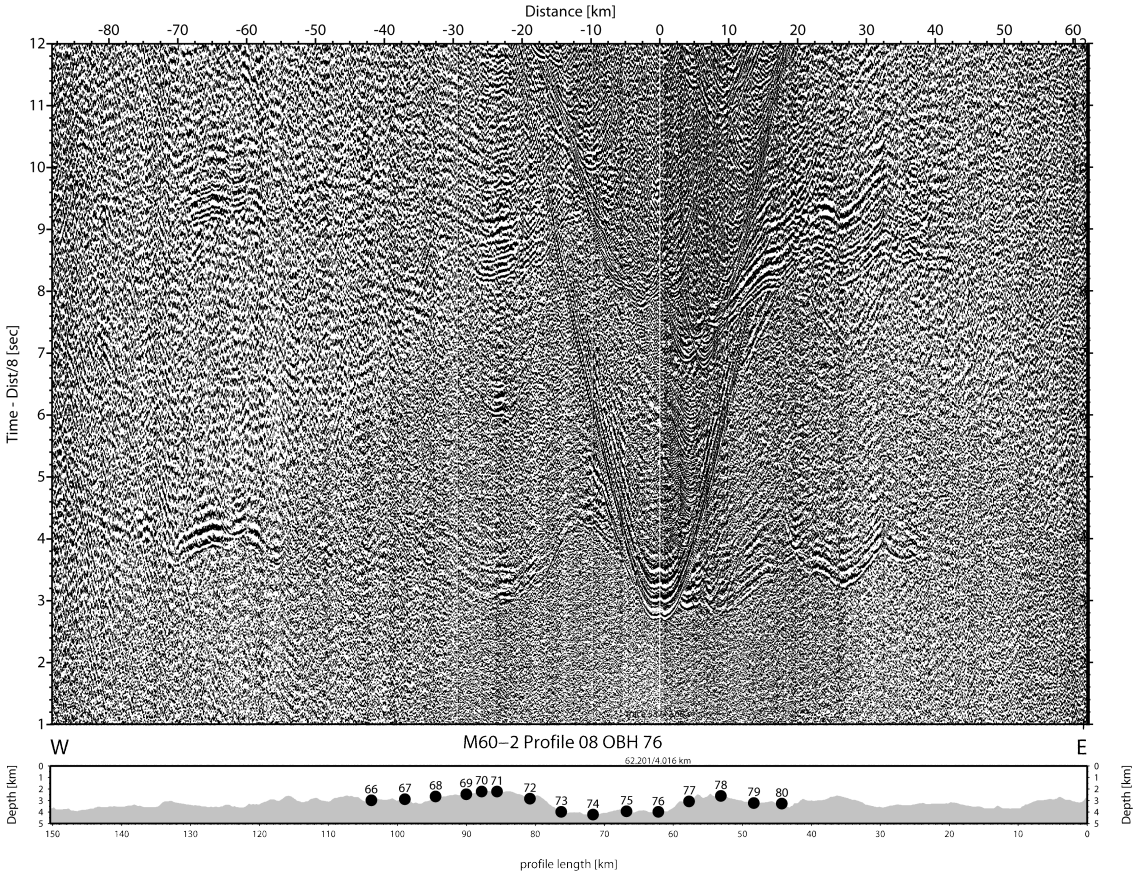

Figure D–13: Record section from OBH 76.

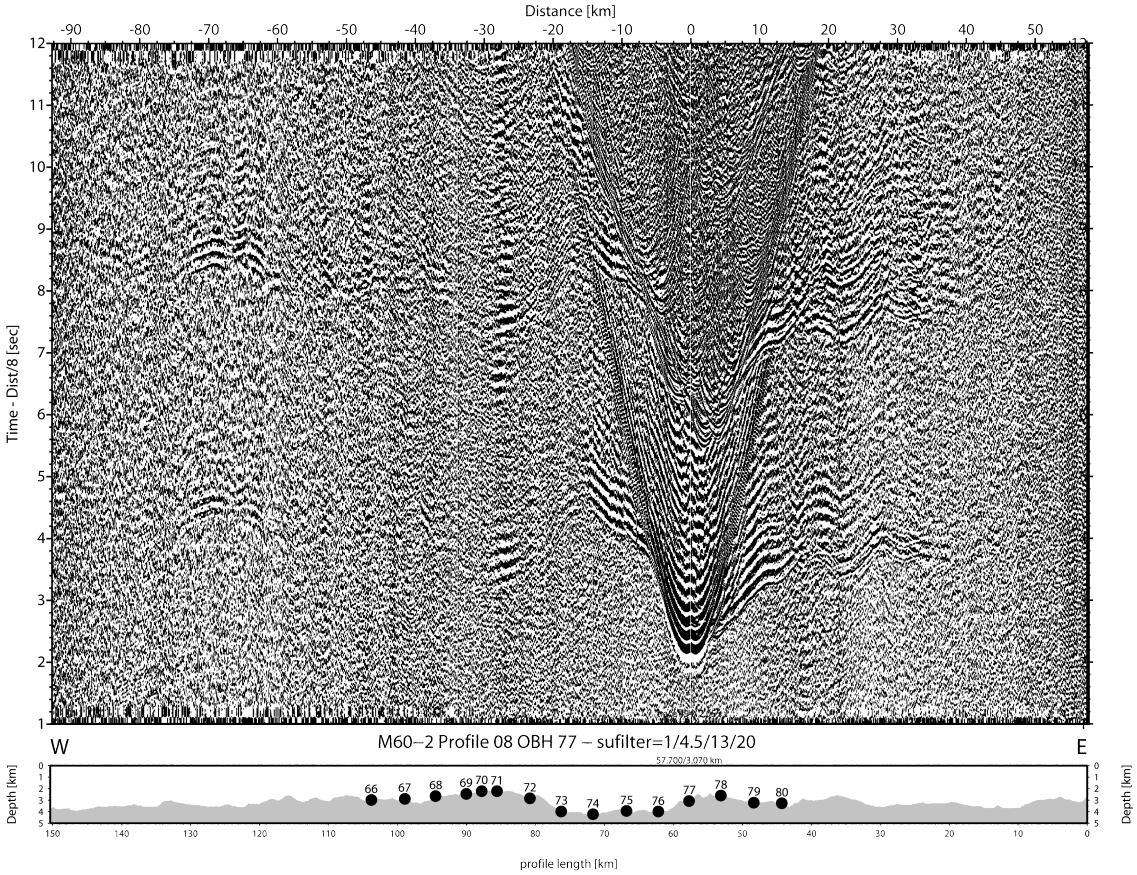

Figure D–14: Record section from OBH 77.

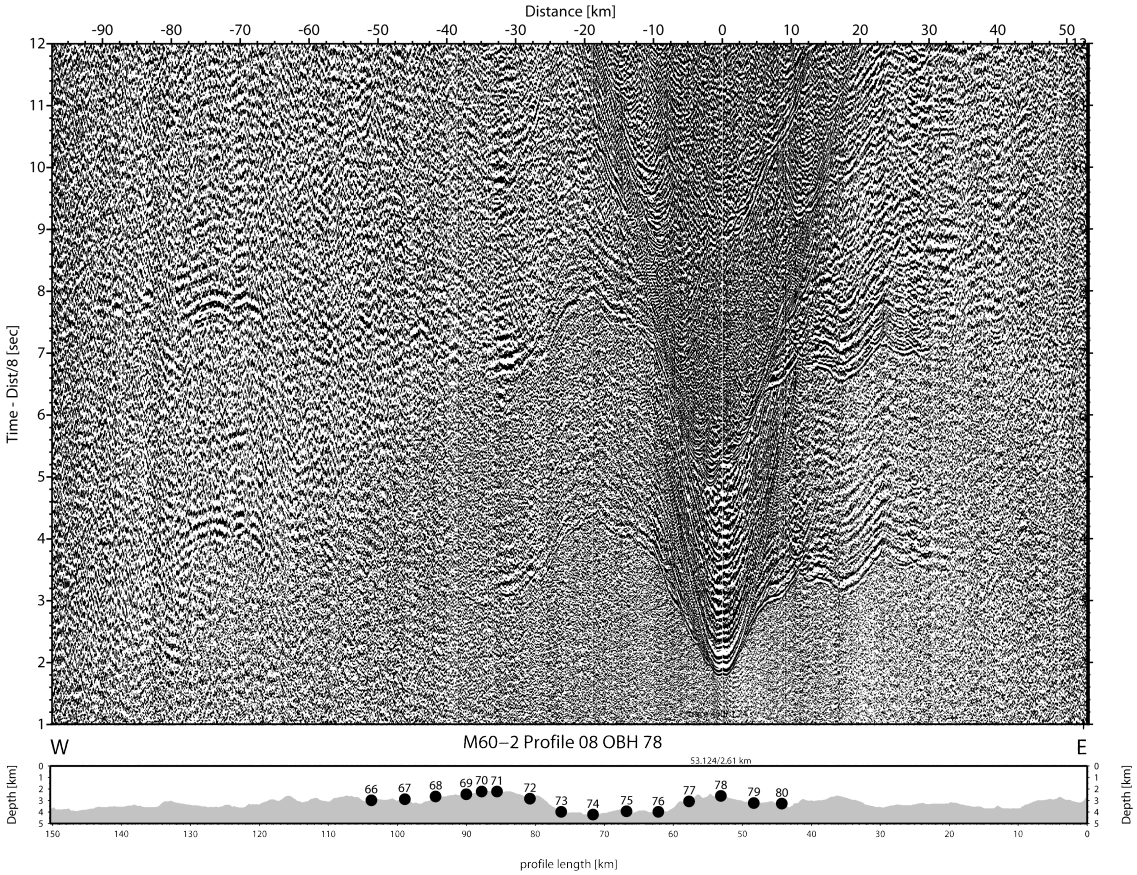

Figure D–15: Record section from OBH 78.

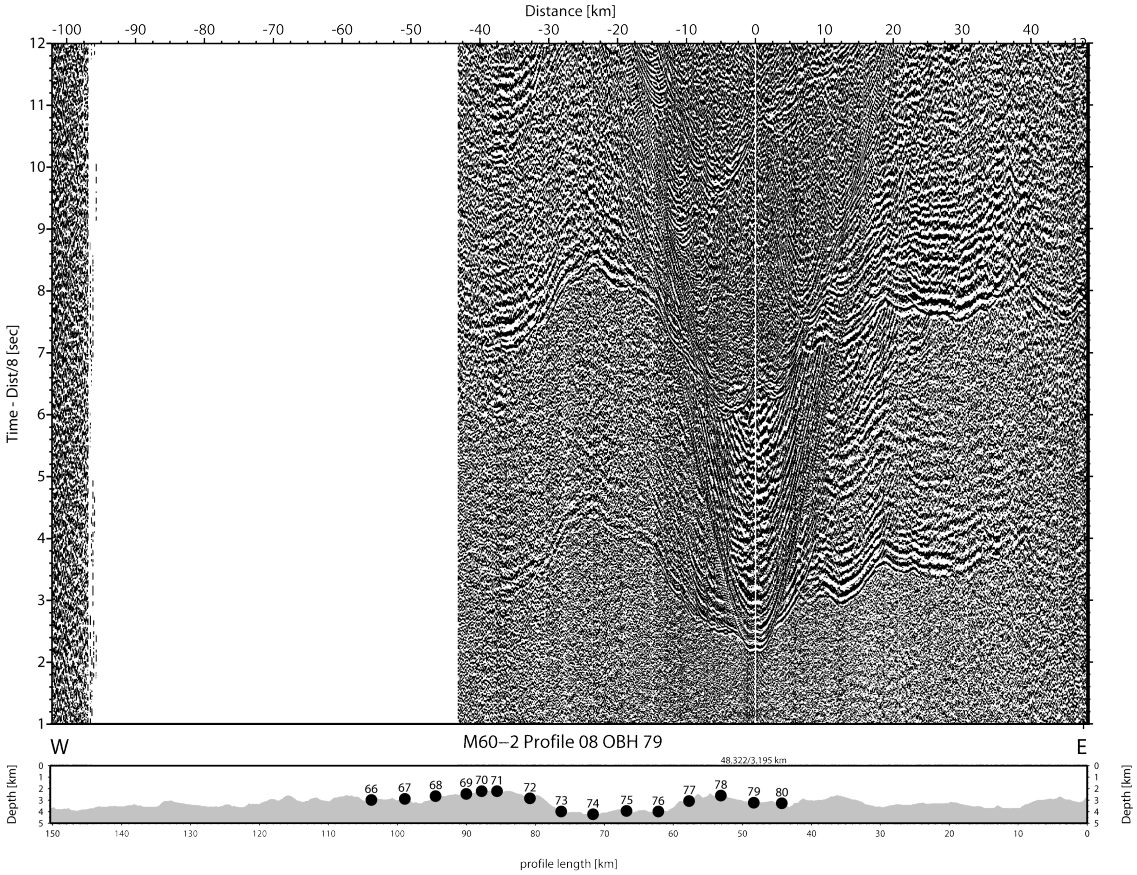

Figure D–16: Record section from OBH 79.

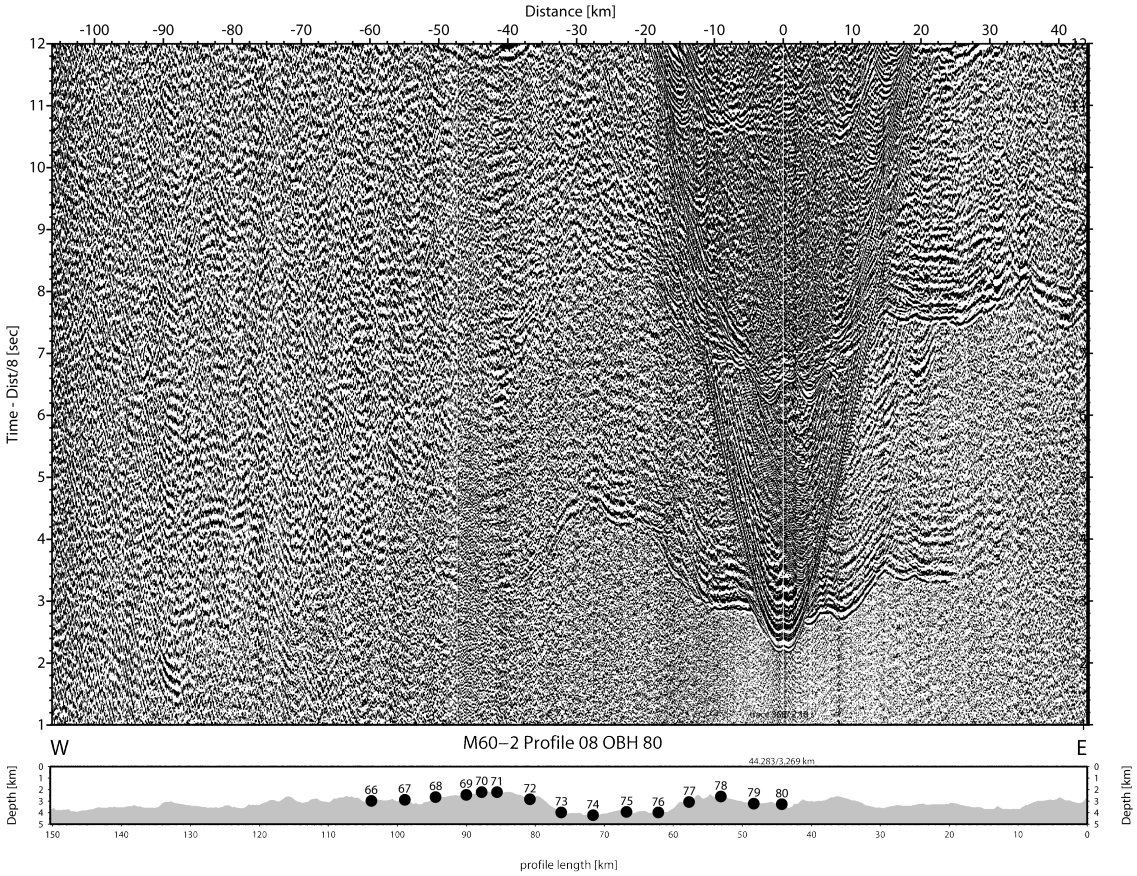

Figure D–17: Record section from OBH 80.